DOE/ET-53088-315

IFSR #315

Drift Wave Simulation in Toroidal Geometry

Maurice Joseph LeBrun, III

Institute for Fusion Studies
The University of Texas at Austin
Austin, Texas 78712

March 1988

DRIFT WAVE SIMULATION IN TOROIDAL GEOMETRY

by

MAURICE JOSEPH LEBRUN III, B.S.

DISSERTATION

Presented to the Faculty of the Graduate School of

The University of Texas at Austin

in Partial Fulfillment

of the Requirements

for the Degree of

DOCTOR OF PHILOSOPHY

THE UNIVERSITY OF TEXAS AT AUSTIN

May, 1988

Dedicated to my wife, Kathy,

and my daughter, Stefanie.

Abstract

The drift wave, a general category of plasma behavior arising from a plasma inhomogeneity, is studied using the particle simulation method. In slab geometry, the drift wave (or universal mode) is stabilized by any finite amount of magnetic shear. In toroidal geometry, however, the coupling of the poloidal harmonics gives rise to a new branch of drift wave eigenmodes called the toroidicity-induced mode, which is predicted to be unstable in some regimes. The drift wave in a toroidal system is intrinsically three-dimensional, and is sensitive to the handling of the parallel electron dynamics, the (nearly) perpendicular wave dynamics, and the radial variation of magnetic field vector (shear). A simulation study must therefore be kinetic in nature, motivating the extension of particle simulation techniques to complex geometries. From this effort a three dimensional particle code in a toroidal coordinate system has been developed and applied to the toroidal drift wave problem. The code uses an (r, θ, ϕ)-type coordinate system, and a nonuniform radial grid that increases resolution near the mode-rational surfaces. Full ion dynamics and electron guiding center dynamics are employed. Further, the algorithm incorporates a straightforward limiting process to cylindrical geometry and slab geometry, enabling comparison to the theoretical results in these regimes.

Simulations of the density-driven modes in toroidal geometry retain a single toroidal mode number ($n = 9$). In this regime, the poloidal harmonics are expected to be strongly coupled, giving rise to the marginally unstable toroidicity-induced drift mode. Analysis of the simulation data reveals a strong,

Acknowledgments

I gratefully thank my advisor, Toshiki Tajima, for his enthusiasm and assistance in support of this project. He has helped me to see the bigger picture, a valuable asset when one is faced with a difficult problem. I also thank Jean Noel Lebouef, with whom I have had numerous discussions on the subtleties of particle simulation. I am indebted to Dan Barnes, for pointing the way to a clear and efficient program structure in the supercomputer environment. The iterative field solver was first suggested by Ahmet Aydemir, clearing an important obstacle in the early development of the algorithm. I have also benefitted from discussions with Dave Ross, Jim Van Dam, Richard Sydora, Earnest Zaidman, and Jim Geary.

This work was carried out at the Institute for Fusion Studies at the University of Texas, and the assistance of the staff members is deeply appreciated. I especially thank Joe Sedlak for his help with the interactive rootfinder and shooting codes, used in the analysis of simulation data. In addition, I acknowledge the important role of the National Magnetic Fusion Energy Computer Center in providing an excellent environment for large-scale computation.

Finally, I thank my wife, Kathy, for her love and support through difficult times.

MAURICE JOSEPH LEBRUN III

The University of Texas at Austin

May, 1988

low-frequency response that peaks near each mode rational surface. Further, the characteristic oscillation frequencies persist from one mode rational surface to the next, which identifies them as multiple harmonics of the toroidicity-induced mode. The lowest harmonic occurs at a frequency of $\omega/\omega^* \sim 0.26$, which is reasonably close to the prediction of linear theory. Interferogram analysis of these modes indicates a "ballooning" structure toward the outside of the torus. The amplitude of the potential is observed to grow exponentially for the $m = 8$ through $m = 10$ poloidal mode numbers, with a growth rate of approximately $\gamma/\omega^* \sim 0.075$. Saturation occurs at time $t \sim 1000\,\Omega_i^{-1}$, and may be caused by quasilinear flattening of the density profile.

Table of Contents

List of Figures

Chapter 1

Introduction

An important challenge facing plasma physicists at present is the understanding of anomalous transport in toroidal confinement devices such as tokamaks. This transport is "anomalous" in the sense that it is much greater than classical collisional rates of diffusion; the understanding and possible control of this transport would have a profound impact on the feasibility of a fusion reactor. At present, however, the cause of anomalous transport remains unknown, though it is generally attributed to low-frequency microscopic turbulence. Although no direct evidence exists for this association, light scattering diagnostics in tokamaks uniformly reveal a fine-scale level of turbulence [1]. A good overview of research in this area is given in the review paper by Liewer [1] concentrating on research from 1977 until 1985; earlier work can be found in reviews by Tang [2] and by Kadomtsev and Pogutse [3].

Much progress in identifying large-scale features of tokamak plasmas has been made of late, often accomplished through a cooperation of theory and magnetohydrodynamic (MHD) plasma simulation. One recent example of this cooperation is the use of MHD simulation to model sawtooth oscillations [4,5]. A similar effort, incorporating both theory and particle simulation (which retains the necessary kinetic effects), may ultimately resolve the problem of anomalous transport. At present, likely candidates for driving the microturbulence in tokamaks are drift or trapped particle modes. Existing theories

of drift-wave turbulence have produced scaling laws consistent with the experimentally observed transport in some regimes [1], but much better predictive ability is needed.

This research focuses on the extension of particle simulation techniques to complex geometries, with application to the study of drift waves in toroidal geometry. The motivation is to obtain an independent result, free of many of the assumptions of the existing theories. Furthermore, particle simulation allows us to examine the plasma's temporal behavior and nonlinear dynamics, as well as the nonlinear saturation of a possible instability. This examination is done at the most fundamental level—a fully self-consistent kinetic description. The drift modes studied in this research are very low frequency, with kinetic effects essential, so detailed particle simulations are warranted. To put the current problem into proper perspective, we must first consider some of the recent history of drift wave theory.

A nonuniform plasma in a shear-free magnetic field configuration is unstable to fluctuations near the diamagnetic frequency, known as the drift or universal instability. The analysis for this case typically employs the local approximation, where it is assumed that the equilibrium and magnetic field quantities vary slowly compared with the wavelength of the mode. The resulting instability is "universal" in the sense that it requires only a density gradient—a necessary component of any confined plasma.

In a sheared magnetic field, however, the local treatment is no longer valid, as pointed out in 1969 by Pearlstein and Berk [6]. This treatment differed from the earlier local theories by considering a non-local eigenmode equation, with the solutions subject to outgoing wave boundary conditions. The eigenmode equation thus derived gave rise to a family of normal-mode solutions re-

lated to the Hermite polynomials (known presently as Pearlstein-Berk modes). In addition, the shear stabilization condition from these results predicted that short wavelength modes were unstable, even for strong values of the shear.

This situation changed dramatically in the late 1970's, when several concurrent research efforts showed the drift wave in a sheared slab to be absolutely stable for any finite amount of shear [7,8]. These papers showed that for the correct, stable result to be obtained, the nonresonant electron response must be included in the integration of the eigenmode equation near the mode rational surface. This result was very important, for the universal mode was generally thought to be involved in the electrostatic fluctuations observed in many tokamak plasmas [2]. Therefore, subsequent theoretical investigations have focused on additional effects which may destabilize the drift wave. These effects fall into two main categories.

One destabilizing mechanism, first proposed by Hirshman and Molvig [9], examines the effect of a given level of microturbulence on the stability of the drift mode. Specifically, the turbulent diffusion of electrons across the mode rational surfaces in the sheared slab may modify the nonresonant electron response sufficiently to drive an instability. In three dimensions, the drift-wave resonance regions of adjacent mode rational surfaces may overlap, giving rise to this stochastic electron behavior [10]. Recent self-consistent particle simulations by Sydora *et al.* [11] have confirmed the existence of a growing mode in this configuration. A theoretical treatment by Zhang, Marchand, and Lee [12] also showed the existence of a growing mode in the presence of a stochastic magnetic field, a result qualitatively similar to that of Hirshman and Molvig. This "stochasticity-induced" mode is found to occur for $k_\perp \rho_i \gtrsim 1$, (where ρ_i is the rms ion Larmor radius and $k_\perp$ is the perpendicular wavenumber), and

values of the shear near tokamak levels ($L_s/L_n \gtrsim 10$, L_s and L_n the shear and density scale lengths, respectively).

The other destabilizing mechanism that has been studied is the inclusion of toroidal geometry effects, such as poloidal mode coupling and trapped particles. In a toroidal system, the variation of magnetic field quantities in the poloidal direction (θ), as well as the magnetic drifts of the particles, will strongly couple the poloidal harmonics. Thus, drift waves at different mode rational surfaces (i.e. separated radially) will also be coupled. Using a simplified model, Taylor [13] examined this case and found that the toroidal effects could eliminate the shear damping of the drift wave. An improved analysis of this problem by various researchers [78,79,14] confirmed the existence of a marginally stable mode in the toroidal system. This new drift-wave branch is known as the "toroidicity-induced" mode, and inclusion of additional destabilizing effects have shown it to be absolutely unstable for small values of $k_\perp \rho_i$ (~ 0.3) and values of shear relevant to tokamaks [81,15,16,17]. The mathematics in these analyses is difficult, and simplifying assumptions are often necessary. Furthermore, since the majority of fusion devices are toroidal in nature, the modification to existing theory due to toroidal effects needs additional study. It is for these reasons that this research focuses on the extension of particle simulation techniques to toroidal geometry and the simulation of the drift wave in this system.

Particle simulation has been used to study plasma behavior for nearly a quarter of a century, typically in rather idealized geometrical configurations, and limited spatial dimensionality (one or two). Although much progress has been made with sophisticated time-advancement schemes such as the implicit [18] or magnetoinductive [19] algorithms, simulations are usually limited to

a cartesian (slab) coordinate system. The first well-known research involving more realistic geometries was the effort by Cheng and Okuda [20], which presented new methods for simulation in three dimensions, using a cartesian or cylindrical coordinate system. This system allowed the study of a toroidal plasma, using the "square-torus" configuration (see section 2.1), in which the outer boundary of the simulation region is rectangular in cross-section, but toroidal in shape. The research of Cheng and Okuda demonstrated the feasibility of particle simulation in three-dimensional curvilinear coordinates—a result especially remarkable given the limited computing resources available at that time. The coordinate system employed in their work, however, is not well suited to study of the radially localized modes that are encountered in typical tokamak plasmas. For this, we turn to a natural or flux coordinate system.

The study of plasmas in natural coordinate systems has been common in MHD simulations for a number of years ("natural" coordinates are those in which the magnetic field lines appear as straight lines). There are many reasons why this is important—simpler representation of fields, less numerical diffusion, and grid stretching for improved cross-field resolution, among others. Initially, however, our goal will be restricted to the use of concentric circular flux surfaces and electrostatic fields. One of the first questions to be answered in any algorithm involving complex geometry concerns the efficient solution and time advancement of the fields. In the toroidal system employed in this research, the Poisson equation cannot be directly inverted; therefore an iterative method based on the toroidicity as a smallness parameter has been adopted. For a toroidal aspect ratio of about 2.5, this method converges in less than ten iterations. In addition, this approach should generalize to non-circular flux surfaces reasonably well.

The use of particles creates some problems that are absent in the MHD formulation—the integration of the particle orbit equations, charge assignment, and charge (force) shaping. Of these, the treatment of the electron dynamics is the most straightforward to generalize from the usual slab guiding center approach; the main differences here are the incorporation of the magnetic drift terms and metric effects, including some special handling at $r = 0$. Because the toroidal system employed here is strongly nonuniform, with $r = 0$ usually included, the generalization of the usual slab methods must be undertaken with care. Two properties normally present in particle-in-cell codes are momentum conservation (i.e. particles have no self-forces) and conservation of charge in the charge accumulation and filtering process; these properties are reexamined in the present context. The methods employed in this research have been developed with an emphasis on generality, with the ultimate aim of performing particle simulation in general coordinate systems, perhaps with the aid of a generated mesh. In addition, the vanishing metric at $r = 0$ does not preclude the use of a purely differential approach—a more natural formulation than the Gauss's law approach seen in some cylindrical coordinate models [21]. The full development of the toroidal coordinate model is given in Chapter 2, including discussion of the toroidal metric and representation of the field quantities, the radial nonuniform grid, the solution of the field equations, spatial filtering of the field quantities, and time advancement of the particle quantities.

From a practical viewpoint, one potential problem with any new, complex code is verifying that it gives the proper behavior. To this end, we require that the code properly behave in limiting input conditions, that is, in the cylindrical and slab limits, to give one access to the large body of "standard" simulation and theoretical results in slab geometry. This feature has enabled detailed and rigorous testing of the macroscopic behavior of the simulation

plasma in the slab limit; the results of these tests are presented in Chapter 3. Also presented are tests of the *microscopic* simulation behavior, important for verifying the correctness of the metric-dependent parts of the algorithm.

The successful use of particle simulation for stability problems depends on the existence and proper loading of an equilibrium configuration for the electron and ion distributions. Particle simulations are by nature susceptible to charge separation effects, as was demonstrated by Naitou *et al.* [22] in an investigation of the loading of slab geometry plasma profiles. In slab geometry, the development of a suitable initial load for the particle distributions is aided considerably by the symmetry—only a single strongly nonuniform variable must usually be considered (x). The broken symmetry of the poloidal variable in the toroidal system causes the typical slab loading procedure to be unsatisfactory. The resulting charge separation effects, upon starting the simulation, can easily obscure the subtle behavior that we are attempting to observe. A solution to this problem has been devised, and is discussed in the beginning of Chapter 4.

The remainder of Chapter 4 is devoted to a study of drift waves with the simulation code. The slab geometry drift wave is a useful starting point in our investigation; therefore the theory is briefly considered, and a simulation of this mode is performed in the two-dimensional, slab limit of the toroidal particle code. Following this we review the theory of the toroidicity-induced drift mode, and present simulation results from the toroidal configuration employing a single high-n mode ($n = 9$) with multiple mode rational surfaces due to the varying poloidal mode number.

Chapter 2

Theory of the toroidal particle simulation model

2.1 The coordinate system

The geometry considered in this research is illustrated in Figure 2.1. The (r, χ, ζ) coordinate system we use is orthogonal and right-handed, with the surfaces of constant r being nested, concentric circles of revolution (tori). Since we are using the electrostatic approximation, the magnetic fields can be specified in any manner desired, allowing a great deal of flexibility (discussed more fully in the next section). However, the typical configuration will be one in which the magnetic axis lies at $r = 0$, and flux surfaces lie on surfaces of constant r. The term *toroidal* in this work will apply to this system only.

As mentioned in the introduction, we require a simple transition to the limiting cases of cylindrical or slab (cartesian) geometry. Therefore the *distancelike* coordinates (χ, ζ) are chosen instead of the more usual (θ, ϕ) representation; these lead to straightforward limiting behavior. (Note : we shall often use θ and ϕ interchangably with χ and ζ in this work—the distinction is important mainly when taking limits.) Specifically, the coordinates χ and ζ are given by

$$\begin{aligned} \chi &= r_0\theta \\ \zeta &= -R_0\phi \end{aligned}$$

where R_0 is the major radius and $r_0 = .5 * (r_{\min} + r_{\max})$. This model allows the point at the magnetic axis to be included, although a small amount of special

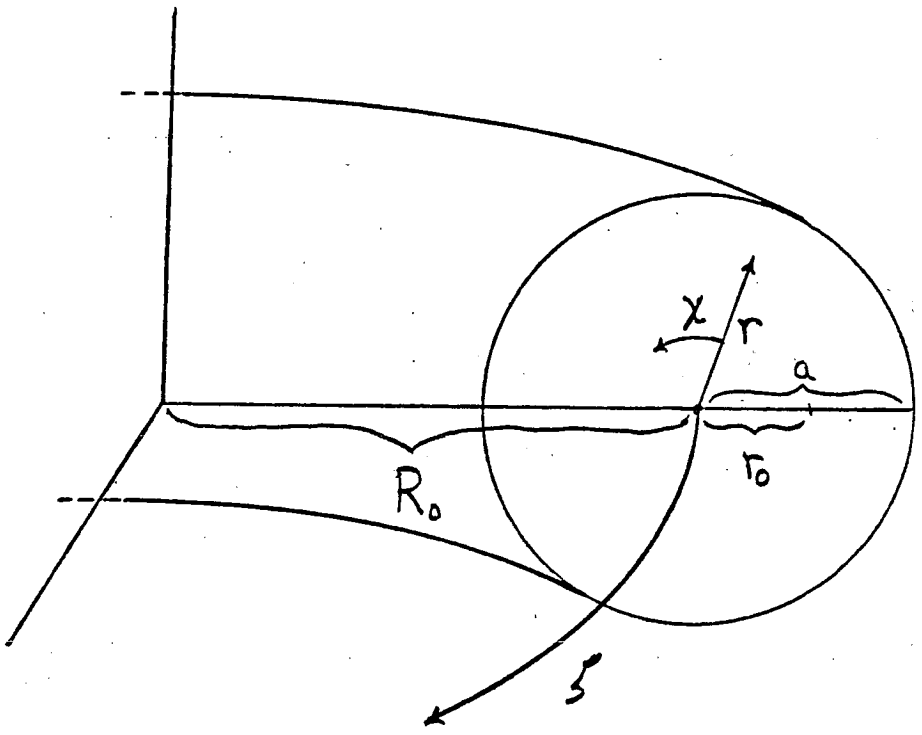

Figure 2.1: Toroidal coordinate system.

handling is required (details given in later sections). The metric components for this system are

$$\begin{aligned} h_r &= 1 \\ h_\chi &= r/r_0 \\ h_\zeta &= R/R_0 \end{aligned} \tag{2.1}$$

where $R = R_0 + r\cos\theta$. Thus the infinitesimal volume element is given by

$$\begin{aligned} J\,d\mathbf{V} &\equiv h_r h_\chi h_\zeta\, dr\, d\chi\, d\zeta \\ &= \frac{r}{r_0}\frac{R}{R_0}\, dr\, d\chi\, d\zeta \\ &= rR\, dr\, d\theta\, d\phi \end{aligned}$$

as expected. For the (χ, ζ) coordinates, the limit to cylindrical or cartesian coordinates is now well-defined :

$$\begin{aligned} \zeta &\to z \qquad \text{for } R_0 \to \infty, \quad \text{and} \\ \chi &\to y \qquad \text{for } r_0 \to \infty \end{aligned}$$

The next step in obtaining proper limiting behavior is to choose a local variable $u = r - r_0$ to represent radial displacement. If the $r_0 \to \infty$ limit is taken, keeping the radial length $L_r = r_{\max} - r_{\min}$ constant, the local variable u remains finite. Now we introduce the auxiliary parameters

$$\begin{aligned} \epsilon_\zeta &\equiv r_0/R_0 \\ \epsilon_\chi &\equiv (L_r/2)/r_0 \end{aligned}$$

which measure the strengths of the cylindrical and toroidal effects, respectively (ϵ_ζ is half the typical inverse aspect ratio). The relationship between the angular coordinates (θ, ϕ) and the present coordinates is expressed in terms of the

curvatures

$$\begin{aligned} \kappa_\zeta \equiv 1/R_0 &= \kappa_\chi \epsilon_\zeta \\ \kappa_\chi \equiv 1/r_0 &= \epsilon_\chi/(L_r/2) \end{aligned}$$

where κ_ζ is the curvature along ζ at the magnetic axis, and κ_χ is the curvature along χ at $r = r_0$. The metric components become

$$\begin{aligned} h_u &= 1 \\ h_\chi &= 1 + \kappa_\chi u \\ h_\zeta &= 1 + \epsilon_\zeta(1 + \kappa_\chi u)\cos(\kappa_\chi \chi) \end{aligned} \tag{2.2}$$

The geometry is then completely specified by the quantities $(L_r, \epsilon_\chi, \epsilon_\zeta)$ in the toroidal system—to take the cylindrical limit one sets $\epsilon_\zeta = 0$ and specifies L_z, and to take the slab limit one sets $\epsilon_\chi = 0$ and specifies L_y. The configuration in these limits is illustrated in Figures 2.2–2.4 (the main distinction between the two cylindrical configurations involve the field representations and magnetic field specification; this is discussed further in section 2.2). It should be emphasized that by choosing appropriate metric components in Eqs. (2.2), we can realize nearly any well-behaved geometry using the methods given in this dissertation.

The adoption of this type of scheme has clear benefits regarding code verification and debugging, as discussed previously. There are at least two additional benefits as well. First, the non-cartesian effects in the metric are easily seen. This is helpful in developing good methods for the solution of the fields and the particle advancement. Second, it is more flexible than a straightforward (r, θ, ϕ) method, allowing us to isolate the effect of the metric from many of the more routine aspects of the code.

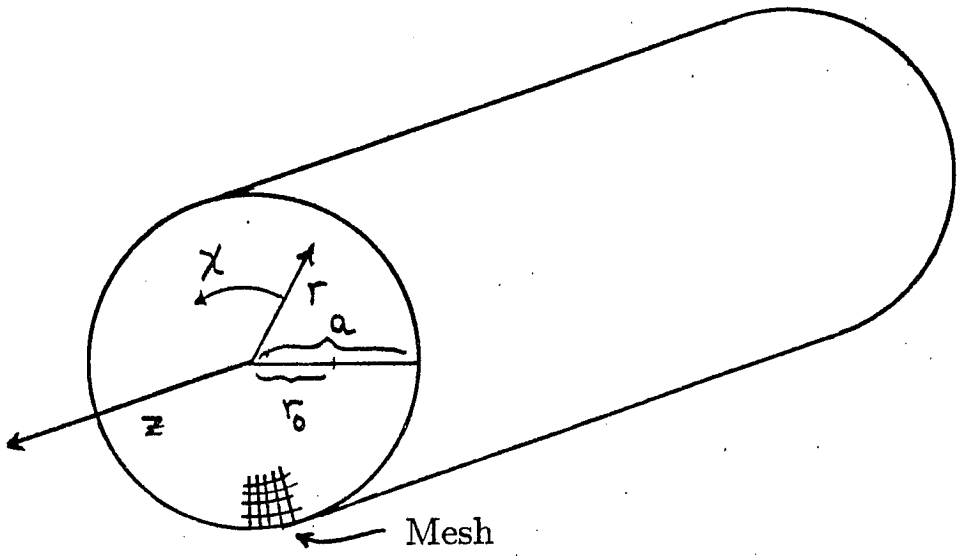

Figure 2.2: Cylindrical coordinate system, type I (Long dimension along ζ coordinate).

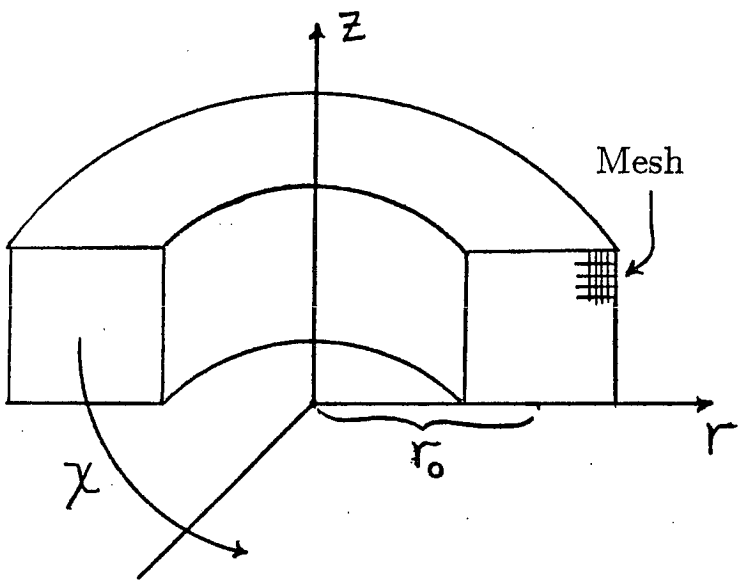

Figure 2.3: Cylindrical coordinate system, type II (Long dimension along χ coordinate).

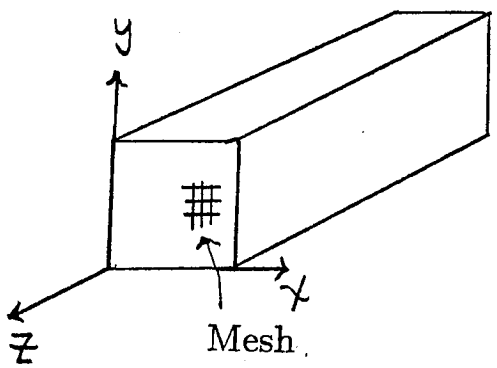

Figure 2.4: Slab coordinate system.

One last point should be made concerning this system's Fourier representation. Since χ and ζ are both periodic variables, we may transform an arbitrary field component (the electric potential, for example) to get

$$\Phi(r, k_\chi, k_\zeta) = \sum_{m,n} \Phi(r, \chi, \zeta) \exp\left(ik_\chi \chi + ik_\zeta \zeta\right)$$

where the wavevector components are given by

$$\begin{aligned} k_\chi &= \frac{2\pi m}{L_\chi}, \qquad L_\chi = 2\pi r_0 \\ k_\zeta &= \frac{2\pi n}{L_\zeta}, \qquad L_\zeta = 2\pi R_0 \end{aligned}$$

If the slab limit is taken, this becomes the familar (x, k_y, k_z) Fourier representation. Yet, in the toroidal system, we may cancel factors of 2π, r_0 and R_0 in the exponential to obtain

$$\Phi(r, m, n) = \sum_{m,n} \Phi(r, \theta, \phi) \exp\left(im\theta - in\phi\right)$$

which is a representation seen quite often in the theoretical literature. Thus we have limited compatibility with the "standard" simulation codes in the slab limit, while retaining the usual toroidal mode representation.

2.2 Representation of the field quantities

The central idea in particle simulation is to study the behavior of a many-body system at a very low level—that of the individual particle. The first application of this idea to plasma simulation was by Dawson in the early 1960's [23]. Dawson's model incorporated particles as one-dimensional "sheets" of charge, with the the force on each particle determined by a direct sum of the interparticle forces. However, due to the large number of simulation particles involved, a direct extension of this method to two dimensions involves considerable computational expense. The extension to two dimensions was accomplished by researchers at Stanford [24,25], who introduced a grid for the storage and calculation of field quantities. The use of a grid decreases computational effort dramatically for two reasons—the number of grid points may be much less than the number of particles, and efficient numerical methods exist for solving the field equations on a regular mesh (known as rapid elliptic solvers [26]). The most common rapid elliptic solver to be used in particle simulation is the Fast Fourier Transform (FFT), where one can efficiently obtain the field arrays in a k-space representation, then directly invert the resulting (algebraic) field equations.

The grid formulation in particle simulation has proven valuable in several ways. In addition to the reduction of computational expense, a grid also reduces the collisionality, which is unphysically large when a direct force calculation is used. A reduction in collisionality occurs because the grid method

modifies the interparticle force law, such that the force between two particles vanishes as their separation distance goes to zero [27]. Further, the modification of the short-wavelength behavior allows the simulation of realistic plasma behavior with far less particles per Debye sphere than found in typical plasmas. Finally, a grid formulation allows other subtle modifications to the dynamics, such as in the magnetoinductive or implicit schemes, where the exact interparticle force law may no longer be known.

While grid methods have been applied with much success to the two-dimensional simulation of plasmas, limitations in computer memory have prevented a wide-scale extension to three dimensions. In the mid 1970's, Cheng and Okuda [20] proposed a three-dimensional simulation method that avoided the large memory requirement of a full 3-d grid. This method employs a *mode expansion* in the third (long) dimension, instead of a grid. The field quantities are Fourier-decomposed in the dominant direction of the magnetic field; this is usually taken as the (z) coordinate. The cross-field components x, y are discretized via a grid, and the representation of the fields becomes

$$\begin{aligned} \rho(x,y,z) &= \sum \rho_n(x,y) e^{ik_z z} \\ \Phi(x,y,z) &= \sum \Phi_n(x,y) e^{ik_z z} \\ \mathbf{E}(x,y,z) &= \sum \mathbf{E}_n(x,y) e^{ik_z z} \end{aligned} \tag{2.3}$$

where $k_z = 2\pi n/L_z$ and the sum goes from $n = -N$ to $n = N$, N being the number of modes in the z-direction ($N \lesssim 5$). If we assume symmetry in the third dimension, the field components for each mode can be calculated independently, and later summed in the interpolation phase. Since the toroidal system has azimuthal symmetry, the above equations are applicable to the toroidal algorithm simply by associating (x, y, z) with (r, χ, ζ).

At this point one might ask, "Is this really three-dimensional?" Admittedly, the number of modes retained in the third dimension seems somewhat small. However, in a strongly magnetized plasma, most of the important behavior is characterized by wavevectors nearly perpendicular to the magnetic field. The electrons can freely stream along the magnetic field to neutralize charge. Accurate modeling of small parallel-wavelength behavior like ballooning will require higher mode numbers, but only a few long-wavelength modes may be necessary for other phenomena. (It was this configuration that was used by Sydora *et al.* [11] in the simulation of the 3-d slab "stochasticity-induced" drift mode.) Another argument for the small number of modes is that the mode expansion method is very accurate compared to interpolation on a grid. In the direction of the mode expansion, the charge density accumulation and interpolation of the fields are done at the particle's exact position, while the grid method interpolates from the values at nearby gridpoints.

The main drawback to the mode-expansion method is that the mode-particle loop for accumulation and interpolation is extremely time-consuming, easily dominating the rest of the code. In the accumulation/interpolation phase, the mode expansion requires roughly n_z trigonometric evaluations per particle, where n_z is the number of modes in the calculation. On the other hand, a grid method requires only a small number of relatively inexpensive algebraic evaluations for each particle. (The grid method may require trigonometric evaluations at the *gridpoints* if a transform method is employed, but these are efficiently handled by the FFT).

In recent years, a full three-dimensional grid representation has become feasible due to the appearance of very large memory machines such as the Cray-2 supercomputer. A 3-d grid has the advantage of speed and ease

of implementation, and if sufficient computer memory exists, is preferred over a combination 2-d grid/mode-expansion due to the large disparity in speed. Aside from limitations in computer memory, the most important exception to this choice is when operating with reduced degrees of freedom. This includes a small total number of toroidal modes, a small number of high-n modes, or two-dimensional simulation, where the mode-expansion method "collapses" to 2-d more easily than the grid method. The decision of which method to implement is therefore difficult, depending both on computer architecture and the problem at hand. In this research both the grid and the mode-expansion method in the third dimension are employed. Not only does this dual approach offer increased flexibility, but a more elegant and flexible code architecture results as well.

One last comparison between the mode expansion and the grid method involves systems that are very long in the direction of the magnetic field. Langdon [28] has numerically solved the dispersion equation for the simulation plasma, finding a critical value for the ratio of the Debye length to the grid spacing, λ_D/Δ. Below this value, numerical instability will result. This is known variously as the "aliasing-instability", "thermal-instability", or "cold-plasma instability", and is caused by a sampling effect known as *aliasing*. The threshold value for λ_D/Δ is about 0.3 for a simulation with nearest-grid-point (NGP) weighting. This threshold can be reduced significantly by the use of a higher-order spline interpolation scheme. For example, the second-order quadratic spline method reduces the maximum λ_D/Δ to about 0.1 [29], and recent work by Abe *et al.* [30] showed that values of $\lambda_D/\Delta \sim .01$–$.001$ are possible with fifth-order spline interpolation. The numerical instability associated with small values of the Debye length is absent in the mode-expansion method, a consequence of its greater accuracy. In this research, numerical heating is

only a concern in the full 3-d grid representation; a combination of quadratic weighting in the third dimension and a gaussian shape factor reduce unphysical heating to unobservable levels in most parameter regimes studied.

The application of the methods discussed above to the toroidal system is reasonably straightforward. The grid is mapped onto the system in such a way that the simulation boundaries are located *between* grid points. This is the simplest representation for periodic coordinates, and when used radially, helps to avoid the singularities in the Laplacian at $r = 0$. In this case, there is no grid point at $r = 0$, the inner "boundary" of the coordinate system.

One complication arises in the cylindrical limit of the code, using the 2-d grid/mode-expansion configuration. For a cylindrical system, there are two combinations of a grid and mode-expansion that might be used, according to the direction of the dominant external magnetic field. One configuration would be a grid in (r, χ) and mode expansion in z (type-I cylindrical, Figure 2.2), which is the natural way to take the cylindrical limit from the toroidal system. The toroidal system employs this type of configuration because of the strong toroidal magnetic field; in addition the grid in χ (θ) is a necessary computational device for the toroidal field solver. The alternative is to use a dominant magnetic field in the χ direction, turning the system into a "square torus". The grid is then in (r, z), with the mode expansion in χ (type-II cylindrical, Figure 2.3). This is the approach originally used by Cheng and Okuda [20] to study global modes in a toroidal-type system. It was also the first system modeled in the course of this research, and was very helpful for testing and debugging the full toroidal system. Though it is still possible to run the code in the type-II cylindrical configuration, this option is infrequently used.

2.3 The nonuniform radial grid

2.3.1 Motivation

In any numerical calculation, the motivation for using a nonuniform mesh is to more closely match the sampling method (i.e. grid) with the behavior of the solution. This idea was perhaps first used in fluid simulations. For example, in laminar flow around solid bodies, the character of the flow in the boundary layer varies much more rapidly than in the interior of the flow region. Thus, there is the desire to increase resolution in the boundary layer by concentrating grid points there, and spread out grid points elsewhere, to minimize computational expense. The term *boundary-fitted coordinates* is used in fluid dynamics to describe the generated-grid system for studying flow around a solid object [31]. In plasma simulation, this boundary is manifested by the magnetic field. Generated grids which conform to the shape of the magnetic field are commonly seen in modern MHD simulations. These most often employ orthogonal or non-orthogonal (e.g. Hamada) flux coordinates; occasionally an adaptive system is used [32].

The use of nonuniform or generated grids in particle simulation has been rare, however. This may be due to the fundamental differences between particle and fluid simulation. First, particle simulations have been primarily aimed at *local* phenomena, and therefore the exact specification of the magnetic fields is less important than in the global, fluid simulations. It is this local emphasis that permits the adoption of slab geometry for many particle simulations. Second, existing particle simulations often rely on k-space representations for the solution of the fields, making it difficult to incorporate even a single, stretched variable. And third, the resolution in a particle simulation *is not determined by the grid alone.* In a particle simulation we must

keep the number of particles per cell appreciable in order to accurately model plasma behavior there, which limits the amount of grid stretching that may be employed.

This is not to say that nonuniform grids are ill-suited to particle simulations. Even local problems often show multiple scales of length, and a nonuniform grid could help considerably. For example, this research will consider the problem of drift wave eigenmodes; the nonuniform grid in r gives good resolution near the mode rational surfaces, while allowing the ion resonance surfaces to remain within the simulation region. Another example application is in the study of tearing modes—the resolution immediately surrounding the tearing layer could be much improved by using a nonuniform mesh.

The implementation of a nonuniform grid in one variable (also known as grid-stretching), will usually require the adoption of a finite-difference formulation. (The use of nonunform grids in a purely k-space representation is considered by Cain *et al.* [33].) In our case, radial finite-differencing is necessary for solution of the toroidal field equations, and the addition of the nonuniform radial grid is straightforward. Further, the finite-difference approach seems more logical for a simulation highly nonuniform in x (or r). Birdsall and Langdon [21, Appendix E] discuss this point in examining properties of local versus non-local differencing operators.

Finally, the need to maintain acceptable numbers of particles per cell represents a definite limitation. However, the effect of this restriction is minimal when *the region of the greatest number of particles coincides with the region of maximum resolution.* For a simulation in slab geometry that includes a density profile, this location will be at the inward boundary. See Figure 2.5 for a typical grid and profile choice, with number of particles/cell plotted also. Often we

want the region of interest to lie in the center of our simulation "window" to minimize boundary effects. This situation is shown in Figure 2.6, for the same density profile. As can be seen, the proportion of particles in the central cells is extremely small in this case.

The situation improves markedly when one moves to cylindrical geometry (therefore toroidal geometry as well), as a result of the uniform-grid cell area being proportional to r. In cylindridal geometry, the density profile should be flat at $r = 0$. If we also assume that the density vanishes faster than $1/r$ for large r, and a uniform grid, then the number of particles per cell will be nearly zero at the origin, rise to a peak, and then decay. Careful choice of the nonuniform grid will allow roughly equal numbers of particles per cell, which is the ideal situation. In this case, the maximum resolution will be governed by the sharpness of the plasma profile. A example density profile (gaussian), grid spacing, and number of particles per cell in a cylindrical coordinate system is given in Figure 2.7. A typical (r, θ) grid configuration is shown in Figure 2.8, employing 64 radial gridpoints (nonuniformly distributed), and 32 theta gridpoints.

2.3.2 Local theory

In order to rigorously justify the use of a nonuniform grid, we consider the local properties of such a system. To start, we examine a uniform grid system of grid spacing Δ. The centered, second order finite-difference representation of the first and second derivatives on a uniform grid are given by

$$\frac{f_{i+1} - f_{i-1}}{2\Delta} = f_i' + \frac{\Delta^2}{6} f_i''' + \ldots \tag{2.4}$$

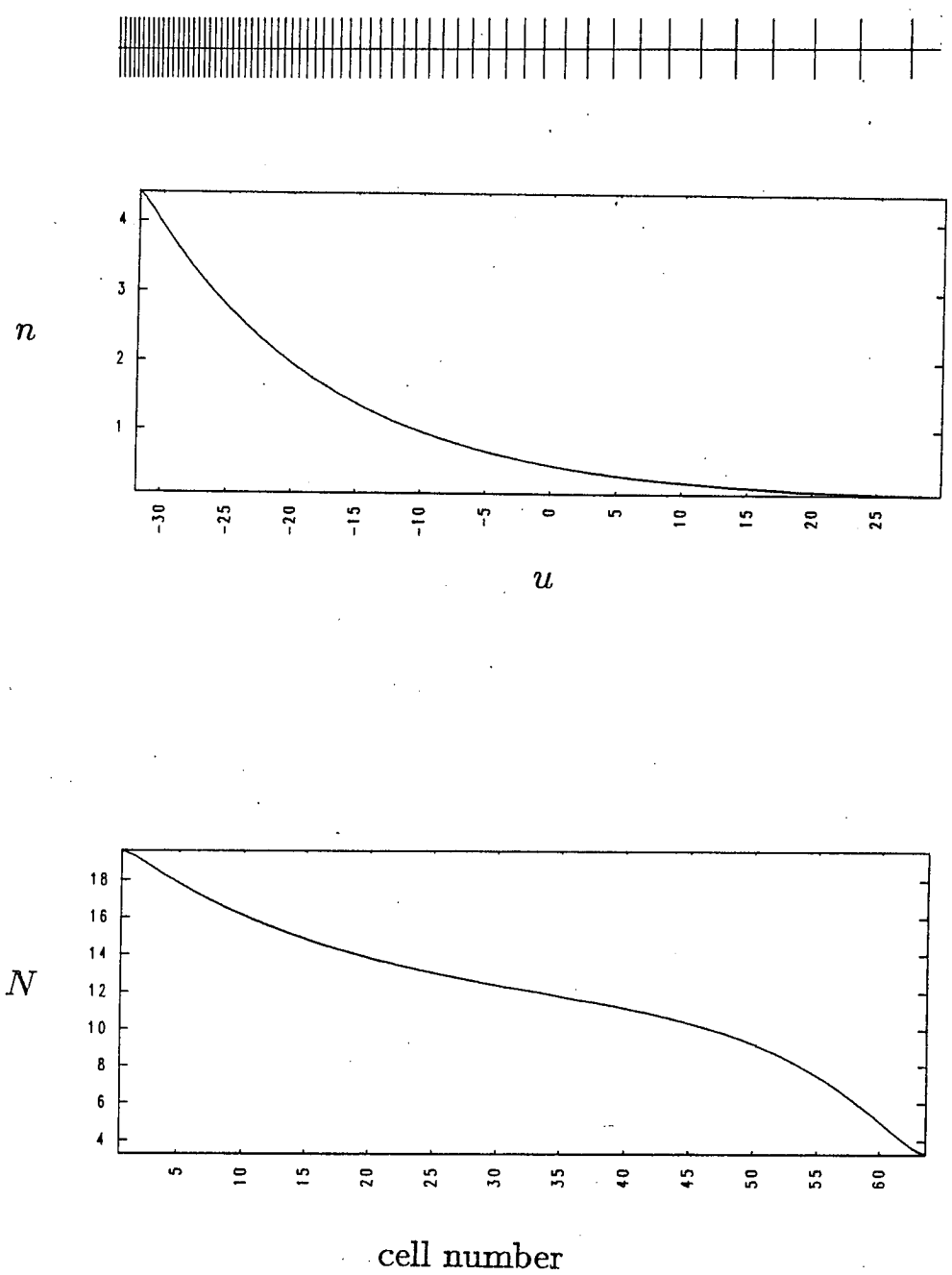

Figure 2.5: Nonuniform grid, plasma profile, and number of particles per cell for slab geometry. Region of interest is near the left boundary.

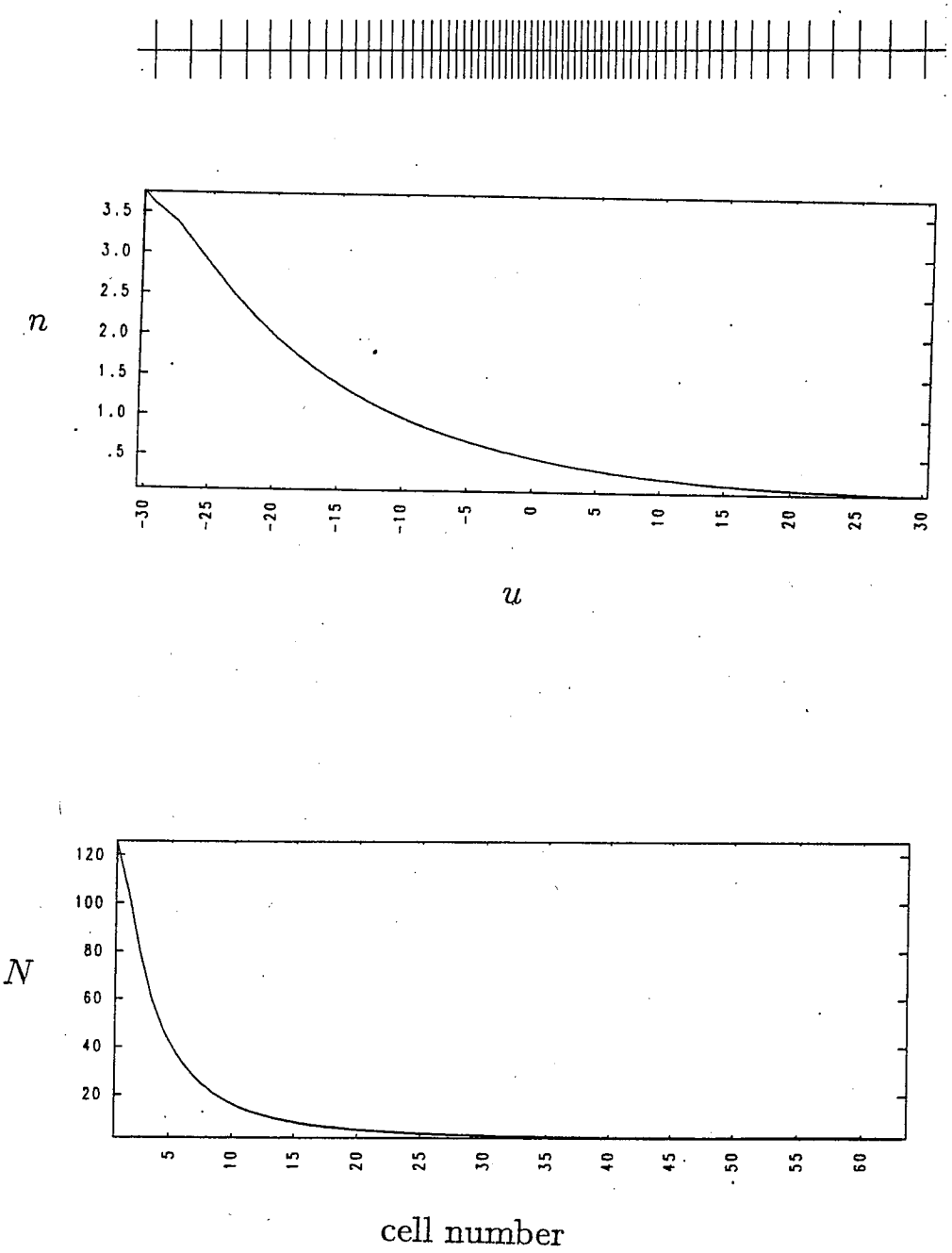

Figure 2.6: Nonuniform grid, plasma profile, and number of particles per cell for slab geometry. Region of interest is in the center.

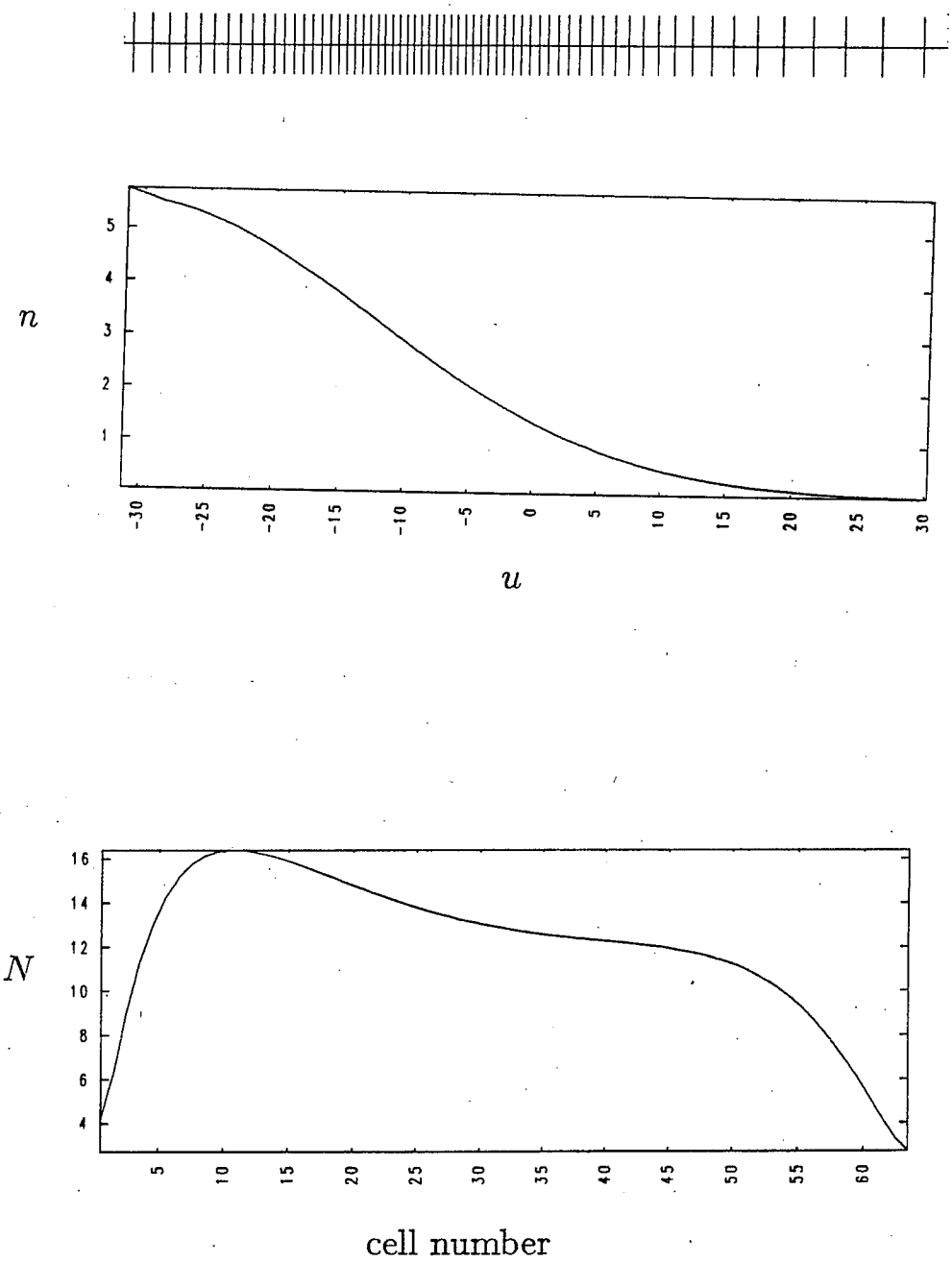

Figure 2.7: Nonuniform grid, plasma profile, and number of particles per cell for cylindrical geometry. Region of interest is in the center.

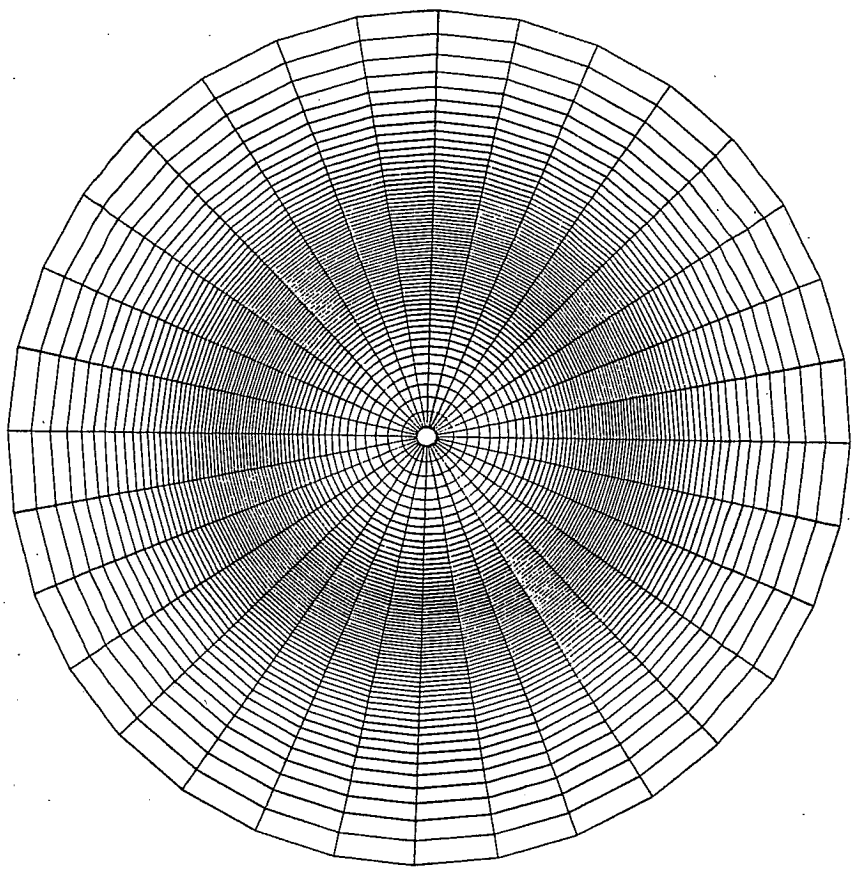

Figure 2.8: Schematic of (r, θ) grid for a typical case.

$$\frac{f_{i+1} - 2f_i + f_{i-1}}{\Delta^2} = f_i'' + \frac{\Delta^2}{12} f_i^{\mathrm{IV}} + \ldots \qquad (2.5)$$

where f is some arbitrary function. The justification for using these approximations is often based on their second-order behavior, but this is only an asymptotic relation between local error and grid spacing, and leaves out the effects of the higher-order derivatives of f. It is useful to assume a particular form for f and re-examine the accuracy of these equations. For the phenomena of interest here, solutions have an oscillatory character, so it is reasonable to express f in terms of its Fourier harmonics. Then f and f' are of the form

$$\begin{aligned} f(x) &= \sum f_k e^{ikx} \\ f'(x) &= \sum f_k \, ik \, e^{ikx} \end{aligned}$$

and finite difference approximation to f' is given by

$$\begin{aligned} f'(x) &\approx \left(f_{i+1} - f_{i-1}\right)/2\Delta \\ &= \sum f_k e^{ikx} \left(e^{ik\Delta} - e^{-ik\Delta}\right)/2\Delta \\ &= \sum f_k e^{ikx} \, i \left(\sin k\Delta\right)/\Delta \end{aligned}$$

which equals the exact result in the limit of small $k\Delta$. The result for the second derivative is similarly given by

$$\begin{aligned} f''(x) &\approx \left(f_{i+1} - 2f_i + f_{i-1}\right)/\Delta^2 \\ &= -\sum f_k e^{ikx} \left(\sin[k\Delta/2]\right)^2/(\Delta/2)^2 \end{aligned}$$

The accuracy of the finite difference approximation to the first derivative is shown by plotting the ratio

$$\frac{\left(\sin[k\Delta/2]\right)^2/(\Delta/2)^2}{k}$$

as a function of $k\Delta$ in Figure 2.9.

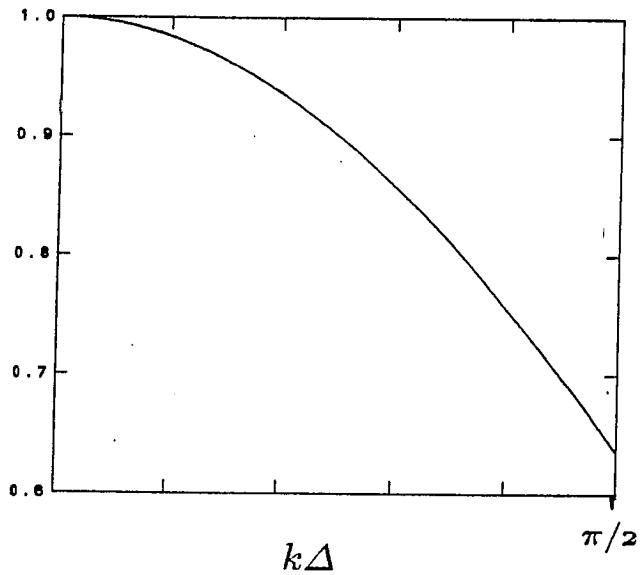

Figure 2.9: Ratio of the first derivative finite difference approximation to the exact result, as a function of $k\Delta$.

Clearly, the finite-difference approximation does well for long wavelength modes, but becomes very inaccurate for $k\Delta \gtrsim \pi/2$. For $k\Delta = \pi/4$, the first derivative approximation is accurate to within about 10 percent; this is reduced to about 5 percent for the second derivative approximation. This is an important observation, because most particle codes do not resolve mode numbers much higher than this range ($k\Delta \sim \pi/4$–$\pi/2$). Particle codes usually employ k-space filters to eliminate the high mode numbers (discussed in section 2.5); the weakening effect due to such a filter will often far exceed that of the finite-difference operator. For example, a gaussian filter, for a particle the size of the grid spacing, halves the signal strength at $k\Delta = \pi/4$. This leads us to conclude that the second-order finite difference expressions will usually be sufficiently accurate for use in a particle code.

We proceed now to the consideration of a one-dimensional, nonuniform (stretched) grid. The finite-difference approximation to the first derivative

generalizes easily :

$$\frac{df}{dx} \simeq \frac{f_{i+1} - f_{i-1}}{x_{i+1} - x_{i-1}} \tag{2.6}$$

However, the expressions for the second derivative approximation and the truncation errors are somewhat cumbersome. It is helpful to adopt the notation

$$\begin{aligned} \bar{\Delta}_i &\equiv \left(\Delta_{i+1/2} + \Delta_{i-1/2}\right)/2 \\ \delta_i &\equiv \left(\Delta_{i+1/2} - \Delta_{i-1/2}\right) \\ \gamma_i &\equiv \delta_i/(2\bar{\Delta}_i) \end{aligned} \tag{2.7}$$

where $\bar{\Delta}_i$ is the mean cell size and δ_i is the change in grid spacing at the ith grid point. The quantity γ_i is approximately $1/2$ the rate of change of the grid spacing, a useful measure of the nonuniformity of the grid. With these definitions, the finite difference approximation for the first derivative is

$$\frac{f_{i+1} - f_{i-1}}{2\bar{\Delta}_i} = f_i' + \gamma_i \bar{\Delta}_i f_i'' + \left(1 + 3\gamma_i^2\right) \frac{\bar{\Delta}_i^2}{6} f_i''' + \ldots \tag{2.8}$$

and for the second derivative is

$$\frac{(1-\gamma_i)\, f_{i+1} - 2f_i + (1+\gamma_i)\, f_{i-1}}{\bar{\Delta}_i^2 (1-\gamma_i^2)} = f_i'' + \gamma_i \frac{2\bar{\Delta}_i}{3} f_i''' + \left(1 + 3\gamma_i^2\right) \frac{\bar{\Delta}_i^2}{12} f_i^{\mathrm{IV}} + \ldots \tag{2.9}$$

which, aside from notation, match the expressions given by de Rivas [34]. These expressions show clearly the effect of the stretched variable, and are different from their uniform grid counterparts in an important qualitative way—these approximations are no longer formally second-order accurate in the grid spacing. The reason for this loss of formal accuracy is that for a nonuniform grid, these approximations to the first and second derivatives are *no longer perfectly centered*, resulting in the first-order Δ_i term in the truncation error. For extremely rapidly varying grid size, γ_i can become of order unity, which will

cause the approximation to be first order accurate only (in this case, the finite-difference approximations have become essentially one-sided). It is clear that by changing the grid spacing sufficiently slowly, γ_i can be neglected and formal second order accuracy will be retained. This is the idea behind the condition given by Blottner and Roache [35], which in this notation takes on the form

$$\gamma_i \sim \bar{\Delta}_i \tag{2.10}$$

recovering the formal second order accuracy. (This condition assumes the above equations to be in dimensionless form, since the quantity γ_i is itself dimensionless.)

While Eqs. (2.8)–(2.9) give us insight into the accuracy of a nonuniform grid, they have the disadvantages of complexity and difficult extension to higher order. It is usually much simpler to express derivatives in terms of a transformed variable. We define the transformed coordinate

$$\xi = \xi(x)$$

where the $\xi(x)$ is our *stretching-function*, and grid-points occur in ξ-space at intervals of constant $\Delta\xi$ (arbitrarily set to 1). Then expressing the derivatives of f in terms of ξ, we have

$$\frac{\partial f}{\partial x} = \frac{\partial \xi}{\partial x}\frac{\partial f}{\partial \xi} \tag{2.11}$$

$$\frac{\partial^2 f}{\partial x^2} = \left(\frac{\partial \xi}{\partial x}\right)^2 \frac{\partial^2 f}{\partial \xi^2} + \frac{\partial^2 \xi}{\partial x^2}\frac{\partial f}{\partial \xi} \tag{2.12}$$

Since the partial derivatives of $\xi(x)$ are assumed to be known, all that remains is to replace $\partial f/\partial \xi$ and $\partial^2 f/\partial \xi^2$ by their corresponding *uniform grid* finite difference representations. This method is guaranteed to be second order in $\Delta\xi$, which might seem to be an improvement over Eqs. (2.8)–(2.9). This is

an erroneous conclusion (although seen in some of the literature, e.g. [35]); either representation can be shown to have *exactly* the same truncation error. This was probably first indicated in the work by de Rivas [34], where it was shown that Eqs. (2.8)–(2.9) could be transformed via a stretched coordinate, yielding second order equations. This was also discussed by Hoffman [36], who noted that the $\mathcal{O}(\Delta\xi^2)$ dependence of the truncation error implies that these equations behave in a second order way if the grid points are chosen appropriately.

The question as to the formal order of these methods, while being a concern, still leaves us without a clear estimate of the total error. To obtain a more meaningful measure of accuracy, we again adopt an oscillatory form for the arbitrary function f. Upon Fourier-analysis, the finite-difference approximation to the first derivative becomes

$$\begin{aligned} f'(x) &\approx \left(f_{i+1} - f_{i-1}\right)/(2\bar{\Delta}_i) \\ &= \sum f_k e^{ikx}\left(e^{ik\Delta_{i+1/2}} - e^{-ik\Delta_{i-1/2}}\right)/(2\bar{\Delta}_i) \\ &= \sum f_k e^{ikx}\, ie^{ik\delta_i/2}\left(\sin k\bar{\Delta}_i\right)/\bar{\Delta}_i \end{aligned}$$

This is virtually equivalent to the uniform grid result, the main difference being the presence of a phase factor $e^{ik\delta_i/2}$. We obtain an accuracy condition on the nonuniformity of the grid, relevant to particle simulation, by requiring the argument of this phase factor to be small at the "cut-off" value $k\bar{\Delta}_i \sim \pi/2$. Given $k\delta_i/2 \ll \pi/2$, we then have

$$\gamma_i \ll 1 \tag{2.13}$$

for our nonuniform grid condition.

In this research, the transformation function approach is used exclusively. This approach has the advantages of smoothness and simplicity. For the

nonuniform grids employed, γ_i is typically smaller than 0.1 (but is a function of position), giving an accurate finite-difference representation for most of the wavenumber spectrum. The error estimation argument followed here is still largely *ad hoc*, and may not give the best results for highly nonuniform situations. In such situations, the choice of the optimum grid is mostly an educated guess and highly problem-dependent; it is probably best to be conservative in the choice of grid parameters, and keep γ_i small.

2.3.3 Construction of stretching function

We now wish to construct a stretching function according to some prescribed grid spacing. Denoting the grid spacing by $\Delta(x)$, we have the relation

$$\begin{aligned} \Delta(x) &\equiv \frac{\Delta x}{\Delta \xi}(x) \\ &\simeq \frac{1}{\partial \xi / \partial x} \end{aligned} \tag{2.14}$$

which gives the expression for the stretching function

$$\xi(x) = \int \frac{dx}{\Delta(x)} \tag{2.15}$$

This specification of $\xi(x)$ is taken to be exact; the resulting grid spacing will not precisely match the function $\Delta(x)$ because of discreteness effects, but will usually be close. The first restriction on $\Delta(x)$ is that it yield a $\xi(x)$ with continuous first and second partial derivatives (this will be true if $\Delta(x)$ and $\Delta'(x)$ are continuous and nonzero). These derivatives are required to solve the Poisson equation. In general, this condition is not difficult to satisfy.

The second restriction we will make on the generation of the stretching function is that $\xi(x)$ be *simple*, that is, $\xi(x)$ should be analytically expressible

$\Delta(x)$	$\xi(x)$
$c_1 \cosh^2(c_2\tilde{x})$	$c_1' + c_2' \tanh(c_3'\tilde{x})$
$c_1 (c_2 + c_3\tilde{x}^2) / (c_2 + \tilde{x}^2)$	$c_1' + c_2'\tilde{x} + c_3' \tan^{-1}(c_4'\tilde{x})$

Table 2.1: Examples of stretching functions ($\tilde{x} \equiv x - x_a$)

with a minimum of special function evaluations. This is done to simplify the transformation of the particle positions x_i to the transformed coordinate, which is necessary in both the charge accumulation and the field interpolation phases. The result is a reasonably fast, vectorized loop. This simplification is not an absolute requirement. For increased generality, one could solve for $\xi(x)$ at discrete values only, then interpolate to get ξ as a function of the particle coordinates. This loop would vectorize on computers that support gather/scatter-type vectorization (Cray-2, Cray X-MP 48), and would probably be faster than the loop employing the exact stretching function.

For the type of grid we are interested in, $\Delta(x)$ has a minimum at some point $x = x_a$, and increases outward from that point (possibly reaching some limit). We give two such functions in Table 2.1 that satisfy the above restrictions. Note that each function has only one special function evaluation in the expression for $\xi(x)$. It is this evaluation that is the most time-consuming part of the entire method, and timing tests show an increase in total cpu-time of only a few percent for a typical configuration. The second function in Table 2.1 is the one employed in this research—it allows choice of a limiting (maximum) value for the grid spacing, as well as the degree of grid stretching. The main disadvantage with this stretching function is that an exact expression for $x(\xi)$ is not known. However, $x(\xi)$ is only needed at grid points for diagnostics; these values can be obtained through the use of a simple root-finder routine.

2.3.4 General remarks

We do not intend to fully discuss the implementation of a nonuniform grid to a particle code here; this is done in the following sections of this chapter, along with the inclusion of the toroidal metric. Here we focus on two remaining concerns, of which the first considers the meaning of particle *shapes* in a simulation with a nonuniform grid.

The concept of a particle shape in a particle simulation enters primarily through the grid. When one interpolates to the nearest two to three gridpoints in each direction, the response of the system indicates an effective particle size on the order of a cell-width. This response is often modified by a filter (or finite-size particle shape factor). The use of a nonuniform grid does not alter this appreciably. If we modify our filter so that it filters only locally, then the relationship between the effective particle size and the cell size is maintained. (This is accomplished using a technique known as *digital filtering*, discussed in section 2.5.) As the cell-width changes due to the nonuniform grid, so does the effective particle width. This is a natural effect, and is an essential property to have true control over the resolution.

It should be noted that if particles can easily move along a given coordinate, a nonuniform grid in that direction is not appropriate. The nonuniform grid method must be chosen in accordance with the boundary conditions and the problem at hand. In the present simulation, the use of a nonuniform grid is appropriate in the direction of the density gradient, and perpendicular to the dominant magnetic field direction.

Finally, we once again consider the most serious limitation with the nonuniform grid method in particle simulation—the decrease in number of particles per cell as the cell size decreases. As shown previously, this problem is

considerably less severe in a cylindrical or toroidal coordinate system due to the radial dependence of the cell size. Even in these systems, however, the need to maintain a given density profile limits the maximum resolution attainable via a nonuniform grid. Here we briefly discuss a technique that addresses this problem, to be be referred to as nonuniform *number* (or mass) weighting.

Each "particle" in a particle simulation is often conceptualized as a large collection of point particles, with spatial extent on the order of a Debye radius. This is called a *macroparticle* or *superparticle*, and each is assumed to represent a larger collection of physical particles. The number of physical particles represented is normally assumed to be a constant for each of the simulation particles, but here we allow a *varying* number of particles to be represented. The motivation for this kind of assignment is to allow us to adopt a small grid spacing in a critical region through the use of the nonuniform grid, while retaining an acceptable number of particles per cell. The prescribed density function in this case is maintained by weighting the particles in the smaller grid region correspondingly less. Since it is the *number* of represented particles that is being varied, both the charge and the mass vary by the same amount, preserving the charge-to-mass ratio for the given species. Then the charge and mass for a given particle are of the form

$$m_j = m_0 d_j \tag{2.16}$$

$$q_j = q_0 d_j \tag{2.17}$$

Here d_j is the number weight of the jth particle. Note that d_j is a *particle* quantity which is fixed in time—ensuring conservation of both the charge and mass. The initial value of the number weights are determined via $d_j = d(x_j)$, where x_j is the initial position of the jth particle and $d(x)$ is the weighting function that gives the desired density profile and number of particles per cell.

The use of this weighting technique requires that the amount of transverse diffusion is small, at least where $d'(x)$ is appreciable. Unrestricted diffusion will tend to interchange the heavier weighted particles for an equivalent amount of lighter weighted particles, thus reducing the number of particles per cell in the small grid region. This should not be a problem for problems that are only marginally unstable or involving a local instability—the weighting function can be given such that $d'(x) = 0$ at the point of maximum instability.

We now consider the noise properties of the nonuniform number weighting scheme for two simplified cases. The first concerns a uniform grid and an exponential density profile. An appealing weighting scheme in this case would be to weight the particles so that the density profile is maintained, with an equal number of particles per cell. However, this would cause the physics to be dominated by discreteness effects caused by the particles with high weights. This fact has indeed been observed in short time scale simulations of this situation.

The second case involves starting with a uniform grid and the particles loaded to some prescribed density profile. The grid is then stretched to the desired configuration, *keeping the number of particles per cell constant*. The number weights of the particles are changed in conjunction with grid spacing, to maintain the necessary density profile. In this case, the charge density fluctuations can be written in terms of an averaging operator $\langle \cdots \rangle$ as

$$\langle \rho(x) \rangle = \left\langle q(\xi) \frac{\partial \xi}{\partial x} \right\rangle \tag{2.18}$$

$$= \langle q(\xi) \rangle \frac{\partial \xi}{\partial x} \tag{2.19}$$

where $q(\xi)$ is the particle charge times the number weight in the transformed coordinate system, and $\partial \xi / \partial x$ is the transformation weight (see section 2.5 for

discussion of metric effects in the charge accumulation). If we now assume no transverse diffusion, then we can approximate

$$\langle q(\xi) \rangle \sim q_0 \langle N(\xi) \rangle d(x) \frac{\partial \xi}{\partial x} \tag{2.20}$$

where q_0 is the average charge and $d(x)$ is initial number weighting function. Thus, we choose

$$d(x) \sim \frac{1}{\Delta_0 \partial \xi / \partial x} \qquad (\approx \Delta(x)/\Delta_0) \tag{2.21}$$

for the weighting function, where Δ_0 is the average grid spacing. We then have

$$\langle \rho(x) \rangle = \frac{1}{\Delta_0} \langle N(\xi) \rangle \tag{2.22}$$

This shows that as the grid spacing changes, the fluctuation level of the charge density due to discreteness effects alone remains approximately constant, since the number of particles per cell does not change.

The latter case has been studied in several test simulations. The ability of a nonuniform mass-weighted plasma to reproduce a uniform plasma response for the ion Bernstein spectrum was studied and found to be reasonable. In this case, the transverse diffusion over the course of the run was minimal, and no numerical difficulties were observed. Although the variation of the number weighting in accordance with the cell size has shown no obvious ill effects, the results at this time are preliminary due to the limited simulation results and analysis. Thus the remainder of this research relies on the ordinary particle weighting scheme, in combination with the nonuniform grid. A more complete analysis of the nonuniform number weighting method is left for future research.

2.4 Solution of the electrostatic fields

For the electrostatic model, the only field equation that must be solved is the Poisson equation

$$\nabla^2\Phi = -4\pi\rho \tag{2.23}$$

$$\mathbf{E} = -\boldsymbol{\nabla}\Phi \tag{2.24}$$

where this ordering is used because of the difficulty in solving for the electric field directly from the charge density (this would require finding an eigenfunction expansion for the Laplacian, which is not generally possible for an arbitrary metric). Given the metric coefficients for our system (Eqs. (2.1)), the Laplacian is given by

$$\nabla^2 = \nabla_c^2 + \mathcal{C} \tag{2.25}$$

with ∇_c^2 and $\mathcal{C}$ given by

$$\nabla_c^2 = \frac{\partial^2}{\partial r^2} + \frac{1}{r}\frac{\partial}{\partial r} + \frac{r_0^2}{r^2}\frac{\partial^2}{\partial \chi^2} + \frac{\partial^2}{\partial \zeta^2} \tag{2.26}$$

$$\mathcal{C} = \frac{\cos\theta}{R}\frac{\partial}{\partial r} - \frac{\sin\theta}{R}\frac{r_0}{r}\frac{\partial}{\partial \chi} + \frac{R_0^2 - R^2}{R^2}\frac{\partial^2}{\partial \zeta^2} \tag{2.27}$$

Here ∇_c^2 is the cylindrical Laplacian, and $\mathcal{C}$ represents the toroidal corrections. The cylindrical Laplacian can be inverted by a standard technique—finite differencing in r then applying the recurrence solution for a tridiagonal matrix. However, the toroidal Laplacian as a whole is *not* directly invertible. This leads us to introduce an approximate method, based on the observation that

$$\nabla^2 = \nabla_c^2(1 + \mathcal{O}(\epsilon_\zeta)) \tag{2.28}$$

that is, the correction terms are formally of order ϵ_ζ compared to the cylindrical Laplacian. Since ϵ_ζ tends to be small ($\lesssim .2$), we expand the potential in powers of ϵ_ζ,

$$\Phi = \sum_n \epsilon_\zeta^n \psi^n \tag{2.29}$$

and substitute into the Poisson equation, obtaining

$$\sum_n \epsilon_\zeta^n \psi^n = \sum_n (\nabla_c^2)^{-1} \left[-4\pi\rho - \mathcal{C}(\epsilon_\zeta^n \psi^n) \right] \tag{2.30}$$

Equating terms of the same order in ϵ_ζ yields the following chain of equations:

$$\begin{aligned} \psi^0 &= (\nabla_c^2)^{-1} \left[-4\pi\rho \right] \\ \psi^1 &= -\frac{1}{\epsilon_\zeta} \mathcal{C} \left[\psi^0 \right] \\ &\vdots \\ \psi^n &= -\frac{1}{\epsilon_\zeta} \mathcal{C} \left[\psi^{n-1} \right] \end{aligned}$$

The sum is truncated upon reaching the desired order in ϵ_ζ for convergence. This method is closely related to the fixed point iteration scheme

$$\Phi^{p+1} = (1-\alpha)\Phi^p + \alpha(\nabla_c^2)^{-1} \left[-4\pi\rho - \mathcal{C}(\Phi^p) \right] \tag{2.31}$$

where α is a relaxation parameter, typically on the order of one, and p represents the iteration count. When no relaxation is used ($\alpha = 1$), the two methods are identical. In practice, the code uses Eq. (2.31) in the field solver. The convergence criterion for the potential is

$$\frac{\|\Phi^{p+1} - \Phi^p\|}{\|\Phi\|} \leq \epsilon$$

with $\epsilon \sim 10^{-5}$. Since $\|\Phi\|$ is unknown, the larger of $\|\Phi^{p+1}\|$ or the norm of a previous n-mode is used. (The outer loop over toroidal mode number starts with lowest mode numbers first, which are also the strongest modes due to the filtering effect at high n.) This prescription avoids excessive computation for the high mode-number, weak modes.

The inversion of the cylindrical Laplacian is done in (ξ, k_χ, k_ζ) space, where ξ is the transformed coordinate for the nonuniform grid. The finite

difference representations of the radial derivatives at the ith gridpoint become

$$\begin{aligned}\left(\frac{\partial\Phi}{\partial r}\right)_i &= \left(\frac{\partial\xi}{\partial r}\frac{\partial\Phi}{\partial\xi}\right)_i \\ &\approx \left(\frac{\partial\xi}{\partial r}\right)_i\left(\frac{\Phi_{i+1}-\Phi_{i-1}}{2}\right)\end{aligned} \tag{2.32}$$

for the first derivative and

$$\begin{aligned}\left(\frac{\partial^2\Phi}{\partial r^2}\right)_i &= \left[\left(\frac{\partial\xi}{\partial r}\right)^2\frac{\partial^2\Phi}{\partial\xi^2}+\frac{\partial^2\xi}{\partial r^2}\frac{\partial\Phi}{\partial\xi}\right]_i \\ &\approx \left(\frac{\partial\xi}{\partial r}\right)_i^2(\Phi_{i+1}-2\Phi_i+\Phi_{i-1})+\left(\frac{\partial^2\xi}{\partial r^2}\right)_i\left(\frac{\Phi_{i+1}-\Phi_{i-1}}{2}\right)\end{aligned} \tag{2.33}$$

for the second derivative. These employ the usual two and three-point centered difference formulas on the transformed grid. The cylindrical Poisson equation at the ith gridpoint then has the form

$$\alpha_i\Phi_{i+1}+\beta_i\Phi_i+\gamma_i\Phi_{i-1}=s_i \tag{2.34}$$

with the coefficients given by

$$\begin{aligned}\alpha_i &= \left[\left(\frac{\partial\xi}{\partial r}\right)^2+\frac{1}{2}\frac{\partial^2\xi}{\partial r^2}+\frac{1}{r}\frac{\partial\xi}{\partial r}\right]_i \\ \beta_i &= -\left[2\left(\frac{\partial\xi}{\partial r}\right)^2+\frac{r_0^2}{r^2}k_x^2+k_\zeta^2\right]_i \\ \gamma_i &= \left[\left(\frac{\partial\xi}{\partial r}\right)^2-\frac{1}{2}\frac{\partial^2\xi}{\partial r^2}-\frac{1}{r}\frac{\partial\xi}{\partial r}\right]_i\end{aligned} \tag{2.35}$$

and s_i represents the source term. The direct recurrence solution for this type of equation is well known in finite-difference fluid simulation (the method is discussed by Potter [37, pages 88-91] and Hockney and Eastwood [38, pages 185-186]). The idea is to look for a recurrence relation of the the form

$$\Phi_{i-1}=x_i\Phi_i+y_i \tag{2.36}$$

where x and y are to be determined (the roles of i and $i-1$ are often reversed, yielding similar results). Substitution into the field equation (Eq. (2.34)) gives

$$\alpha_i \Phi_{i+1} + \beta_i \Phi_i + \gamma_i (x_i \Phi_i + y_i) = s_i$$

which can be rearranged to yield

$$\Phi_i = -\frac{\alpha_i}{\beta_i + \gamma_i x_i} \Phi_i + \frac{s_i - y_i \gamma_i}{\beta_i + \gamma_i x_i}$$

Since this is of the same form as Eq. (2.36), the coefficient terms are given by

$$x_{i+1} = \frac{-\alpha_i}{\beta_i + \gamma_i x_i} \tag{2.37}$$

$$y_{i+1} = \frac{s_i - y_i \gamma_i}{\beta_i + \gamma_i x_i} \tag{2.38}$$

which are calculated in a *forward* scan. The field component (Φ_i) is subsequently obtained by a backward scan, given by Eq. (2.36). The only work remaining is to determine the starting values for each scan; these are determined by the boundary conditions on the potential. This is complicated by the location of the boundaries—the only case usually considered (as in the above references) is that of Dirichlet boundary conditions with the boundaries on the end grid points. For the current system, with the boundaries between grid points, we represent the parity at the boundaries by

$$\Phi_{N+1} = \eta \, \Phi_N$$

$$\Phi_0 = \eta \, \Phi_1$$

where the cells in the system number from 1 to N. The *virtual* grid-points at $i = 0$ and $i = N + 1$ only serve to define the parity at the boundary, which is even parity for $\eta = +1$ ($\Phi' = 0$), and odd parity for $\eta = -1$ ($\Phi = 0$). The field equation at the $i = 1$ grid point is then

$$\begin{aligned} s_1 &= \alpha_1 \Phi_0 + \beta_1 \Phi_1 + \gamma_1 \Phi_2 \\ &= (\eta \alpha_1 + \beta_1) \Phi_1 + \gamma_1 \Phi_2 \end{aligned}$$

which can be rearranged to the form of the recurrence relation (2.36) :

$$\Phi_1 = -\frac{\gamma_1}{\eta\alpha_1 + \beta_1}\Phi_2 + \frac{s_1}{\eta\alpha_1 + \beta_1}$$

The recurrence relation then requires that

$$\begin{aligned} x_2 &= \frac{-\gamma_1}{\eta\alpha_1 + \beta_1} \\ y_2 &= \frac{s_1}{\eta\alpha_1 + \beta_1} \end{aligned}$$

for the starting values of the coefficient arrays in the forward scan. For the backward scan to solve for the potential, a similar calculation gives

$$\Phi_N = \frac{s_N - \alpha_N y_N}{\beta_N + \eta\,\gamma_N + x_N}$$

as the starting value.

The last question with the tridiagonal inversion concerns execution speed. Since this is a direct solution, it is much faster than general matrix inversion techniques (tridiagonal inversion is one of the fastest of the rapid elliptic solvers). However, this solution is a marching-process in i, inhibiting straightforward vectorization. We therefore vectorize in the perpendicular direction (χ) by looping over the second coordinate in the inner-most loop, which requires two-dimensional arrays for the coefficients of the recurrence relation (2.36). The result is a fast and accurate solution; using it as the core part of an iteration method is reasonable.

Once the cylindrical Laplacian is inverted, the correction term is evaluated. This must be performed in (r, θ) space, due to the terms involving $\cos\theta$ and $\sin\theta$, and thus involves two extra one-dimensional Fourier transforms per iteration. The extra expense introduced in the mode representation could be avoided by finite-differencing the χ (or θ) derivatives in real space instead;

the resulting equation would then be solved by cyclic reduction [38]. In this research the mode representation was kept due to its greater utility—the representation of the periodic variables in terms of mode number is attractive both from diagnostic and theoretical points of view. Timing tests show that the the overall computational cost of the present implementation is small for less than about ten iterations. In a typical run for the three-dimensional grid configuration (the worst case, because of the large number of toroidal modes present), the Poisson solver accounts for between 15 and 25 percent of the cpu time of the entire time-step loop.

For $\epsilon_\zeta \lesssim .2$ (corresponding to an aspect ratio of 2.5), the method usually converges to at least five decimal places accuracy in 4-6 iterations for a typical plasma profile. The Poisson solver is structured so that each toroidal mode is calculated separately, which is possible due to the azimuthal symmetry. This allows numerous temporary arrays to be generated to assist in the inversion. The independent calculation of each toroidal mode also forces the adoption of a "separated" (k_χ, k_ζ) mode representation—the Fourier transforms in χ, required for the toroidal corrections, must be independent of the transforms in ζ. In the usual mode representation (i.e. FFT2 structure), the modes cannot be transformed independently.

The last consideration in the Poisson solver is with the radial accuracy. The finite difference approximations are accurate to second order in $\Delta\xi$, which is probably satisfactory for most applications, as discussed in section 2.3. One way to improve the accuracy of this method would be to substitute higher-order finite-difference approximations for the derivatives and then invert the equations using the more general block-tridiagonal inversion method [39]. In this case, speed considerations would probably restrict the accuracy of the

scheme to no more than fourth-order.

The electric field components are calculated from the potential, using the toroidal metric :

$$\begin{aligned} E_r &= -\frac{\partial \Phi}{\partial r} \\ E_\chi &= -\frac{r_0}{r}\frac{\partial \Phi}{\partial \chi} \\ E_\zeta &= -\frac{R_0}{R}\frac{\partial \Phi}{\partial \zeta} \end{aligned} \tag{2.39}$$

For the radial field, we again apply the two-point finite difference approximation for the derivative to get

$$(E_r)_i = \left(\frac{\partial \xi}{\partial r}\right)_i \left(\frac{\Phi_{i+1} - \Phi_{i-1}}{2}\right) \tag{2.40}$$

The χ and ζ derivatives are simply multiplications in (r, k_χ, k_ζ) space. The r_0/r multiplication for the E_χ component is straightforward, but the R_0/R multiplication for the E_ζ component requires transformation to (r, θ) space because of the θ dependence in R (and must be transformed back again, for filtering).

2.5 Charge accumulation and field interpolation

In this section we discuss interpolation methods for an arbitrary coordinate system that are accurate, easily implemented, and independent of the metric wherever possible. The three stages of the charge accumulation are considered first—interpolation of the density to the grid, transformation weighting, and filtering.

The initial interpolation is done on a *computational* grid, that is, with no reference to the actual metric (aside from constant scale factors). The resultant pseudo-charge density (ρ') is identical to that which would be the result in

a slab coordinate system. This procedure views the coordinate transformation as a property of the *grid*, freeing us from the difficulties in considering particle "shapes" in arbitrary coordinate systems. Additionally, this procedure enables us to employ the same interpolation routines independent of geometry, which simplifies the implementation considerably.

The actual interpolation methods used in this research fall into the category of *Area-Weighting* methods, so called because the interpolation weight from (or to) a particular cell depends on how much of a particle's *area* overlaps that cell. The particle "shape" is rectangular for the two-point method and triangular for the three-point method. These methods are known as linear weighting, or Cloud-In-Cell (CIC), and quadratic weighting, or Triangular-Shaped-Cloud (TSC). Although the association of a given particle area or volume with an interpolation scheme is important from a conceptual point of view, in terms of smoothness it is more important that these interpolating functions are *splines*. This point is further discussed below.

Letting x_j denote the position of the jth particle, x_g an arbitrary grid-point, and $\delta = x_j - x_g$, the particle weight for that grid point will be given by

$$w(x) = \begin{cases} 1 - \frac{\delta}{\Delta} & |\delta| \leq \Delta \\ 0 & \text{otherwise} \end{cases} \tag{2.41}$$

for linear weighting, and

$$w(x) = \begin{cases} \frac{3}{4} - \left(\frac{\delta}{\Delta}\right)^2 & |\delta| \leq \frac{\Delta}{2} \\ \frac{1}{2}\left(\frac{3}{2} - \frac{\delta}{\Delta}\right)^2 & \frac{\Delta}{2} \leq |\delta| \leq \frac{3\Delta}{2} \\ 0 & \text{otherwise} \end{cases} \tag{2.42}$$

for quadratic weighting (from Hockney and Eastwood [38]). In the toroidal nonuniform grid system, the radial particle coordinates u_i are transformed to the stretched coordinates ξ_i for the interpolation.

Linear weighting is second-order accurate in the grid spacing and the interpolated function is continuous as the particle crosses a cell boundary. Quadratic weighting is also second-order accurate, but both the interpolated function and its first derivative are continuous as the particle crosses a cell boundary. The additional smoothness of quadratic weighting results in less error due to undersampling—the aliased wavenumber contributions are much smaller than in linear weighting [21, pages 168-170]. The simulation will thus be better able to tolerate small values of λ_D/Δ without numerical heating, as well as needing less k-space filtering. This is important mainly along the direction of the magnetic field (long dimension). Therefore, we typically use quadratic weighting in the ζ coordinate for the usual 3-d grid configuration; linear weighting is used in the cross-field variables ξ and χ. Both weighting methods cause an order $(k\Delta)^2$ flattening of the spectrum at low wavenumbers. This flattening can be corrected to order $(k\Delta)^4$ by using a k-space *compensating* factor [21, Appendix B] (this type of post-sampling correction is also known as *deconvolution* [40]). Finally, note that the flat-metric type of interpolation allows straightforward substitution of higher-order methods.

The next step in obtaining the charge density for the Poisson solver is to include the effects due to the metric. The actual charge density is determined from the differential relation

$$\rho = \frac{\partial V'}{\partial V}\rho' = \frac{1}{J}\rho' \tag{2.43}$$

where J is given by $J = h_r h_\chi h_\zeta$ and represents the transformation Jacobian for the toroidal coordinate system (h_r includes the effect of the nonunform grid). This becomes

$$\rho = \frac{\partial \xi / \partial r}{h_\chi h_\zeta}\rho' \tag{2.44}$$

which must be performed in (r, χ) space, due to the θ-dependence in h_ζ. The main problem with this approach is when the Jacobian vanishes at some point within the simulation region, as it does in the toroidal system at $r = 0$. This problem can be avoided by placing the boundaries between gridpoints; there will be no grid point at $r = 0$ and thus no singularity. The given method of charge accumulation, together with the filter techniques discussed below, allow the adoption of a wide variety of coordinate metrics, in principle. A similar approach to handling the metric was used by Brackbill and Ruppel [41] for two-dimensional particle-in-cell fluid simulations with an adaptive grid.

Finally, the filtering (or finite-size-particle shaping) must be considered. A commonly-used filter in particle simulations is the convolution of the accumulated charge density with a shape-factor, often a Gaussian, which is performed in k-space :

$$\rho(\mathbf{k}) \rightarrow \rho(\mathbf{k}) \exp\left(-[\mathbf{k} \cdot \mathbf{a}]^2/2\right)$$

where $\mathbf{k}$ is the wavevector and $\mathbf{a}$ is a measure of the particle size. This type of global filtering operator has the advantages of flexibility and ease of implementation, and can be used to partially compensate for errors introduced in the Poisson solver or the sampling method [21, Appendix B]. At present, a simple Gaussian shape-factor in the χ and ζ variables is used.

The use of a global filtering operator for a highly nonuniform or non-cartesian coordinate is questionable, however. For the radial variable in a cylindrical system, a non-standard (Bessel) representation must be used in order to have a rigorously convergent eigenfuction expansion. This problem can be avoided by considering a region far from the origin, as in the work of Cheng and Okuda [20]. In the case of a nonuniform grid, the non-locality of

the above operator is somewhat inappropriate, although a transform in the stretched variable ξ is reasonable if a rigorously convergent transform can be found.

A better alternative exists for such situations, known as *digital* filtering, and is described by Birdsall and Langdon [21, Appendix C]. (Although the term *digital filtering* may refer to any discrete filtering process, we follow the convention of Birdsall and Langdon in applying it only to filtering in the natural coordinate, i.e. without resorting to a transform of some sort.) The digital filter employed here is written as $\hat{S}_D^N$, denoting the N-fold application of the simple filter

$$\hat{S}_D(\rho_i) = \frac{\rho_{i-1} + 2\rho_i + \rho_{i+1}}{4} \tag{2.45}$$

where i stands for the ξ-coordinate. This is known as a *binomial* filter, and is equivalent to a gaussian shape factor in the limit of $N \to \infty$. To see this, we write this filter in terms of its k-space representation in a uniform grid system [21] and then expand, assuming small $k\Delta$:

$$\begin{aligned} \hat{S}_D^N(k) &= \left(\cos\frac{k\Delta}{2}\right)^{2N} \\ &\approx \left[1 - \left(\frac{k\Delta}{2}\right)^2\right]^N \end{aligned}$$

When using this filter, the effective particle size will increase as N increases. Anticipating the result, we let

$$a_* = \sqrt{\frac{N}{2}}\,\Delta \tag{2.46}$$

whereupon the $N \to \infty$ limit of the filter becomes

$$\begin{aligned} \lim_{N\to\infty} \hat{S}_D^N(k) &= \lim_{N\to\infty} \left[1 - \frac{k^2 a_*^2/2}{N}\right]^N \\ &\equiv \exp\left(-\frac{k^2 a_*^2}{2}\right) \end{aligned}$$

Although this only holds exactly in the large N, small $k\Delta$ limit, it nevertheless gives some feel for the particle "size" associated with the application of the filter. The total filtering operator can thus be written as

$$\rho(\xi, k_\chi, k_\zeta) \rightarrow \hat{S}_D^N(\rho)\, \hat{S}(k) \tag{2.47}$$

where $\hat{S}(k)$ is given by

$$\hat{S}(k) = \exp\left[-(k_\chi^2 a_\chi^2 + k_\zeta^2 a_\zeta^2)/2\right] \tag{2.48}$$

Next we consider the filtering of the electric fields and their interpolation onto the particle positions. This is handled in the same way as the charge accumulation and filtering, except that no transformation weighting is required. It is important here to determine the conditions under which there is no numerical *self-force* term. The early research in particle simulation showed that for this type of code, a self-force was avoided by using the same interpolation scheme in the field interpolation as in the charge accumulation, and by adopting a filter that was symmetric in its argument [38]. These conditions are relevant in the toroidal system as well. One problem with the early proof is its assumption of periodicity, which is inapplicable in our radial coordinate. In the presence of non-periodic boundaries, there will in general be a self-force—from an induced image charge. However, this boundary term can be included in the theory, and we refer to a numerical self-force more accurately as a failure to conserve momentum by the algorithm.

To examine the approximations that have been made in our model and determine whether it is momentum-conserving we must express formally the interpolation steps that have been given. The interpolation (accumulation) and filtering are two distinct processes, but we shall initially express these in

terms of some general operator $\mathcal{L}$. The interpolation and filtering operations on the charge density can then be written in terms of a continuous variable as

$$\mathcal{L} \circ \rho(\mathbf{x}) = \int \rho(\mathbf{x}')\, \mathcal{L}(\mathbf{x}';\mathbf{x})\, J(\mathbf{x}')\, d\mathbf{x}' \tag{2.49}$$

where $\rho(\mathbf{x}')$ is the charge distribution, $\mathcal{L}(\mathbf{x}';\mathbf{x})$ is the interpolation or filter distribution, and $J(\mathbf{x}')\, d\mathbf{x}' = J(\mathbf{x}')\, dx'_1, \ldots, dx'_n$, is the volume element, for dimensionality n. In this operation we are simply summing the weights given to the point at $\mathbf{x}$ from every point in space ($\mathbf{x}'$); this will naturally depend on the geometry at $\mathbf{x}'$. Therefore we generally will have $\mathcal{L}(\mathbf{x}';\mathbf{x}) \neq \mathcal{L}(\mathbf{x};\mathbf{x}')$, where the coordinate in the second position denotes the fixed point. Furthermore, we require that $\mathcal{L}$ be linear, so the distribution satisfies

$$\int \mathcal{L}(\mathbf{x}';\mathbf{x})\, J(\mathbf{x}')\, d\mathbf{x}' = 1 \tag{2.50}$$

The interpolation and filter distributions will be simply the transformed flat-metric distributions :

$$\mathcal{L}(\mathbf{x}';\mathbf{x}) = \frac{1}{J(\mathbf{x}')} \prod_{i=1}^{n} L_i(x'_i - x_i) \tag{2.51}$$

where $L_i(x'_i - x_i)$ is the flat-metric distribution of the ith coordinate. Note that $L_i(x'_i - x_i) = L_i(x_i - x'_i)$. The interpolation distribution is now written as

$$\mathcal{W}(\mathbf{x}';\mathbf{x}) = \frac{1}{J(\mathbf{x}')} \prod_{i=1}^{n} W_i(x'_i - x_i) \tag{2.52}$$

$$\equiv \frac{1}{J(\mathbf{x}')}\, W(\mathbf{x}' - \mathbf{x}) \tag{2.53}$$

and the filtering distribution as

$$\mathcal{S}(\mathbf{x}';\mathbf{x}) = \frac{1}{J(\mathbf{x}')} \prod_{i=1}^{n} S_i(x'_i - x_i) \tag{2.54}$$

$$\equiv \frac{1}{J(\mathbf{x}')}\, S(\mathbf{x}' - \mathbf{x}) \tag{2.55}$$

Here we have employed the symbols $W(\mathbf{x}' - \mathbf{x})$ and $S(\mathbf{x}' - \mathbf{x})$ to denote the total flat-metric distribution (i.e. the product of the individual coordinate distributions). The metric-dependent distributions $\mathcal{W}$ and $\mathcal{S}$ are analogous to the general distribution $\mathcal{L}$.

We now take the general charge density distribution $\rho(\mathbf{x}')$ to be the charge density due to an individual point source at $\mathbf{x}_j$:

$$\rho_j(\mathbf{x}') = q_j\,\delta(\mathbf{x}' - \mathbf{x}_j) \tag{2.56}$$

$$\equiv \frac{q_j}{J(\mathbf{x}')}\prod_{i=1}^{n}\delta(x_i' - x_j) \tag{2.57}$$

Using this value in the interpolation equation (2.49), the charge density becomes

$$\rho_j(\mathbf{x}) = q_j\,\mathcal{W}(\mathbf{x}_j;\mathbf{x}) = \frac{q_j}{J(\mathbf{x}_j)}W(\mathbf{x}_j - \mathbf{x}) \tag{2.58}$$

Although Eq. (2.58) can be used as a basis for a charge accumulation scheme (as in Ref. [20]), there are several problems with this approach. First, conservation of charge requires that

$$q_j = \int \rho_j(\mathbf{x})\,J(\mathbf{x})\,d\mathbf{x} \tag{2.59}$$

$$= q_j\int d\mathbf{x}\,\frac{J(\mathbf{x})}{J(\mathbf{x}_j)}\,W(\mathbf{x}_j - \mathbf{x}) \tag{2.60}$$

which cannot in general be satisfied simultaneously with condition (2.50). Further, one must decide how to handle the $1/J(\mathbf{x}_j)$ term for particles that pass too close to a point where the metric vanishes (as for $r = 0$ in a cylindrical or toroidal system).

These problems may be avoided, while retaining our differentialapproach, by approximating the charge density equation (Eq. (2.58)) by

$$\rho_j(\mathbf{x}) \approx \frac{q_j}{J(\mathbf{x})}W(\mathbf{x}_j - \mathbf{x})$$

$$
\begin{aligned}
&= \frac{q_j}{J(\mathbf{x})} W(\mathbf{x}-\mathbf{x}_j) \qquad (2.61)\\
&\equiv q_j \mathcal{W}(\mathbf{x};\mathbf{x}_j)
\end{aligned}
$$

This is a reasonable since the interpolation distribution is strongly peaked about zero. The conservation of charge equation (2.60) is now automatically satisfied when using the transformed slab-like interpolation and filtering distributions, regardless of the metric. Further, since the particle coordinates are virtually continuous and the grid is discrete, the vanishing of the metric at a point in the simulation region is no longer a problem—we simply avoid placing a grid-point at that location. In this case, the first grid-point is a half-cell away from the $r = 0$ point (farther when grid stretching is employed).

Given these preliminaries, the calculation of the self-field of an individual particle is as follows :

1. Interpolation. The charge density for a single particle of charge q_j and position $\mathbf{x}_j$ is given by

$$
\begin{aligned}
\rho_j(\mathbf{x}) &= q_j \mathcal{W}(\mathbf{x};\mathbf{x}_j)\\
&= \frac{q_j}{J(\mathbf{x})} W(\mathbf{x}-\mathbf{x}_j)
\end{aligned}
$$

   in terms of the flat-metric weight function W.

2. Filtering. The charge density is filtered to obtain the source term in the field equations,

$$
\begin{aligned}
s_j(\mathbf{x}) &= \int \rho_j(\mathbf{x}')\, \mathcal{S}(\mathbf{x}';\mathbf{x}) J(\mathbf{x})\, d\mathbf{x}'\\
&= \int \rho_j(\mathbf{x}')\, S(\mathbf{x}'-\mathbf{x})\, d\mathbf{x}'
\end{aligned}
$$

   using the filter function in its flat-metric form S.

3. Field solution. Here we are solving for $\mathbf{E}$ in terms of s_j :

$$\boldsymbol{\nabla} \cdot \mathbf{E} = 4\pi\, s_j(\mathrm{x})$$

4. Filtering. The filtered electric fields are given by

$$\begin{aligned} \mathbf{e}_j(\mathrm{x}) &= \int \mathbf{E}_j(\mathrm{x}')\, \mathcal{S}(\mathrm{x}';\mathrm{x})\, J(\mathrm{x}')\, d\mathrm{x}' \\ &= \int \mathbf{E}_j(\mathrm{x}')\, S(\mathrm{x}'-\mathrm{x})\, d\mathrm{x}' \end{aligned}$$

5. Interpolation to particles. The force on the jth particle (due to its own field) is

$$\begin{aligned} \mathbf{F}_j(\mathrm{x}_j) &= \int \mathbf{e}_j(\mathrm{x})\, q_j\, \mathcal{W}(\mathrm{x};\mathrm{x}_j) J(\mathrm{x})\, d\mathrm{x} \\ &= \int \mathbf{e}_j(\mathrm{x})\, q_j\, W(\mathrm{x}-\mathrm{x}_j)\, d\mathrm{x} \end{aligned}$$

We may now combine these expressions, to obtain the force on the jth particle due to its self-field (written as $\mathbf{F}_{jj}$) :

$$\begin{aligned} \mathbf{F}_{jj} &= \int d\mathrm{x}\, q_j\, W(\mathrm{x}-\mathrm{x}_j)\, \mathbf{e}_j(\mathrm{x}) \\ &= \int d\mathrm{x}\, J(\mathrm{x})\, \rho_j(\mathrm{x})\, \mathbf{e}_j(\mathrm{x}) \\ &= \int d\mathrm{x}\, J(\mathrm{x})\, \rho_j(\mathrm{x}) \int d\mathrm{x}'\, J(\mathrm{x}')\, \mathbf{E}_j(\mathrm{x}')\, \mathcal{S}(\mathrm{x}';\mathrm{x}) \end{aligned}$$

Interchanging the integrals gives

$$\begin{aligned} \mathbf{F}_{jj} &= \int d\mathrm{x}'\, J(\mathrm{x}')\, \mathbf{E}_j(\mathrm{x}') \int d\mathrm{x}\, \rho_j(\mathrm{x})\, J(\mathrm{x})\, \mathcal{S}(\mathrm{x}';\mathrm{x}) \\ &= \int d\mathrm{x}'\, J(\mathrm{x}')\, \mathbf{E}_j(\mathrm{x}') \int d\mathrm{x}\, \rho_j(\mathrm{x})\, S(\mathrm{x}'-\mathrm{x}) \\ &= \int d\mathrm{x}'\, J(\mathrm{x}')\, \mathbf{E}_j(\mathrm{x}') \int d\mathrm{x}\, \rho_j(\mathrm{x})\, S(\mathrm{x}-\mathrm{x}') \\ &= \int d\mathrm{x}'\, J(\mathrm{x}')\, \mathbf{E}_j(\mathrm{x}')\, s_j(\mathrm{x}') \end{aligned}$$

where the symmetry of the flat-metric filter

$$S(\mathrm{x}-\mathrm{x}') = S(\mathrm{x}'-\mathrm{x})$$

has been used in deriving the result.

The above expression for the self-force can be cast into a more illuminating form by substituting for s_j from the field equation, and enforcing the electrostatic condition ($\nabla \times \mathbf{E} = 0$), giving

$$\begin{aligned} \mathbf{F}_{jj} &= \frac{1}{4\pi} \int \mathbf{E}_j \, \nabla \cdot \mathbf{E}_j \, dV \\ &= \int \nabla \cdot \mathbf{T}_{jj} \, dV \end{aligned}$$

where $\mathbf{T}$ is the maxwell stess tensor in the electrostatic limit :

$$\mathbf{T} = \frac{1}{4\pi} \left[\mathbf{E}\mathbf{E} - \frac{1}{2} (\mathbf{E} \cdot \mathbf{E}) \, \mathbf{I} \right]$$

and $\mathbf{I}$ is the identity tensor. This takes on the form of a conservation law :

$$\frac{d\mathbf{P}_{jj}}{dt} - \oint_S \mathbf{T}_{jj} \cdot \mathbf{dS} = 0, \qquad \frac{d\mathbf{P}_{jj}}{dt} \equiv \mathbf{F}_{jj}$$

which is in agreement with the more general conservation of momentum relation as given by Decyk [42]. Thus the given procedure has the desired momentum-conserving character.

The last concern with the interpolation/filtering in a non-cartesian system is whether the filter operation conserves charge; i.e. whether

$$\int (\mathcal{S} \circ \rho) \, dV = \int \rho \, dV = Q$$

where $\mathcal{S}$ is the filter operator and Q is the total charge. Although it is usually taken for granted that the filter operator conserves charge, in a non-cartesian system this may not be generally true. In a uniform grid slab geometry, any *neutral* filter such as a k-space filter will conserve this quantity, because the sum over gridpoints $\sum_{i=1}^{N_g} \rho_i$ is preserved by the Fourier transform. If the geometrical weighting factors of an arbitrary metric system are included, however, this filter

fails to conserve charge. In a cylindrical coordinate system, the charge will be given by

$$\int \rho \, dV \approx \sum_{i}^{N_g} \rho_i r_i \Delta r$$

which is not preserved by the k-space filter in general. In many cases the difference will be small, but when the curvature is large (e.g. where the point $r = 0$ is included) this discrepancy may be important.

We first examine the effect of a simple digital filter on the total charge in slab geometry. For simplicity, we choose a single application of the binomial digital filter for our filter operator, and consider only a single dimension. Then we have

$$\begin{aligned} (\mathcal{S} \circ \rho)_i &= \frac{\rho_{i-1} + 2\rho_i + \rho_{i+1}}{4} \\ &= \rho_i + \frac{\Delta^2}{4} \frac{\rho_{i-1} - 2\rho_i + \rho_{i+1}}{\Delta^2} \\ &= \rho_i + \frac{\Delta^2}{4} \rho_i'' + \mathcal{O}(\Delta^4) \end{aligned}$$

If we neglect the $\mathcal{O}(\Delta^4)$ contribution, and approximate this by a continuous system, the conservation of charge equation in slab geometry becomes

$$\begin{aligned} \int (\mathcal{S} \circ \rho) \, dV &= \int \rho \, dV + \frac{\Delta^2}{4} \int \rho'' \, dV \\ &= \int \rho \, dx + \frac{\Delta^2}{4} \left[\rho'(L_x) - \rho'(0) \right] \end{aligned}$$

for boundaries at $x = 0$ and $x = L_x$. For periodic or even-parity boundary conditions on ρ the extra term on the right hand side vanishes; for odd parity an unavoidable sheath effect is responsible for the lack of charge conservation by the filter.

Turning now to an arbitrary metric, we adopt ψ as our one-dimensional variable and obtain

$$\int (\mathcal{S} \circ \rho) \, dV = \int \rho \, dV + \frac{\Delta^2}{4} \int \frac{\partial^2 \rho}{\partial \psi^2} \, dV$$

$$= \int \rho\, dV + \frac{\Delta^2}{4} \int d\psi\, J \frac{\partial^2 \rho}{\partial \psi^2}$$
$$= \int \rho\, dV + \frac{\Delta^2}{4} \left[J \frac{\partial \rho}{\partial \psi} \Big|_0^{L_\psi} - \int d\psi\, \frac{\partial J}{\partial \psi} \frac{\partial \rho}{\partial \psi} \right]$$

having integrated by parts to obtain the last expression. The boundary term in the above expression is analogous to that for the slab geometry result, and can be ignored (in addition to vanishing for even or periodic parity, it also vanishes for continuity boundary conditions, i.e. at an $r = 0$ point). The new effect is the term depending on the partial derivative of the Jacobian, and only vanishes in general if J has no dependence on ψ.

At this point we can construct a charge-conserving filter simply by absorbing the new term into the definition of the filter, which becomes

$$(\mathcal{S} \circ \rho)_i = \rho_i + \frac{\Delta^2}{4} \left[\frac{1}{J} \frac{\partial}{\partial \psi} \left(J \frac{\partial \rho}{\partial \psi} \right) \right]_i \tag{2.62}$$

where the derivatives are calculated by finite-difference approximations. A simple and elegant solution to the charge conservation constraint has emerged, although some new concerns are raised. First, this filter does not correspond to a metric-independent, "slab-like" filter, as previously assumed. Thus, the use of such a charge-conserving filter would likely destroy the momentum-conserving property. In addition, this filter has questionable properties near a point where the metric vanishes (see Appendix A).

The loss of exact charge conservation by the filter operation is therefore unavoidable in our algorithm. This can be shown for an arbitrary filter distribution $\mathcal{S}$. The total charge after the filter operation is given by

$$Q = \int d\mathbf{x}\, J(\mathbf{x})\, (\mathcal{S} \circ \rho(\mathbf{x}))$$
$$= \int d\mathbf{x}\, J(\mathbf{x}) \int d\mathbf{x}'\, J(\mathbf{x}')\, \rho(\mathbf{x}')\, \mathcal{S}(\mathbf{x}'; \mathbf{x})$$

$$= \int dx\, J(x) \int dx'\, \rho(x')\, S(x'-x)$$
$$= \int dx'\, J(x')\, \rho(x') \int dx\, \frac{J(x)}{J(x')} S(x'-x)$$

Since the flat-metric filter distribution satisfies

$$1 = \int dx'\, S(x'-x)$$

it is clear that charge will only be conserved in general if $J(x) = J(x')$, i.e. for a constant metric.

Given the favorable properties of the present approach, the lack of charge conservation by the filter is tolerable. The interpolation/filtering algorithm employed here is conceptually simple and straightforward to implement, even in the vicinity of a point where the Jacobian vanishes. An important feature of particle simulation in slab geometry is conservation of momentum, which is retained by the present algorithm. Further, since the charge density is the important dynamical quantity (not the charge), discrepancies in the total charge introduced in the filtering process may not have observable consequences.

2.6 Particle pusher: Ions

The usual scheme for the time advancement of the ions in particle simulations employs the leap-frog method [37], which considers the particle positions and field quantities to be known at integer timesteps and the velocities at half-integer timesteps. Applied to the system of differential equations employed in this model, the leap-frog method is non-dissipative and second-order accurate in the time-step. Although the technique for applying the leapfrog method in slab geometry is straightforward, there are serious obstacles to implementation in a general non-cartesian coordinate system. We start with the

equations of motion for an arbitrary metric :

$$h_k\ddot{q}_k + \sum_j h_j\dot{q}_j\left(2\dot{q}_k\frac{\partial h_k}{h_j\partial q_j} - \dot{q}_j\frac{\partial h_j}{h_k\partial q_k}\right) = \frac{q}{m}\left\{E_k + \sum_{ij} h_i\dot{q}_i B_j\epsilon_{ijk}\right\}, \quad (2.63)$$

which can be directly derived from the Lagrange equations, using the transformed Lorentz force law. A simpler representation is obtained in terms of the angular momenta, giving $q_k = l_k/h_k^2$ for the coordinates, and

$$\frac{\dot{l}_k}{h_k} - \sum_j(\frac{l_j}{h_j})\left(\frac{l_j}{h_j^2}\frac{\partial h_j}{h_k\partial q_k}\right) = \frac{q}{m}\left\{E_k + \sum_{ij}\frac{l_i}{h_i}B_j\epsilon_{ijk}\right\} \quad (2.64)$$

for the angular momenta. If the toroidal metric is used, the orbit equations become

$$\begin{aligned}
\ddot{u} - \kappa_\chi\frac{l_\chi^2}{(1+\kappa_\chi u)^3} - \epsilon_\zeta\frac{l_\zeta^2\cos\theta}{(1+\epsilon_\zeta(1+\kappa_\chi u)\cos\theta)^3} &= F_u \\
\frac{\dot{l}_\chi}{(1+\kappa_\chi u)} + \epsilon_\zeta\frac{l_\zeta^2\sin\theta}{(1+\epsilon_\zeta(1+\kappa_\chi u)\cos\theta)^3} &= F_\chi \quad (2.65)\\
\frac{\dot{l}_\zeta}{(1+\epsilon_\zeta(1+\kappa_\chi u)\cos\theta)} &= F_\zeta
\end{aligned}$$

in which the right-hand-terms are determined from Eq. (2.64). One standard way of handling the rotation of the velocity vector in slab geometry is to finite difference the velocities using

$$\dot{v}_k^n = \frac{v_k^{n+1/2} - v_k^{n-1/2}}{\delta t} + \mathcal{O}(\delta t^2) \quad (2.66)$$

$$v_k^n = \frac{v_k^{n+1/2} + v_k^{n-1/2}}{2} + \mathcal{O}(\delta t^2) \quad (2.67)$$

which give a centered, second-order accurate finite-difference equation. The components are then collected into a matrix equation

$$\mathbf{M}\mathbf{v}^{n+1/2} = \mathbf{N}\mathbf{v}^{n-1/2} + \frac{q}{m}\,\delta t\,\mathbf{E} \quad (2.68)$$

where M, N, and E all depend on quanties at the nth time level. This equation is then inverted to give the velocities at the $n+\frac{1}{2}$ timestep in terms of those

at the $n - \frac{1}{2}$ timestep. Since only three coordinates are involved, the solution is calculated analytically and implemented in the code to give a direct, fast inversion.

A straightforward implementation of this method will not work in a general coordinate system, due to the nonlinear terms in the equations of motion (2.63)–(2.64). In this case, there is a choice of three quantities that may be considered given at the half-integer timestep and correspondingly finite-differenced. These are the time derivative of the coordinates $\dot{q}_k$, the velocities $h_k\dot{q}_k$, or the angular momenta $h_k^2\dot{q}_k$. Regardless of which variable is differenced, the nonlinearities remain, causing the standard leap-frog method to fail.

One alternative is to adopt a predictor-corrector type approach based on the smallness of the nonlinear terms in equations (2.63) or (2.64). The simplest method would be to obtain predicted values by ignoring the nonlinear terms altogether, then solve for the corrected values. The first full-dynamics pusher employed in this research took a variant of this approach. The angular momenta in χ and ζ were used to take advantage of the simpler equations of motion. The accuracy of the predictor-corrector method was improved by treating the nonlinear terms as the product of two terms—a predictive term, determined by a half-timestep push, and a linear term, to be inverted in the usual way. In the cylindrical type-II system with tokamak fields, this method accurately reproduced the drift orbits and showed little damping. This pusher was used with good results in simulations of the field-reversed configuration [43].

In the full toroidal system, however, this type of pusher becomes ill-defined near $r = 0$. Tests show that even when the particle is kept well away from the origin, significant loss of energy occurs. This is demonstrated

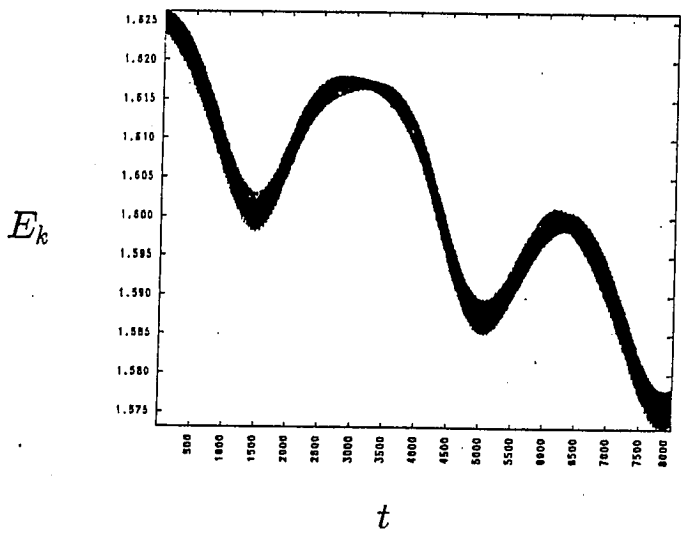

Figure 2.10: Particle energy vs time, predictor-corrector algorithm

in Figure 2.10, where the particle energy in a test run is plotted as a function of time (8000 timesteps, $\delta t = 0.2\,\Omega_i^{-1}$) for particles in a tokamak-like field configuration. In this case the ions lose about 10% of their inital energy, which is unacceptable.

The problem with this method is that the second term in Eq. (2.65) is not small and is a poor expansion parameter in the typical toroidal case. The resulting de-centeredness causes the rapid cyclotron motion to slowly decay. Although the damping of cyclotron motion is often an intended effect in an implicit code [18], it is undesirable for it be an unavoidable by-product of the metric. Since *any* predictor-corrector method will be at least partially decentered in time, the integration of the cyclotron orbit will be subject to damping, and may cause problems depending on the time scale of the simulation.

The solution to this problem is to push in a coordinate system that is

better-suited to the physics of the particle motion. The approach chosen in this research is simple—to push completely in cartesian coordinates. This somewhat crude, "obvious" method, though involving time-consuming transformations, has several advantages. First, it is rigorously centered and second-order, with little or no numerical damping. A test run comparing to the previous method showed excellent energy conservation over the course of the run. The second advantage of the transformation approach is that it can be used for any coordinate system, as long as the transformations can be done accurately. (More precisely, there must exist a transform function together with an exact inverse—since the velocity components never "leave" cartesian coordinates, the rotation will be handled correctly, even if the transform itself is not exact [see below].) For the toroidal system the transformations are straightforward but somewhat expensive; it is likely, however, that the cost of a sophisticated predictor-corrector routine as previously given is comparable (although no detailed timing comparisons were performed).

In a polar coordinate system, the transformation of the velocity vector to cartesian coordinates at the beginning of the particle push is given by

$$v_x^{n-1/2} = v_r^{n-1/2}\cos(\theta^{n-1/2}) - v_\theta^{n-1/2}\sin(\theta^{n-1/2}) \tag{2.69}$$

$$v_y^{n-1/2} = v_r^{n-1/2}\sin(\theta^{n-1/2}) + v_\theta^{n-1/2}\cos(\theta^{n-1/2}) \tag{2.70}$$

where $\theta^{n-1/2}$ must be computed via

$$\theta^{n-1/2} = \frac{1}{2}\left(\theta^{n-1} + \theta^n\right) \tag{2.71}$$

since all the terms in the transformation must be given at the same time level, to second order in δt. Due to the size of the particle arrays, storing the θ values at more than one time-level is undesirable. Therefore, the velocity components must be kept in cartesian coordinates thoughout the entire time-step loop.

During the pushing phase itself, both the old and new coordinates are known simultaneously. If the pusher loop is structured so that one is operating only on relatively small "blocks" of particles, then one can obtain the velocities in (ξ, χ, ζ) space at minimal computational expense. This will be necessary to allow accumulation of the velocities to a grid to satisfy a magnetoinductive or electromagnetic algorithm. For diagnostics, we may "transform" the velocities to toroidal coordinates in an uncentered way, as long as we are careful to exactly invert this "transformation" before pushing.

The only remaining concern is the amount of numerical diffusion associated with this method of pushing. The amount of deviation from the field line for a single particle in one timestep is proportional to $(v_\parallel \delta t)^2$ since the pushing method is second order accurate. This quantity will be small for the ion species in most cases. For a Lorentz-force pusher, the need to accurately reproduce the cyclotron motion is the dominant constraint; numerical diffusion will not be an issue except when large anisotropies in the ion temperature distribution exist ($T_\parallel \gg T_\perp$).

A better solution to the pusher problem than the one employed here may be to adopt a hybrid method—transforming in the r–θ plane, but predictor-corrector in ζ. This type of scheme would probably be somewhat faster than the full transformation approach, and would suffer from less numerical diffusion. It would also be more sensitive to the details of the metric. However, the current method is straightforward to implement, and conserves the particle invariants remarkably well in tests (given in Chapter 3). Therefore, further research into full dynamics pusher algorithms in a complex metric is left for future efforts.

2.7 Particle Pusher: Electrons

In a strongly magnetized plasma, keeping full electron dynamics poses a severe timestep restriction due to the high electron gyrofrequency. The adoption of a guiding center formulation allows us to circumvent this restriction, while retaining most of the important physical effects. An algorithm for this method in particle simulation was first given by Cheng and Okuda [20], and has been employed in many recent simulations [11,19,44].

In toroidal geometry, the guiding-center drift equations include the important first order Larmor radius magnetic effects—mirroring (banana orbits), drifts from the flux surface, and so on. The most important elements missing in this description are the polarization current and the finite larmor radius electric effects; these are usually small for electrons in a strongly magnetized plasma ($\rho_e \lesssim \lambda_e$). For non-relativistic dynamics ($E \ll B$) and low frequencies the electron drift equations given by Northrup [45] reduce to

$$\mathbf{v}_d = \mathbf{u}_e + \frac{\mathbf{b}}{\Omega_e} \times \left\{ (\mu/m)\nabla B + v_\parallel^2 (\mathbf{b}\cdot\nabla\mathbf{b}) \right\} \tag{2.72}$$

$$\frac{dv_\parallel}{dt} = -\frac{e}{m}E_\parallel - \frac{\mu}{m}\mathbf{b}\cdot\nabla B \tag{2.73}$$

where $\mathbf{u}_e = \mathbf{E}\times\mathbf{b}/B$, $\mathbf{b} = \mathbf{B}/B$, $\mu = \frac{1}{2}mv_\perp^2/B$, $\Omega_e = eB/mc$, and m is the electron mass. The particles would normally pushed by time differencing

$$\frac{d\mathbf{x}}{dt} = \mathbf{v}_d + v_\parallel \mathbf{b} \tag{2.74}$$

however, it is seen from Eq. (2.72) that the perpendicular drift motion is not compatible with the leapfrog method since the fields and drift velocity are given at the same time level. This is the rationale behind the predictor-corrector method [20] for the perpendicular component, which is third order accurate in δt (and is slightly dissipative, unlike the leap-frog method). The parallel

velocity component is pushed in the normal way :

$$v_{\|}^{n+1/2} = v_{\|}^{n-1/2} + F_{\|}^{n}\,\delta t \tag{2.75}$$

The prediction step uses the velocities at time step n and the positions at time step $n-1$ to estimate the positions at time step $n+1$:

$$\left(\mathbf{x}^{n+1}\right)^{*} = \mathbf{x}^{n-1} + 2\,\delta t\,\left(\mathbf{v}_d^{n} + \frac{1}{2}\left[v_{\|}^{n+1/2} + v_{\|}^{n-1/2}\right]\mathbf{b}\right) \tag{2.76}$$

The predicted positions are used to calculate values for the fields at the next time-step, giving the drift velocity for the correction step :

$$\begin{aligned}\left(\mathbf{v}_d^{n+1}\right)^{*} &\equiv \mathbf{v}_d^{n+1}\left[\left(\mathbf{x}^{n+1}\right)^{*}\right] \\ \mathbf{x}^{n+1} &= \mathbf{x}^{n} + \delta t\,\left(\mathbf{v}_{\|}{}^{n+1/2} + \frac{1}{2}\left[\mathbf{v}_d^{n} + \left(\mathbf{v}_d^{n+1}\right)^{*}\right]\right)\end{aligned} \tag{2.77}$$

It is important to properly time-center the magnetic field components in this equation since inhomogeneities may be strong. We currently use only magnetic fields that can be expressed analytically, so that the ∇B and $\mathbf{b}\cdot\nabla\mathbf{b}$ terms are known exactly, avoiding the need for magnetic field interpolation. The $\mathbf{b}\cdot\nabla\mathbf{b}$ term is evaluated using the identity

$$\mathbf{b}\cdot\nabla\mathbf{b} = \frac{1}{B}\left[\nabla B - \mathbf{b}\times(\nabla\times\mathbf{B})\right]$$

Derivation of the necessary drift terms is then straightforward, given expressions for the gradient and curl in an arbitrary coordinate system [46].

The only remaining subtlety is in the advancement the particle coordinates from the velocities. For an arbitrary metric, the velocity for the jth component is $h_j\dot{q}_j$, so that Eqs. (2.76)–(2.77) become

$$\begin{aligned}\left(q_j^{n+1}\right)^{*} &= q_j^{n-1} + 2\,\delta t\, v_j^{n}/h_j^{n} \qquad \text{(predict)} \\ q_j^{n+1} &= q_j^{n} + \delta t\, v_j^{n+1/2}/h_j^{n+1/2} \qquad \text{(correct)}\end{aligned}$$

where h_j is in general a function of all three coordinates, (q_1, q_2, q_3). The prediction step utilizes the metric components h_j^n, obtained from the coordinates at the nth time level. The correction step, however, requires unknown quantities $h_j^{n+1/2}$. One way of addressing this problem is to use the *predicted* positions in the calculation of h_j :

$$\begin{aligned} h_j^{n+1/2} &\equiv h_j\left(\mathbf{q}^{n+1/2}\right) \\ &\approx h_j\left(\left[\mathbf{q}^n + \left(\mathbf{q}^{n+1}\right)^*\right]/2\right) \end{aligned} \tag{2.78}$$

A more accurate method also exists when the metric is of the form $h_1 \equiv$ constant, $h_2 \equiv h_2(q_1)$, $h_3 \equiv h_3(q_1, q_2)$, as in the toroidal system. This allows the push to be ordered so that the coordinates needed for each metric component are known (to second order in δt). The results of the r-push enable the calculation of h_χ for the χ-push, which enables the calculation of h_ζ for the ζ-push. However, the accuracy gained by using this ordering does not change the overall accuracy of the push significantly, as seen in long test runs. Therefore, we use the predicted coordinates as in Eq. (2.78) for the push, to allow simple application of the pusher algorithm in more general metrics.

A major liability of this predictor-corrector algorithm is the need to repeat the entire field calculation for the electrons at the predicted positions. This is common to both the present implementation and the usual slab implementation [20], and is costly both in terms of computation and programming effort. The amount of programming effort can be reduced through the use of a modular field solver—the field loop can be reduced to a few subroutine calls within the guiding center pusher routine. Another liability is the increased number of particle quantities necessary. A three-dimensional slab implementation of the guiding center pusher requires nine particle quantities in general—the three coordinates and velocities, and a temporary vector that

holds the coordinates of the previous time-step for the predictive step, as well as the predicted positions for the corrective step. The implementation in the toroidal system adds two additional particle quantities—the magnetic moment (μ), which does not evolve but is different for each electron (determined by the initial loading), and the velocity component parallel to the magnetic field ($v_{\|}$). The three-component velocity vector holds the projection of the drift velocity onto the (u, χ, ζ) coordinate system.

The guiding center formulation works well when the electrons are "tied" to the field lines, as in tokamak-type magnetic fields, with only small drifts perpendicular to the field lines. In the time scale of interest in the typical numerical experiment, a typical untrapped electron will execute many orbits about the torus, remaining reasonably localized about a given flux surface. In such a system, the numerical diffusion away from the flux surface caused by the finite time-step is certainly a concern, and is one reason for using a flux coordinate system—the parallel motion causes no numerical diffusion in a Hamada-type coordinate system. (Orthogonal flux coordinate systems are also free from numerical diffusion perpendicular to the flux surface, though numerical diffusion may occur on the flux surface itself.) For example if we examine the amount of numerical diffusion in the "square torus" configuration (type-II cylindrical, tokamak fields) due to the poloidal field, we find that the deviation per time step from the flux surface will be on the order of

$$\delta \sim \left(v_{\|} \, \delta t \, \frac{B_{\chi}}{B} \right)^2 \tag{2.79}$$

Although this is second order in δt, the product $v_{\|} \, \delta t$ for electrons may be appreciable for typical simulation parameters, creating a definite concern about numerical diffusion in this system.

2.8 Boundary handling and the point at the origin

In a simulation code, the boundary conditions enter in several places—the field solver, the filtering of the field quantities, and the interpolation between the particles and the grid. For the particle/grid interpolations, the boundary conditions can be handled in a number of ways: decision-making (IF-THEN constructs), indirect lookup-table methods, or guard cells. The guard cell method used in this research employs an extra grid-point immediately outside the system that is mapped back on to the interior values in a manner consistent with the boundary conditions. This has the advantage of speed—the interpolation routines do not have to deal explicitly with the boundaries, nor are there any indirect lookup tables that may slow execution or inhibit vectorization. Another advantage of the guard cell technique is that unusual boundary conditions can be easily handled, since the boundary treatment (filling and emptying guard cells) is completely isolated from the rest of the calculation. In particular, the transition to the $r = 0$ boundary conditions at the inner boundary is eased by a guard cell formulation.

The boundary conditions at $r = 0$ must ensure continuity there, and the conditions for single-valuedness and continuity of first derivative are given by Aydemir and Barnes [47]. For a scalar field $f(r, \theta, \phi)$, we require that

$$\begin{aligned} \left.\frac{\partial f}{\partial r}\right|_{r=0} &= 0 \qquad \text{for } m = 0 \\ f(r, m, n)|_{r=0} &= 0 \qquad \text{for } m \neq 0 \end{aligned}$$

where m and n are the mode numbers for the transformed function f. A vector field $\mathbf{u}(r, \theta, \phi)$ must satisfy the conditions

$$\begin{aligned} u_r(r, m, n)|_{r=0} + im\ u_\theta(r, m, n)|_{r=0} &= 0 \qquad \text{for } |m| = 1 \\ u_r(r, m, n)|_{r=0} &= 0 \end{aligned}$$

$$u_\theta(r,m,n)|_{r=0} = 0 \qquad \text{for } |m| \neq 1$$

for the (r,θ) components; the u_ϕ component has the same boundary conditions as a scalar function. The boundary conditions for a scalar field apply to the charge density, potential, and E_ζ field component; those for a vector field apply to the E_r, E_χ field components.

The implementation of the continuity boundary conditions is straightforward when the k-space (in θ) values of the field are readily available, as with the electric fields. The boundary handling of the charge density entails mapping the guard cell particle contributions to the interior of the charge density array using the continuity boundary conditions. However, since the real-space multiplication of the transformation weight $1/J$ immediatedly follows this step, handling of the continuity boundary conditions in k-space introduces two additional transformations of the charge density array. These extraneous transformations can be avoided by redistributing the guard cell values among the first grid points in real space, so that the scalar field continuity condition is satisfied. A particle inside the "central cell" can be linearly interpolated between the first radial grid point and the virtual point at the origin; the contribution at the origin is then uniformly spread out among all the neighboring theta points. Although the interpolation has already been done, this numerical "trickery" is possible because all the guard cell values have been kept. Thus a particle exactly at $r = 0$ will assign charge equally to all of the points on the boundary of the central cell, a result that is not only aesthetically appealing but compatible with the continuity boundary condition there.

The last modification necessary in the presence of the $r = 0$ point concerns the particle dynamics. No modification of the ion push is required, since the ions are being pushed in a cartesian coordinate system, but the $1/r$ terms

in the electron guiding-center pusher require some special handling. Although the number of electrons near the origin will typically be small, eventually an electron will pass close enough to $r = 0$ to cause very inaccurate integration of the equations of motion (possibly a floating-point overflow as well). This problem is resolved by letting electrons undergo a collision when passing too close to the origin. We can imagine a small, hard cylinder (or torus) centered at $r = 0$; the continuity condition demands that an electron passing within the critical radius will exit with its θ coordinate shifted by 180° (i.e. $r \rightarrow -r$). Since the electron orbits in the (r, θ) plane are drift-dominated at the origin, and the dominant magnetic drifts vertical, this treatment is reasonable. The location of this critical radius can be estimated given the maximum tolerable theta increment in a given time-step for a thermal particle, and assuming the drift is dominated by the gradient-B term. The critical radius is then given approximately by

$$\frac{r_{\min}}{\bar{\Delta}} \sim \frac{4\epsilon_\zeta(\omega_e/\Omega_e)v_e^2}{N(\Delta\theta)_{\max}}$$

where $\bar{\Delta}$ is the average grid spacing, N is the number of radial grid-points, ω_e and Ω_e are the electron plasma and cylotron frequencies, and v_e is the electron thermal velocity, normalized to $\bar{\Delta}\omega_e$. The maximum tolerable theta increment is of order one, where the distortion of the "true" particle motion due to the finite integration step rivals that from a collision with the artificial boundary near $r = 0$. Using typical simulation parameters, we obtain

$$\frac{r_{\min}}{\bar{\Delta}} \sim 10^{-2}\text{–}10^{-3}$$

The smallness of this value indicates that a collision is not likely to influence the calculated fields significantly. Depending on the plasma profile and other simulation parameters, actual runs of approximately 50,000 particles suffer at most only a few collisions per time-step at the origin; often no collisions occur.

Chapter 3

Tests of the simulation code

There are many analogies that can be drawn between plasma simulation and experiment. The simulator and experimentor must both design experiments that will be of interest to the research community. They must both decide what quantities are important to measure, becoming well-versed in the existing diagnostic tools as well as being able to construct new tools, in response to unique situations. In addition, they must draw conclusions from the massive amount of data gathered in the typical experiment, using spectral analysis and other statistical tools.

At the same time, there are certainly large differences between simulation and experiment. The simulator has many more diagnostic options at his disposal, since they can be applied anywhere in the plasma without disturbing the system. In a simulation, one can in principle observe the evolution of any desired quantity. Simulation is also unlike nature in that one is free to arbitrarily specify details of the system that are either difficult or impossible to modify in an experiment. These include the electron/ion mass ratio, temperature and density profiles, currents, and even the force law itself.

Unfortunately, simulation is susceptible to problems that are absent in a real plasma. Algorithms may be inefficiently or inflexibly designed, and "bugs" may find their way into the program, which are difficult to isolate in large-scale projects. In addition, limitations in computer accuracy, speed, and memory size necessitate the adoption of simplified models which may not give

realistic results. If designed well, the model should approximate plasma behavior in some limit, but we must always be aware of the intrinsic limitations of both the model and the computing environment. The particle simulation model is essentially a completely independent system, with its own laws governing the behavior. These laws involve a discretization of the spatial and temporal coordinates, as well as the use of a relatively small number of "finite-size" particles to represent the plasma.

It is therefore of great importance to closely examine the effects of the numerical constructs on the resulting behavior. The verification of our numerical model is assisted by our knowledge of actual physical systems. The "particles" in particle simulation behave similar to real particles, and this microscopic behavior is important as a diagnostic tool. Ultimately, the ability to reproduce macroscopic plasma behavior is one of the major goals of particle simulation; we therefore shall give detailed comparisons to theory in simple, well-understood configurations.

3.1 Diagnostic methods and post-processing

Some of the most powerful tools at our disposal fall into the category of statistical analysis. In the course of a simulation run, the values of field quantities or densities can be stored for later analysis, referred to as post-processing. The electric potential is a convenient and relevant quantity for analysis in the electrostatic model, and is almost exclusively used in this research. For the toroidal system, the form of the data output (and most of the analysis) closely matches the description of the physical system—local in radial coordinate, and global in the periodic coordinates θ and ϕ. Thus the stored quantity (Φ) is dependent on three types of variables—spatial (r), wave number (k_χ, k_ζ), and

time. Here we shall briefly consider some of the diagnostic methods used in the course of this research, centering primarily on spectral analysis techniques. An in-depth examination of spectral analysis (with an emphasis on autocorrelation and spectral density estimators) can be found in the text by Priestley [48]; a shorter and less formal examination by Press *et al.* [40, Chapter 12] is also illuminating.

3.1.1 Autocorrelation of the potential

The autocorrelation of the potential as a function of time and space is useful primarily for obtaining the spectral density (discussed below), but can also be used to measure damping rates. For example, the autocorrelation of the electric field was employed extensively in simulation studies of Bernstein modes by Kamimura, Wagner and Dawson [49]. The autocorrelation of the potential is defined by

$$C_{\mathbf{k}}(\tau) = \langle\, \Phi_{\mathbf{k}}(t)\, \Phi^*_{\mathbf{k}}(t+\tau)\,\rangle \tag{3.1}$$

where the angle brackets denote an ensemble average. The ergodic hypothesis of equilibrium statistical mechanics allows this to be written as a time average :

$$C_{\mathbf{k}}(\tau) = \lim_{T\to\infty} \frac{1}{T} \int_{-T/2}^{T/2} dt\, \Phi_{\mathbf{k}}(t)\, \Phi^*_{\mathbf{k}}(t+\tau) \tag{3.2}$$

Here we have also assumed that Φ is *stationary*—the amplitude of the potential must not change significantly in time. In practice, this requires that the characteristic frequencies of oscillation satisfy $|\mathrm{Re}\,\omega| \gg |\mathrm{Im}\,\omega|$. Note that for a perfectly stationary signal ($\mathrm{Im}\,\omega = 0$) the autocorrelation given by Eq. (3.2) is real; thus the degree of nonstationarity can be estimated by comparing the magnitudes of $\mathrm{Re}\, C_{\mathbf{k}}(\tau)$ and $\mathrm{Im}\, C_{\mathbf{k}}(\tau)$.

In order to evaluate Eq. (3.2) to get the autocorrelation for a simulation run, we assume time reversal invariance and adopt a discrete time coordinate and finite time sample, obtaining [49] :

$$C_{\mathbf{k}}(\tau) = \frac{1}{N-m} \sum_{n=1}^{N-m} \Phi_{\mathbf{k}}[n\Delta t]\ \Phi^*_{\mathbf{k}}[(n+m)\Delta t] \tag{3.3}$$

where N is the number of data points, $\tau = m\Delta t$, and m is the lag factor, varying from 0 to M. As M approaches the sample length, the number of terms in the sum gets small for large m, resulting in poor accuracy. Thus the maximum lag factor M should be much smaller than the sample length to maintain accuracy, though this results in a small sample of lags.

For long time samples, the direct calculation of Eq. (3.3) is computationally expensive because of the double sum (the sum is done for each value of τ). The calculation of this type of equation was one of the earliest uses of the FFT (fast fourier transform), and its use in spectral analysis has become widespread [48]. Specifically, the transform of the time series $\Phi(t)$ may be followed by an inverse transform of the squared fourier amplitudes $|\Phi(\omega)|^2$ to give the autocorrelation.

While the solution of the autocorrelation via the FFT is fast, it has some disadvantages. First, the FFT technique is not capable of handling arbitrary sample lengths—usually the sample length must equal a power of two (though FFT algorithms exist that allow powers of other small prime numbers, such as 3 or 5 [50]). This constraint forces the artificial truncation or extension of the sample length to fit the transform requirement (setting unknown entries to zero in the latter case). Second, use of the FFT will ordinarily introduce unphysical periodicities into the time series. The assumption of periodicity can be avoided through doubling the time series and initializing the unknown

values to zero, which results in an "isolated" transform [38]. Whether this is truly an improvement is unclear, however, since the assumption of zero entries for the unknown values of the time series cannot be rigorously justified. Note also that the sharp cutoff in data at some time $t = T$ may give rise to high frequency noise due to Gibbs effect [46]; this can be minimized by smoothing near the cutoff.

3.1.2 Spectral density of the potential

The spectral density (or power spectrum) of the potential is a measure of the fluctuation level as a function of wavevector (or space) and frequency. The spectral density is perhaps the most important diagnostic at our disposal, giving the oscillation frequencies for the modes of interest, as well as the radial extent. The spectral density of some observable $O(\mathbf{k}, t)$ is defined by [51]

$$S_{\mathbf{k}}(\omega) = \lim_{T\to\infty} \frac{1}{T} \int\int_{-T/2}^{T/2} dt\, dt'\, O(\mathbf{k}, t)\, O(\mathbf{k}, t')\, e^{i\omega(t-t')} \tag{3.4}$$

$$= \int_{-\infty}^{+\infty} d\tau\, e^{i\omega\tau}\, C_{\mathbf{k}}(\tau) \tag{3.5}$$

where C is the autocorrelation of the observable (in this case, the potential). An alternative representation of the spectral density in terms of the dielectric response function is given by [51,52]

$$S_{\mathbf{k}}(\omega) = (4\pi)^2 \frac{2\pi}{k^5} \frac{\mathrm{Im}\, U(\mathbf{k}, \omega)}{|\epsilon(\mathbf{k}, \omega)|^2} \tag{3.6}$$

where U is defined by

$$U(\mathbf{k}, \omega) = \frac{k}{\pi} \sum_{\sigma} n_\sigma e_\sigma^2 \int d\mathbf{v}\, \frac{f_\sigma(\mathbf{v})}{\omega + \mathbf{k}\cdot\mathbf{v} + i0^+} \tag{3.7}$$

This expression clearly shows that when we approach $\epsilon(\mathbf{k}, \omega) = 0$, the spectral density becomes very large—giving us a powerful tool for detection of frequency

spectra, assuming $S_{\mathbf{k}}(\omega)$ can be measured with sufficient accuracy. (For small $\epsilon(\mathbf{k},\omega)$ the theory must be modified, and the spectral density remains finite, as discussed by Oberman and Williams [52]. The expression given in that paper is for $\langle\rho\rho\rangle_{\mathbf{k},\omega}$ and is proportional to $1/k$; the simple relationship between Φ and ρ in slab geometry immediately gives the above dependence of $1/k^5$. The expession originally given by Rostoker [51] concerned the fluctuations of the electric field, resulting in a tensor form $S_{\alpha\beta}$ for the spectral density.)

The standard method of obtaining the spectral density consists of solving for the autocorrelation, then employing the discrete coordinate analogue of Eq. (3.5) :

$$S_{\mathbf{k}}(\omega) = \sum_{m=-M}^{M} \lambda(\tau)\, C_{\mathbf{k}}(\tau)\, e^{i\omega\tau} \tag{3.8}$$

where the windowing function $\lambda(\tau)$ has been introduced, and $\tau = m\Delta t$ as before. The use of a window function which smoothly goes to zero as $m \longrightarrow M$ improves the spectrum when computed in this manner [48]. Many windowing functions are commonly employed in spectral estimation (a consideration of several of the most popular are given by Priestley); a windowing function often used in the analysis of particle simulations has been the Parzen window [49].

An examination of this method shows that a fundamental resolution versus accuracy dilemma exists. In order to obtain an accurate estimate of the autocorrelation, one must keep the lag time as short as possible. However, the maximum lag time determines the time sample length for the calculation of the spectral density, which must be as long as possible to achieve good frequency resolution. This relationship between accuracy and resolution has been referred to as the "uncertainty principle of spectral estimation" [48], and is a characteristic of spectral estimation methods in general. Methods exist for estimating the optimal maximum lag M for a given process, but these require

previous knowledge of the statistical properties of the system.

The problems associated with the standard method inspired the development of the nonlinear spectral estimation techniques, the most well-known being the *maximum entropy method* (this is a member of the class known as *autoregressive* models [40,48]). The maximum entropy method assumes "maximum disorder" outside of the given time sample—the addition of information to the sample is assumed to not increase the information content, or entropy, of the process. This assumption essentially extends the temporal length of the known autocorrelation values, resulting in a large gain in resolution in the frequency. The entropy rate of the process is related to the spectral density via the relation

$$h = \frac{1}{4B}\int_{-B}^{B} \log S(\omega)\, df + \text{constant} \tag{3.9}$$

where $B = 1/2\Delta t$ is the Nyquist frequency and $S(\omega)$ is the spectral density. We next express the spectral density in terms of the autocorrelation $c(\tau)$

$$h = \frac{1}{4B}\int_{-B}^{B} \log\left[\sum_{m=-M}^{M} c(\tau) exp(-i\omega\tau)\right] df + \text{constant} \tag{3.10}$$

and maximize h subject to the constraint that $S(\omega)$ is consistent with the known values of the autocorrelation. This results in a variational problem of the form

$$\frac{\delta}{\delta S}\int_{-B}^{B}\left\{\log S(\omega) - \sum_{m=-M}^{M}\lambda_m\left[S(\omega)\exp(-i\omega\tau) - c(\tau)\right]\right\} df = 0 \tag{3.11}$$

The solution to the above problem is too involved to give here, but the resulting spectral estimate can be written in the form [53]

$$S_{\text{mem}}(\omega) = \frac{P_M}{B\left|1 + \sum_{m=1}^{M} g_m \exp(-i\omega\tau)\right|^2} \tag{3.12}$$

with the constant P_M and coefficients g_m to be determined.

The maximum entropy method has previously shown its superiority to the standard method in analysis of plasma turbulence [54]; a similar improvement has been seen in this research as well. This improvement is essentially due to a better match between the statistical process being observed and the corresponding spectral analyser. In this case, the presence of poles in the expression for the spectral density (3.12) enables highly peaked features in the spectrum to be resolved. On the other hand, a fourier representation has no poles, so sharp peaks are only obtained when a large number of terms contribute to the sum. The main disadvantage of the maximum entropy method is that short sample lengths may give rise to spurious peaks, especially for continuous spectra.

The upper bound (M) to the sum in Eq. (3.12) is often referred to as the *order* of the method, and plays a role similar to the maximum lag factor used in the standard method. That is, when the order is small, accuracy is greatest, with resolution the poorest. For large order, the reverse occurs. The optimal value will depend on the type of statistical process being observed. A small M ($M \ll N$) has been recommended for autoregressive (AR) processes [48]; for harmonic processes with noise, however, values in the range $N/3-1 \leq M \leq N/2-1$ are more appropriate [53]. For the physical problems studied here, a value of $M \sim N/2$ is observed to give spurious peaks and a definite degradation of the spectrum; therefore a value near $N/4$ is typically used.

3.1.3 Other statistical methods

When simulating the evolution of a confined plasma, it is important to detect the presence of an instability, and obtain estimates of growth rate and spatial extent. These statistics can be obtained simply by plotting the quantity $\|(e\Phi/kT)\|$ as a function of time on a logarithmic plot and calculating

the growth rate by hand.

The spatial structure of a given mode can be examined through the interferogram [55]. This diagnostic interferes the potential with a pure signal of a given frequency, which acts as a mask to eliminate all other frequency components. Simply put, we obtain a function $R(\Phi)$ such that

$$R(r,m,n) = \int_{t_{\min}}^{t_{\max}} dt\, \Phi(r,m,n,t)\, \exp\left(-i\omega t + \varphi\right). \tag{3.13}$$

The frequency to use in this calculation is typically given from a previous diagnostic, such as a maximum entropy power spectrum. The amplitude of the interfered function R will show a dramatic increase in the vicinity (in space and frequency) of a normal mode of the plasma. It is often possible to compare this function to the theoretically predicted eigenfunction shape as well. When the total averaging time ($t_{\max} - t_{\min}$) exceeds the damping time for the mode, the calculation of the eigenfunction in this manner becomes inaccurate due to phase errors [56]; in this case, the amplitude of the eigenfunction can be used instead. Note that the squared amplitude of the eigenfunction equals the spectral density for the given frequency (although the measured frequency will show some variability over the radial extent, so this association is not exact). Thus, the measured power as a function of radius is also used in examining spatial mode structure.

A diagnostic frequently performed on simulation codes is the measurement of the equilibrium fluctuation spectrum [57]. This involves the calculation of time-averaged field components by wave number (typically the electric fields) in an equilibrium configuration. The results are then compared with the result from the fluctuation-dissipation theorem, or from kinetic considerations [51]. This calculation for the slab limit of the toroidal particle code was performed

early in the code's development, giving reasonable results, but was omitted from this dissertation due to the lack of a more recent result.

3.1.4 Test particle methods

The last diagnostic method to be discussed involves the use of marker or test particles. The test particle method is straightforward in principle—one or more additional species of particles is employed, typically far less numerous than the actual electron and ion species. These test particles, by virtue of their limited number, can be followed precisely in time, storing the entire history if desired. Additional particle quantities can be introduced for little increase in memory usage. Furthermore, although these particles respond to the fields just as the normal species, they contribute no perturbing influence since they are typically not included in the charge accumulation. This allows the creation of any desired distribution of test particles, which is important in measurements of a diffusion coefficient from test particle motion [55]. The methods implemented in the present code for storing such data enable on the order of 100 test particles to be followed in time, giving good statistics for such a measurement.

Although the test particle method can be very useful for giving estimates of quantities such as diffusion coefficients, test particles can be more valuable for simple *microscopic* tests of the simulation code. Researchers in particle simulation have cautioned that the microscopic particle motions are not always faithfully reproduced in particle simulation codes, since that is not their design [21]. However, this does not mean that the microscopic behavior should be ignored. In a strongly magnetized plasma, the dominant particle motions are the acceleration parallel to the field lines, $\mathbf{E} \times \mathbf{B}$ drifts, ∇B and curvature drifts, and the polarization and nonuniform electric field drifts. Through test

particles, these can readily be observed in at least a qualitative way. This is very important in the early and intermediate stages of code development, when algorithmic and programming difficulties are prevalent. Further, including the test particle distribution in the charge accumulation is straightforward and allows self-consistent motion of the test particles to be observed. This motion allows a qualitative but sensitive test of the dynamics, on a scale far smaller than the typical plasma simulation (which may involve many tens of thousands of particles and thousands of timesteps).

3.1.5 Remarks

The diagnostic methods discussed above play a crucial role in this research. The accurate measurement of the power spectrum is very important for understanding the plasma behavior, especially for low frequency, marginally unstable (or stable) phenomena. The maximum entropy method is usually used for analysing the bulk plasma simulation results, due to its superior frequency resolution. The interferogram diagnostic is used in the study of the drift wave in the slab limit, where the linear theoretical eigenfunction can be readily calulated.

Finally, the extension of particle simulation methods to toroidal geometry is accompanied by unique problems in program and algorithm verification. Simulation in slab geometry is well served by current theoretical plasma physics, but there are few (if any) "standard" tests available for the toroidal system. Thus, there is a strong reliance in this research on bulk plasma tests in the slab limit, for examining the simulation plasma's kinetic response. This is reasonable; the inclusion of toroidal effects involves few major conceptual changes *per se*. Aside from consistency checks and other debugging methods,

the correctness of the the toroidal field solver and dynamics have been demonstrated through test particle motion; these results are presented below.

3.2 Test particle results

In actual plasma devices, the magnetic field structure may be very complicated and is usually highly nonuniform. The resultant magnetic drifts and trapped particles can have a large effect on the stability of the plasma. Including these effects in a simulation is therefore very important. In this research, the only restriction on the form of the prescribed magnetic fields is that the flux surfaces be nested, concentric tori. This restriction is imposed so that there exist no zeroth-order (in Larmor radius) particle fluxes into the boundaries, as well as minimizing numerical diffusion. More general magnetic field configurations are possible, while still satisfying this condition, by using a generated grid for storage of the cross-field variables.

In practice, the magnetic field configuration usually adopted is essentially tokamak fields—a vacuum field for the toroidal component with the poloidal component specified in terms of the safety factor. These can be written

$$B_\zeta = B_{\zeta_0}\frac{R_0}{R} \tag{3.14}$$

$$B_\chi = \frac{r}{R_0 q(r)}B_\zeta, \tag{3.15}$$

where the safety factor $q(r)$ is usually an increasing function of r. The parallel motion of the particles will be predominantly in the toroidal direction, since r/qR_0 is usually much smaller than unity. However, the poloidal component guarantees that a particle on the outside of the torus will eventually move into a region of stronger magnetic field, causing low parallel-velocity particles to reverse directions. Coupled with the dominant inhomogeneous magnetic field

drifts, this gives rise to the famous *banana* orbit in this system. Test particle trajectories reproduce this behavior in the toroidal code, both for the full-dynamics ions and the guiding center electrons (see Figures 3.1–3.2). For this test, no electric fields are used. Additionally, the electron orbit was obtained by using identical parameters as the ion orbit, but inverting the magnetic field and increasing the electron mass to that of the ion.

The conservation of various particle invariants like energy, magnetic moment (μ), and the toroidal canonical momentum often play central roles in plasma phenomena. We therefore closely examine the conservation of these quantities by our pusher algorithms in the absence of electric fields. The time histories of these quantities, for a representative pair of particles, is given in Figures 3.3–3.6. In the interest of brevity, this pair will be referred to as the FD (full dynamics) or the GC (guiding center) particle, since these may be used on an arbitrary species. The particle quantities shown in the plots are the parallel velocity ($v_\parallel$), kinetic energy (E_k), zero-order magnetic moment (μ_0, FD particle only), canonical toroidal momentum (p_ϕ), toroidal angular momentum (L_ϕ), magnetic flux (ψ), and the radial position normalized to the minor radius (r/a, GC particle only). The two trajectory plots at top are r versus χ (toroidal cross section), and R versus ζ (view from above).

For the most part, the orbits as given by the two algorithms are in excellent agreement, improving for the smaller Larmor radius case. Part of the discrepancy involves small errors in initialization, since the initial GC particle quantities must represent the "averaged" initial FD quantities, which is handled only approximately. The magnetic moment of the FD particle is on the average well conserved, but oscillates once per cyclotron rotation. Note that only the lowest order expression for the magnetic moment is shown ($\mu_0 = v_\perp^2/2B$); the

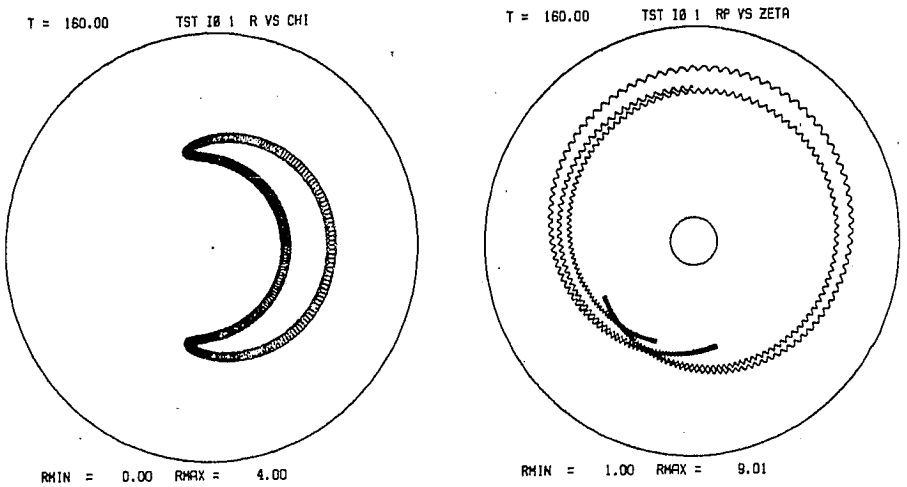

Figure 3.1: Trajectory of a mirroring full dynamics particle in a tokamak field. On the left is the projection onto the (r, θ) plane; on the right is the view from above.

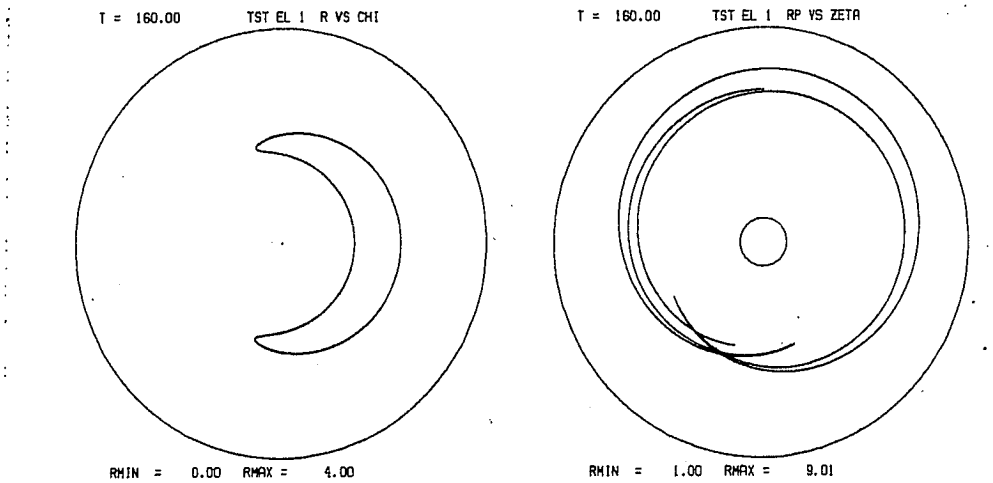

Figure 3.2: As above, but for a guiding center particle.

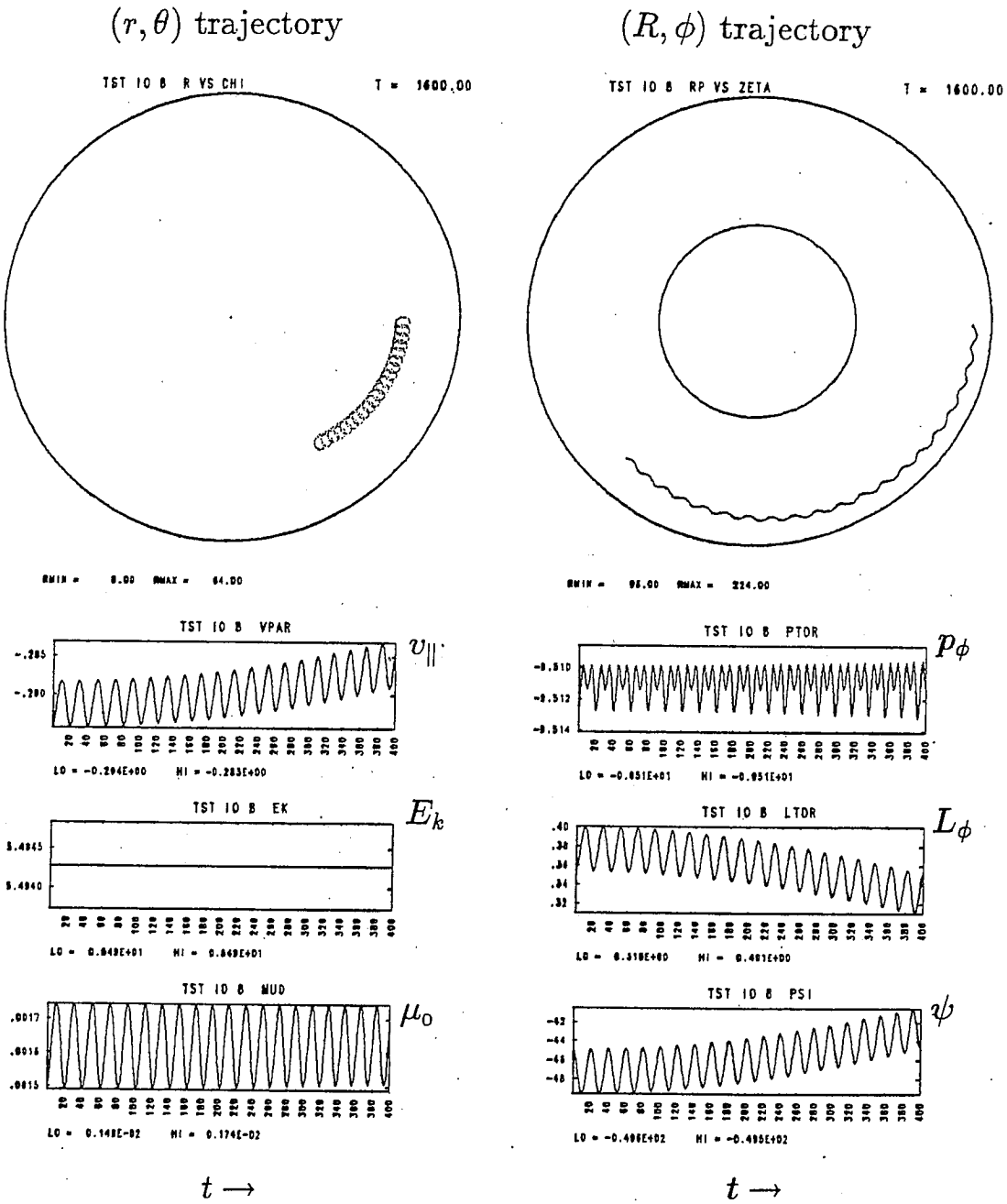

Figure 3.3: Time histories of full dynamics particle, large Larmor radius case.

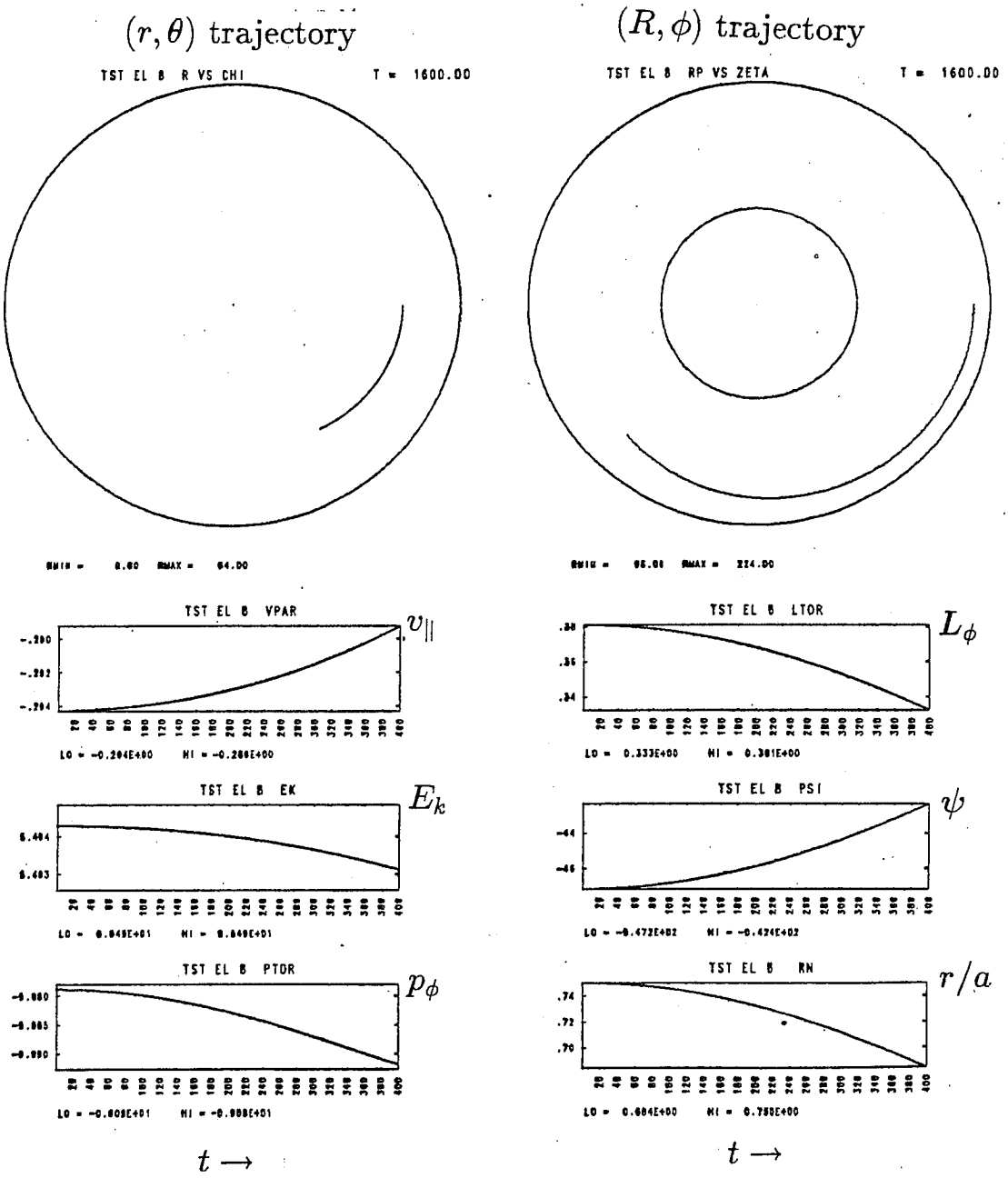

Figure 3.4: Time histories of guiding center particle, large Larmor radius case (same parameters as in Figure 3.3).

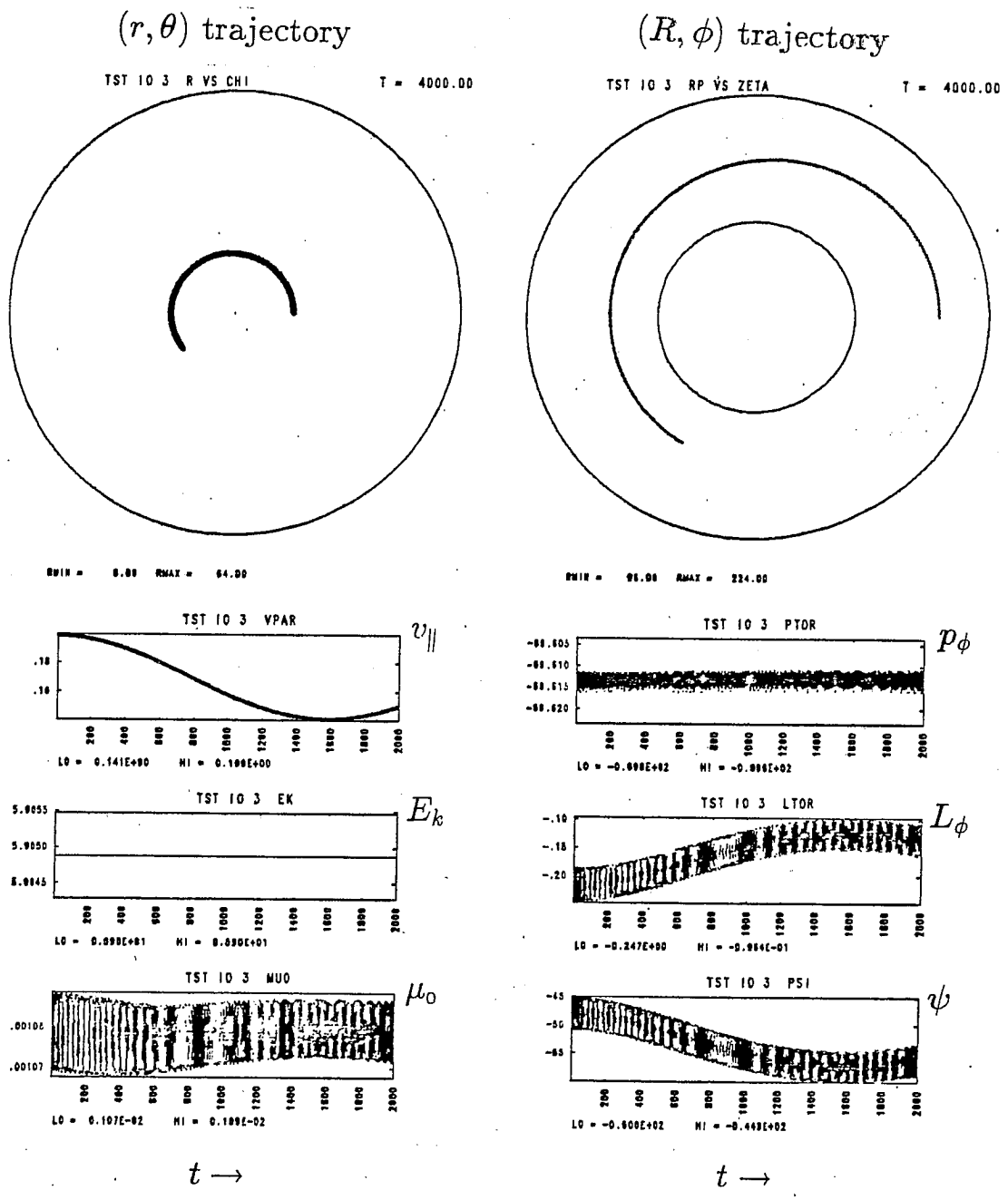

Figure 3.5: Time histories of full dynamics particle, small Larmor radius case.

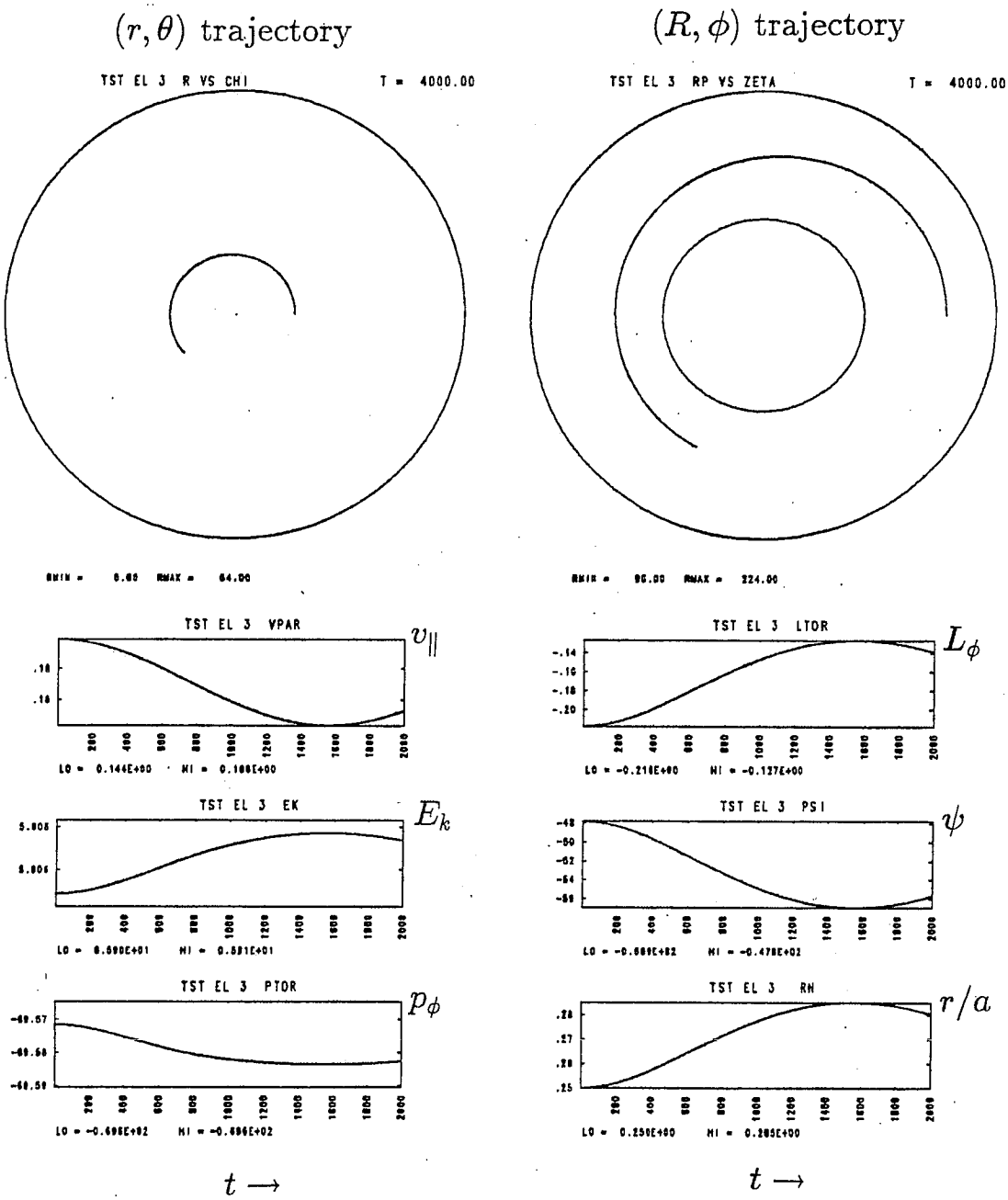

Figure 3.6: Time histories of guiding center particle, small Larmor radius case (same parameters as in Figure 3.5).

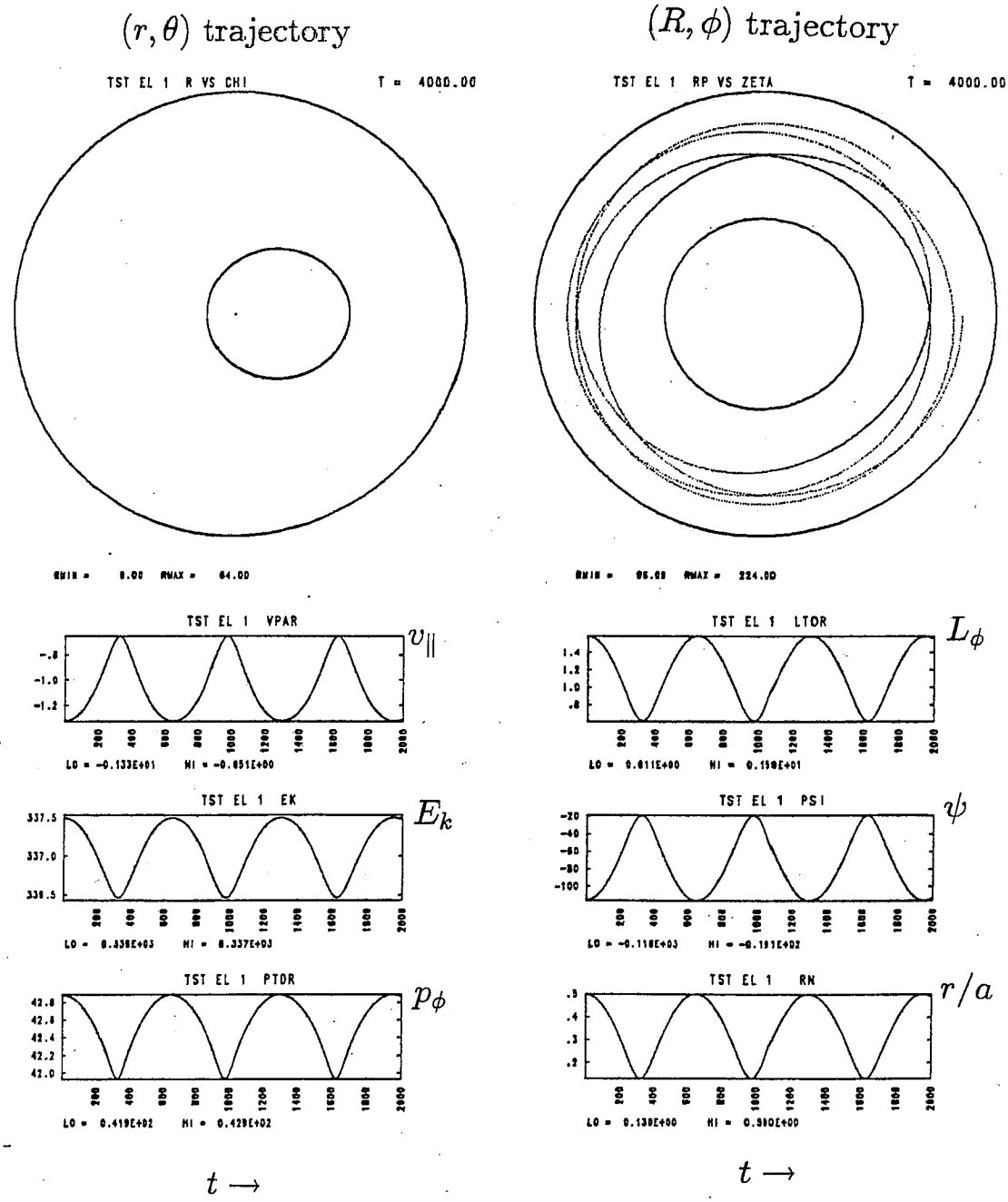

Figure 3.7: Time histories of high velocity, large Larmor radius guiding center particle.

inclusion of higher order terms in this diagnostic would presumably show better conservation of μ. This is supported by the better conservation at smaller Larmor radius.

The canonical toroidal momentum is conserved very well by both algorithms, and the energy is extremely well conserved in the FD algorithm. The energy conservation by the GC algorithm is good, but shows a significant variation as the particle transits the torus (see Figure 3.4). This variation of the energy is not numerical dissipation, but seems to be a result of drift into a region of higher magnetic field strength. This can happen when a non-vacuum field component is present, in which case the guiding center drift is no longer perfectly perpendicular to ∇B (due to the curvature drift term).

A final set of time histories is shown in Figure 3.7, given a high velocity GC particle (large effective Larmor radius). A strong variation is seen in both the energy and the toroidal canonical momentum, which are nevertheless well conserved when averaging over transits. Though this velocity is comparable to a simulation electron, the effective Larmor radius of a simulation electron is smaller by the square root of the mass ratio, making it much less susceptible to these effects.

The next test involves the self-consistent fields generated by test particles. First, it is desired to examine the potential generated by a particle in the vicinity of $r = 0$, for continuity boundary conditions there. The result is shown in Figure 3.8, and the potential contours clearly reflect the continuity boundary conditions. The potential contours for an odd parity at the origin and the same particle position are shown for comparison.

We next address the issue of verifying the correctness of the toroidal field solver. Aside from calculating the divergence of the electric fields, and see-

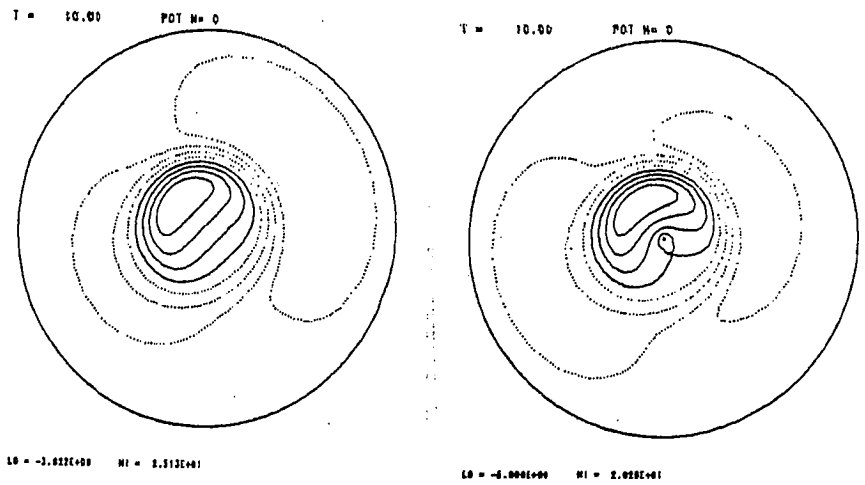

Figure 3.8: Test particle potential contours for particle near $r = 0$. Field calculation for case on left uses continuity boundary at the origin; on the right, an odd parity boundary condition is used.

ing how well it approximates the source term $4\pi\rho$, the field solver can be checked via test particle motion. In particular, we can compare test particle motion in the toroidal configuration to that in the cylindrical type-II configuration, both using tokamak-type fields in the "toroidal" direction. Some creativity must be applied to get a reasonable comparison, since the toroidal configuration has better radial resolution (at the expense of resolution in theta), and has circular boundaries, rather than square. Therefore the test particles are located midway between the boundary and the center to minimize coordinate system effects; the number of grid points in each coordinate are adjusted to keep the cell size comparable in the vicinity of the particles. Further, the particle "size" used in the filter is increased to minimize grid effects, and the total volume enclosed in each simulation is scaled to be equal.

For the configuration described above, the fields generated by particles

at a given location are shown in Figures 3.9–3.10 for the lowest toroidal mode numbers (the mode expansion in the toroidal dimension was employed). The sign of the imaginary part is reversed for the two cases because the mode expansion variable is in the opposite direction. The shape of the contours in each case are very close, the differences appearing most clearly near the boundaries. The magnitude of the potential at maximum agrees within five percent.

Next we "turn-on" the self-consistent electric fields, and advance the test particles in time. Without the shielding presence of a plasma, the forces generated by the test particle fields (and the image fields from the conducting boundary) are very large. Therefore it is necessary to use a very large magnetic field strength and small timestep to ensure good behavior. The electron and ion trajectories in each case is shown in Figures 3.11–3.14. The electron oscillates about the ion on the field line, with the ion cyclotron motion subject to strong time-varying drifts. Despite the somewhat violent nature of the motion, the two cases give good qualitative agreement. This is an excellent test of the code, because in each case very different calculations are being performed to advance the system in time, and all the important effects have been included.

3.3 Normal modes in a uniform equilibrium plasma

The starting point for most theoretical treatments of plasma waves is the Vlasov-Maxwell equations, which assumes that the total distribution function is well approximated by the one particle distribution function $f_\sigma(\mathbf{r}, \mathbf{v}, t)$. The evolution equation is then [58,59]

$$\left\{ \frac{\partial}{\partial t} + \mathbf{v} \cdot \frac{\partial}{\partial \mathbf{r}} + \frac{q_\sigma}{m_\sigma} \left[\mathbf{E}(\mathbf{r}, t) + \frac{\mathbf{v}}{c} \times \mathbf{B}(\mathbf{r}, t) \right] \cdot \frac{\partial}{\partial \mathbf{v}} \right\} f_\sigma(\mathbf{r}, \mathbf{v}, t) = 0 \qquad (3.16)$$

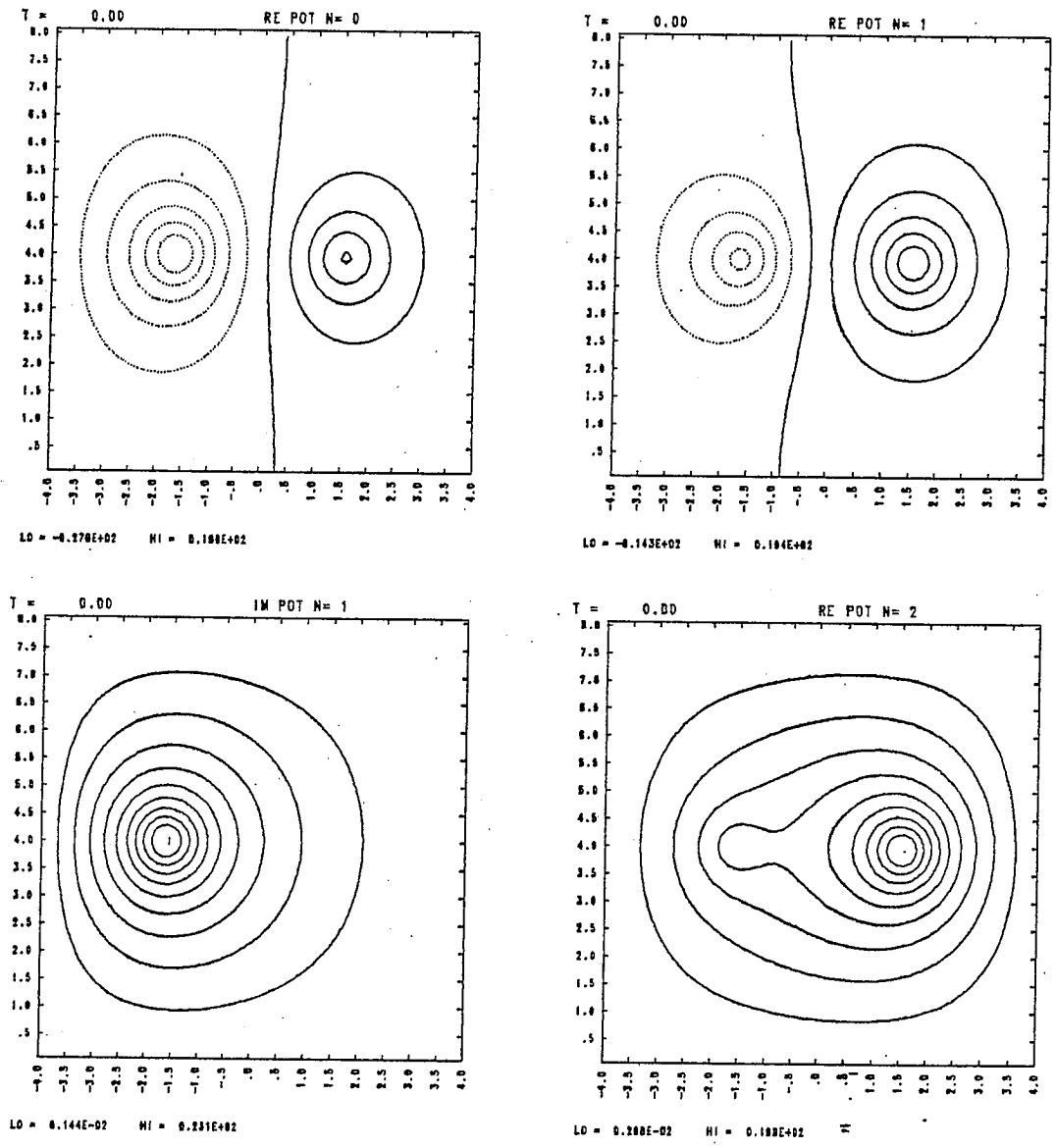

Figure 3.9: Potential contours, for cylindrical type-II configuration. Shown are the $n = 0$ mode, $n = 1$ (real and imaginary), and $n = 2$ (real).

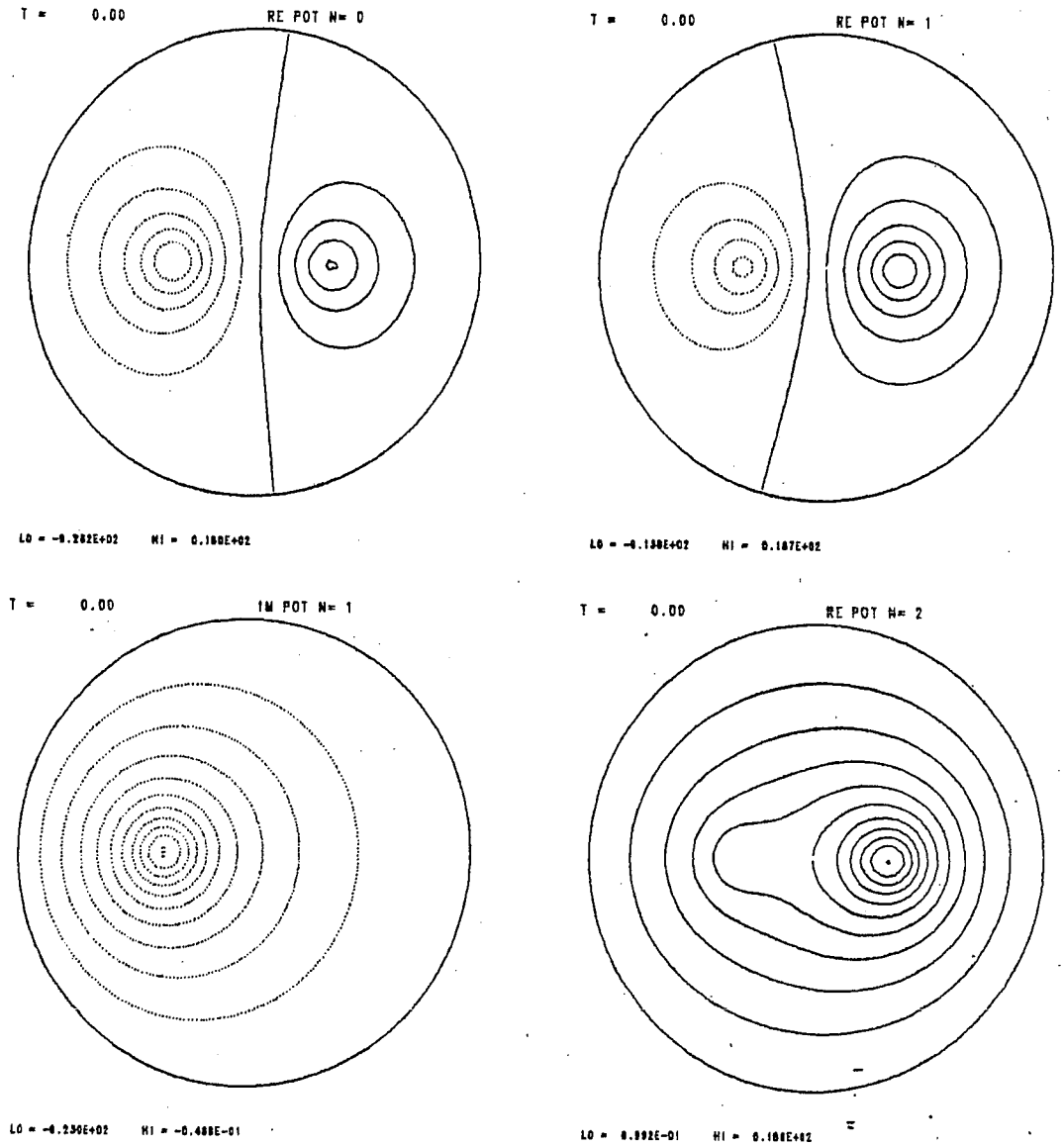

Figure 3.10: Potential contours as in Figure 3.9, but for the full toroidal configuration.

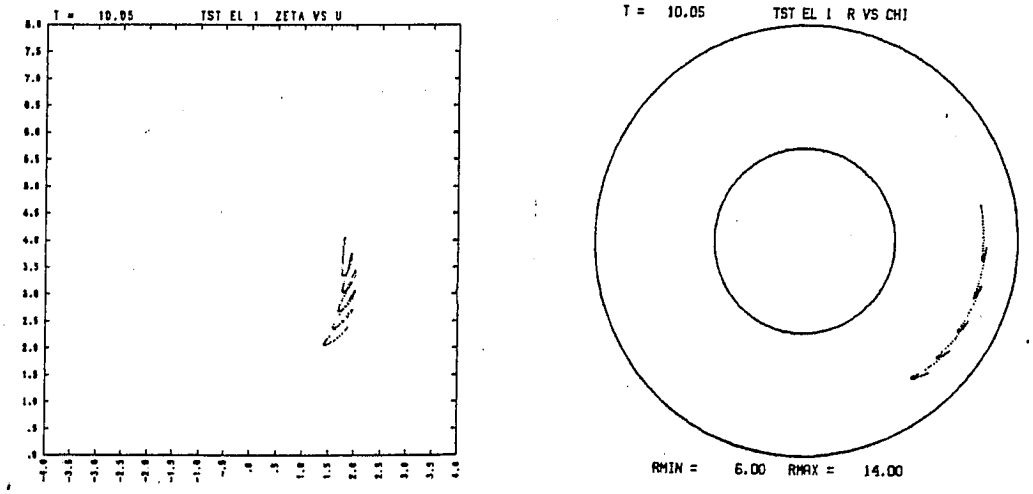

Figure 3.11: Electron trajectory for self-consistent test particle dynamics, in cylindrical type-II configuration. The left plot shows the cross-section view, while the right shows the view from above.

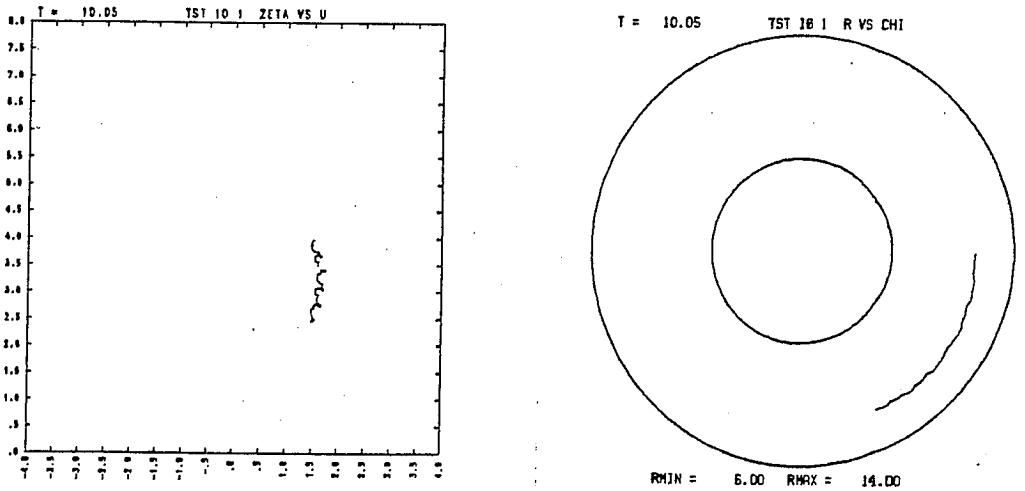

Figure 3.12: Ion trajectory for above case.

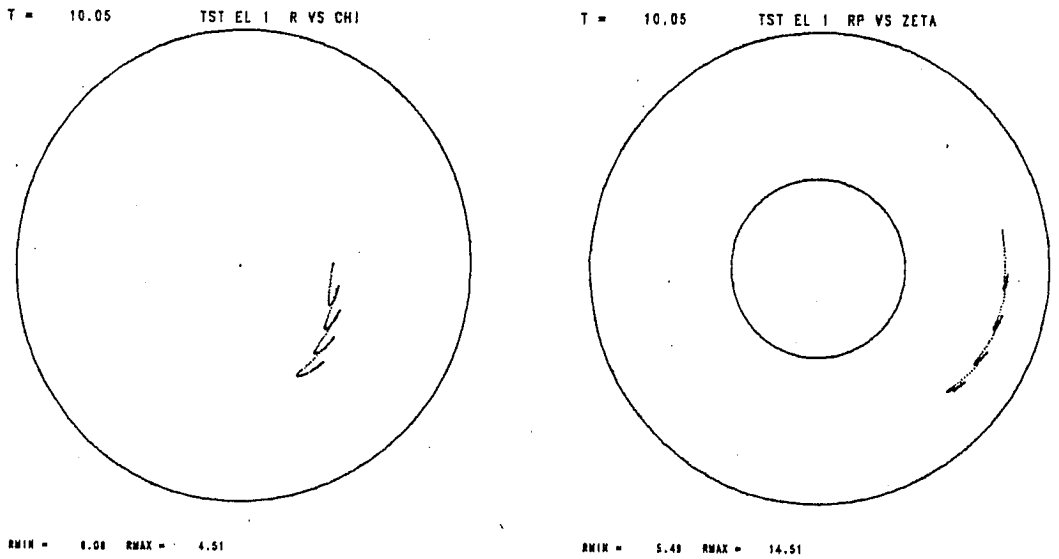

Figure 3.13: Electron trajectory with self-consistent dynamics as in Figure 3.11, but in the full toroidal configuration. The left plot shows the cross-section view, while the right shows the view from above.

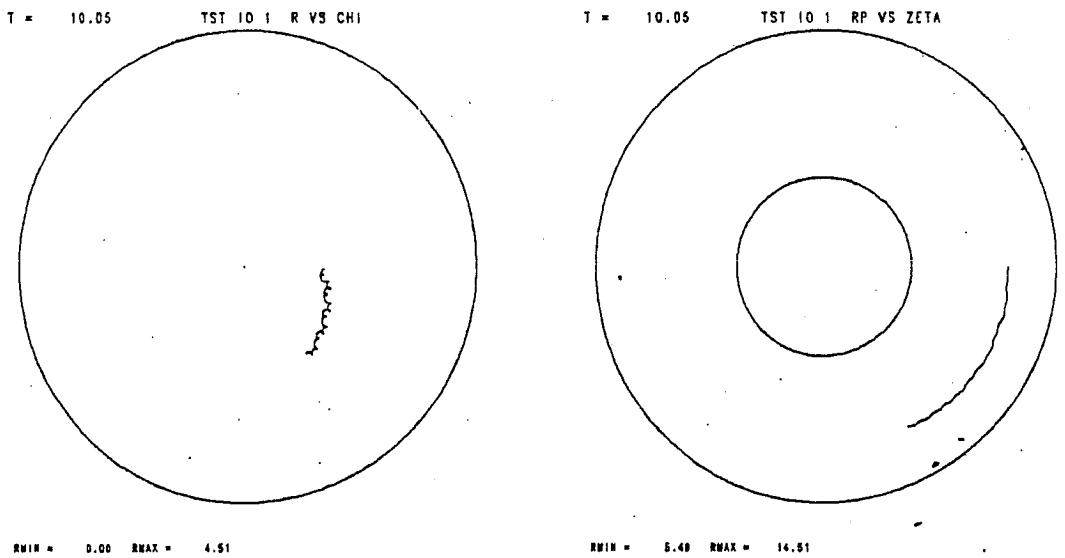

Figure 3.14: Ion trajectory for above case.

where $\mathbf{E}(\mathbf{r},t)$ and $\mathbf{B}(\mathbf{r},t)$ are the electric and magnetic fields, σ indicates the species, and q and m are the charge and mass, respectively. The electric and magnetic fields are calculated from the Maxwell equations, given the charge and current densities

$$\rho(\mathbf{r},t) = \sum_\sigma q_\sigma n_\sigma \int d\mathbf{v}\, f_\sigma(\mathbf{r},\mathbf{v},t) \tag{3.17}$$

$$\mathbf{J}(\mathbf{r},t) = \sum_\sigma q_\sigma n_\sigma \int d\mathbf{v}\, \mathbf{v}\, f_\sigma(\mathbf{r},\mathbf{v},t) \tag{3.18}$$

which are connected by the continuity equation

$$\frac{\partial \rho}{\partial t} + \boldsymbol{\nabla}\cdot\mathbf{J} = 0 \tag{3.19}$$

For an infinitesimal perturbation of the distribution function, the Maxwell equations and linearized Vlasov equation give a solution of the form

$$\boldsymbol{\epsilon}(\mathbf{k},\omega)\cdot\delta\mathbf{E} = 0 \tag{3.20}$$

where $\delta\mathbf{E}$ is the amplitude of the perturbed electric field and $\boldsymbol{\epsilon}(\mathbf{k},\omega)$ is known as the *dielectric tensor*. This equation has nontrivial solutions for

$$\|\boldsymbol{\epsilon}(\mathbf{k},\omega)\| = 0 \tag{3.21}$$

establishing a relationship between the frequency and wavevector of electromagnetic disturbances in the plasma, known as the dispersion relation. For a plasma in an external magnetic field, the derivation of Eq. (3.20) employs the method of characteristics; the cyclotron motion of the particles is assumed to be unperturbed by the disturbance. The full expression of the dielectric tensor can be found elsewhere [58,60]. Of interest here is the longitudinal response, which is relevant to the electrostatic approximation employed. The result for this is

$$\epsilon(\mathbf{k},\omega) = 1 - \sum_\sigma \frac{\omega_\sigma^2}{k^2} \sum_{n=-\infty}^{\infty} \int d\mathbf{v} \left(\frac{n\Omega_\sigma}{v_\perp}\frac{\partial f_\sigma}{\partial v_\perp} + k_\parallel \frac{\partial f_\sigma}{\partial v_\parallel} \right) \frac{J_n^2(b_\sigma)}{n\Omega_\sigma + k_\parallel v_\parallel - \omega} \tag{3.22}$$

where ω_σ and Ω_σ are the plasma and cyclotron frequencies relevant to the given species, and $b_\sigma = k_\perp v_\perp / \Omega_\sigma$. This is usually called the *dielectric response function*, and the dispersion relation (3.21) becomes simply

$$\epsilon(\mathbf{k}, \omega) = 0 \tag{3.23}$$

where $\epsilon(\mathbf{k}, \omega)$ is a complex scalar function. We now assume a Maxwellian velocity distribution

$$f_\sigma(v_\perp, v_\parallel) = \left(\frac{m_\sigma}{2\pi T_\sigma}\right)^{3/2} \exp\left[-\frac{v_\perp^2 + v_\parallel^2}{2(T_\sigma/m_\sigma)}\right] \tag{3.24}$$

and keep only the $n = 0$ electron cyclotron harmonic, since we are considering electron guiding center dynamics only. The dielectric response function is then given by

$$\epsilon(\mathbf{k}, \omega) = 1 + \frac{k_e^2}{k^2}\left[1 + \zeta_e Z(\zeta_e)\right] + \frac{k_i^2}{k^2}\left[1 + \sum_n \frac{\omega}{\omega - n\Omega_i} \zeta_{i_n} Z(\zeta_{i_n}) \Gamma_n(b_i)\right] \tag{3.25}$$

where Z is the plasma dispersion function [61]; its arguments in the above equation are given by

$$\zeta_e \equiv \frac{\omega}{|k_\parallel|(2T_e/m_e)^{1/2}} \tag{3.26}$$

$$\zeta_{i_n} \equiv \frac{\omega - n\Omega_i}{|k_\parallel|(2T_i/m_i)^{1/2}} \tag{3.27}$$

Here we have made the assignment $k_\sigma \equiv 1/\lambda_\sigma$, and introduced the function

$$\Gamma_n(b) \equiv I_n(b)\, exp(-b) \tag{3.28}$$

where I_n is the modified Bessel function.

At this point the usual practice is to look for solutions to Eq. (3.23) in a frequency regime where the arguments to the plasma dispersion function are either very large or very small, using an asymptotic form of Z to get a

tractible expression. A normal mode solution is found by assuming a frequency dependence of the form $\omega = \omega_0 + i\gamma_0$, with $|\gamma_0| \ll |\omega_0|$. For the plasma wave, the relevant regime is [58]

$$k_\parallel v_i \ll k_\parallel v_e \ll \omega \ll \Omega_i \tag{3.29}$$

giving for the real part of the frequency

$$\omega_0^2 \simeq \frac{k_\parallel^2 v_e^2}{k^2\lambda_e^2 + k_\perp^2 \rho_s^2} \tag{3.30}$$

where $\Gamma(b)$ has been expanded as $\Gamma(b) \simeq 1 - b$ for small b, and $\rho_s^2 \equiv \tau\rho_i^2$, $\tau \equiv T_e/T_i$. If the ion Larmor radius term is neglected, Eq. (3.30) reduces to

$$\omega_0 \simeq \omega_e \frac{k_\parallel}{k} \tag{3.31}$$

which is the usual result.

The above procedure, involving the expansion of both the plasma dispersion function and the exponentially-scaled modified Bessel function, is a valuable analytical tool to gain insight into the behavior of these modes. However, for comparison to simulation results a more accurate method is desired. Therefore, the procedure used in this work for comparison to the theoretical frequency is to solve the dispersion Eq. (3.23) directly from Eq. (3.25), using a complex root finder (IMSL library routine ZANLYT). The full plasma dispersion function is calculated using a continued fraction method. Although it is usual to keep only the $n = 0$ cyclotron harmonic of the ion response term, we find that it is necessary to keep at least the $n = 1$ or $n = 2$ terms for close comparison with the simulation results. Given an initial guess reasonably close to the root, the method converges rapidly.

The tests given here of the simulation plasma in the plasma wave regime consider only a single harmonic in ζ ($n = 6$) but all of the perpendicular

dynamics; this configuration is similar to that studied in association with the toroidal drift mode in Chapter 4. The simulation parameters are given by : $N_p = 50625$ (number of particles), $L_x = L_y = 64\,\Delta$, $L_z = 3L_x$, $N_x = N_y = 64$ (slab geometry and uniform grid, with a mode representation in z), $\Delta t = 0.2\,\omega_e^{-1}$, $v_{th} = .51\,\Delta\omega_e^{-1}$, $\tau = 1$, $m_e/m_i = 0.01$, $\Omega_e/\omega_e = 10$, and particle "size" of $a_x = a_y = \Delta$, $a_z = 0$ (no additional smoothing was employed in z due to the accuracy of the mode expansion; also note that the particle size in x only approximates one grid spacing, using two passes of the binomial digital filter). The energy was conserved within 0.03% for 2000 time steps. The plasma frequency is obtained by the maximum entropy method. Although the potential is stored in the form of (r, m, n), for a slab geometry simulation we can Fourier transform in the post-processor to get the k_x dependence. The frequency, power, and mode numbers for the strongest signals are output by the post-processor. The frequency is then plotted versus the perpendicular wavevector, and compared to the theoretical result in Figure 3.15. In this figure, the solid line represents the theoretical plasma response with the filtering effects included (finite size particle effects), and the dashed line representing the theoretical response alone. The filtering effects are included in the theory in a very simple way—we replace ω_σ^2 by $\omega_\sigma^2 S^2$ in Eq. (3.22), where $S(\mathbf{k}\cdot\mathbf{a})$ is a gaussian shape factor and $\mathbf{a}$ is the effective particle size. The agreement is good, and the remaining systematic error is likely due to grid effects, which have not been corrected for in the rootfinder (i.e. modification of the spectrum from the interpolation and Poisson solver). The flattening of the theoretical solution at higher values of $k_\perp\rho_i$ is caused by connection to the $n = 2$ ion Bernstein branch. A sample plot of the spectral density is given in Figure 3.17.

We further check the variation with the perpendicular wavenumber

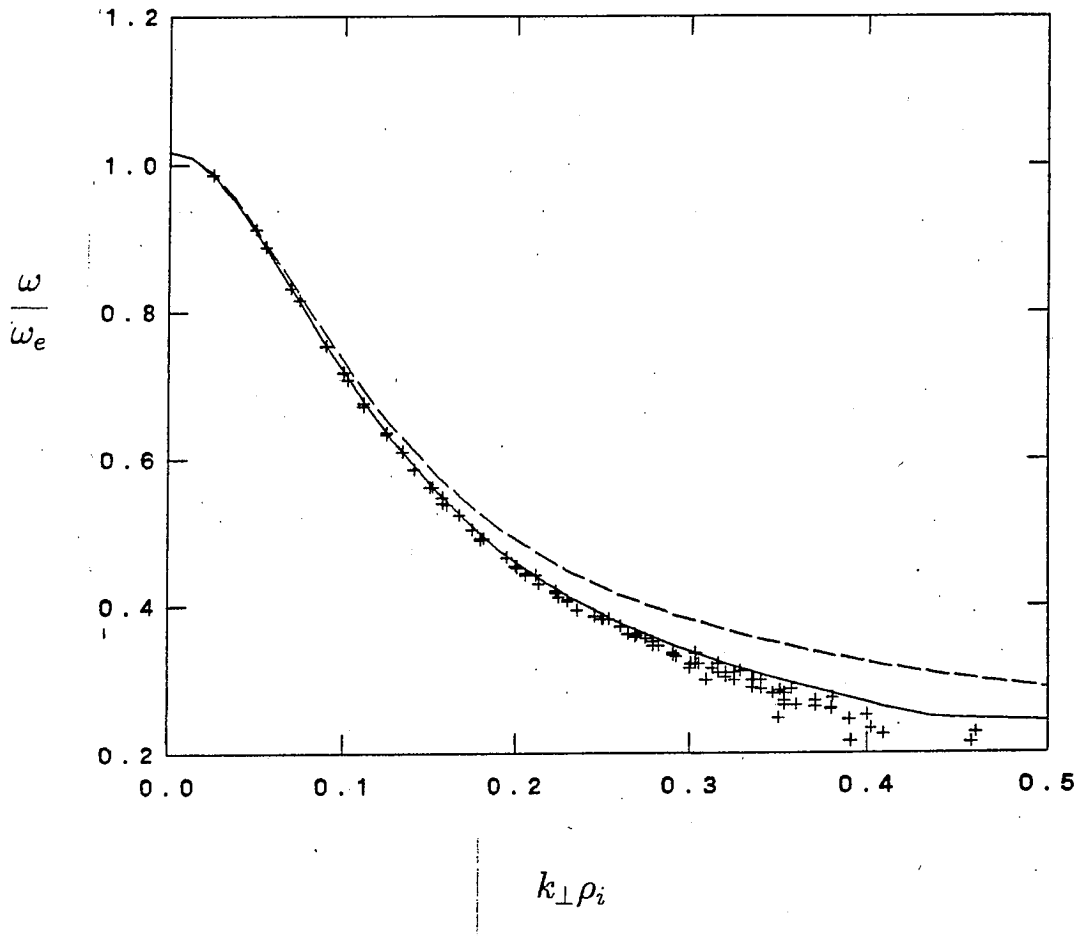

Figure 3.15: Frequency versus perpendicular wavenumber, plasma wave regime.

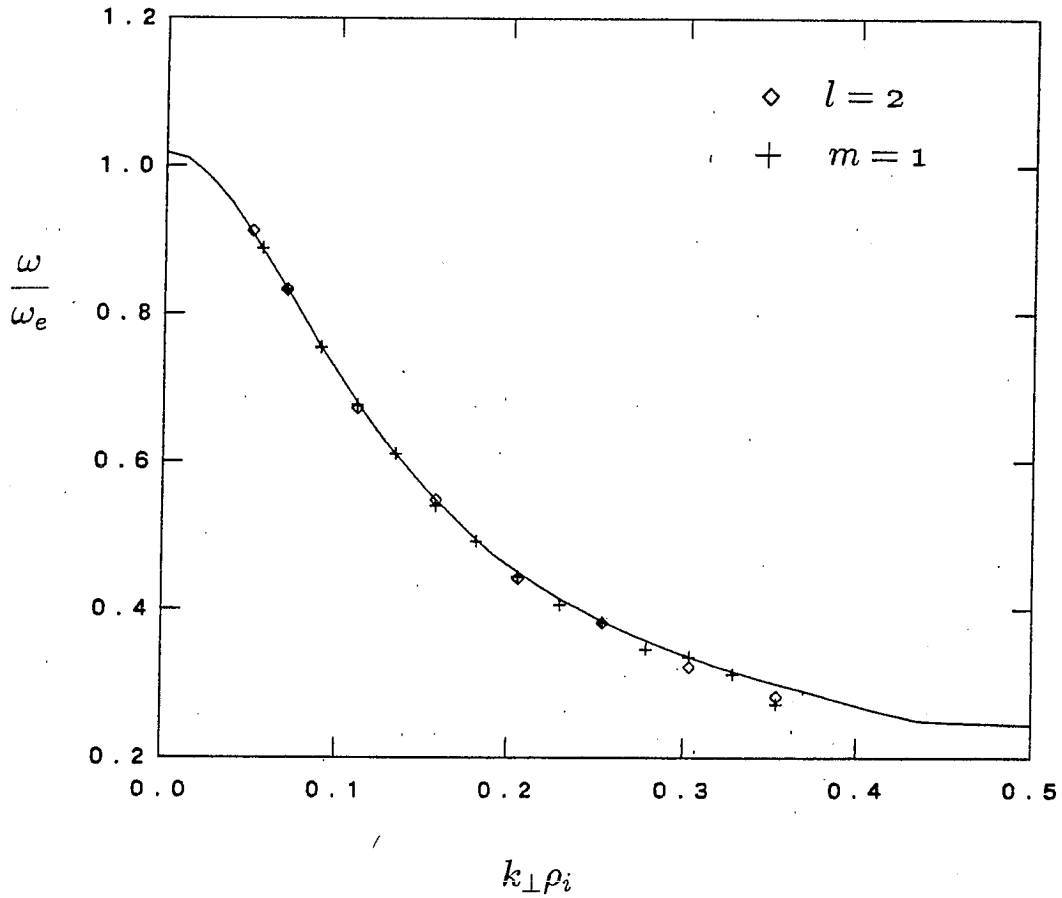

Figure 3.16: Same as in Figure 3.15, but including only the $l = 2$ and $m = 1$ wavenumbers.

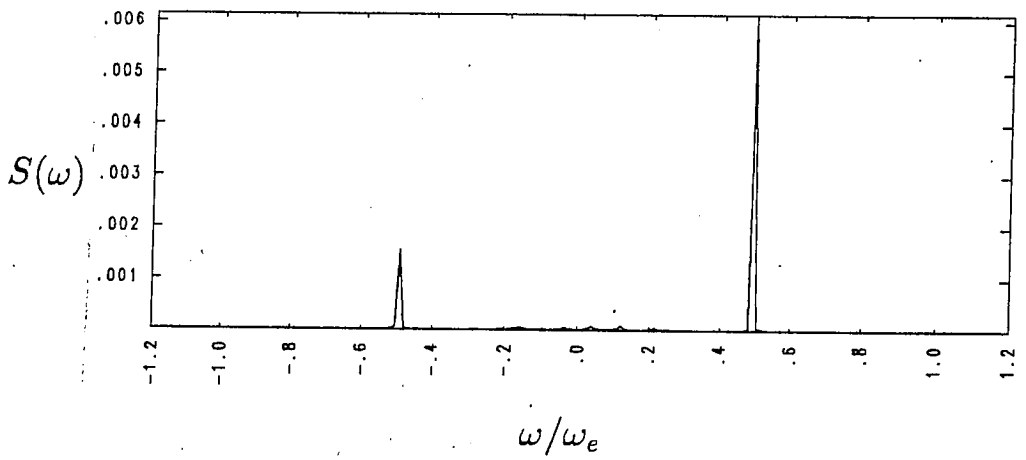

Figure 3.17: Sample plot of spectral density for the $(6, 2, 6)$ mode using the maximum entropy method.

while holding the x-coordinate mode number fixed ($l = 2$, doubled because of the odd parity) or the y-coordinate mode number fixed ($m = 1$, periodic). This check will illuminate any discrepancies caused by the combination finite-difference/digital-filter method used in x compared to the more usual k-space treatment in y. As seen from the plot in Figure 3.16, there are no apparent differences at low mode number, as expected.

At this point we also wish to test the ability of the code to reproduce the plasma wave spectrum in the presence of a nonuniform grid. This test ensures that the nonuniform grid has not altered the plasma dynamics in any unexpected way—the nonuniform grid should reproduce the long wavelength behavior as well as the uniform grid. As with the case with the uniform grid, the x-space data is transformed into a k-space representation, although an FFT

cannot be used because the data is not uniformly distributed (i.e. must be done by direct expansion). The simulation parameters are as given above, except for the addition of the nonuniform grid. A plot versus perpendicular wavenumber for all modes is given in Figure 3.18, and for the $l = 2$ and $m = 1$ modes in Figure 3.19. The results in this case are not substantially different from the uniform grid case, proving the ability of the nonuniform grid to correctly model the long-wavelength modes. A sample sample spectral density plot is given in Figure 3.20 and the nonuniform grid employed is illustrated in Figure 3.21.

An additional mode often examined in magnetized simulation plasmas is the electron or ion Bernstein mode, which is characterized by frequencies near multiples of the cyclotron frequency for each species. In this algorithm, only the ion modes are observed, since the electron cyclotron motion has been gyro-avergaged via the guiding center equations. The direct solution of Eq. (3.23) for the cyclotron harmonics using the dielectric response function given by Eq. (3.25) is an ill-conditioned problem, however. In this case, we must re-arrange the terms in the response function, based on our knowledge that the roots are near the cyclotron harmonics. In particular, we assume $\omega \simeq n\Omega_i$, whereby the ordering of the terms casts the dispersion relation in the form

$$\omega - \frac{n\Omega_i}{1 - \beta(\mathbf{k}, \omega)} = 0 \tag{3.32}$$

where $\beta(\mathbf{k}, \omega)$ will be small, and is given by

$$\beta(\mathbf{k}, \omega) = \frac{k_i^2}{k^2} \zeta_{i_n} Z(\zeta_{i_n}) \Gamma_n(b_i) \frac{1}{R(\mathbf{k}, \omega)} \tag{3.33}$$

and

$$R(\mathbf{k}, \omega) = 1 + \frac{k_e^2}{k^2} [1 + \zeta_e Z(\zeta_e)] + \frac{k_i^2}{k^2} \left[1 - \sum_{j \neq n} \frac{\omega}{\omega - j\Omega_i} \zeta_{i_j} Z(\zeta_{i_j}) \Gamma_j(b_i) \right] . \tag{3.34}$$

with ζ_e and ζ_{i_n} as previously defined.

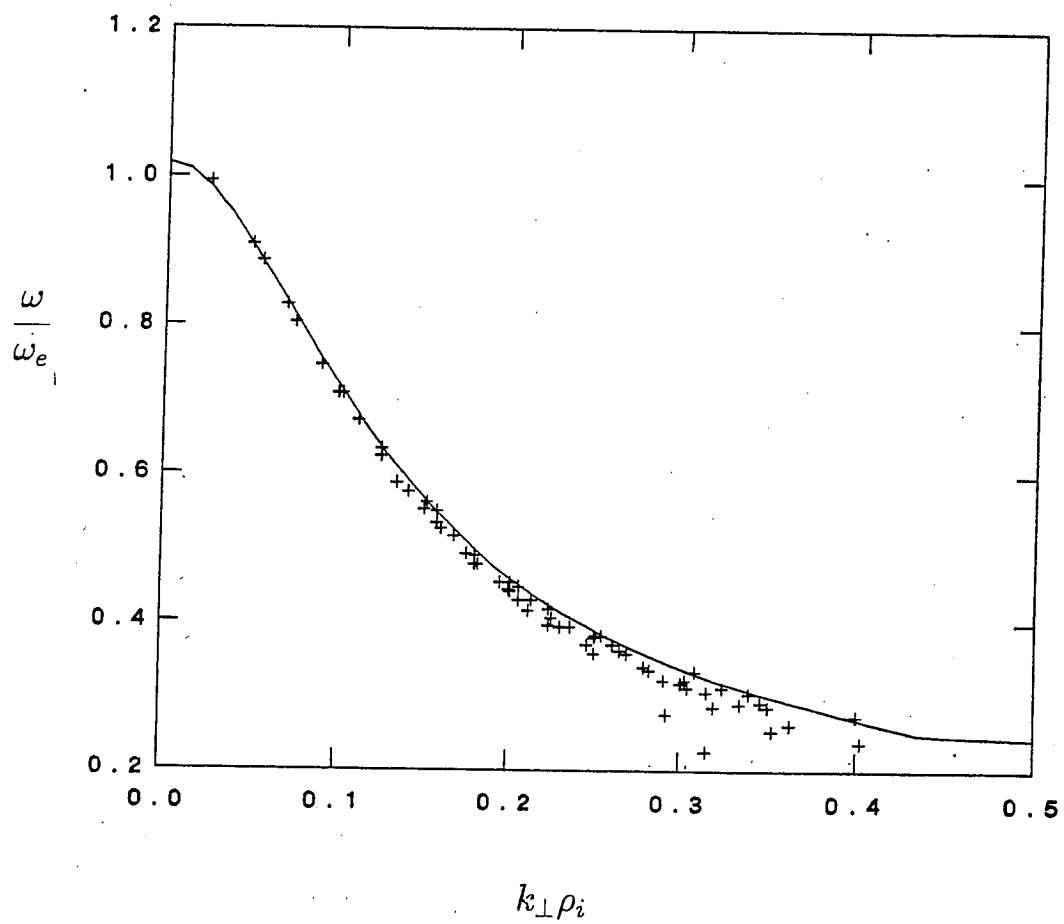

Figure 3.18: Plasma frequency versus perpendicular wavenumber, nonuniform grid case.

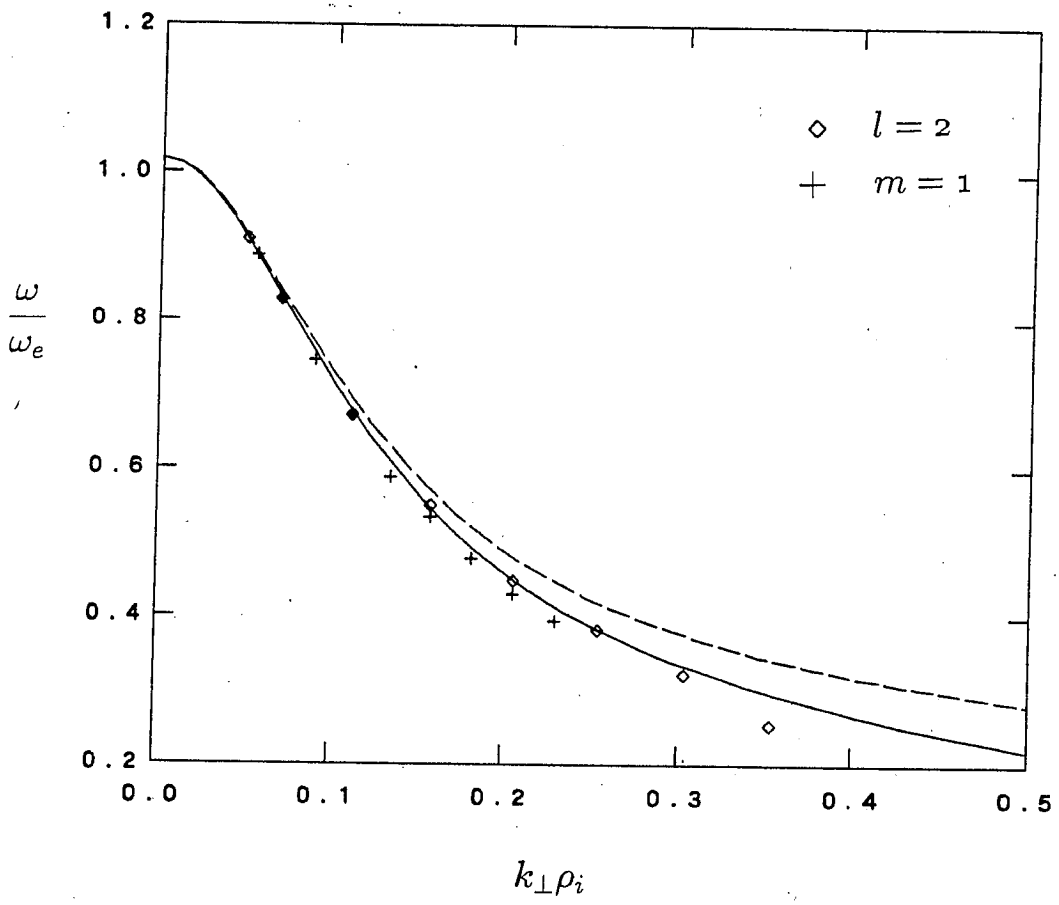

Figure 3.19: Same as in Figure 3.18, but including only the $l = 2$ and $m = 1$ wavenumbers.

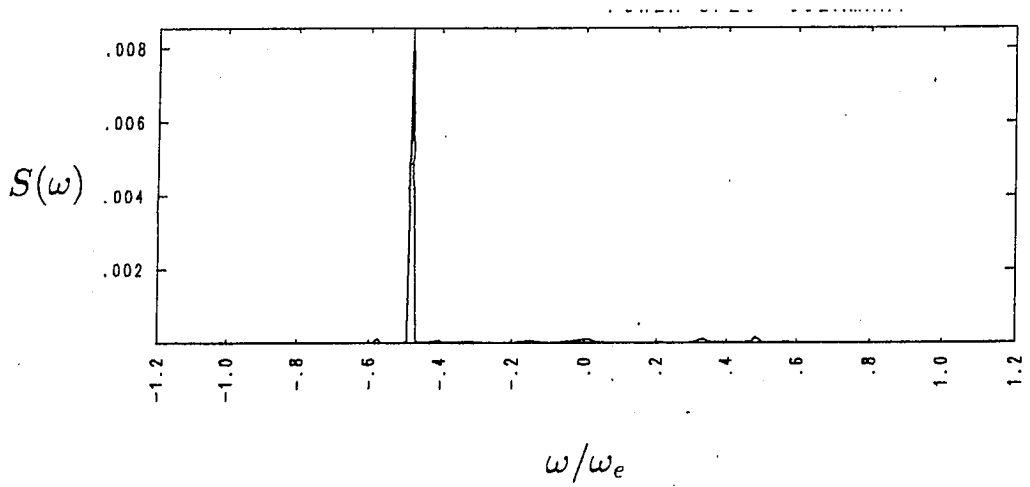

Figure 3.20: Plot of spectral density for the $(6, 2, 6)$ mode using the maximum entropy method.

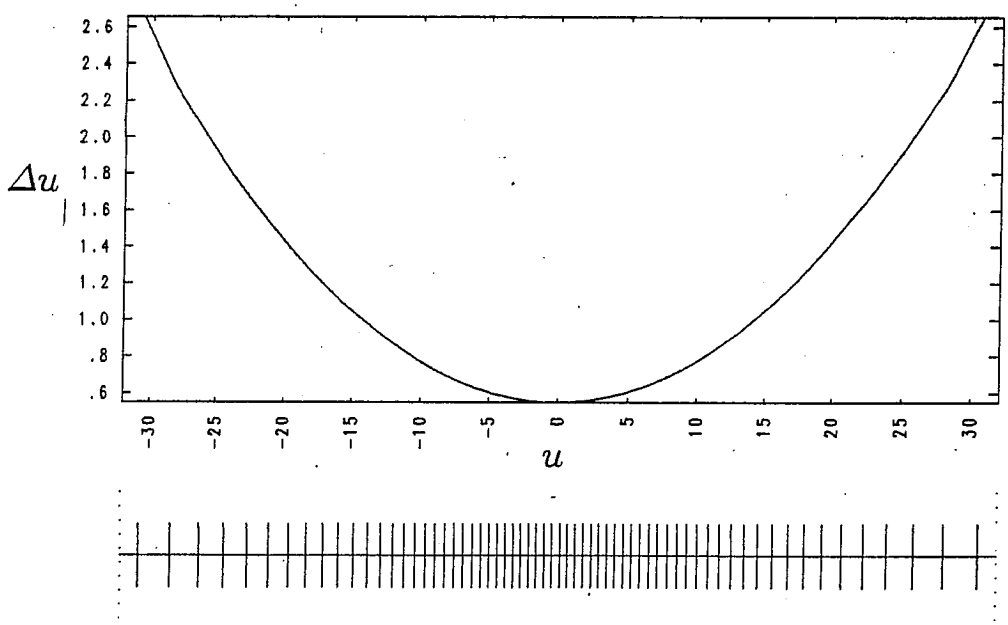

Figure 3.21: Grid configuration for plasma wave test.

The complex rootfinder will converge with the dispersion equation in the form given by Eqs. (3.32)–(3.34), but we can simplify a bit more for the purely perpendicular-propagating mode. In this case, $k_{\|}$ is identically zero, so the large argument expansion of the plasma dispersion function must be used. Expressing the frequency as

$$\omega = n\Omega_i \left(1 + \Delta_n(\mathbf{k}, \omega)\right) \tag{3.35}$$

we have

$$\Delta_n(\mathbf{k}, \omega) = \frac{\beta(\mathbf{k}, \omega)}{1 - \beta(\mathbf{k}, \omega)} \tag{3.36}$$

with β given by

$$\beta(\mathbf{k}, \omega) = \frac{k_i^2 \, \Gamma_n(b_i)}{k^2 + k_i^2 \left(1 - \sum_{j \neq n} \omega / (\omega - j\Omega_i) \Gamma_j(b_i)\right)} \tag{3.37}$$

To obtain an explicit expression for ω, we keep only the largest term in the sum, given by $j = 0$. If we also assume that β is much less than unity, we obtain

$$\Delta_n(\mathbf{k}) \approx \beta \tag{3.38}$$

$$\approx \frac{k_i^2 \Gamma_n(b_i)}{k^2 + k_i^2 \left(1 - \Gamma_0(b_i)\right)} \tag{3.39}$$

Note that this differs from the expression for $\Delta_n(\mathbf{k})$ given by Ichimaru [58, Eq. (4.89a)]. For the purely perpendicular mode, there is no contribution from the electron response, since electrons are tied to the field lines and cannot interact with the wave. Only for a finite angle of propagation will electron screening and Landau damping effects enter. In this case (finite $k_{\|}$), one must solve using the full dispersion function to get an accurate dispersion relation, using Eqs. (3.32)–(3.34).

For the ion Bernstein mode test, we consider the two-dimensional slab geometry limit of the code ($n = 0$ only). The simulation parameters are given

by : $N_p = 50625$ (number of particles), $L_x = L_y = 64\,\Delta$, $N_x = N_y = 64$ (slab geometry, uniform grid), $\Delta t = 2.0\,\omega_e^{-1}$, $v_{th} = 1.0\,\Delta\omega_e^{-1}$, $\tau = 1$, $m_e/m_i = 0.04$, $\Omega_e/\omega_e = 5$, and particle "size" of $a_x = a_y = \Delta$ (using two passes of the binomial digital filter in x). The energy was conserved within 0.5% for 2000 time steps. The frequencies are again obtained by the maximum entropy method. The frequency is plotted versus perpendicular wavenumber, and compared to the theoretical result using the rootfinder in Figure 3.22. As previously, the solid line represents the theoretical response with the gaussian filter correction, and the dashed line is the theoretical response alone. A sample plot of the spectral density is given in Figure 3.23, showing the strong response near harmonics of the cyclotron frequency. For the parameters chosen in this run, the plasma response is concentrated in the lowest Bernstein harmonics, as seen in the spectral density plot.

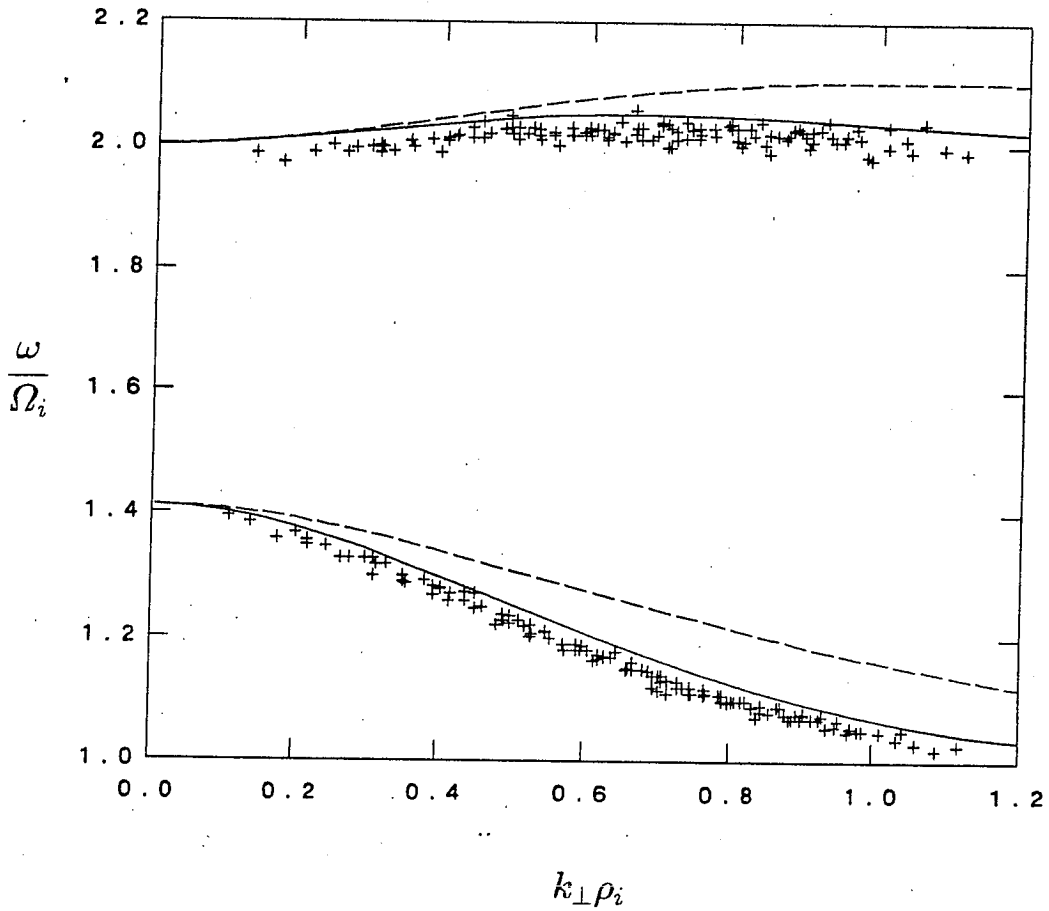

Figure 3.22: Frequency versus perpendicular wavenumber.

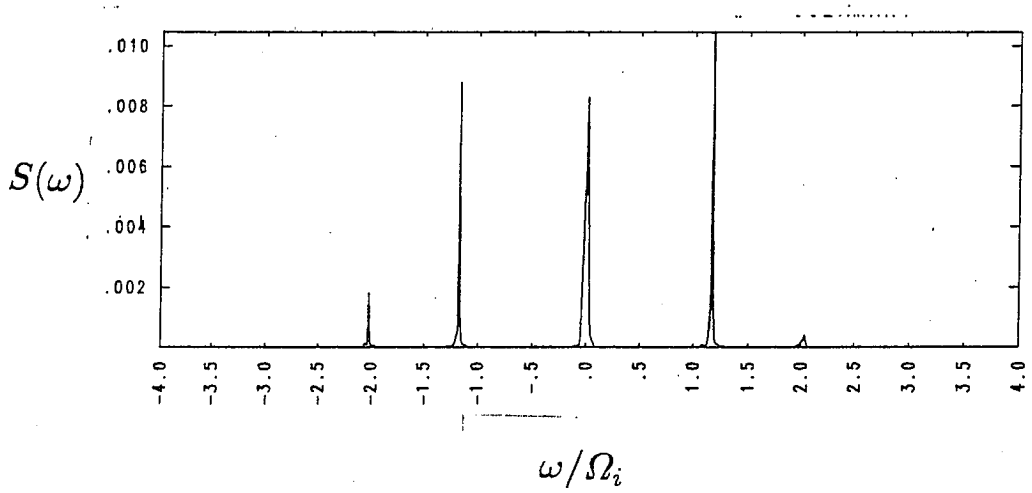

Figure 3.23: Plot of spectral density for the $(8, 5, 0)$ mode using the maximum entropy method.

Chapter 4

Drift wave theory and simulations

In this chapter we apply the toroidal simulation model to the study of drift wave instabilities in toroidally confined plasmas. We will first consider the problem of initialization, that is, the loading of stationary distributions in the toroidal system. Stability problems require an initial equilibrium configuration; however, satisfying this constraint proves to be much more difficult than in slab geometry. In section 4.2 the theory of the drift wave in the slab limit is discussed, and a simulation of this mode is performed using the toroidal particle code in the appropriate limit (two-dimensional, slab). Consideration of the slab-like drift mode provides a useful starting point towards understanding of the toroidal mode, and provides an additional demonstration of the validity of the simulation model. In section 4.3 we discuss the important modifications to the slab theory that are necessary when considering realistic geometries, followed by a description of the toroidal simulation and analysis of the results.

4.1 Establishment of the toroidal equilibrium

The study of collective plasma effects via particle simulation must be preceded by consideration of the equilibrium. Since particle simulation utilizes multiple charged species, coupled only through the self-consistent electric (or magnetic) fields, enhanced fluctuation levels by charge separation is a concern. It is well known [22] that incorrect loading of electron and ion profiles in slab geometry can cause fluctuation levels well in excess of equilibrium levels. This

energy is concentrated in the $k_y = 0$ mode (for an x variation of the density profile), and is caused by the large-scale separation of charge perpendicular to the magnetic field. This type of enhanced fluctuation level can easily obscure subtle collective effects, in an otherwise stable (or marginally unstable) plasma. Furthermore, charge separation effects can persist for extremely long times for simulations of the type considered here—the collisionality is low, preventing rapid collisional relaxation, and the magnetic fields are static, so that field line tearing cannot occur.

The driving mechanism for charge separation effects in toroidal geometry is the gradient-B and curvature-B drifts. These drifts are of opposite sign for ions and electrons, leading to the well-known vertical charge separation in a toroidal device without rotational transform [62]. The inclusion of rotational transform, however, ensures that a particle that drifts away from a flux surface will eventually return to it, as it moves along the poloidal component of the magnetic field (see Figure 4.1). This results in confined trajectories for individual particles, as well as a cancellation of the charge separation effects.

In a particle simulation of the toroidal system, however, the transit time for the typical ion is much longer than other characteristic times of the system (an ion gyration period, for example). The initial particle load, which uses a straightforward extension of the slab procedure, leaves the particles in a highly correlated state, and the effects of the rotational transform are not immediately felt. This leads to large-scale charge separation (primarily due to the ion drifts) and electric field fluctuations far in excess of equilibrium values.

The charge separation seen in the toroidal particle simulation is a result of the loading of non-stationary particle distributions. In theory, a stationary distribution can be obtained by utilizing a function of the constants of

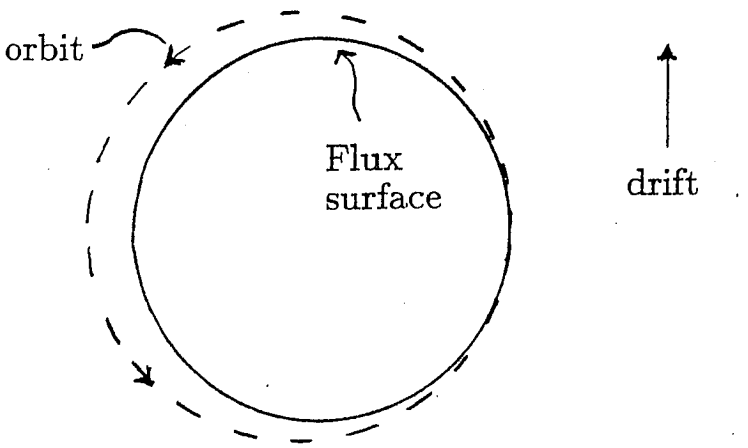

Figure 4.1: Drift orbit of transiting particle in system with rotational transform.

motion :

$$f \equiv f(\mathbf{x}, \epsilon, \mu, p_\phi) \tag{4.1}$$

where x is the coordinate, ϵ is the energy, μ is the magnetic moment, and

$$p_\phi = mR\,v_\phi + q\,\psi(r) \tag{4.2}$$

is the toroidal canonical momentum. The theoretical procedure for writing the distribution as a function of r is to expand $f(p_\phi)$, with the assumption that

$$mRv_\phi \ll \psi(r) \tag{4.3}$$

The problem with this approach is that relation (4.3) is not valid for typical simulation parameters. What is required is a distribution that generates some desired density profile, and is stationary to *all* orders in the ion Larmor radius.

Such a constraint may be difficult (if not impossible) to satisfy, so we therefore consider alternate methods for loading the particle distributions.

One alternative is to directly load a distribution in terms of the constants of motion as in (4.1), using some general function of p_ϕ. This procedure will not allow the exact generation of a desired density profile, but a reasonably close match could be obtained through variation of the function $f(p_\phi)$. In applying this to the phase space of the particles, however, an additional problem arises. The function we are trying to load takes on the form of

$$f(\mathbf{x}, p_\phi) = f(r, \theta, v_\parallel, v_\perp) \tag{4.4}$$

subject to the constraint that the energy distribution $f(\epsilon)$ be specified (usually a constant temperature Maxwellian, but in general the temperature may be a function of r). The distribution function must approximately give the desired density profile, that is,

$$n_{\text{spec}}(r) \approx n(r) = \left\langle \int d\mathbf{v}\, f(\mathbf{x}, \mathbf{v}) \right\rangle_{\theta,\phi} \tag{4.5}$$

In addition, the resulting pitch angle dependence (μ/ϵ) and density variation in θ must be reasonable. Note that the ϕ dependence is ignorable; the gyrophase angle dependence is usually small and has been neglected in the distribution function.

The generation of random variables corresponding to the distribution given by Eq. (4.4) subject to the given constraints is a very complex problem, and is likely to be computationally very expensive. A straightforward method would utilize a discretization of the variables $(r, \theta, v_\parallel, v_\perp)$ and would require enormous amounts of temporary storage for an accurate representation of the distribution. A use of the rejection method [40] to generate the random variables would lessen the memory requirements, but either method is expected

to be very costly in cpu time, for the large number of particles typically employed. Schemes based on the direct loading of (4.4) are still being studied, but a completely different approach has proven feasable.

The use of a distribution function that is not a function of the constants of the motion is responsible for the failure of the "standard" slab load in the toroidal system. This distribution is not stationary and will rapidly evolve. In the absence of electric fields, the mechanism by which it evolves is known as phase-mixing (since the particles are non-interacting in this case, so there is no physical dissipation). Eventually, a stationary distribution is reached, which may be used as a starting point for our toroidal particle simulation. Thus, the generation of a stationary distribution is accomplished by initializing the particle positions in the standard way, then advancing them in time according to the given magnetic field configuration, without the self-consistent electric fields. Phase-mixing eventually results in quasi-stationary distributions. This argument assumes that no zero-order electric potential is necessary for equilibrium.

For this "equilibrium via phase-mixing" to succeed computationally, we require first an efficient method for pushing the particles (primarily ions) on time scales very long compared with the cyclotron gyration. This requirement is satisfied by utilizing the guiding center equations of motion (ordinarily used for the electrons). These equations are accurate even for large Larmor radii in the absence of electric fields, as long as the magnetic field varies slowly on this scale. The second requirement is to develop a criterion by which we can gauge the closeness to stationarity and thereby terminate the initialization procedure. A simple symmetry argument will suffice here. The initial load, as well as the time-averaged particle orbits, are vertically symmetric (i.e. symmetric about

the $\theta = 0$ and $\theta = \pi$ half-planes). Therefore, since the time-averaged distribution is vertically symmetric as well, the ensemble-averaged distribution must also share this symmetry, by the ergodic hypothesis for a system in statistical equilibrium. This requirement of vertical symmetry proves to be a good criterion by which to terminate the initialization push.

The initialization procedure is illustrated by following various moments of the particle distribution (for the ions) in time, as the particles are pushed in the absence of electric fields. The case studied uses a fairly large Larmor radius ($\rho/a = 0.025$, where a is the minor radius), which emphasizes the non-equilibrium effects since these effects scale as some function of $\kappa\rho$ and ρ/r, where κ is the inverse density scale length. The particle distribution moments shown in Figure 4.2 are the parallel and perpendicular temperatures ($T_\parallel(r,\theta) - \langle T_\parallel \rangle$, $T_\perp(r,\theta) - \langle T_\perp \rangle$), zero-th order magnetic moment ($\mu_0(r,\theta) - \langle \mu_0 \rangle$), and parallel velocity ($v_\parallel$). These are all given at time $t = 0$ and show no global vertical asymmetry, aside from velocity space fluctuations. The initial load was such that the total energy and magnetic moment had no global theta dependence.

The same moments are plotted in Figure 4.3, at a time $t = 500\,\Omega_i^{-1}$. Here there is a strong vertical asymmetry seen in the distributions. The electric fields that would result from the charge separation are much larger than the thermal equilibrium field level. This situation will at best cause an artificial modification of the plasma response, or at worst drive the plasma to the boundary, as in a system without rotational transform. Note the appearance at this stage of a large-scale structure in theta of the parallel velocity.

Finally, we plot the distribution moments at the much later time $t = 4000\,\Omega_i^{-1}$ in Figure 4.4. The vertical symmetry at this time has become

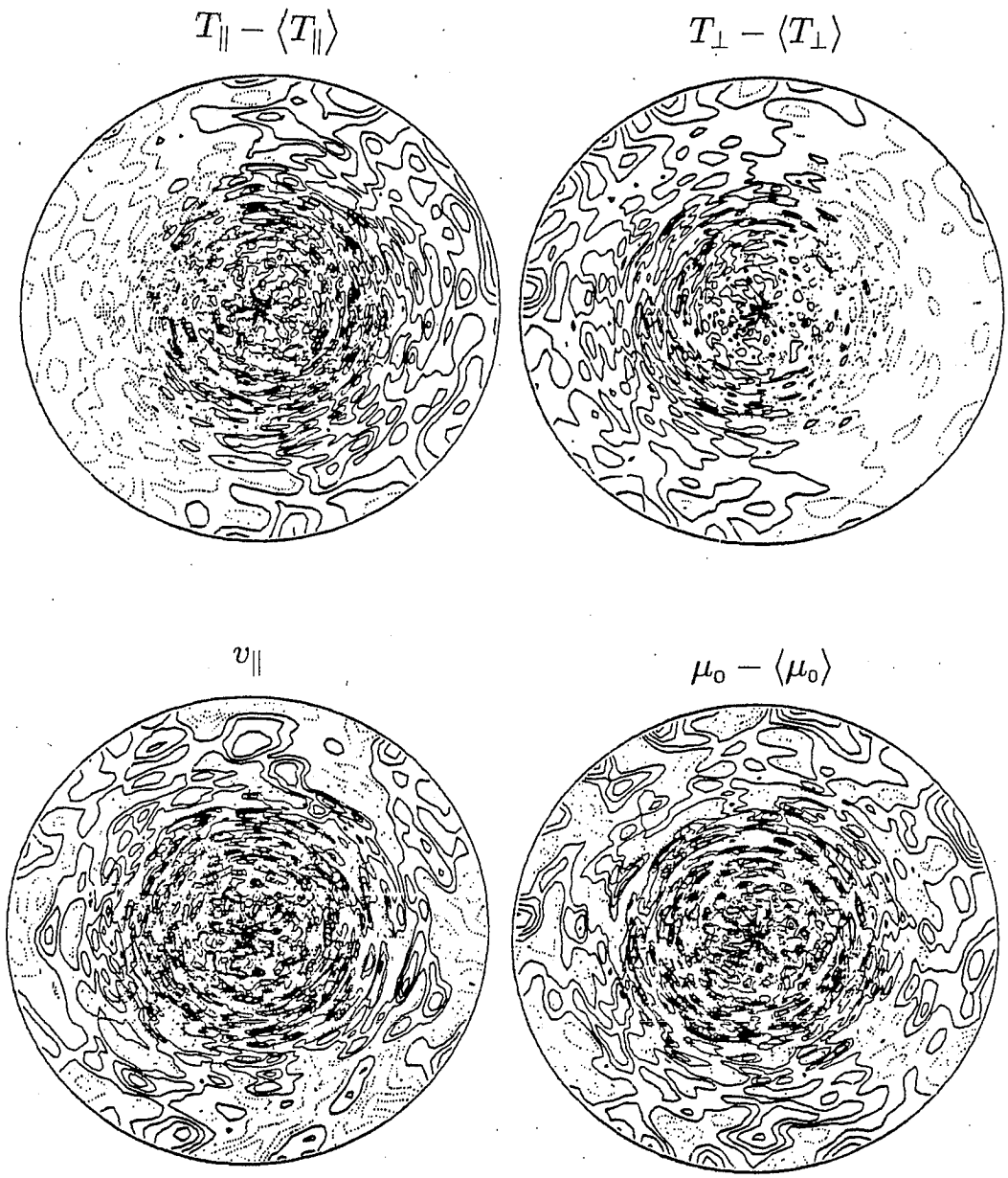

Figure 4.2: Particle distribution moments at time $t = 0$

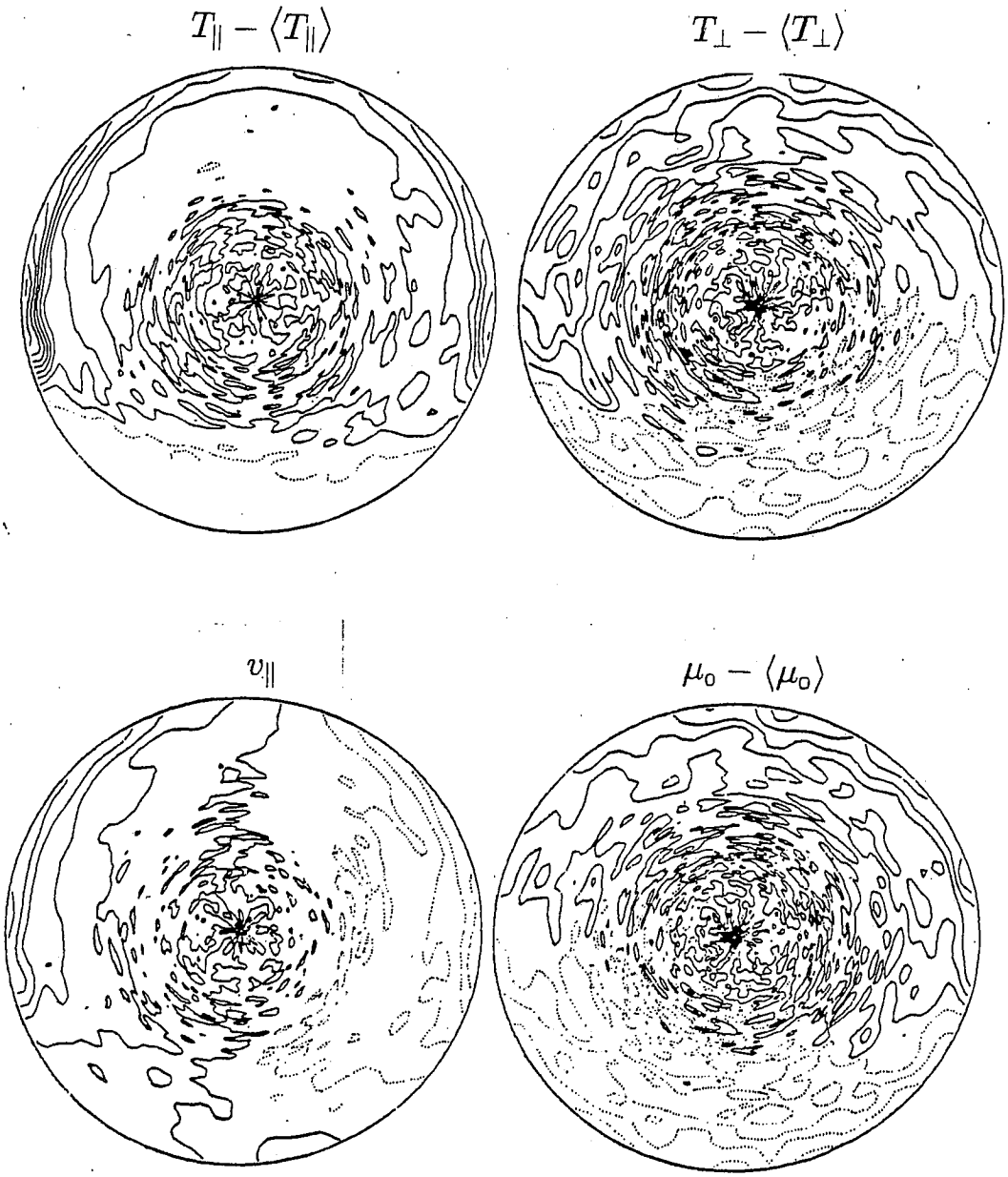

Figure 4.3: Particle distribution moments at time $t = 500\,\Omega_i^{-1}$.

well established. Any remaining asymmetry results from either velocity space fluctuations or from the very slowly-moving particles, which take much longer to phase-mix than the bulk of the distribution. The parallel velocity, in addition to having the observed structure in theta, has shifted to a negative net value on the average. This is shown in a plot of the distribution function at the three times ($\Omega_i t$ = 0, 500, 4000) in Figure 4.5. Although this shift is somewhat large, it is probably tolerable. Also, the parallel velocity shift decreases if the ion Larmor radius is decreased. The theta structure of the parallel velocity results from the variation of a drifting particle's distance from the flux surface (δr), coupled with the plasma inhomogeneity.

The initialization is accomplished by pushing the ion species via the guiding center pusher until the vertical symmetry criterion is approximately satisfied. On the order of 2000 time-steps are typically required, for $\delta t = 2\,\Omega_i^{-1}$ (as in the above case). The computational expense for this calculation is reasonable, since the guiding center pusher is very fast when the electric fields do not need evaluation. At the conclusion of the initialization run, particle quantities are output to disk and then re-read for the actual simulation run, making the necessary transformation from guiding-center coordinates to the full dynamics coordinates. The electron positions (guiding centers) are loaded on "top" of the ion positions, which is one standard method of ensuring approximate quasineutrality at time $t = 0$ (and is equivalent to the method of Naitou *et al.* [22] in the limit of large number of particles). The electron velocity distribution is loaded in the usual way, which ignores any non-equilibrium effects that may be caused by the geometry. Since the electron drifts are much smaller than the ion drifts, this is usually justifiable.

The final problem to be investigated in this section concerns the effect

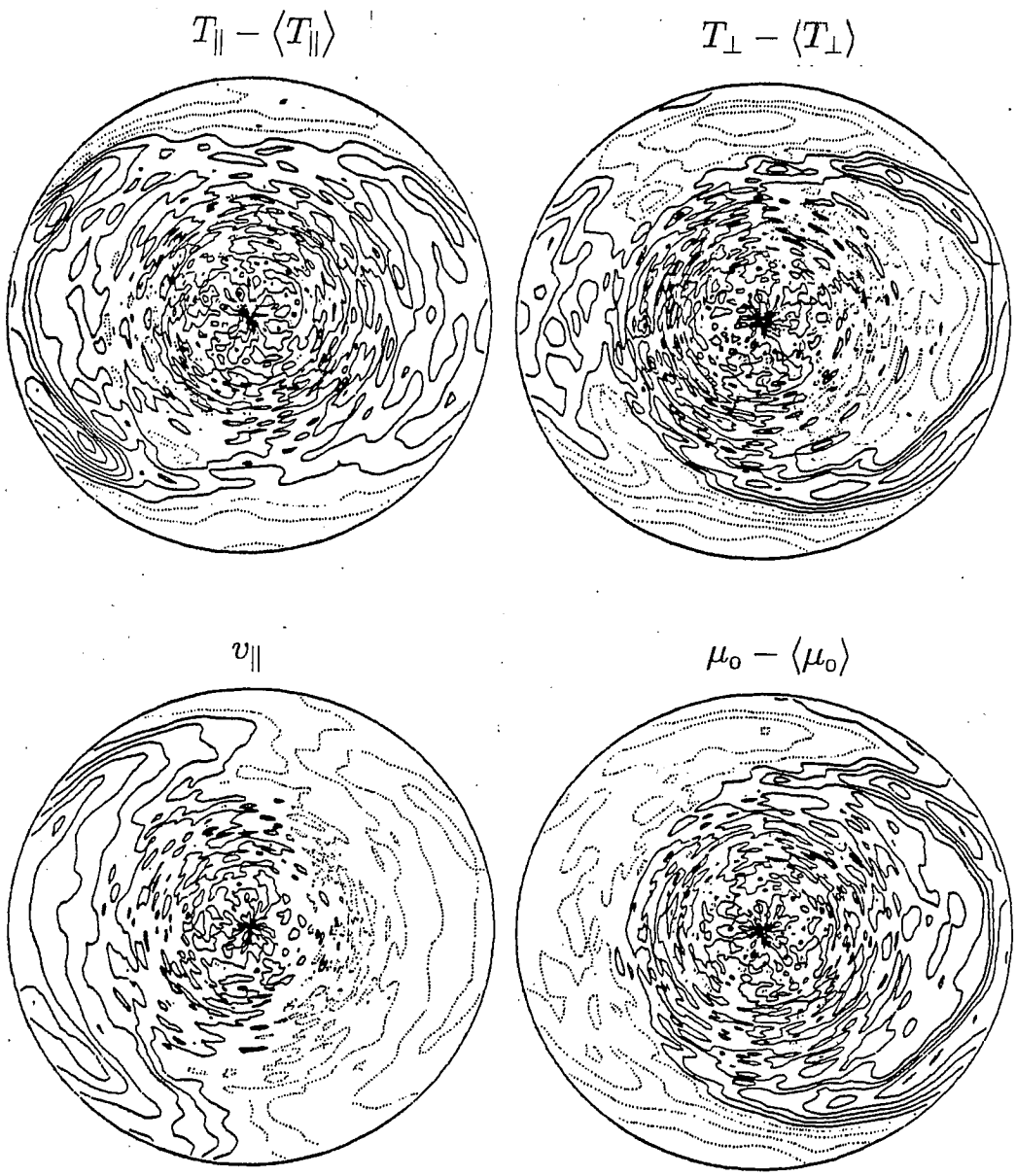

Figure 4.4: Particle distribution moments at time $t = 4000\,\Omega_i^{-1}$.

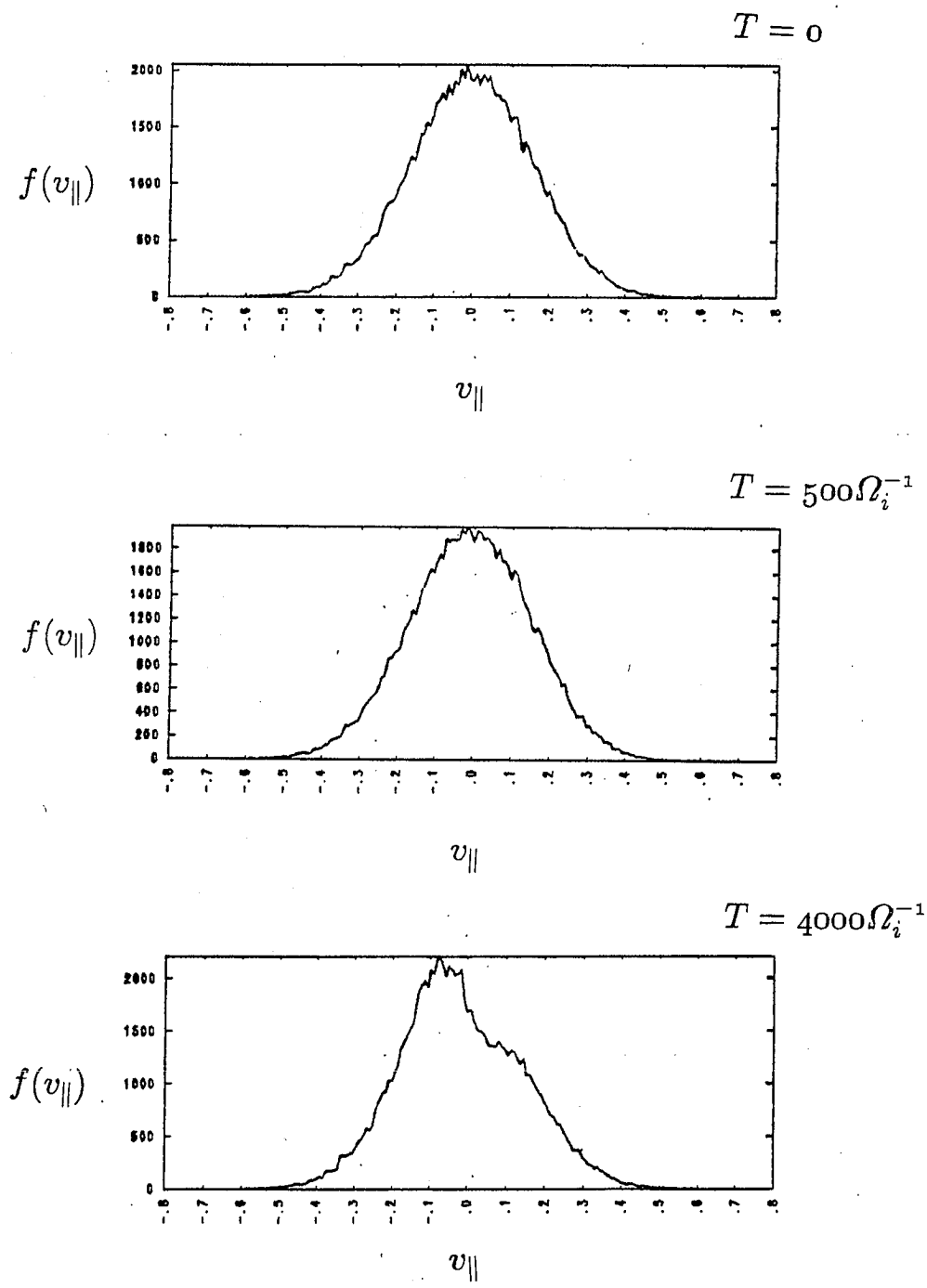

Figure 4.5: Parallel velocity distribution at times $\Omega_i t = 0$, 500, 4000.

of boundaries on the simulation plasma in the toroidal system. As with the equilibrium, the magnetic drifts play an important role. Specifically, the first-order (in Larmor radius) drifts into the boundary may have an important effect on the dynamics. This effect can be examined indirectly by a comparison of the time advancement of the particle distributions via the guiding center pusher versus the full dynamics pusher, in the absence of electric fields. The tests performed in section 3.2 show excellent consistency between these algorithms for single particle motion. Therefore, discrepancies observed when advancing the entire ensemble must be a result of the different boundary handling employed in each method. The guiding center pusher simply reflects the guiding center of the particle upon a collision with the boundary; the full dynamics pusher reflects the particle specularly, causing it to "bounce" along the boundary. (The specular reflection method is not entirely satisfactory due to the shift in the particle's guiding center, but this must be tolerated to avoid undesirable macroscopic currents [63].) Thus the differences observed when pushing with these two methods illustrates the modification of the dynamics caused by the boundaries. (Only an outer radial boundary is employed.)

The particle distribution moments after advancement to time $t = 400\,\Omega_i^{-1}$ using the full dynamics pusher is shown in Figure 4.6, and for the guiding center pusher in Figure 4.7. In both cases, the electric fields were not evaluated, and similar parameters to the equilibrium studies above were used. (A coarser mesh for display of the variables was used, so the resolution is somewhat poorer.) The particle distributions show some clear discrepancies near the outer boundary, reaching as far as 25% of the way into the simulation region. Thus, the outer boundary does cause a significant modification to the dynamics for these parameters. However, since the density tends to be very small at the outer boundary, the bulk of the simulation plasma is unlikely to

be affected. The region of interest can be kept reasonably far from the outer boundary, using the nonuniform radial grid. In addition, reduction of the ion Larmor radius will reduce this boundary effect, and extend the usable portion of the simulation region.

Although the usual configuration is expected to be free of undesired boundary effects (based on the previous discussion), a larger impact would be seen in a configuration that employs an *inner* boundary at some finite value of r (e.g. see Figure 4.8). The use of such a radial "slice" is advantageous due to the fine resolution in r that one may obtain. The modification of the dynamics due to the inner boundary, however, will often be unacceptable since the density has its largest value there. Further, equilibrium may not even be theoretically possible in such a case. (In the usual configuration, the outer boundary can in theory be neglected because we can make the density arbitrarily small there.) This model may give acceptable results for a very small Larmor radius, but this constraint is not satisfactory for the drift-wave phenomena we wish to investigate. The adoption of a more sophisticated boundary handling technique may help to avoid deleterious effects at the inner boundary, but this remains untested. Therefore, the usual model considered in this work retains the inner boundary at $r = 0$, utilizing the nonuniform radial grid to improve resolution.

4.2 Drift waves in the slab approximation

4.2.1 Introduction

A confined plasma is subject to a variety of unstable modes, due to the free energy associated with the spatial inhomogeneity. These modes often fall into one of two categories—magnetohydrodynamic, which are primarily large scale in nature, and microinstabilities, which are primarily microscopic. These

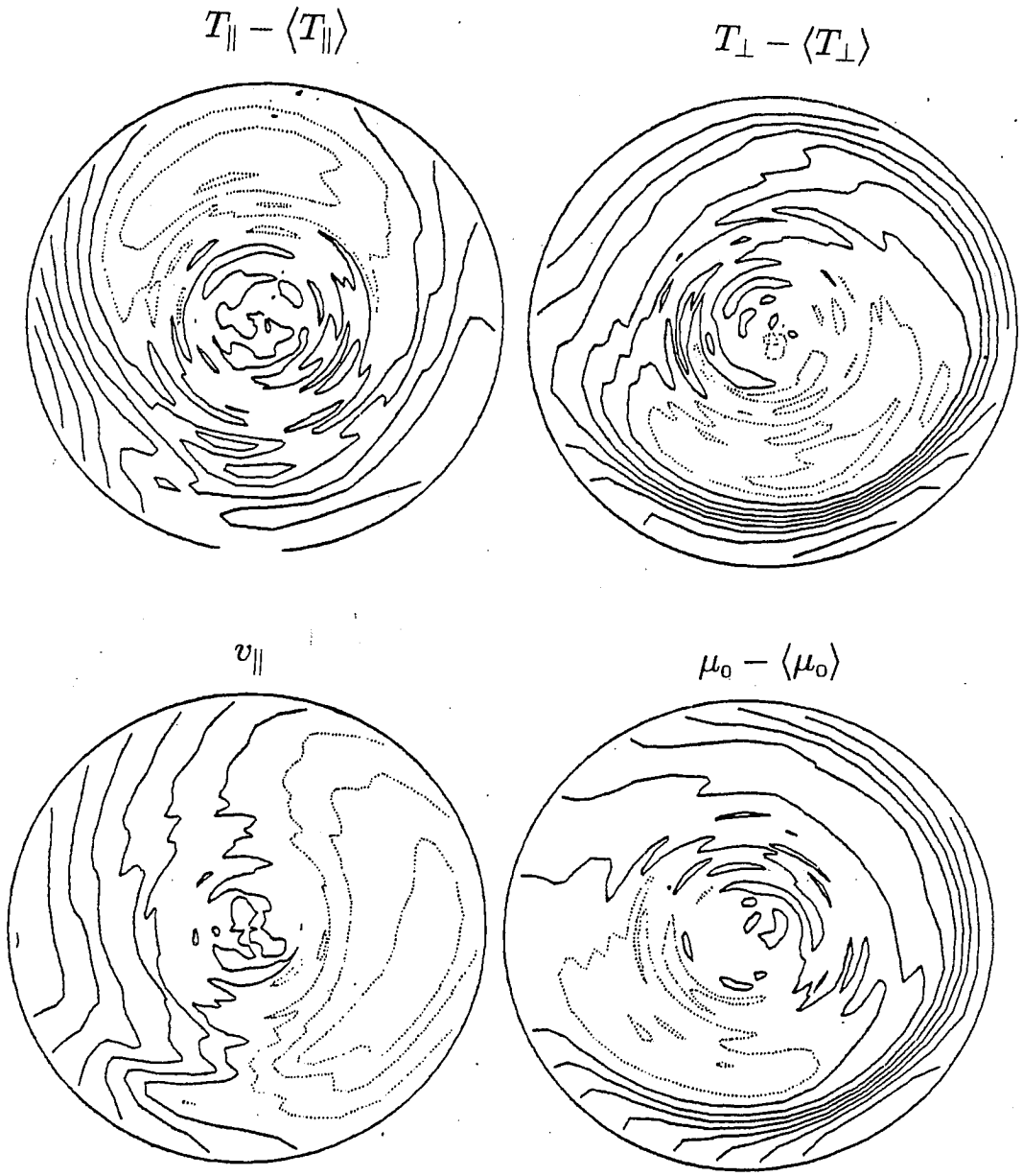

Figure 4.6: Particle distribution moments at time $t = 400\,\Omega_i^{-1}$, using the full dynamics pusher.

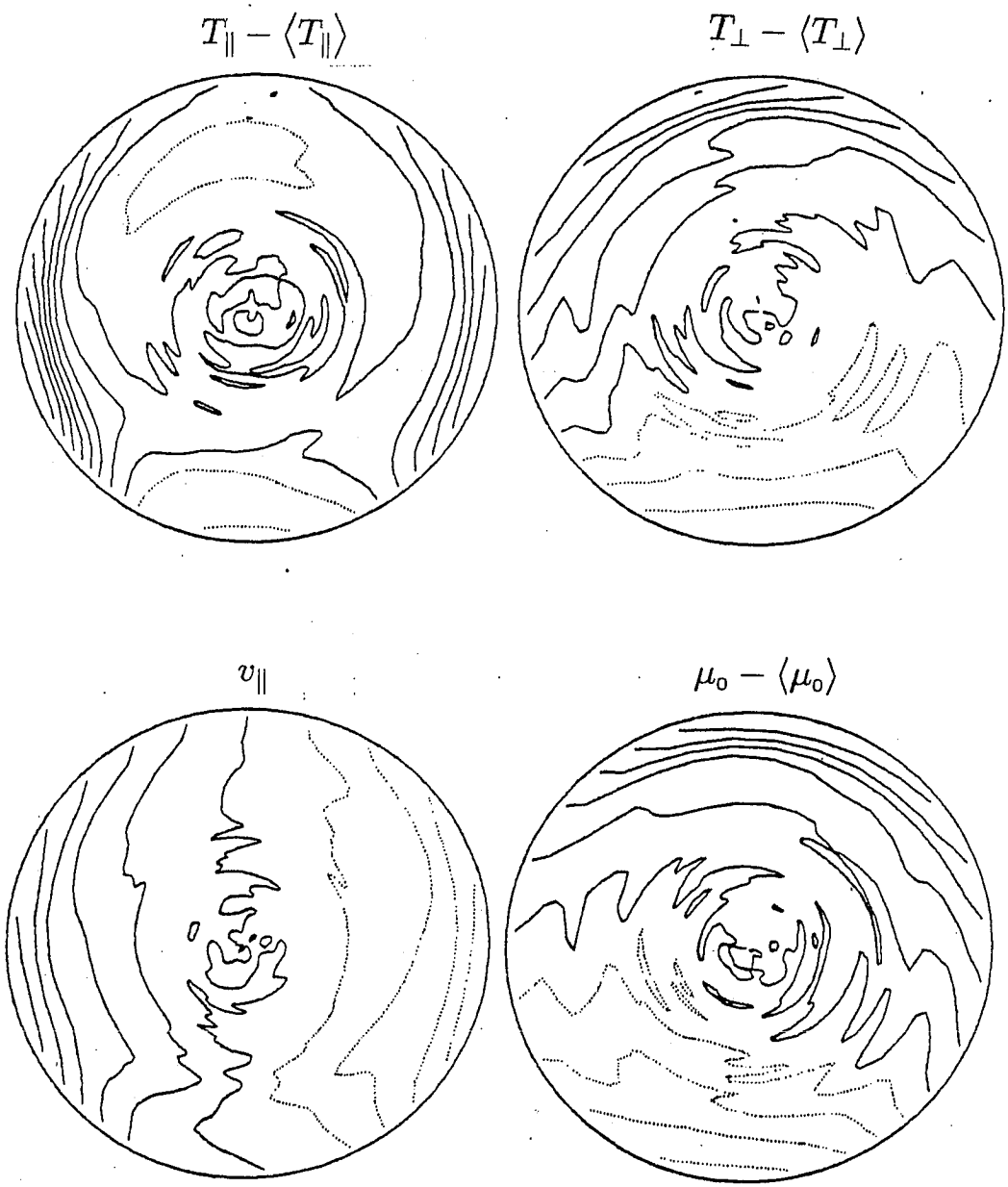

Figure 4.7: Particle distribution moments at time $t = 400\,\Omega_i^{-1}$, using the guiding center pusher.

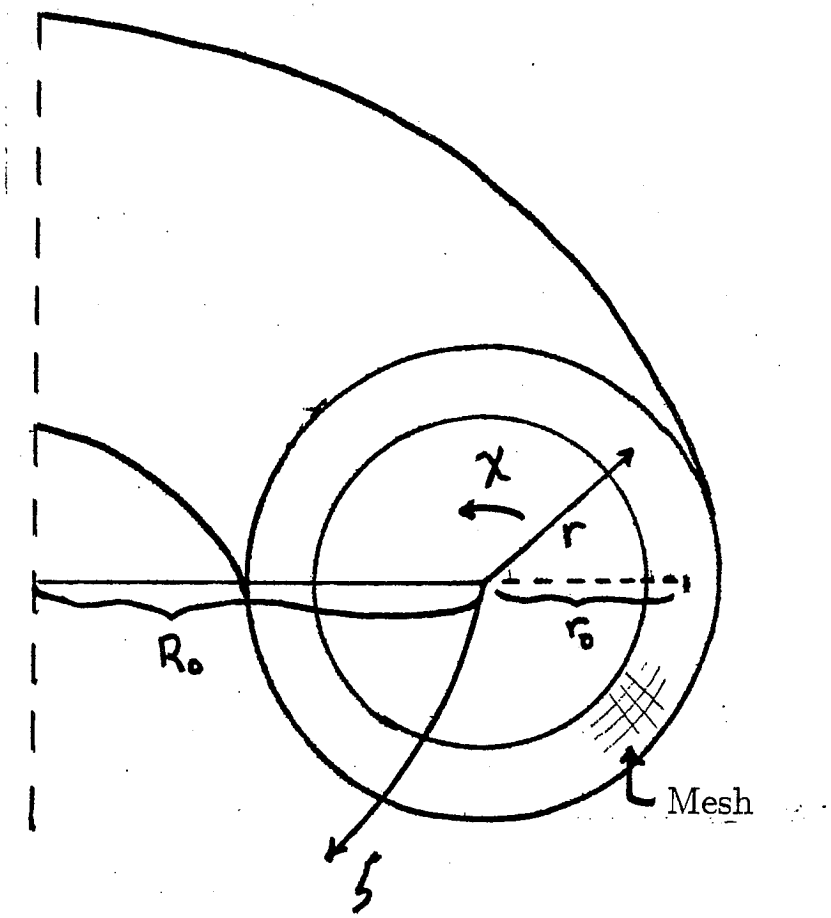

Figure 4.8: Alternate configuration for the toroidal model, employing a radial "slice" with inner boundary located at $r = r_{\min}$.

descriptions differ fundamentally through their treatment of the electron/ion motion. The magnetohydrodynamic description uses an averaged velocity field, so that the electrons and ions move together, which is generally valid on a macroscopic scale. Microinstabilities, however, are usually associated with the separation of charge; the resulting $\mathbf{E} \times \mathbf{B}$ drifts coupled with the plasma inhomogeneity can result in an instability. Drift modes fall into the latter class, and are long parallel wavelength, short perpendicular wavelength modes with phase velocity near the diamagnetic drift velocity. The diamagnetic drift itself results from the interplay between the plasma inhomogeneity and the finite Larmor orbits.

The drift or "universal" mode has been extensively researched, due to its serious threat to plasma confinement. A local slab model was adopted by Krall and Rosenbluth [64] for studying the drift wave in a sheared magnetic field and was the basis of many subsequent investigations. In 1969 Pearlstein and Berk [6] showed that for outgoing wave boundary conditions, the eigenmode equation of Krall and Rosenbluth gives rise to a normal mode solution, propagating in the radial direction. These "Pearlstein-Berk" modes are characterized by Hermite polynomials modified by an exponential. In addition, it was found that values of shear typical for tokamaks were insufficient to stabilize the mode.

The drift-wave eigenmode equation was analyzed numerically by Gladd and Horton [65] to determine the variation of the critical shear on the parameters, using a shooting method for solution of the eigenmode equation. In 1978, similar techniques were employed by Ross and Mahajan [7] and by Tsang *et al.* [8], who found the drift wave to be absolutely stable, contrary to previous results. In these efforts, the inclusion of the nonadiabatic electron response was

responsible for the stabilization of the mode (neglected in earlier studies). The nonadiabatic electron term is small for most of the radial extent of the eigenfunction, but it cannot be neglected near the mode rational surface. The full electron response gives the potential an "anti-well" character near the mode rational surface, which stabilizes the mode. An analytical proof was subsequently given by Antonsen [66] showing that no unstable, bound modes exist in the slab configuration. (The convective mode, however, is still subject to shear stabilization criteria.)

Particle simulations of the drift wave in the slab model began in the mid-1970's with the work of Lee and Okuda [67]. The simulations in the shearless slab exhibited strong instability, with growth rates close to the theoretical result. Saturation of the instability was due to quasilinear flattening of the density profile. However, the addition of shear in this and a later work [68] did not completely stabilize the mode except for very strong shear—the weak shear cases showed little difference from the shearless result. As a result of the theoretical discoveries of the absolute stability of the drift wave, a series of runs satisfying the linear theory boundary conditions (discussed below) was performed by Lee *et al.* [69]. These runs were dominated by local transients, and the linear eigenmode was not observed.

The discrepancy from the results of linear theory in the earlier particle simulations [67,68] may have resulted from improper boundary conditions. In order to obtain the theoretically predicted eigenmode, the ion resonance layer must lie sufficiently far inside the simulation region that the outgoing wave boundary conditions are satisfied. This is a crucial condition, because the ion resonance layer represents the sink for the outward-convected energy of the drift wave. By satisfying this criterion, it was shown by Sydora *et al.*

[70] that particle simulations in a sheared slab reproduce the theoretical eigenmode. One *configuration* employed in Ref. [70] consisted of an exponential density profile with the mode rational surface in the center of the simulation region, and the ion resonance layers included. This placement of the mode rational surface ensured that boundary effects would not alter the result, and both the even and odd parity eigenmodes were observed. With the mode rational surface at one boundary, however, only the even parity eigenmodes were observed, in agreement with the result of Lee *et al.* [69]. The failure to observe the odd parity drift wave eigenmode with the mode rational surface lying at the boundary is evidently the result of unphysical boundary effects. This is plausible since the dominant $\mathbf{E} \times \mathbf{B}$ drift of the ions is not sampled correctly when specular reflection is used in the presence of an odd parity boundary, and may alter the response. (The E_y/B drift is of odd parity, but the ions only sample "half" of this field. Thus the bulk ion motion near the boundary will be modified. However, it is difficult to predict the effect of this modification on the response.) Thus the slab mode simulation that we shall consider employs the mode rational surface in the center of the simulation region, with the ion resonance layers occuring within the boundaries (as in Ref. [70]). This minimizes boundary effects, enabling comparison with theory for either the even or odd parity modes.

4.2.2 Theory

The model adopted in this section is the slab model of Krall and Rosenbluth [64], in which the region about a mode-rational surface has been "unrolled" into a local (x, y, z) coordinate system. This is illustrated in Figure 4.9, for a given flux surface (ι is the rotational transform). Note that as one

moves in r, the pitch of the field line varies due to shear.

A mode rational surface is defined by the vanishing of the wave-vector in the direction of the magnetic field, that is, $\mathbf{k} \cdot \mathbf{b} = 0$. In the toroidal system, the magnetic field components are given by

$$B_\phi = B_{\phi_0} \frac{R_0}{R} \tag{4.6}$$

$$B_\theta = \frac{r}{R_0 q(r)} B_\phi \tag{4.7}$$

where $q(r)$ is the safety factor (inverse rotational transform). The coordinates θ and ϕ give $k_\theta = m/r$ and $k_\phi \approx -n/R_0$ (negative so that the system is right-handed). Then we have

$$k_\parallel = \mathbf{k} \cdot \mathbf{b} \approx \frac{1}{R_0} \left(\frac{m}{q(r)} - n \right) \tag{4.8}$$

Therefore, the vanishing of the parallel wave-vector is equivalent to the requirement that the safety factor be rational (i.e. $q(r_{mn}) = m/n$), or that the magnetic field line eventually close on itself.

Since we seek a local coordinate system about a particular mode rational surface, we expand the parallel wave-vector in a Taylor series around the mode rational surface, obtaining

$$\begin{aligned} k_\parallel(r) &= k_\parallel(r_{mn}) + (r - r_{mn}) \left. \frac{\partial k_\parallel}{\partial r} \right|_{r=r_{mn}} + \cdots \\ &\approx -\frac{m}{r_{mn}} (r - r_{mn}) \left. \left(\frac{r}{q R_0} \frac{1}{q} \frac{\partial q}{\partial r} \right) \right|_{r=r_{mn}} \end{aligned} \tag{4.9}$$

since $k_\parallel(r_{mn}) = 0$. Choosing a local radial coordinate $x = r - r_{mn}$, the local magnetic field is given by

$$\mathbf{B} = B_0 \left(\hat{\mathbf{z}} - \frac{x}{L_s} \hat{\mathbf{y}} \right) \tag{4.10}$$

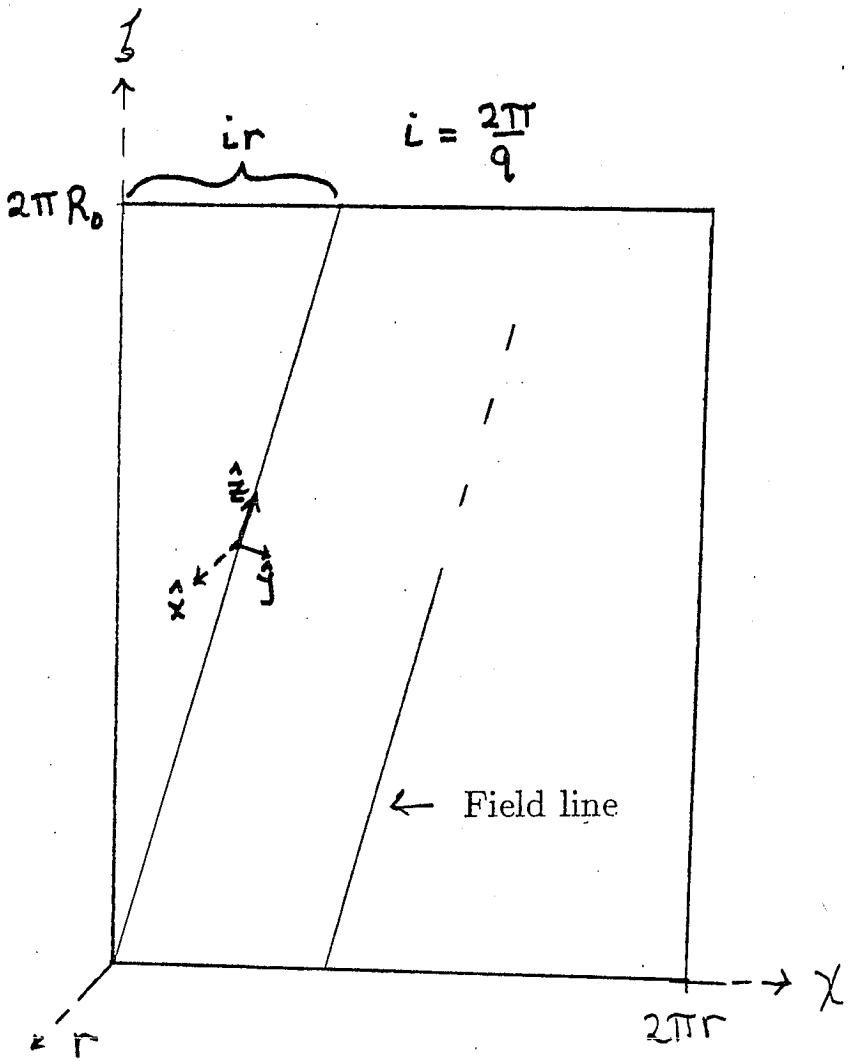

Figure 4.9: Schematic of an unrolled torus, at a given radial position.

and the parallel wave-vector by

$$k_{\parallel} = k_z - \frac{x}{L_s} k_y \tag{4.11}$$

In order for the wave-vector to vanish at the mode rational surface, we must have $k_z \equiv 2\pi n/L_z = 0$, or $n = 0$, so that the problem has become essentially two-dimensional. The shear length L_s is obtained by comparison to Eq. (4.9), which gives

$$L_s = \left(\frac{r}{qR_0} \frac{1}{q} \frac{\partial q}{\partial r} \right)^{-1} \tag{4.12}$$

for $k_y \equiv 2\pi m/L_y$, $L_y \equiv 2\pi\, r_{mn}$. The shear length is assumed constant in the local coordinate system (i.e. terms involving radial position are evaluated at r_{mn}).

The local expansion outlined above simplifies the problem considerably from a simulation standpoint. The third dimension has been eliminated, and by restricting the system length in y, "high" poloidal mode numbers are mapped to low y mode numbers. The typical choice $L_y \sim L_x$ (as used in the present test) in the slab model corresponds to roughly 1/6 of the poloidal extent in the toroidal system. If poloidal inhomogeneities can be neglected, this represents a substantial gain in resolution (although the y–modes no longer represent a complete space). However, additional effects such as multiple mode rational surfaces require a third dimension, as studied in the slab model by Sydora *et al.* [11]. Finally, inclusion of the inhomogeneities in θ that are present in a realistic system (such as poloidal coupling and magnetic drifts) necessitate simulation in the full three-dimensional, toroidal system.

The development of an eigenmode equation for the drift wave in the sheared slab will now be briefly considered. The distribution function f_j for

each species satisfies the Vlasov equation

$$\frac{\partial f_j}{\partial t} + \mathbf{v} \cdot \frac{\partial f_j}{\partial \mathbf{x}} + \frac{e}{m_j}\left(\mathbf{E} + \frac{\mathbf{v} \times \mathbf{B}}{c}\right) \cdot \frac{\partial f_j}{\partial \mathbf{v}} = 0 \tag{4.13}$$

For an electrostatic perturbation, we write the distributions, potential, and densities as the sum of equilibrium and perturbed quantities

$$\begin{aligned} f_j &= f_{0j} + f_{1j} \\ \Phi &= \Phi_0 + \Phi_1 \\ n_j &= n_{0j} + n_{1j} \end{aligned}$$

where the equilibrium potential Φ_0 is assumed to be zero, and the densities are calculated from

$$n_j = \int d\mathbf{v}\, f_j(\mathbf{x}, \mathbf{v}, t) \tag{4.14}$$

The linearized Vlasov equation thus gives the zeroth order equation for f_{0j}

$$\mathbf{v} \cdot \frac{\partial f_{0j}}{\partial \mathbf{x}} + \frac{e}{m_j c}(\mathbf{v} \times \mathbf{B}) \cdot \frac{\partial f_{0j}}{\partial \mathbf{v}} = 0 \tag{4.15}$$

and the first order equation for f_{1j}

$$\frac{\partial f_{1j}}{\partial t} + \mathbf{v} \cdot \frac{\partial f_{1j}}{\partial \mathbf{x}} + \frac{e}{m_j c}(\mathbf{v} \times \mathbf{B}) \cdot \frac{\partial f_{1j}}{\partial \mathbf{v}} = \frac{e}{m_j}\frac{\partial \Phi_1}{\partial \mathbf{x}} \cdot \frac{\partial f_{0j}}{\partial \mathbf{v}} \tag{4.16}$$

If equilibrium quantities are assumed to vary slowly on the scale of an ion Larmor radius ρ_i, the equilibrium distribution function can written as

$$f_{0j}(\mathbf{x}, \mathbf{v}) = n_0 \left(\frac{m_j}{2\pi T_j}\right)^{3/2} \left[1 + \epsilon\left(x + \frac{v_y}{\Omega_j}\right)\right] \exp\left[-\frac{v_\parallel^2 + v_\perp^2}{2T_j/m_j}\right] \tag{4.17}$$

where, in the absence of temperature gradients,

$$\epsilon = \frac{1}{n}\frac{\partial n}{\partial x}$$

is the inverse density scale length ($\epsilon\rho_i \ll 1$). It is necessary that the term proportional to ϵ be small compared to unity so that the distribution function f_{0j} satisfies the lowest order equation.

For the slab mode, the inclusion of the full perturbed distribution functions is reasonably straightforward, especially when a numerical solution is being pursued (as for a shooting code method of solution). To simplify the analytical result, however, various fluid approximations are often used. One is to assume the electrons follow the perturbation adiabatically, so that they are described by the Boltzmann distribution. This leads to a perturbed density of the form

$$n_{1e} = \frac{e\Phi_1}{T_e} n_0 \tag{4.18}$$

although in general, the non-adiabatic response $\hat{N}$ must be included as well :

$$n_{1e} = \frac{e\Phi_1}{T_e} n_0 + \hat{N} \tag{4.19}$$

The effect of the non-adiabatic response on the stability of the mode is crucial, as pointed out by Ross and Mahajan [7] and by Tsang *et al.* [8]. The ions, on the other hand, may usually be treated as a fluid—the perturbed density is obtained through the continuity equation, with the $\mathbf{E} \times \mathbf{B}$ drift for the fluid velocity. Since it is straightforward to do so, we use the full kinetic description for both electrons and ions, in order to get as accurate a comparison as possible to the particle simulation.

The formal solution for the perturbed distribution function can now be written as

$$f_{1j}(\mathbf{x}, \mathbf{v}, t) = \frac{e}{m_j} \int_{-\infty}^{0} dt' \, \frac{\partial \Phi_1(\mathbf{x}'_j, t')}{\partial \mathbf{x}'} \cdot \frac{\partial f_{0j}(\mathbf{x}'_j, \mathbf{v}'_j, t')}{\partial \mathbf{v}'} \tag{4.20}$$

where the integration is over the unperturbed particle orbits. These orbits are particularly simple in the slab model, being just the helical orbit of a particle along a constant magnetic field. The constants of motion are therefore $v_\parallel^2$ (energy), $v_\perp^2/B_0$ (magnetic moment), and $x + v_\perp/\Omega_j$ ($= p_y$, the canonical

momentum corresponding to the y coordinate). To solve this equation, we adopt a perturbed potential of the form

$$\Phi_1(\mathbf{x},t) = \hat{\Phi}(x)\,\exp\left\{i\left(k_y y + k_z z\right) - i\omega t\right\} \tag{4.21}$$

In order to perform the integral in Eq. (4.20) we expand the potential in a Taylor series about $x = x'_j$, keeping only terms to second order :

$$\hat{\Phi}(x'_j) \approx \hat{\Phi}(x) + (x'_j - x)\left.\frac{d\hat{\Phi}}{dx'_j}\right|_{x'_j=x} + \frac{1}{2}(x'_j - x)^2\left.\frac{d^2\hat{\Phi}}{dx'^2_j}\right|_{x'_j=x} \tag{4.22}$$

This expansion is valid when the wavelength in x is much larger than the ion Larmor radius. The resulting perturbed distribution function is then integrated over velocity space to get the perturbed densities. Upon neglect of terms on the order of $\omega/\Omega_{e,i}$ and $k_\perp\rho_e$, we have [71]

$$\hat{n}_e = \frac{en_0}{T_e}\left[1 + \zeta_e Z(\zeta_e)\left(1 - \frac{\omega_e^*}{\omega}\right)\right]\hat{\Phi} \tag{4.23}$$

for the perturbed electron density, and

$$\hat{n}_i = -\frac{en_0}{T_i}\left[1 + \zeta_i Z(\zeta_i)\left(1 - \frac{\omega_i^*}{\omega}\right)\Gamma_0(b_i) - \zeta_i Z(\zeta_i)\left(1 - \frac{\omega_i^*}{\omega}\right)\frac{d\Gamma_0}{db}\rho_i^2\frac{\partial^2}{\partial x^2}\right]\hat{\Phi} \tag{4.24}$$

for the perturbed ion density, where $\zeta_j = \omega/2|k_\parallel|v_j$, $v_j = (T_j/m_j)^{1/2}$, $b_i = k_\perp^2\rho_i^2$, $\rho_i = v_i/\Omega_i$, $\rho_s^2 = \tau\rho_i^2$, $\tau = T_e/T_i$, $\Gamma_0(b_i) = I_0(b_i)\exp(-b_i)$, where I_0 is the modified Bessel function, and Z is the plasma dispersion function. The diamagnetic frequencies can be written in a convenient dimensionless form as

$$\frac{\omega_e^*}{\Omega_i} = -\tau\frac{\omega_i^*}{\Omega_i} = (\kappa\rho_s)(k_\perp\rho_s)$$

where κ is the inverse density scale length. A detailed derivation of the plasma response, with a close examination of the approximations involved, is given by Davidson and Kammash [72].

If we now assume that the perturbation is quasineutral, that is, $\hat{n}_e \approx \hat{n}_i$, the eigenmode equation takes on the form

$$\left[\rho_s^2 \frac{d^2}{dx^2} + Q(x,\omega)\right] \hat{\Phi} = 0 \tag{4.25}$$

where

$$\begin{aligned} Q &= \left[-\zeta_i Z(\zeta_i)\left(1 - \frac{\omega_i^*}{\omega}\right)\frac{d\Gamma_0}{db}\right]^{-1} \\ &\cdot \left\{\left[1 + \zeta_e Z(\zeta_e)\left(1 - \frac{\omega_e^*}{\omega}\right)\right] + \tau\left[1 + \zeta_i Z(\zeta_i)\left(1 - \frac{\omega_i^*}{\omega}\right)\Gamma_0(b_i)\right]\right\} \end{aligned} \tag{4.26}$$

This equation is solved subject to the appropriate boundary conditions, that is, outgoing waves at $x = \pm\infty$. This is represented by the WKB condition

$$\hat{\Phi}(x) \sim \exp\left\{\pm \int^x dx' \, [Q(x')]^{1/2}\right\} \tag{4.27}$$

for large $|x|$. Since this formulation is symmetrical about the mode rational surface ($x = 0$), the equation is solved in the half-space between $x = 0$ and $x \to +\infty$, requiring the specification of even or odd parity about $x = 0$ for the additional boundary condition. The technique employed for solving Eq. (4.25) is to "shoot" inward from a large value of $|x|$, using a variable step two-point ODE solver. The initial guess for ω is supplied by the user. A complex rootfinder is employed to match the integrated solution with the boundary condition at $x = 0$. If convergent, the rootfinder will produce an eigenvalue ω of the above equation. (For asymmetric equations, one must shoot from both positive and negative infinity and attempt to match the two numerical solutions at the origin.)

4.2.3 Simulation results

For the simulation of the drift wave in the slab model, we adopt the configuration in which the mode rational surface is placed in the center of the

simulation region. Although this placement reduces the number of particles in the region of interest (because of the need to maintain the density profile), possible boundary effects are avoided. Some discussion on the choice of parameters is warranted here, with attention to the validity of the theoretical eigenmode equation given by Eq. (4.25).

A simulation model in which the particle quantities are advanced explicitly is subject to the timestep constraint

$$\omega_{\max}\delta t \lesssim 2 \tag{4.28}$$

where $\omega_{\max}$ is the maximum frequency found in the system. If the timestep exceeds this criterion, numerical instability may occur [21], although in practice the timestep must be much smaller for energy conservation to remain acceptable (typically we employ $\omega_{\max}\delta t \sim .2$). For the present system, in which the fast electron gyromotion has been removed, the maximum frequency is approximately given by

$$\omega_{\max} = \max\left(\frac{k_{\|}}{k}\omega_e,\, \Omega_i\right) \tag{4.29}$$

that is, the larger of the magnetized plasma wave frequency and the ion cyclotron frequency. In a typical simulation we have $k_{\|}/k \sim k_{\|}/k_{\perp} \sim 0.1$, and $\Omega_i/\omega_e \sim 0.1$, so that these two frequencies are equally restrictive of the timestep. An additional restriction is the Cherenkov condition, that is, the particles cannot move more than one cell length in a timestep. (This is typically a concern for parallel motion of electrons along the field lines.) Violation of this condition decreases the accuracy of the shorter wavelength modes, since the particle may travel a substantial fraction of one wavelength in a given timestep. This will also have a detrimental effect on energy conservation. Finally, we require that the ion resonance layers are contained within the simulation region.

The constraints in selecting an appropriate parameter regime limit the size of a timestep substantially, which limits the time scales one can observe. These constraints give impetus to the development of more sophisticated time advancement schemes, such as the implicit [18] or gyrokinetic [73] algorithms. In an explicit model, we adopt small mass ratios ($m_i/m_e = 100$ in the present series of runs), and relatively large Debye lengths ($\lambda_e \sim \rho_i$) in order to observe the desired time scales. The diamagnetic frequency, which can be written as

$$\omega^*/\Omega_i = (\kappa\rho_s)(k_\perp\rho_s) \tag{4.30}$$

can be increased by increasing $\kappa\rho_s$, while still maintaining physically interesting values of $k_\perp\rho_s$. The increase in the diamagnetic frequency must be balanced by the increase in the ion thermal velocity in order to keep the ion resonance layers within the system.

Given the parameter choices discussed above, the slab particle simulation model can achieve the necessary time scales for study of the drift wave problem without fundamentally altering the physics. This was demonstrated by Sydora *et al.* in reproducing the linear drift wave eigenmode. Further, the approximations leading to Eq. (4.25) are not violated, and the actual simulation parameters are used for solution by the shooting code. One concern may be the Taylor series expansion of the perturbed potential, Eq. (4.22), especially for large values of $k_\perp\rho_i$, for which the eigenfunction becomes very localized in x (and the wavelength may become comparable to the ion Larmor radius, contrary to assumption). This case has been studied theoretically by a variational method, in which the perturbed potential is expressed as a sum of basis functions, and the resulting matrix equation inverted to obtain the eigenvalue [74,75]. This improved analysis was found to have only a small effect on the frequency, but modified the eigenmode shape substantially in the region $|x| \leq \rho_i$

[75].

The simulation of the slab drift wave was performed using the two-dimensional, slab limit of the toroidal particle code. A weakly nonuniform grid in x was employed to improve the resolution about the mode rational surface, but this was limited by the need to keep the number of particles per cell reasonable (as discussed in section 2.3). The density profile used in the simulation run was exponential, given by

$$n(x) \sim n_0 \exp(-\kappa x) \tag{4.31}$$

with κ the constant inverse density scale length. The grid schematic, density versus u, and number of particles per cell versus the cell number is shown in Figure 4.10. The remaining simulation parameters are given by : $N_p = 49152$ (number of particles in each species), $L_x = L_y = 64\,\Delta_0$ (Δ_0 is the average grid spacing in x), $N_x = N_y = 64$, $\Delta t = 2.0\,\omega_e^{-1}$, $v_{th} = 2.5\,\Delta_0\omega_e^{-1}$, $T_e/T_i = 1$, $m_e/m_i = 0.01$, $\Omega_e/\omega_e = 10$, and particle "size" of a grid spacing in both x and y (using two passes of the binomial digital filter in x). The shear and density scale lengths are given by $L_s/L_n = 13.6$, $\kappa\rho_i = 0.17$, with $\rho_i/\Delta_0 = 2.5$. The mode rational surface is at $u = 0$, where $u = x - L_x/2$ ranges from $-L_u/2$ to $+L_u/2$. The condition that the ion resonance layers remain within the system is given by the condition that $|u_i| \leq L_u/2$, where u_i is given by the resonance condition $\omega = k_\parallel(u_i)\,v_i$. Since the drift wave frequency is smaller than the diamagnetic frequency, this will be satisfied if $\omega^* = k_\parallel(u_i)\,v_i$. Thus, we have

$$|u_i(\omega)| < |u_i(\omega^*)| = \frac{\omega^* L_s}{k_y v_i} \tag{4.32}$$

$$= \rho_i \frac{L_s}{L_n} \tag{4.33}$$

For the current parameters, $u_i(\omega^*)$ lies just outside the simulation region. However, since the ion finite Larmor radius effects reduce the drift wave frequency,

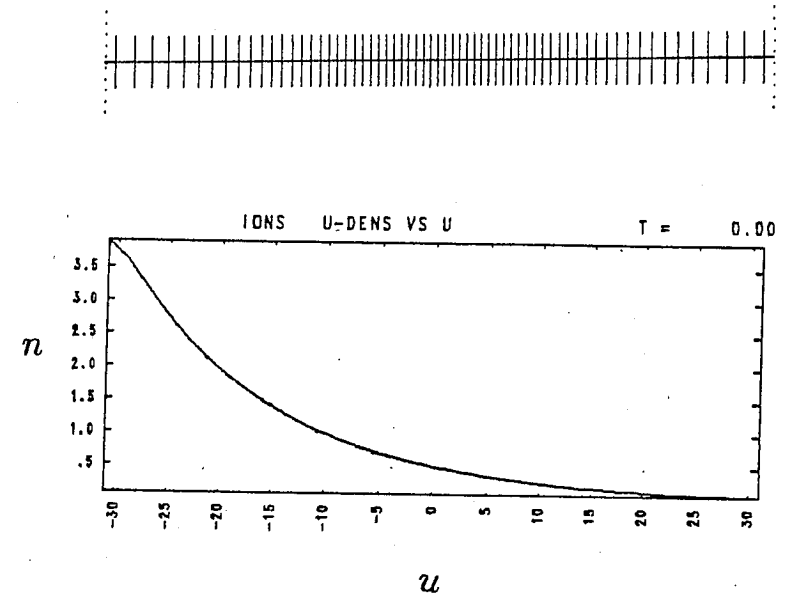

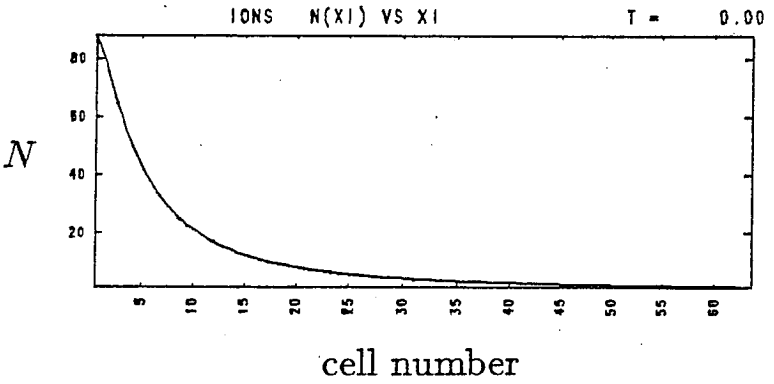

Figure 4.10: Nonuniform grid, density, and number of particles per cell for the slab drift wave simulation.

the actual ion resonance criterion (in terms of ω), will usually be satisfied. This condition will be reexamined in light of the simulation results.

The energy for the run was conserved to within 0.3% for 6000 time steps. The first five modes (in y) of the potential $\Phi(x, k_y)$ was stored for analysis. Note that the $k_y = 0$ mode was excluded from the run entirely; this mode is often unphysically large due to fluctuation effects in the profile loading. Further, the relaxation mechanisms for the reduction of this mode are limited in the electrostatic model, and the resulting enhanced fluctuation level may affect the drift wave at higher mode numbers. For $k_y = 2\pi m/L_y$, with $m = 1, \ldots, 5$, we have

$$k_y \rho_i = 0.24,\ 0.49,\ 0.74,\ 0.98,\ 1.23$$

for the five modes examined. The plasma frequency is obtained by the maximum entropy method (cf. section 3.1.2), and the spectral density at the radial position of greatest power is shown for each mode in Figures 4.11–4.12. The location of the theoretical frequency (obtained via the shooting code solution of Eq. (4.25)) is indicated by an arrow.

For each mode, we observe a peak in the power spectrum close to the theoretically predicted frequency, persisting over much of the simulation region (radially). As the mode number is increased, the signal to noise ratio becomes smaller, which probably results from the smaller frequency (reducing the number of observed periods). The variation of real frequency with mode number is plotted in Figure 4.13 with the simulation values shown.

The theoretical and observed frequencies for the $m = 3$ and $m = 5$ modes agree within the accuracy of the spectral estimator, and frequencies for the remainder agree within a factor of two. The discrepancy in the frequency for

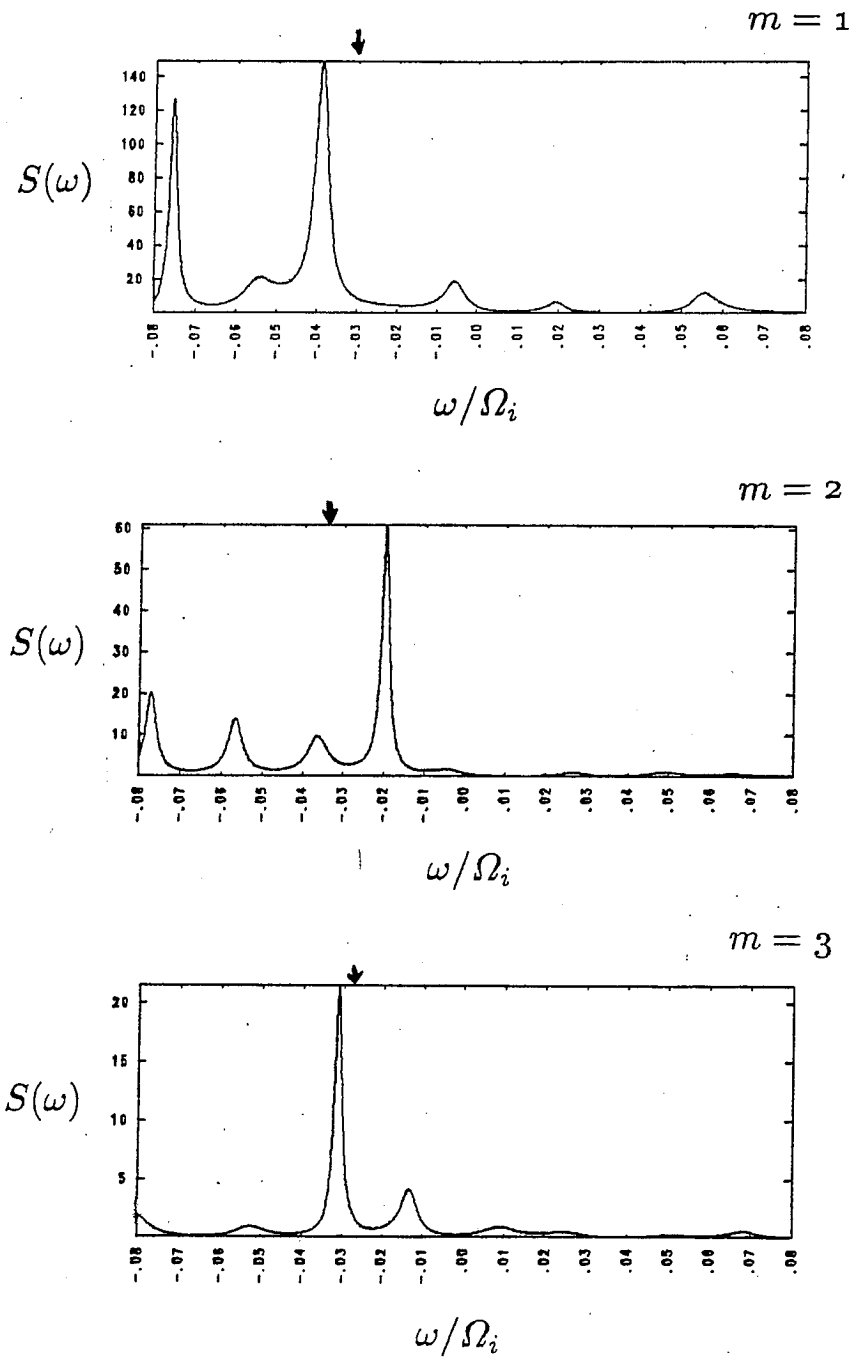

Figure 4.11: Plot of spectral density for the $m = 1, 2, 3$ modes using the maximum entropy method.

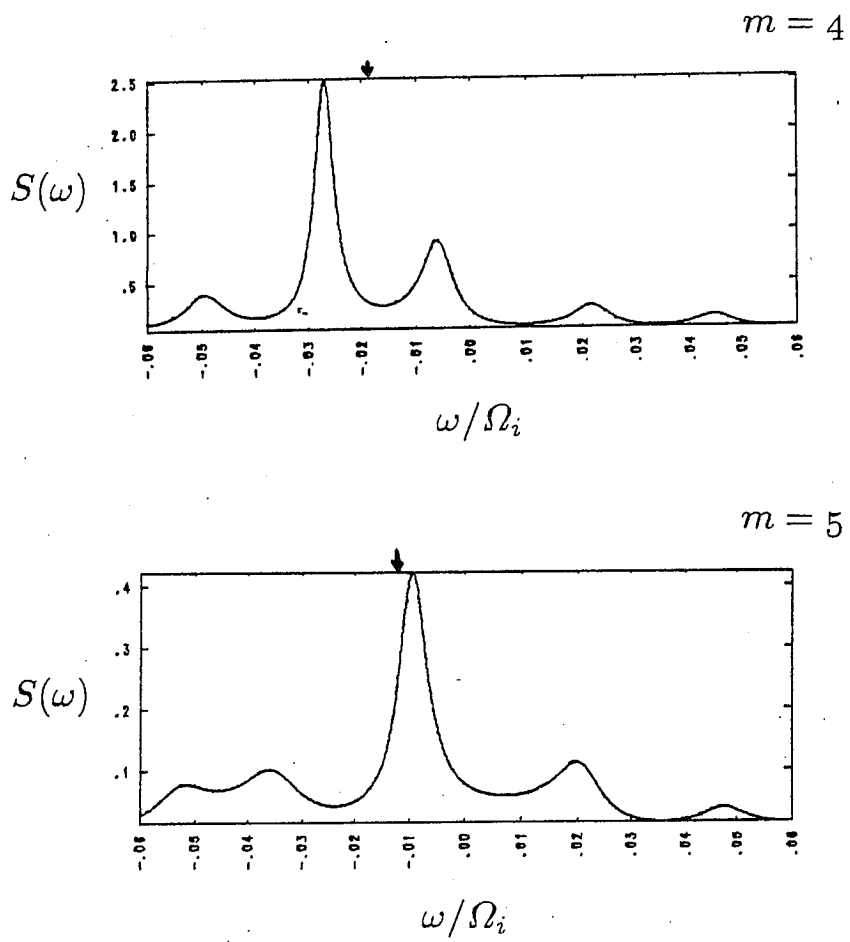

Figure 4.12: Plot of spectral density for the $m = 4, 5$ modes using the maximum entropy method.

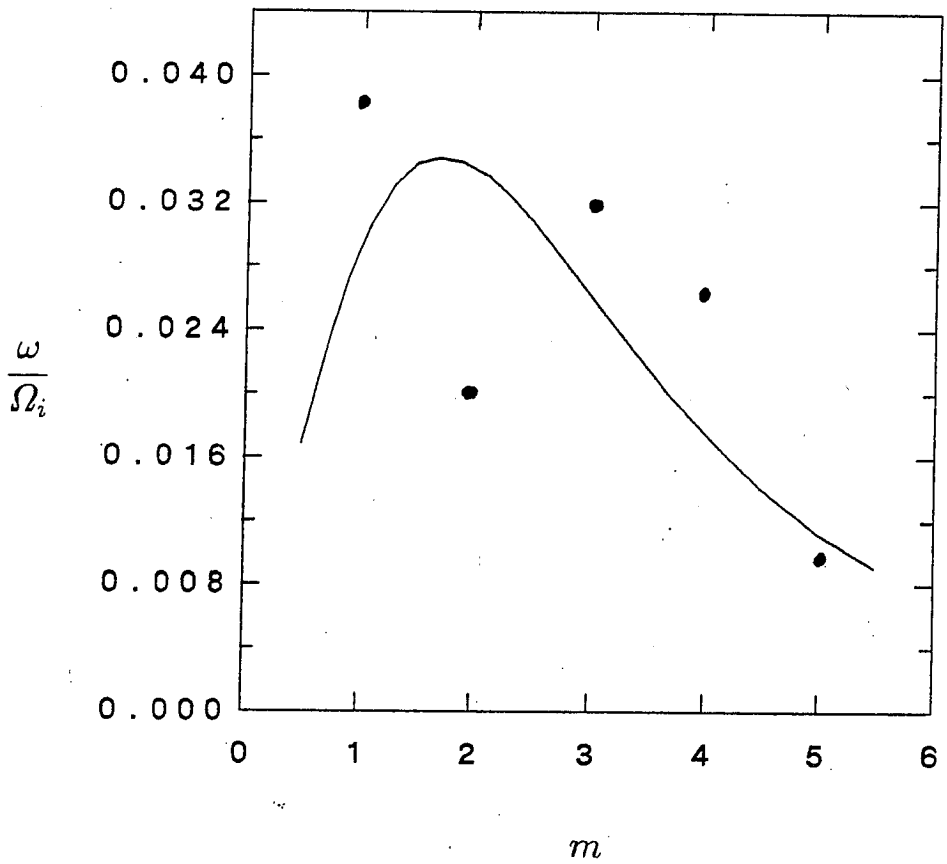

Figure 4.13: Plot of real frequency versus m. The theoretical value is given by the solid line, and simulation values by dots.

the $m = 1$ mode may be due to the interference of the simulation boundaries. In this case, the ratio of the observed mode frequency to the diamagnetic frequency is 0.93, which brings the ion resonance layer only marginally within the system. For the higher m modes, ω/ω^* is greatly reduced, so that the mode is more localized and boundary effects eliminated. This localization can be seen from the spatial structure of the modes (discussed below). In general, differences in the observed frequency from the theoretical result may be partially due to the neglect of significant terms in the theory; the relatively small number of particles in the profile to the outside of the mode rational surface may also play a role.

We turn now to an examination of the spatial structure of the eigenmodes. Using the frequency obtained by spectral analysis, the interferogram method (cf. section 3.1.3) gives estimates for the time-averaged eigenfunctions. We point out that this diagnostic is limited by the finite sample length (so that the filtering is imperfect), and temporal effects, such as damping and recurrence. The latter may cause the signal to become out of phase with the original mode [56], leading to interference (in the diagnostic) and distortion of the eigenfunction shape. In addition, the interfered potential is arbitrary by a phase factor $e^{i\varphi}$, which makes theoretical comparison more difficult.

No parity was forced about the mode rational surface in the simulation, so the eigenfunction is separated into its odd and even components in the post-processor to give simpler comparison to the theoretical eigenfunctions. Although the even parity mode and the odd parity mode are technically not degenerate, the frequencies are so close that spectral analysis can resolve only one signal. The frequency obtained will be sufficient for input to the interferogram for either mode.

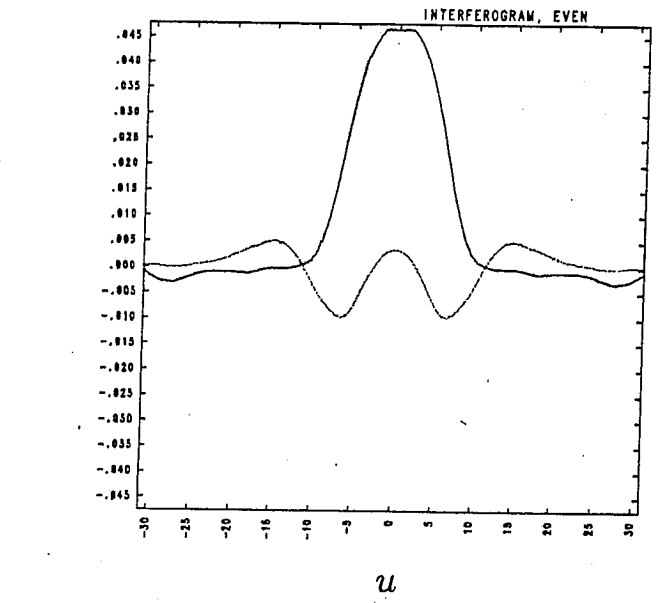

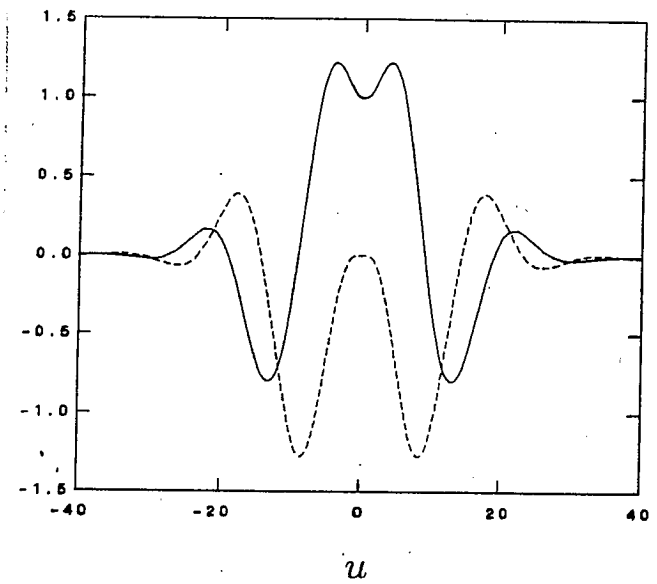

Figure 4.14: Interfered potential for the $m = 2$ even mode (top), and theoretical eigenfunction (bottom). The solid lines represent the real parts and the dashed (or dotted) lines represent the imaginary parts.

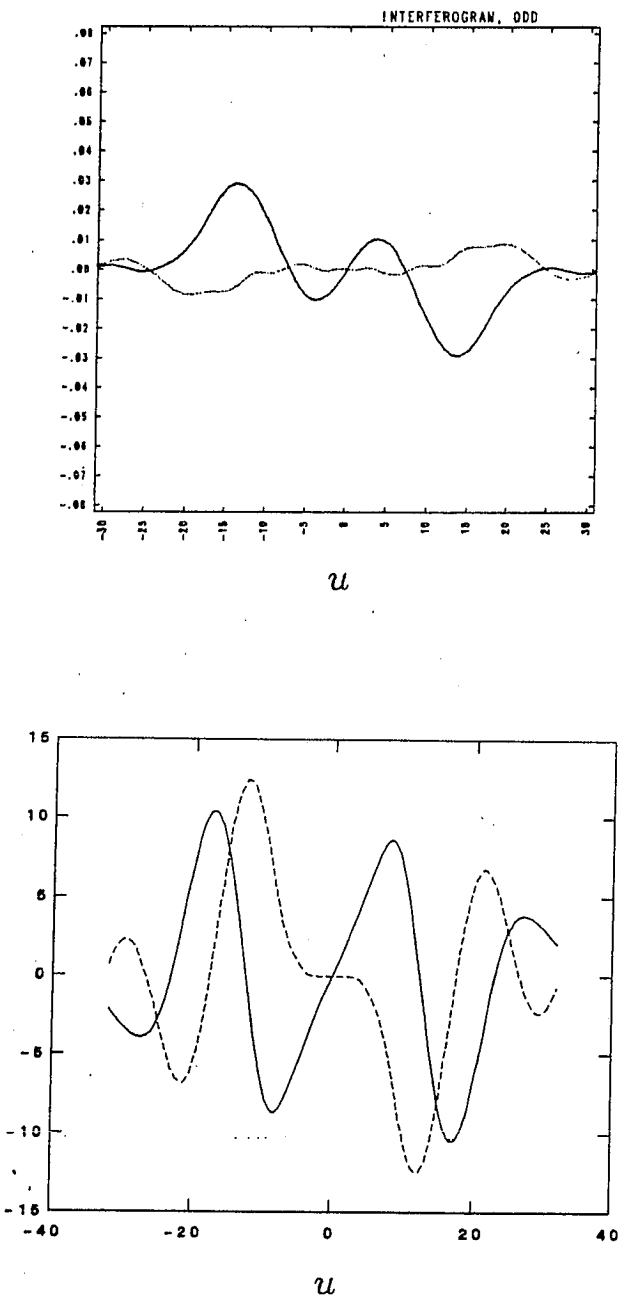

Figure 4.15: Interfered potential for the $m = 1$ odd mode (top), and theoretical eigenfunction (bottom). The solid lines represent the real parts and the dashed (or dotted) lines represent the imaginary parts.

The interfered potential for each mode displays a marked increase in amplitude near the mode rational surface, which is typical of the drift wave eigenmode. For larger values of m the signal/noise ratio is again observed to decrease. In general, both the even and odd parity modes are observed, though the odd parity mode is usually substantially weaker than the even parity mode for most of the mode numbers. This is expected, due to the greater damping for the odd parity mode. The interfered potential for the $m = 2$ even mode is shown at the top of Figure 4.14, with the theoretical eigenfunction shown at bottom (obtained through use of the shooting code). In Figure 4.15 the interfered potential for the $m = 1$ odd mode is given, along with the theoretical result. Both of these show good qualitative agreement with the theoretical result. (The reduced strength of the imaginary part of the odd mode may be caused by the interference effects discussed above, in light of the greater damping of the odd mode.)

In general, the interferograms are somewhat less oscillatory than the theoretical eigenfunctions (perhaps also caused by interference effects). In addition, the signal strengths show only a slight rise away from the mode rational surface, compared with the strong localization away from the mode rational surface seen in the theoretical result (which results from the "anti-well" near the mode rational surface). This behavior is seen most clearly by examining the amplitude of the eigenfunctions, which is shown for the even parity component of modes $m = 1$ through $m = 4$ in Figures 4.16–4.17, along with the theoretical result. Plots involving the amplitude are better suited for theoretical comparison, since the amplitude is free of the arbitrary phase factor and interference effects discussed above. The cause of the discrepancy near the mode rational surface is likely due to a lack of resolution, but inaccuracy in the theoretical eigenmode equation (from violation of the $k_x \rho_i \ll 1$ assumption)

Simulation Theory

$m = 1$

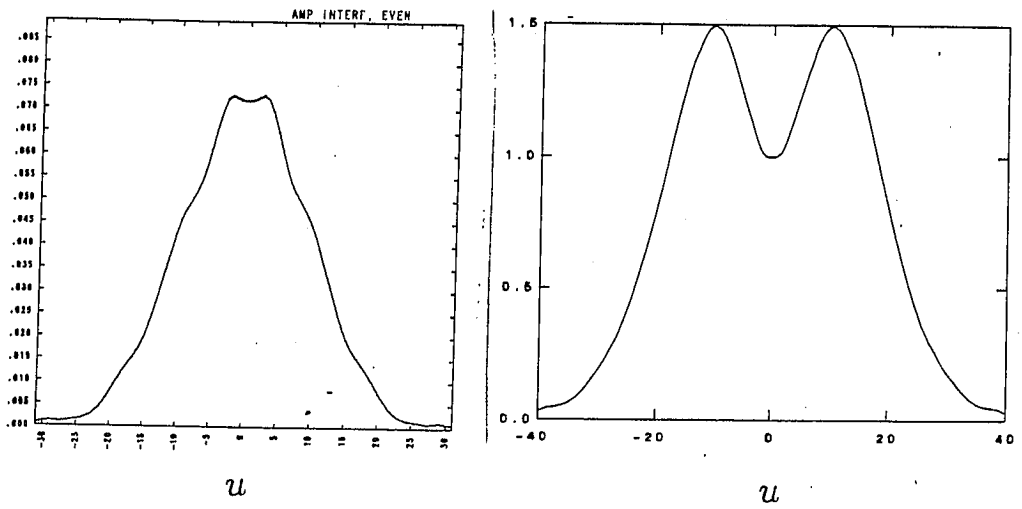

u u

$m = 2$

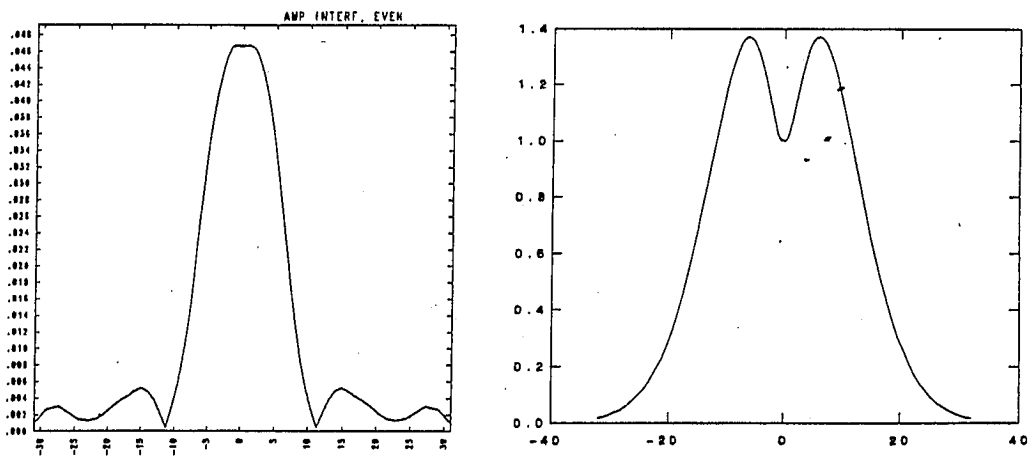

u u

Figure 4.16: Plot of amplitude of interfered potential for the even, $m = 1, 2$ modes, along with the theoretical result.

Simulation Theory

$m = 3$

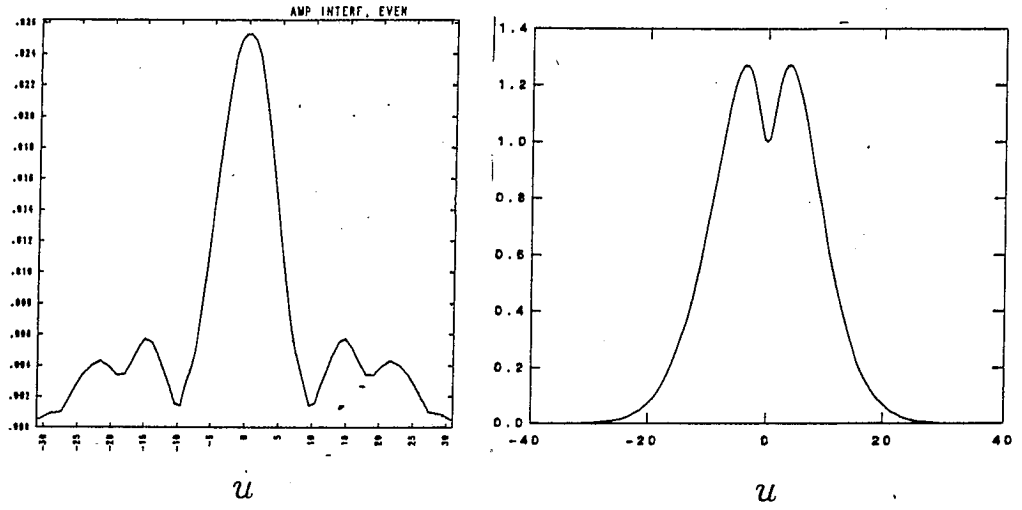

$m = 4$

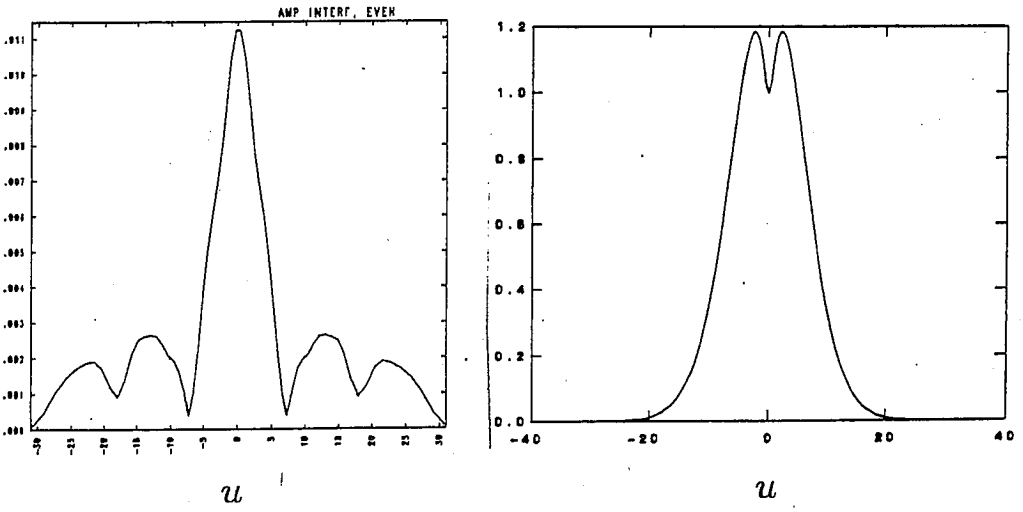

Figure 4.17: As previous, but for the $m = 3, 4$ modes.

is a possibility. The localization of the modes roughly follow the theoretical expectation, as seen from the plots. Finally, the decrease in the amplitude of the $m = 1$ interfered potential towards the boundaries indicates that the ion resonance condition is reasonably well satisfied, though boundary effects may still be a factor.

4.3 Drift waves in toroidal geometry

4.3.1 Introduction

The shear stabilization of the drift wave in the slab model is fundamentally altered by spatial inhomogeneities encountered in a toroidal system, as was pointed out by Taylor [13] in 1977. In a toroidal configuration, the magnetic fields have a strong variation with the poloidal coordinate θ, and the Laplacian operator itself has θ-dependent terms. This results in coupling between the drift wave eigenmodes at neighboring mode rational surfaces, which can inhibit the convection of energy. Since it is this convection that is primarily responsible for the stabilization of the mode in the slab model, the stability properties of the drift wave are substantially modified.

The model employed by Taylor [13] was that of a plane slab, in which the magnetic field strength or shear varied strongly in the "poloidal" direction (represented here by the y coordinate). This variation coupled the poloidal Fourier components, resulting in a differential-difference equation in the (x, y) coordinates. The electron response was assumed to be adiabatic, and the fluid ion response was used. The assumption that the variation with poloidal mode number (m) was weak allowed m to be approximated as a continuous quantity, the so-called "strong-coupling" approximation. This leads to a differential equation in terms of a single variable, expressed in terms of a combination of

both x and m. The main conclusion of this work was that the shear damping normally associated with the drift wave is severely reduced, resulting in a mode that is radially extended over an appreciable length of the plasma (in contrast to the slab-like drift mode, which is very localized around the mode rational surface).

The nullification of the shear damping of the drift wave in a toroidal system was subsequently explored by a number of researchers, using more realistic theoretical models. The radially extended nature of the mode was verified by Ross and Miner [76], using a finite element method to solve the differential equation for the coupled Fourier components of the perturbed potential. The two-dimensional eigenmode equation in a toroidal configuration was considered by Horton *et al.* [77], who obtained solutions in both the weak-coupling and strong-coupling limits. Subsequent research efforts [78,79,14,80,81,82] have employed the ballooning mode representation to express the perturbed quantities, in order to rigorously satisfy periodicity in both θ and ϕ. With this approach, the validity of the solution spans the range from weak to strong coupling. The majority of the research efforts, however, have not pursued a fully kinetic treatment (represented in the nonadiabatic particle response).

The published literature on the toroidal drift wave problem shows a great deal of variation in the handling of the particle response, which is a consequence of the complexity of these terms in toroidal geometry. Adiabatic electrons and fluid ions are often employed, perhaps with the addition of a destabilizing trapped electron response term. This approach is sufficient for investigating the qualitative character of the mode, including its radially-extended ballooning character. However, the importance of the full kinetic effects on the stability is hard to gauge. A formal expression of the full particle

response was given in 1980 by Connor *et al.* [83], but the expressions must undergo considerable approximation before solution is possible. If nonadiabatic terms are kept, the manner of solution will necessarily employ either an integral formulation or an iterative method, which makes theoretical analysis much more difficult.

The nonadiabatic electron passing response was included perturbatively by Chen and Cheng [14] and via an integral method by Hesketh [82]. Each of these papers employed kinetic ions (under the assumption $\omega \gg \omega_{D_i}$) and obtained qualitatively similar results. The growth rate was found to increase without bound as $k_\perp \rho_i$ is increased, as well as with increasing toroidicity (measured by the parameter $\epsilon_n = L_n/R_0$). For the parameters studied by Hesketh, the mode reached a maximum growth for a shear of $\hat{s} \sim 1.7$. The neglect of the ion drift resonances, however, is not justified at larger values of $k_\perp \rho_i$, since the real frequency decreases as this parameter increases. The inclusion of this resonance proves to be an important stabilizing effect, as was shown by subsequent papers [15,16,17]. The result is that the growth is maximized at a value of $k_\perp \rho_i \sim 0.3$–0.4.

To date, the most complete theoretical treatment to date of the toroidal drift wave problem, including the nonadiabatic electron response and ion drift resonance, is found in a paper by Schep and Venema [17]. This investigation was based on the earlier work of Schep *et al.* [84], which considered approximate forms for the integral trapped and passing electron responses. It was found that when both response terms are kept, large cancellations may occur, and the total response gives the proper behavior when one passes to the infinite aspect ratio limit (plane slab). When this was applied to the drift wave problem [17], along with the inclusion of the ion drift resonance, the

real and imaginary frequency variation was found to be qualitatively similar to that predicted by Cheng and Tsang [15] and by Hesketh [16]. In seeking theoretical comparison for the toroidal drift wave simulation, we therefore choose parameters similar to those studied by Schep and Venema [17].

An additional point discussed in the literature concerns the relation of the toroidicity-induced mode to the slab-like mode, as the toroidicity (i.e. ϵ_n) is increased. In the work of Hastie *et al.* [78] and Choi and Horton [79], the slab mode was observed to evolve continuously into the toroidal mode, but was found to be a completely different branch by Chen and Cheng [14]. The apparent conflict between these observations was resolved in a separate investigation by Schep and Venema [85], where it was shown that the slab mode always connects to one of the harmonics of the toroidicity-induced mode. (This is usually one of the higher, more heavily damped harmonics, depending on parameters. The same point was discussed briefly in Ref. [82]).

The appearance of multiple drift wave harmonics in toroidal geometry can be understood by analogy to solid state physics. If the radial variation of the equilibrium quantities is sufficiently weak, the potential will be symmetric with respect to a translation in the radial coordinate (with the exception of a possible phase shift). This situation admits solutions which are Bloch functions and results in a band structure for the eigenvalues known as the Brillouin effect. Similarly, the toroidal drift wave eigenmode equation admits a number of solutions in terms of multiple harmonics, resulting from the additional degrees of freedom in the presence of multiple mode rational surfaces. Although the fundamental harmonic will have the strongest growth (or least damping), the higher harmonics may be unstable or only weakly damped as well. However, the higher order harmonics are usually not considered in the theory. Depending

on parameters, the slab-like mode may connect to the lowest even harmonic (as observed in the earlier papers) or, more usually, to a higher even harmonic. Parameter studies in Ref. [85] were presented in which the slab-like mode connected to the $n = 6$ or $n = 8$ toroidicity-induced mode.

4.3.2 Theory

In this section, we briefly consider the theoretical treatment of the toroidal drift wave problem, with an emphasis on understanding and qualitative behavior. Formally, the procedure is the same as in the slab problem. The particle distributions are assumed to satisfy the Vlasov equation, in which the lowest order distributions represent the equilibrium solutions. For an electrostatic perturbation, the perturbed distributions are obtained via a time integral of the electrostatic potential and zeroth order distributions, with the particles following their unperturbed orbits. (The velocity distributions are usually assumed to be Maxwellian.) The perturbed densities are obtained by velocity space integration, and the quasineutrality condition gives an (integral) equation for the potential.

In the slab analysis, the integral equation for the potential is usually approximated as a differential equation of a single variable. In this case, the integral term is evaluated via the Taylor expansion of the potential (in x), which is valid for sufficiently small radial wavenumber ($k_x \rho_i \ll 1$). For the toroidal problem, however, two difficulties appear. First, the perturbed quantities must be a function of both r and θ due to the poloidal inhomogeneities. This leads to a partial differential equation of two variables, which is generally much more difficult to solve than a one-dimensional equation. Second, an integral term will be necessary in the toroidal problem to retain the nonadiabatic particle

responses. This occurs due to the increased complexity of the particle motion, which cannot be given in a simple, closed form. The perturbed distribution functions can be obtained through adoption of gyrokinetic coordinates [83]; however, the resulting expressions are very complicated and do not exist in closed form. Although approximate forms of the perturbed distributions exist [83,84], the subsequent velocity space integrations (to give the perturbed densities) present additional difficulties.

We will therefore consider a simplified model which retains many of the features of a more careful treatment. (The analysis pursued here follows Refs. [78] and [86]; also see Ref. [79].) The fluid ion response is adopted, and an electron response of the form

$$n_e = n_0 \left(\frac{e\Phi}{T}\right)(1 - i\delta) \tag{4.34}$$

where δ is some (unspecified) operator that governs the nonadiabatic electron response. The perturbed potential is written in the form

$$\phi(\theta, \rho) \exp\left[i(N\zeta - M\theta) - i\omega t\right] \tag{4.35}$$

where $\rho = r - r_0$ is the radial distance from the mode rational surface given by $M = Nq(r_0)$, with q the safety factor, and N the toroidal mode number. The toroidal dependence can be dropped by axisymmetry, and the resulting eigenvalue problem takes on the general form

$$\mathcal{L}(\theta, \rho; \omega)\, \phi(\theta, \rho) = 0 \tag{4.36}$$

The operator $\mathcal{L}$ is in general an integral operator, which is represented by the $i\delta$ operator in this analysis. With some approximation, $\mathcal{L}$ can be given by

$$\mathcal{L} = \frac{\partial^2}{\partial x^2} - \sigma^2 \left(\frac{\partial}{\partial \theta} + ix\right)^2 - \epsilon \left(\cos\theta + is \sin\theta \frac{\partial}{\partial x}\right) - \lambda \tag{4.37}$$

where $k = nq/r$, $s = rq'/q$, $x = k\rho s$, and the parameters σ and ϵ are given by

$$\sigma = \frac{\epsilon_n}{q\tau bs}, \qquad \epsilon = \frac{2\epsilon_n}{\tau bs^2} \tag{4.38}$$

where ϵ_n is the toroidicity ($= L_n/R_0$) and $b = k^2\rho_i^2$. The eigenvalue λ is related to the frequency by

$$\lambda = \frac{\omega/\omega^* - 1 + b(1+\tau) - i\delta}{bs^2(1+\tau)} \tag{4.39}$$

(Note that in Ref. [86] an additional term was included, resulting from the variation of ω^* with radius.)

For the drift wave problem, the modes of interest have long parallel wavelengths and short perpendicular wavelengths. The requirement of long parallel wavelength is given as

$$\mathbf{B} \cdot \nabla\Phi \approx 0 \tag{4.40}$$

This condition is well satisfied in the present analysis only when $q(r) = M/N$, that is, when at a mode rational surface. Alternately, we can adopt an eikonal form of the perturbed potential as

$$\Phi(r,\theta)\exp\left(iS(r,\theta,\zeta)\right) \tag{4.41}$$

such that

$$\mathbf{B} \cdot \nabla S(r,\theta,\zeta) = 0 \tag{4.42}$$

This representation satisfies the long wavelength requirement, but the resulting functions $\Phi(r,\theta)$ and $S(r,\theta,\zeta)$ are periodic in theta only at a mode rational surface. The dual requirements of periodicity and long parallel wavelength can be satisfied through use of the ballooning mode representation for the perturbed potential [87,88]. We then make the expansion

$$\Phi(\theta,x) = \sum_{n=-\infty}^{+\infty} \exp(-in\theta) \int_{-\infty}^{+\infty} d\hat{\theta}\, \hat{\Phi}(\hat{\theta},x)\exp(in\hat{\theta}) \tag{4.43}$$

where the dependent coordinate in the poloidal direction has become $\hat{\theta} = \theta + 2\pi n$ (the "extended" poloidal variable), and $\hat{\Phi}$ is given by

$$\hat{\Phi}(\hat{\theta}, x) = A(x) \exp\left[-ix(\hat{\theta} + \theta_k)\right] f(\hat{\theta}, x) \tag{4.44}$$

Here $A(x)$ is a slowly varying envelope for the mode, and $f(\hat{\theta}, x)$ satisfies to lowest order a one-dimensional eigenmode equation in the extended variable $\hat{\theta}$, for x fixed. (Here, θ_k is a slowly varying function of radius, and is not specified to the lowest order.) The lowest order eigenmode equation in the toroidal model is given in terms of a poloidal variable, compared to a radial equation in the slab model. This occurs as a result of the poloidal inhomogeneities, which dominate the weaker radial dependence. The radial dependence in the present model can be obtained via a radial eigenmode equation to higher order in the expansion parameter $1/N$.

With inclusion of the nonadiabatic response terms (and ion drift resonances), the equation for $f(\hat{\theta}, x)$ takes on the general form

$$\left[\frac{d^2}{d\hat{\theta}^2} - V(\hat{\theta}, \omega)\right] \alpha(\hat{\theta}, \omega)\, \hat{\Phi} = \int d\hat{\theta}'\, K(\hat{\theta}, \hat{\theta}'; \omega) \tag{4.45}$$

(after Schep and Venema [17]). The method of solution for Eq. (4.45) in Ref. [17] employed a shooting code for solution of the homogeneous equation (initially neglecting the integral term); the perturbed potential $\hat{\Phi}$ was then numerically integrated to obtain the right hand side as part of an iteration procedure. Where possible, the full plasma dispersion function was employed.

This theoretical procedure predicts the existence of unstable solutions. The most unstable mode is the lowest harmonic ($n = 0$), and is the only harmonic considered. The ion drift resonance has a stabilizing influence on the mode, so that the perpendicular wavenumber of maximum growth occurs at about $k_\perp \rho_i \sim 0.2$, for system parameters of $\hat{s} = q = \tau = 1$, $\epsilon_n = 0.1$,

$m_i/m_e = 1836$ and $\epsilon = 0.1$ (inverse aspect ratio). For comparison purposes, these parameters were duplicated as closely as possible in the simulation, but numerical constraints prevent an exact match (most significantly in the mass ratio). Furthermore, the need to maintain adequate radial resolution ensures that the equilibrium quantities will vary significantly over the width of the mode. The varying quantities in the simulation are the shear ($\hat{s}$), toroidicity (ϵ_n), and diamagnetic frequency (ω^*). The variation of the equilibrium quanties in the simulation may require the higher order equation for the radial dependence to be solved, in order for close correspondence with theory. In addition, the theory is strictly valid only in the limit of high toroidal mode number; the relative smallness of the toroidal mode number in the simulation ($n = 9$) may require calculation to higher order.

The effect of varying the diamagnetic frequency has been examined by Connor and Taylor [86]; it is shown that a decrease in the strength of coupling between modes at neighboring mode rational surfaces will result. This coupling crucially determines the qualitative nature of the mode. For very weak coupling, the Fourier modes at neighboring mode rational surfaces are nearly independent and are radially localized, as in the slab limit. These modes possess weak "sidebands" on neighboring mode rational surfaces, which become stronger as the coupling is increased. For sufficiently strong coupling, the Fourier modes sum to become a single "quasimode", which extends over many mode rational surfaces. The quasimode tends to be localized in θ, so that it may appear to "balloon" towards the outside of the torus. The parameter regime considered by the simulation does produce the theoretically predicted ballooning behavior, although effects due to the variation of ω^* may also be present.

4.3.3 Simulation results

Simulation in the toroidal configuration employs a single toroidal mode number, $n = 9$. This choice is necessary to allow many coupled poloidal harmonics, given a physically plausible safety factor (q). The mode rational surfaces contained within the system range from $q = 0.56$ ($m = 5$) to $q = 1.67$ ($m = 15$). The safety factor thus varies from about 0.5 at the origin, to about 4.0 at the outer boundary. The MHD constraints on q are inapplicable to this simulation, since the magnetic fields are static. Undesired mode rational surfaces are excluded by eliminating the appropriate Fourier components of the electric potential. The slab-like drift ion resonance layers will therefore be contained within the simulation region for each mode rational surface, satisfying the stability constraint. Although actual tokamak plasmas will unavoidably contain mode rational surfaces for which the ion resonance layer is absent (near the edge or the magnetic axis), this occurs for no more than about 20% of the radial extent (TEXT parameters). Thus it is reasonable to require that all of the ion resonance layers be within the simulation region.

The use of such high mode numbers (high by particle simulation standards) necessitates a fairly large number of particles—nearly 100,000 for each species. These are well distributed throughout the region of interest for the gaussian density profile employed. This allows the use of a highly nonuniform radial grid, while keeping an acceptable number of particles per cell (as discussed in section 2.3). The number of particles per cell as a function of cell number is shown in Figure 4.18, along with the radial variation of the initial electron density and the variation of grid spacing in r. The marks above the nonuniform grid ticks indicate the locations of the mode rational surfaces. The electron/ion profiles have been loaded in the manner discussed in section 4.1.

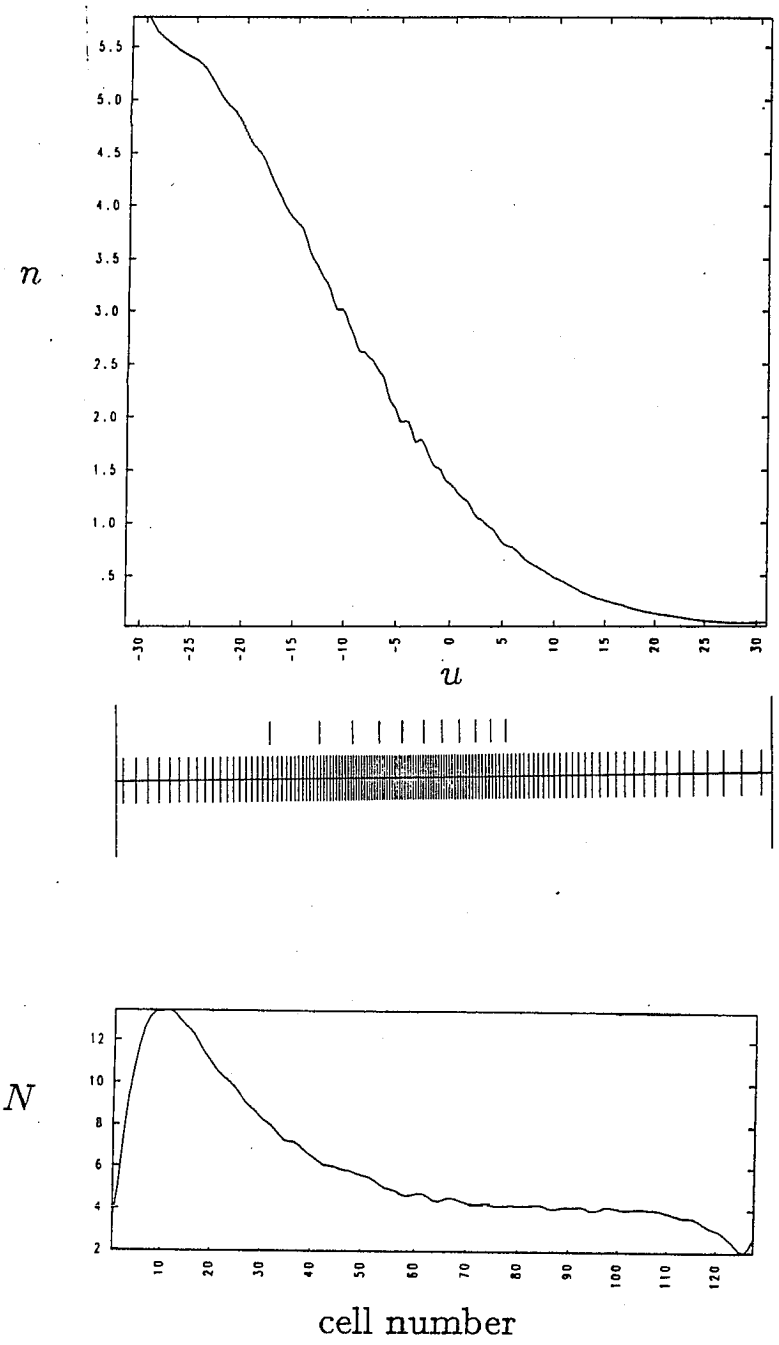

Figure 4.18: Initial electron density profile (top), nonuniform grid (center), and number of particles per cell (bottom). The grid and density profile are plotted versus radial variable; the particles per cell is plotted versus radial cell number. The mode rational surface locations are indicated by the marks above the nonuniform grid ticks.

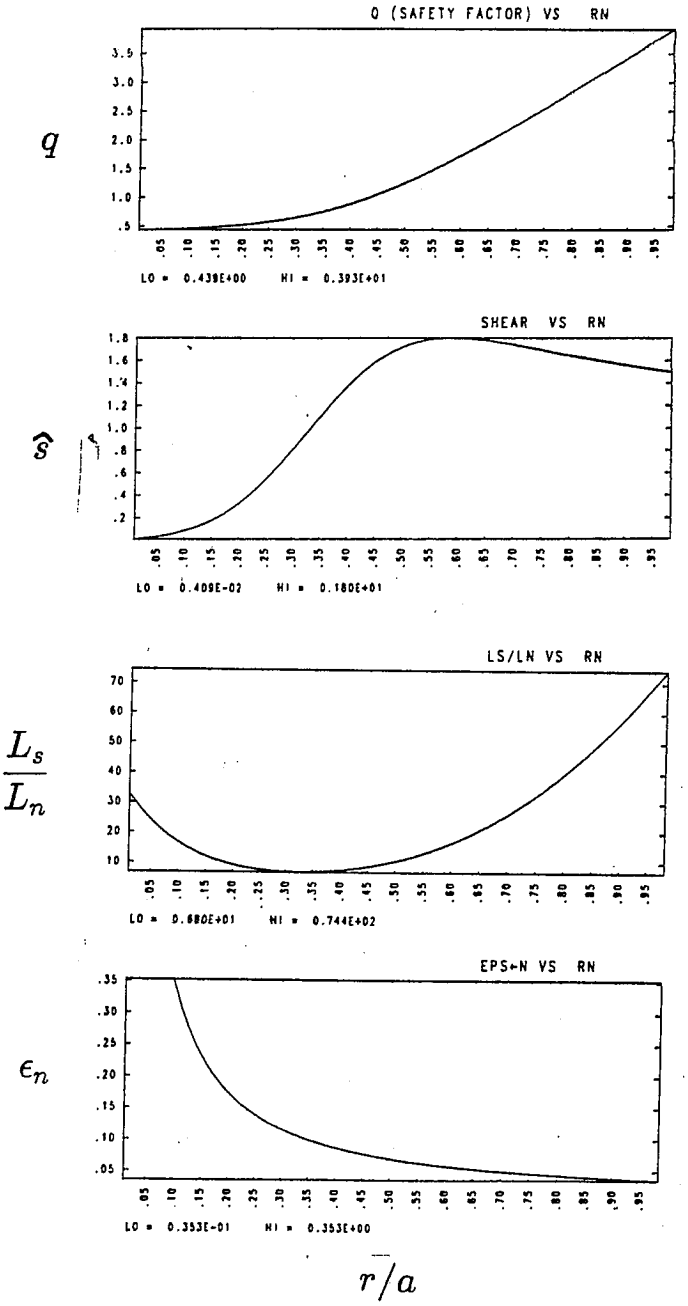

Figure 4.19: Radial variation of simulation quantities, from top to bottom—safety factor q, shear parameter $\hat{s}$, ratio of shear length to density scale length L_s/L_n, and toroidicity parameter ϵ_n. Each is plotted versus r/a.

In Figure 4.19 we give the radial variation of different simulation quantities in r, including the safety factor q, shear parameter $\hat{s}$ $(=rq'/q)$, the ratio of shear scale length to the density scale length L_s/L_n, and the toroidicity parameter ϵ_n $(=L_n/R_0)$. Parameters in the central region are comparable to those used in the theoretical calculation of Schep and Venema [17], for which $\epsilon_n \sim 0.1$ and $\hat{s} \sim 1$. In addition, the simulation employed $k_\perp \rho_i \sim 0.2$, for which the growth is expected to be a maximum. The velocity distributions are Maxwellian, with $T_e = T_i$, $T_\parallel/T_\perp = 2$, and $v_e = 1.56\,\Delta_0\,\omega_e^{-1}$. The remaining simulation parameters are given by : $N_p = 98304$ (number of particles), $\epsilon_\zeta = 0.2$ (inverse aspect ratio of 0.4), $N_u = N_\theta = 128$, $\Delta t = 4.0\,\omega_e^{-1}$, $m_e/m_i = 0.01$, $\Omega_e/\omega_e = 10$, and particle "size" of one grid spacing in both u and χ (using two passes of the binomial digital filter in u). The gaussian density profile was given by

$$n(r) \sim n_0 \exp\left[-(\kappa_0 r)^2/2\right] \tag{4.46}$$

with $\kappa_0\, a = 4.8$, and $a = 128\Delta_0$ the minor radius $(\kappa_0 \rho_s \simeq 0.041)$. We then have

$$\omega^*/\Omega_i = (\kappa\rho_s)(k_\perp \rho_s) \tag{4.47}$$

$$= m(\kappa_0 \rho_s)^2 \tag{4.48}$$

so that the only variation of the diamagnetic frequency is through the poloidal mode number m. The value of $k_\perp \rho_i$ evaluated at the mode rational surfaces varies only weakly, having a minimum value of 0.165 for $m = 6$ and a maximum of 0.219 for $m = 15$. The location of the ion resonance layers for the slab-like drift wave each mode rational surface is calculated using a nonlinear rootfinder, which solves the equation

$$\omega^*_{mn} = \pm k_\parallel(x_i; mn)\, v_i \tag{4.49}$$

using the given safety factor (x_i denotes the location of the ion resonance layer). For the given parameters, the ion resonance condition is well-satisfied for each mode rational surface.

The simulation was run for a total of 15,000 time-steps ($T = 6000\,\Omega_i^{-1}$). Energy conservation was 15% over the length of the run. This gradual increase in energy is caused by inaccuracy in the time integration due to undersampling of the highest frequency waves, and can be reduced through a reduction in the time-step (However, the gain in thermal energy of the simulation plasma does not appear to affect the low frequency response significantly). The time-step was chosen somewhat larger than usual in order to attain the long time scales necessary for resolution of the mode structure. The temporal evolution can be grossly observed by comparing the electron density profile at several points in time to the intial profile. It is observed that significant profile modification takes place until about $1200\,\Omega_i^{-1}$. In Figure 4.20 we plot the electron density profile at time $t = 1200\,\Omega_i^{-1}$ (dashed line) overlaid on the profile at time $t = 0$ (solid line). The positions of the mode rational surfaces are given by vertical lines. The most obvious feature is a definite profile modification about the $m = 5$ mode rational surface, which is highly localized. Significant profile modification also occurs from about the $m = 7$ to the $m = 9$ mode rational surfaces.

The profile modification seen in the early stages of the simulation suggests that an instability may have occured, with saturation due to flattening of the density profile. Thus we examine the temporal behavior of the potential amplitude $|e\Phi/T|$ for evidence of a growing mode. Prior to the calculation of the amplitude, the high frequency components are removed from the potential by the temporal application of a digital filter (cf. section 2.5). Although a

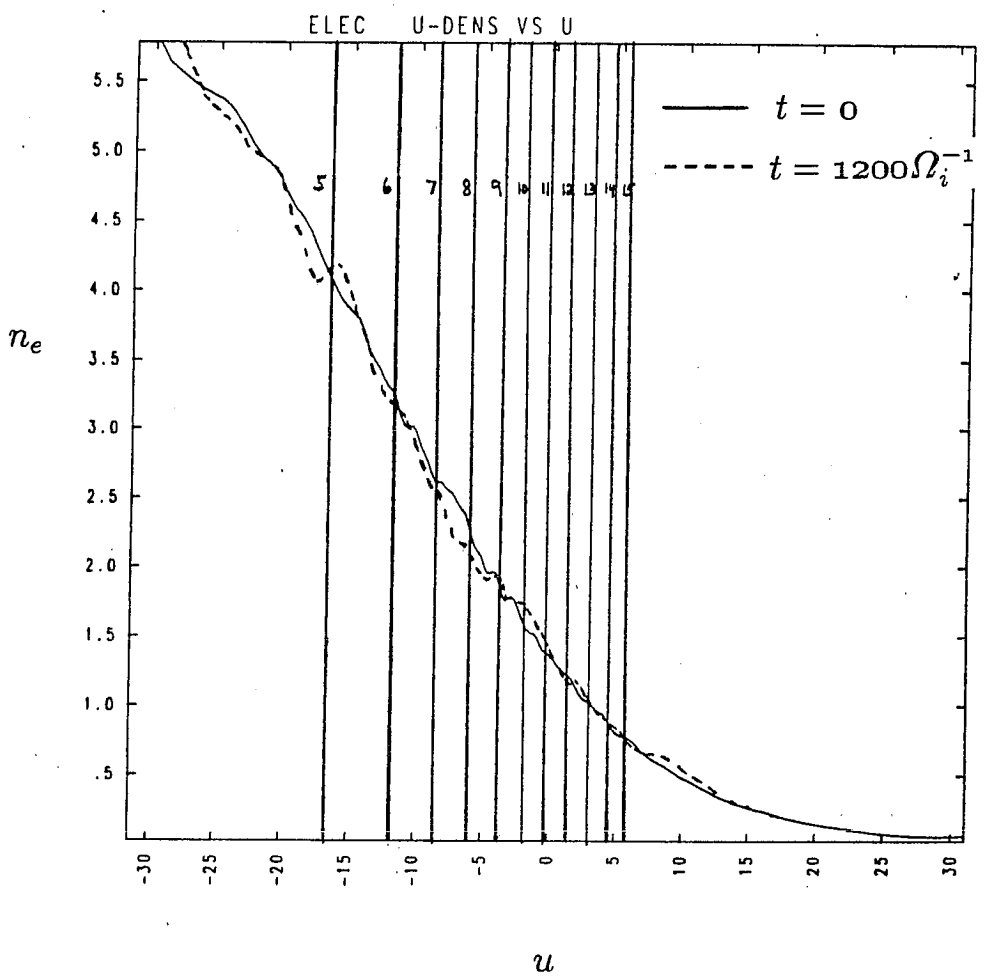

Figure 4.20: Electron density profile at time $t = 0$ (solid line), and time $t = 1200\,\Omega_i^{-1}$ (dashed line). The vertical lines represent the positions of the mode rational surfaces.

large number of digital filter passes is much more computationally intensive than a Fourier filter, this method avoids the imposition of arbitrary boundary conditions by "dropping-off" a point at each end of the time interval for each pass. The resulting loss of information is minimal for the modes of interest. The logarithm of $|e\Phi/T|$ versus time is plotted in Figures 4.21–4.23 for the $m = 8$ through $m = 10$ mode numbers, given at several radial positions near each respective mode rational surface. In each case, there is an indication of exponential growth until roughly $t = 1000\,\Omega_i^{-1}$. The growth rate is measured to be approximately $\gamma/\Omega_i \sim 1.25 \times 10^{-3}$, or $\gamma/\omega^* \sim 0.075$ (using $m = 8$ for calculation of ω^*). The measured value is roughly a factor of three larger than the value predicted by Schep and Venema [17], which may be reasonable given the rough association of parameters between the theory and simulation. Note that the inverse aspect ratio in the simulation was twice the value employed in Ref. [17], and a mass ratio of $m_e/m_i = 0.01$ was used (a realistic mass ratio was employed in the theoretical work). The affect of increasing either of these parameters is expected to be destabilizing [17], which may account for the increased growth rate. Saturation for these modes occurs at a level of $|e\Phi/T| \sim 0.04$ (recall that $k_\perp \rho_i \sim 0.2$, and $T_e = T_i$).

Here we have omitted mention of the $m = 5$ mode, although the growth is very strong at about $\gamma/\omega^* \sim 0.3$. This large growth rate is not easily explained by the TI-mode theory; nor is the mode coupled to neighboring modes toward the inside of the torus as required by theory (the poloidal mode spectrum is truncated at the $m = 5$ mode, and smaller mode numbers not allowed). Further, the profile flattening accompanied by this growth is very localized, unlike the broader flattening seen with the $m = 8$–9 modes. The ion resonant surfaces for absorption of energy associated with the slab-like drift mode are very close to the mode rational surface for $m = 5$, eliminating this

$m = 8$

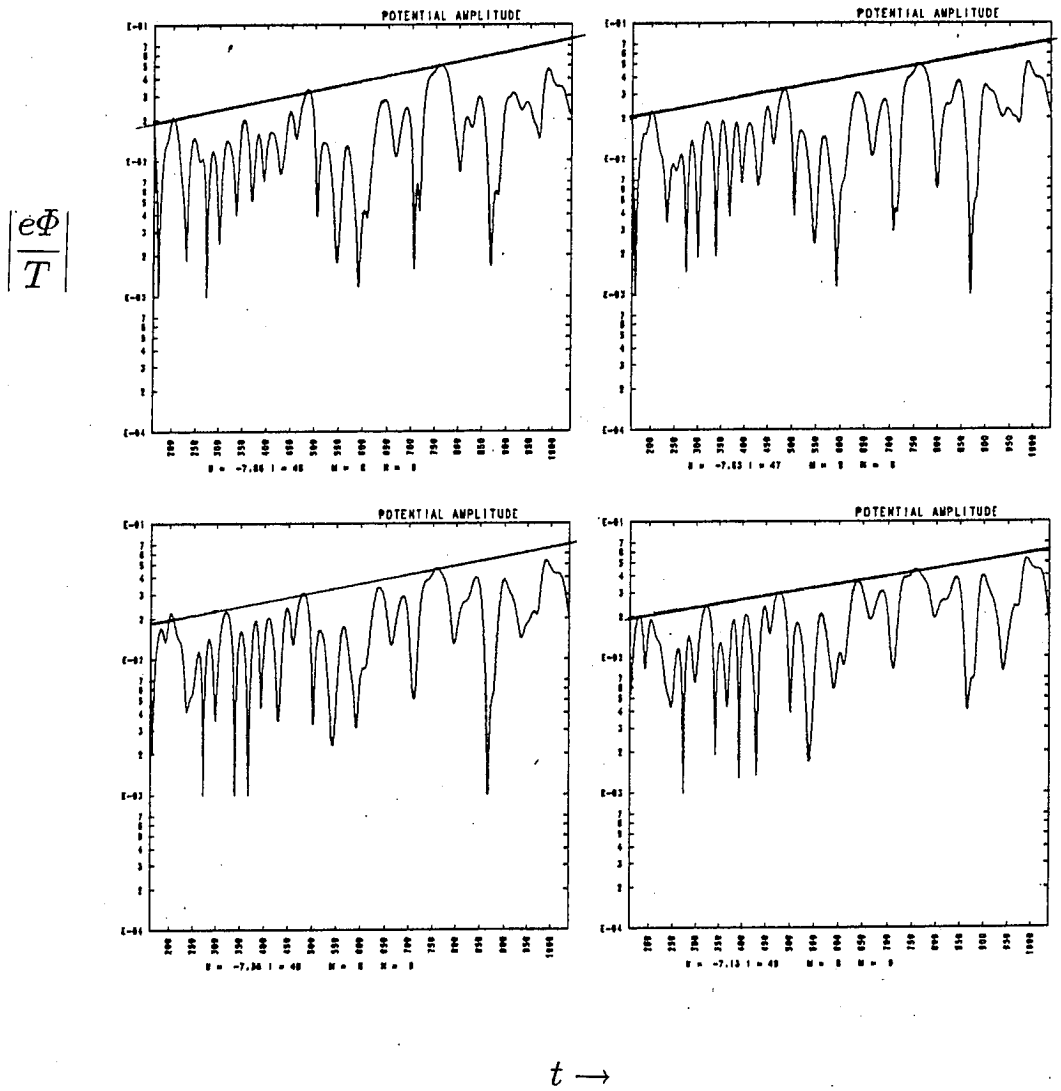

Figure 4.21: Amplitude of the potential $|e\Phi/T|$ for the $m = 8$ mode, at four radial positions near the mode rational surface.

$m = 9$

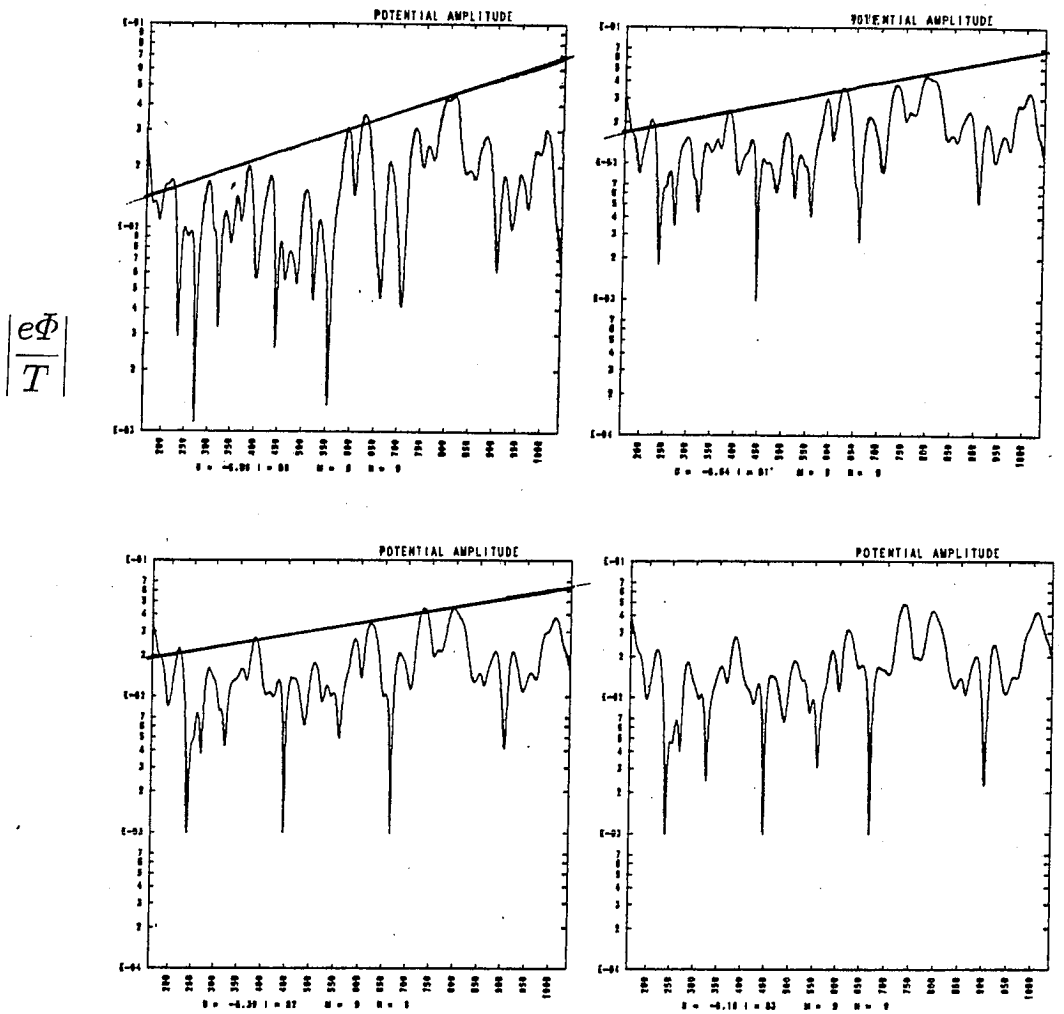

Figure 4.22: Amplitude of the potential $|e\Phi/T|$ for the $m = 9$ mode, at four radial positions near the mode rational surface.

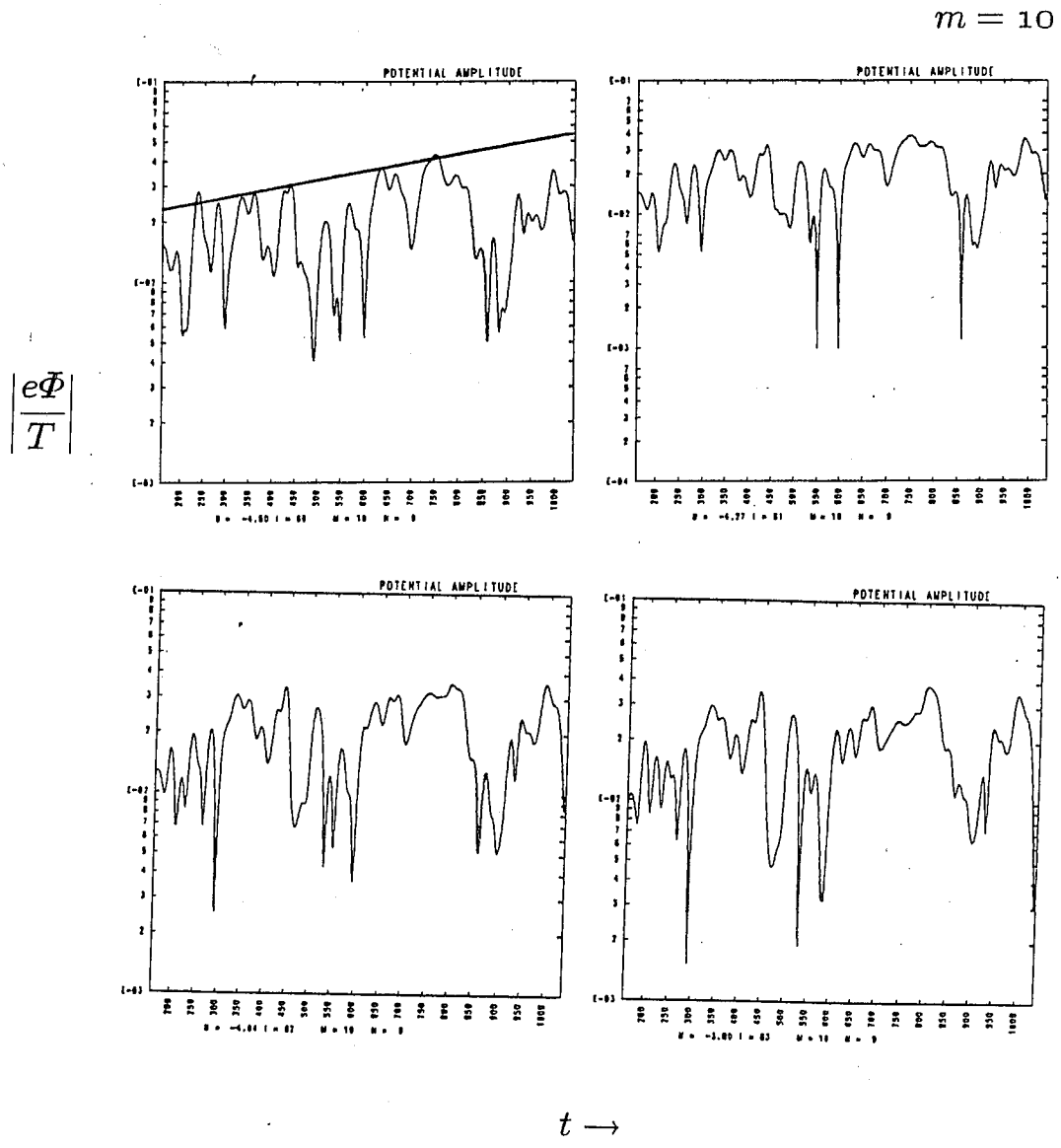

Figure 4.23: Amplitude of the potential $|e\Phi/T|$ for the $m = 10$ mode, at four radial positions near the mode rational surface.

as a candidate for the growth. An identification of the mechanism behind the growth at the $m = 5$ rational surface is therefore left to future analysis. A further concern is the somewhat poor conservation of energy due to the large time step, and its possible effect on the observed growth. This has been minimized by the filtering of the highest frequencies, which are expected to be the most affected by the size of the timestep (although the energy gain is observed to be primarily an increase in *kinetic* energy). Since the low-frequency potential does not show any global (radial) increase, and saturates at a finite time (at which point the profile evolution slows), it is clearly unaffected by the small gain in total energy of the simulation plasma.

We next examine the mode structure of the potential on long time scales via spectral analysis. The spectral density is calculated by the maximum entropy method (cf. section 3.1.2). A peak finding routine is employed to identify the peaks in the spectral density, for each radial position and mode number. The criterion for identification of a peak is that the spectral density must exceed the background level by a factor of about four. Only the strongest power peaks are output, and the resulting data set is compared to the spectral density plots visually to verify correct identification.

The observed frequency spectrum, as a function of radius and mode number, has many interesting features. First, we see a multiplicity of modes with frequencies below the diamagnetic frequency. This is not unexpected, because the many degrees of freedom from the coupled poloidal modes allows multiple toroidal drift harmonics to occur (as was discussed in the previous section). That these are real and not a numerical artifact is indicated by their persistence across many radial grid points. This is shown in Figures 4.24–4.27, where we have plotted ω/Ω_i (top) as a function of radial cell number, and

power versus ω/Ω_i (bottom) for the $m = 7$ through the $m = 10$ modes. In these plots, each mark denotes the presence of a signal, and some of the lowest power signals have been removed. A sample spectral density plot for several of the modes (at different radial positions) is given in Figures 4.28–4.29, clearly showing the multiplicity of frequencies observed. Note that the ion magnetic drift frequency is on the order of $\bar{\omega}_{D_i}/\Omega_i \sim 0.001$, so the ion magnetic drift resonance may significantly affect the lowest harmonic. The propagation of the modes is in the direction of the electron diamagnetic drift.

To obtain a clearer picture of the nature of observed modes, we compare the frequency dependence on the radius for neighboring mode numbers. Plots of ω/Ω_i versus the radial cell number are given in Figures 4.30–4.33 for the $m = 7$ and $m = 8$ mode numbers to the $m = 10$ and $m = 11$ mode numbers, respectively. Points associated with a given mode number are indicated by the chosen symbol ("□" or "+"). In these plots, there is a dramatic preference for certain frequeny "bands" (which may vary with position), especially at low frequency. The lowest two frequency bands show a high degree of overlap. The frequency of the lowest harmonic is given roughly by $\omega/\omega^* \sim 0.26$, compared to the value in Ref. [17] of $\omega/\omega^* \sim 0.4$. This is reasonable agreement given the rough match in parameter regimes.

In order to obtain a more global picture of the mode structure, we plot the frequency versus radial cell number for all the poloidal modes in Figure 4.34. In this figure, we have eliminated many of the lower power signals, in order to concentrate on the strongest components (although some important information inevitably is lost). Nevertheless, the spectrum remains somewhat complex. The overlapping bands are due to signals of different mode number at nearly the same frequency. Since the accuracy of the ω/Ω_i calculation is

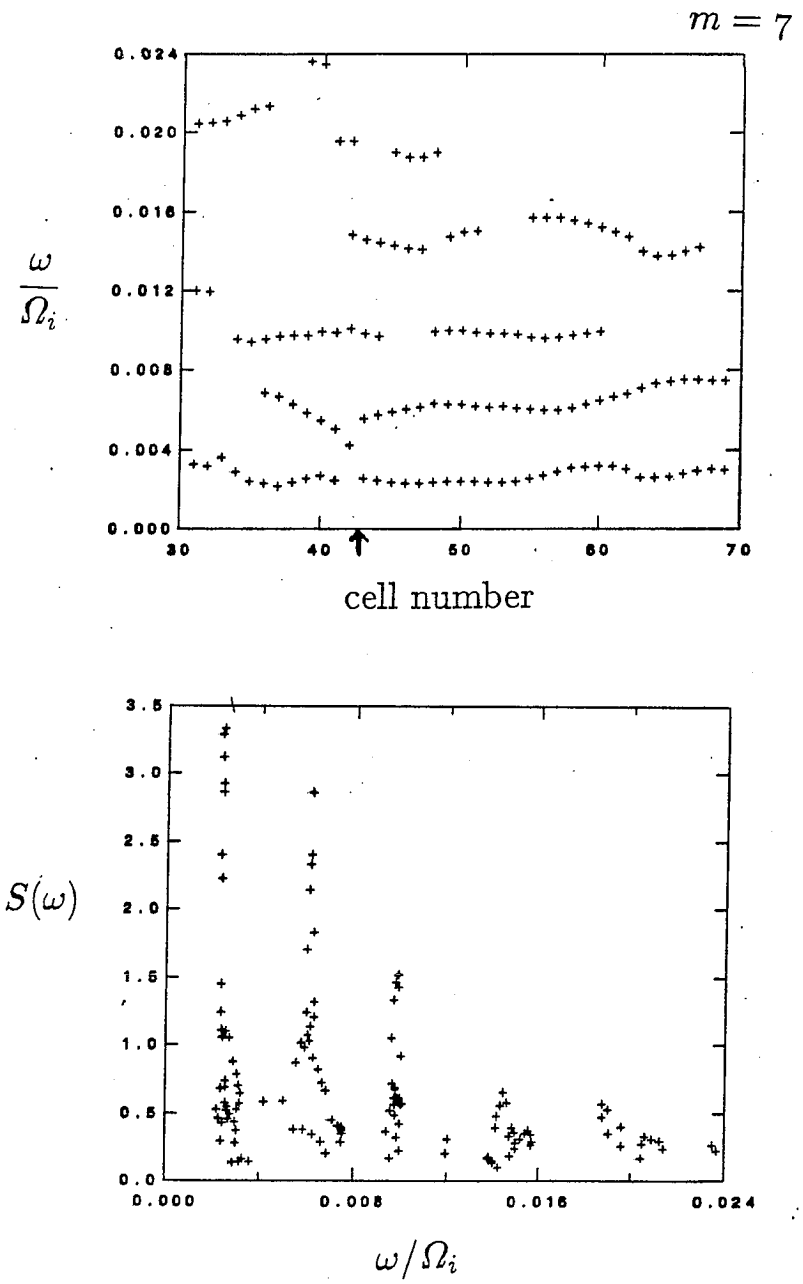

Figure 4.24: Frequencies and power obtained from spectral analyzer for mode number $m = 7$. At top—ω/Ω_i as a function of radial cell number (arrow marks location of mode rational surface). At bottom—power as a function of ω/Ω_i.

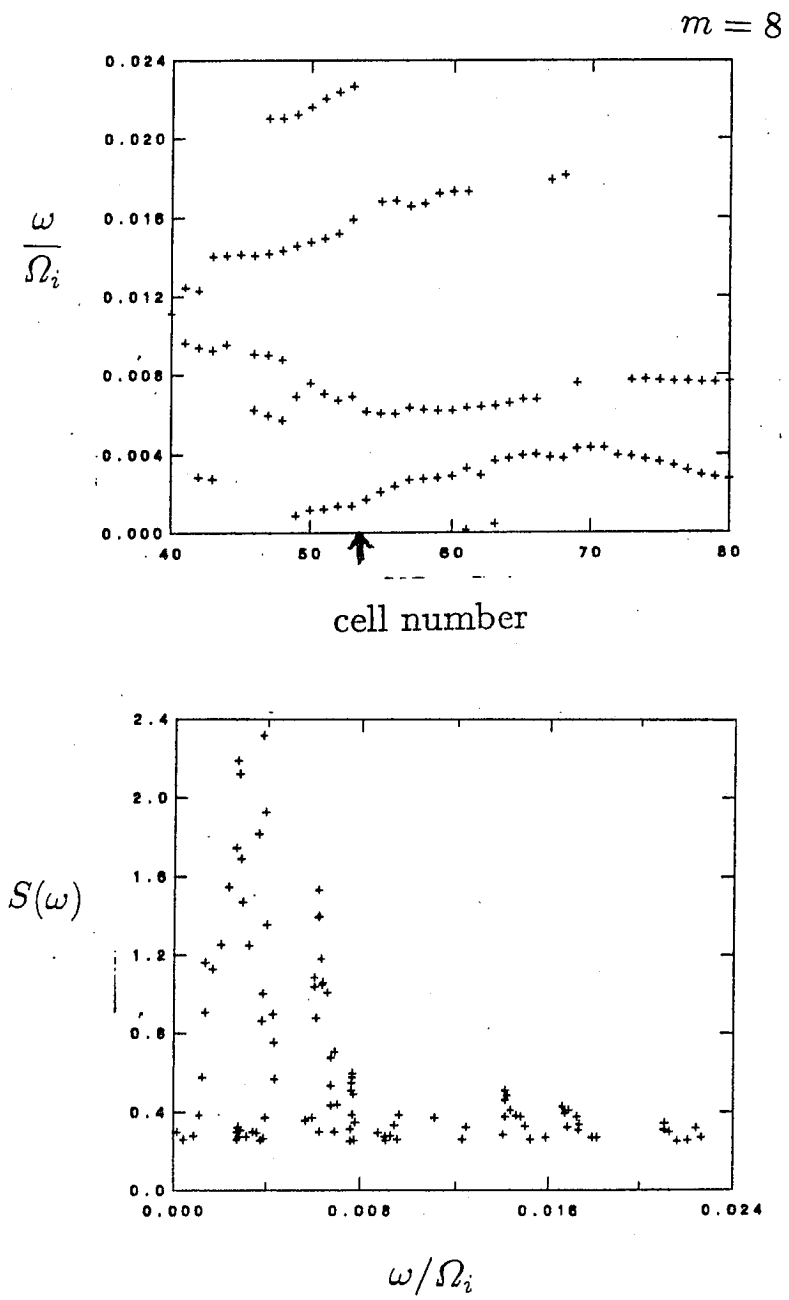

Figure 4.25: As previous, but for $m = 8$.

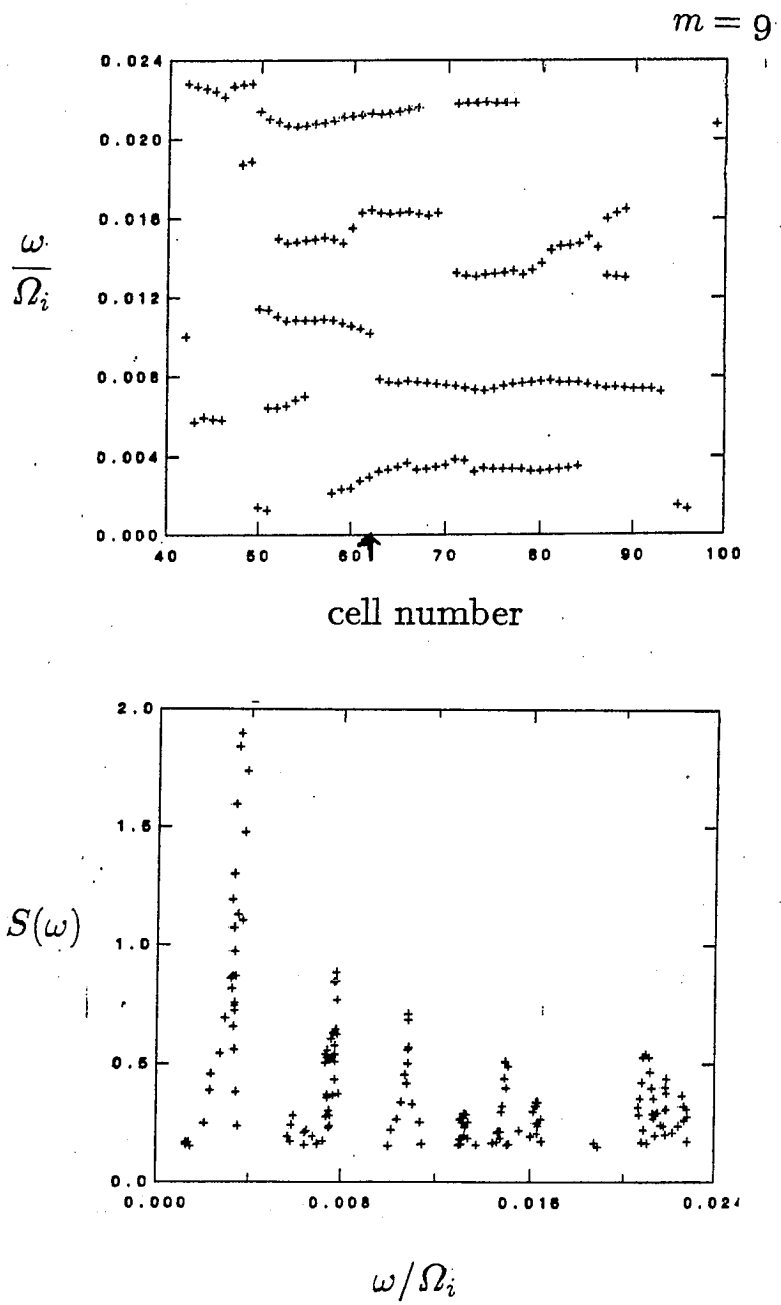

Figure 4.26: As previous, but for $m = 9$.

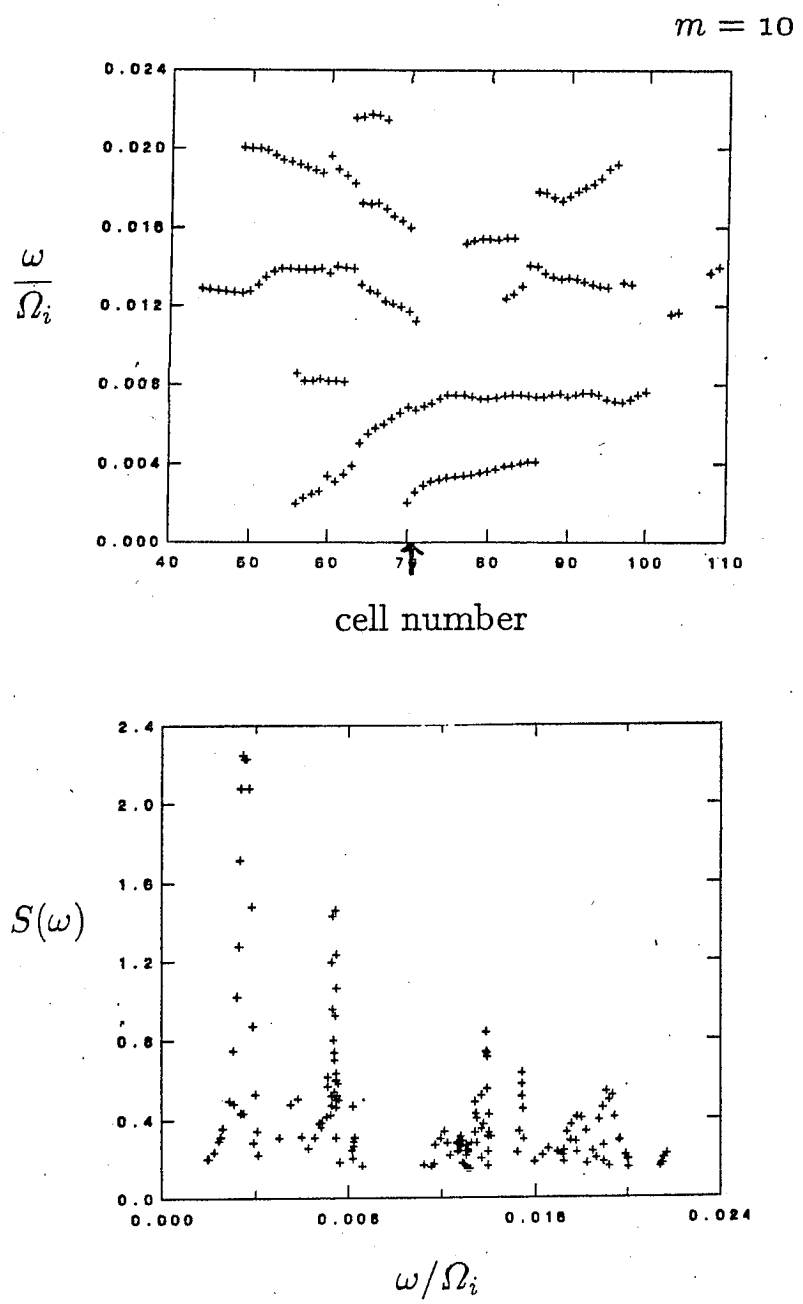

Figure 4.27: As previous, but for $m = 10$.

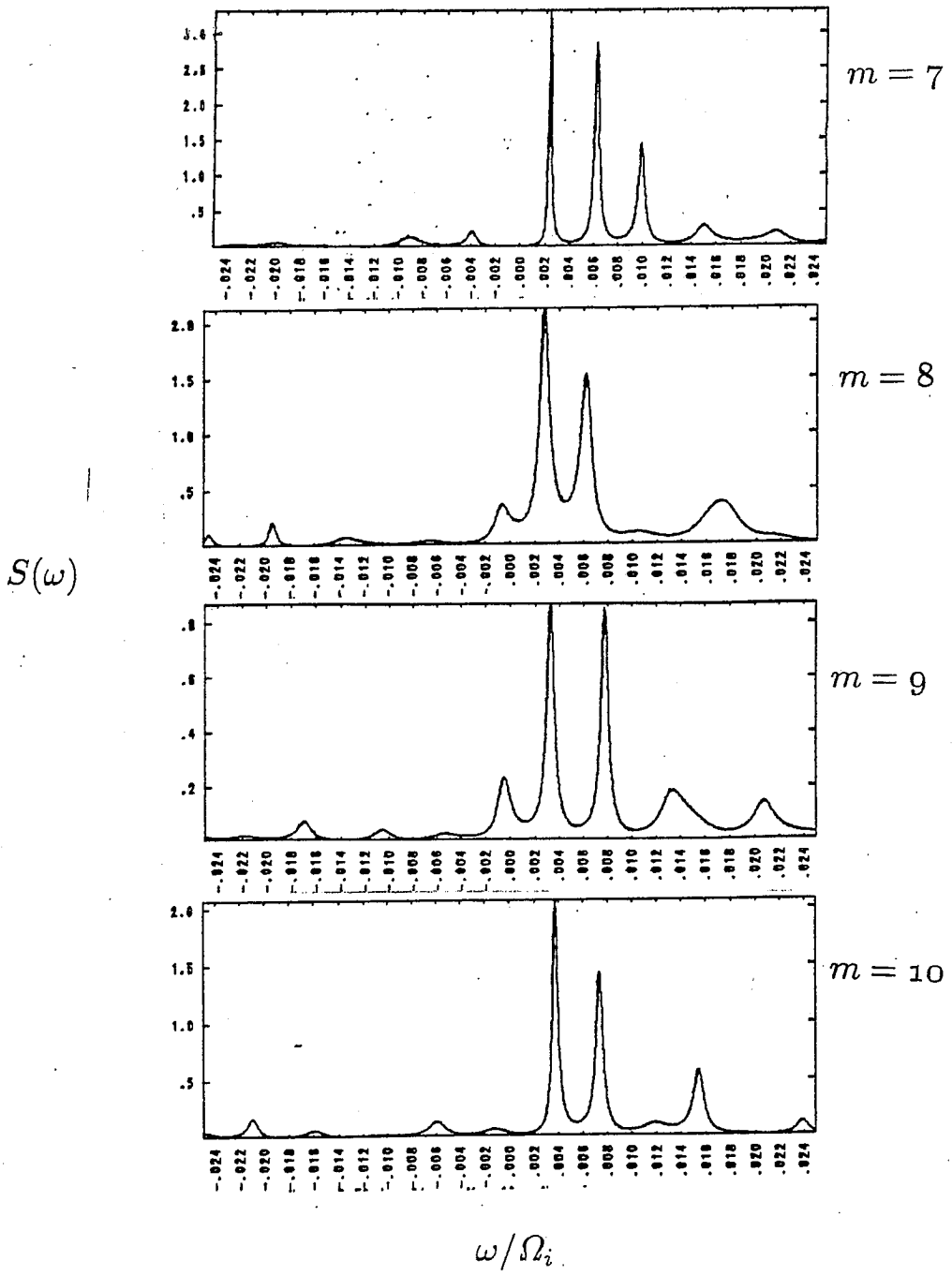

Figure 4.28: Sample spectral density plots for the $m = 7$ through $m = 10$ modes.

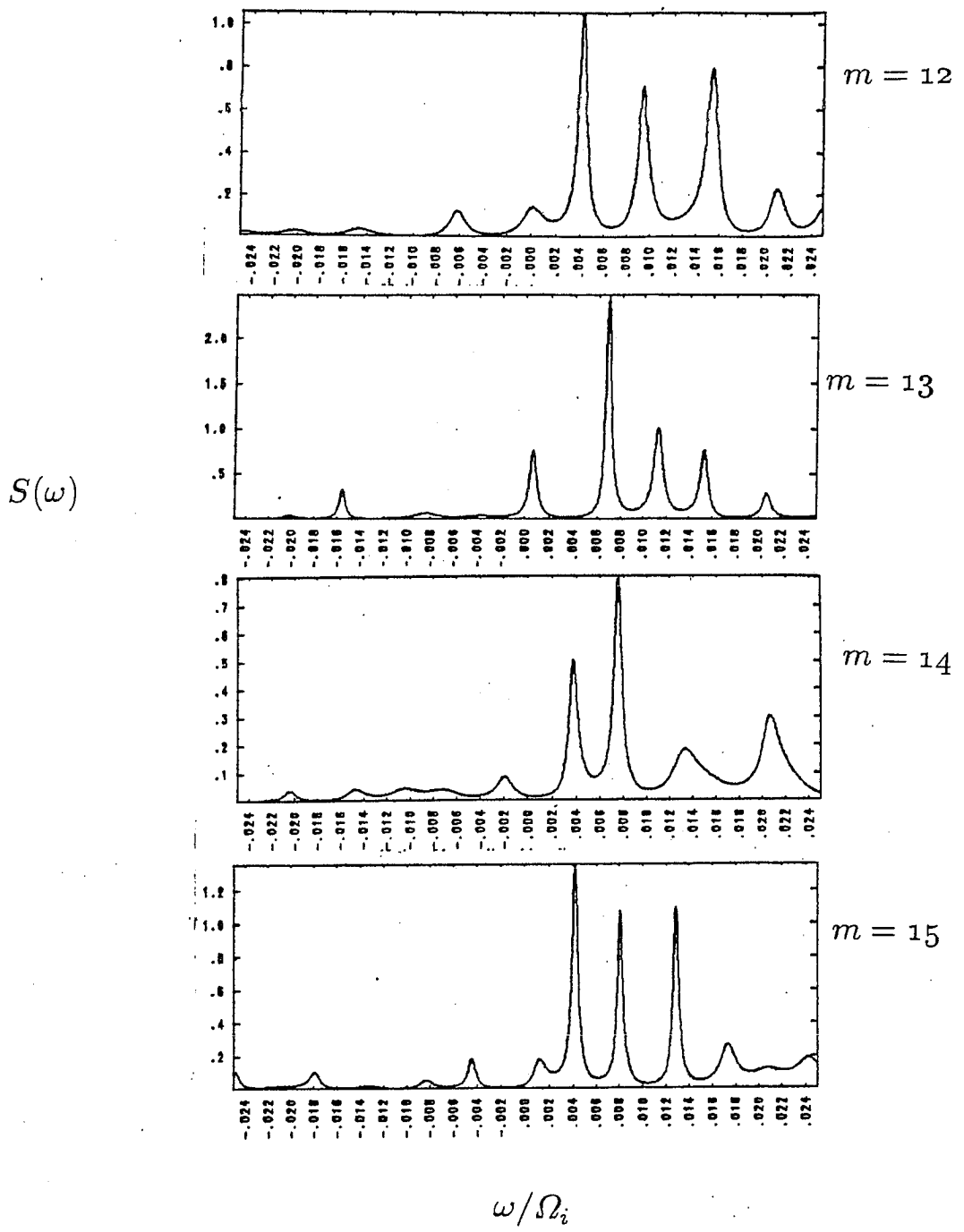

Figure 4.29: Sample spectral density plots for the $m = 12$ through $m = 15$ modes.

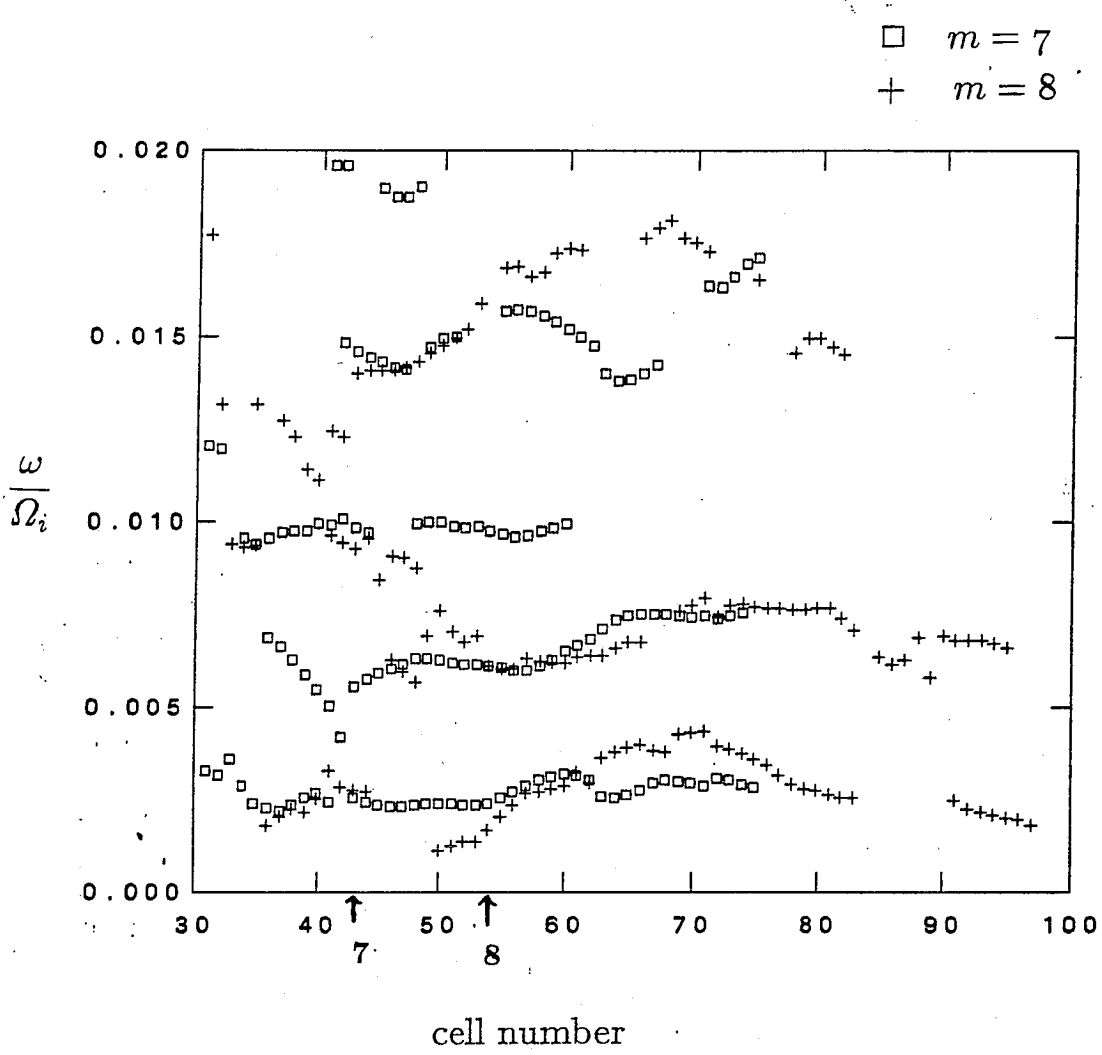

Figure 4.30: Frequency plotted versus radial cell number for the $m = 7$ mode (denoted by a "□") and for the $m = 8$ mode (denoted by a "+") The arrows mark the locations of the mode rational surfaces.

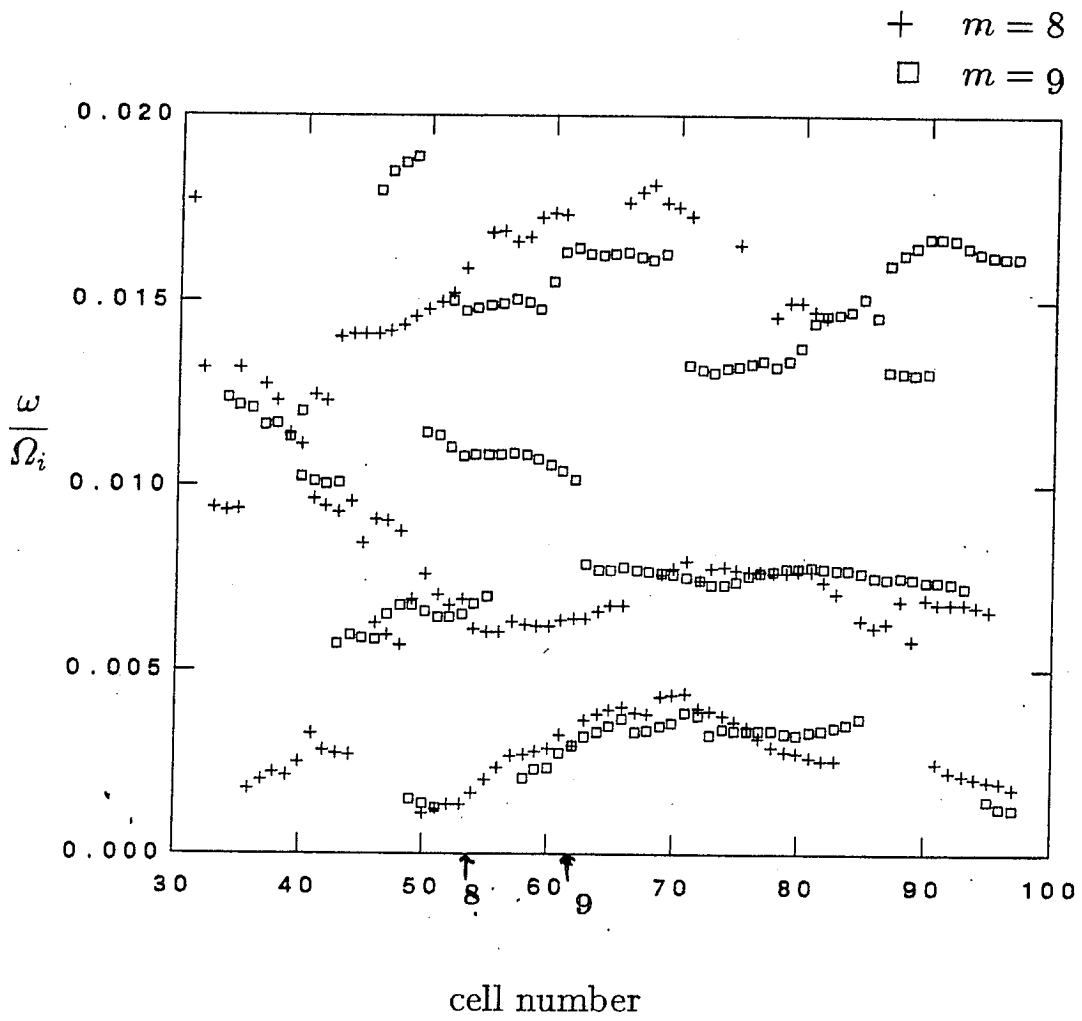

Figure 4.31: Frequency plotted versus radial cell number for the $m = 8$ mode (denoted by a "+") and for the $m = 9$ mode (denoted by a "□") The arrows mark the locations of the mode rational surfaces.

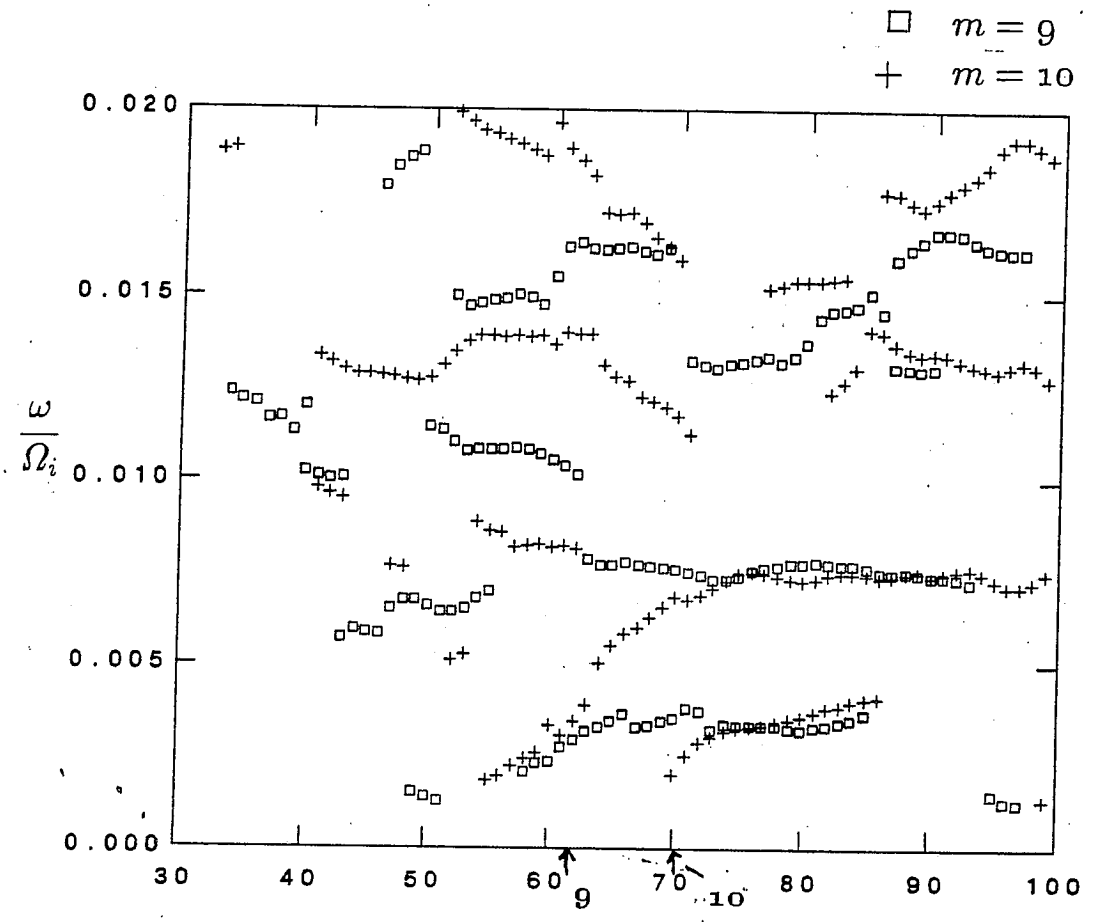

Figure 4.32: Frequency plotted versus radial cell number for the $m = 9$ mode (denoted by a "□") and for the $m = 10$ mode (denoted by a "+") The arrows mark the locations of the mode rational surfaces.

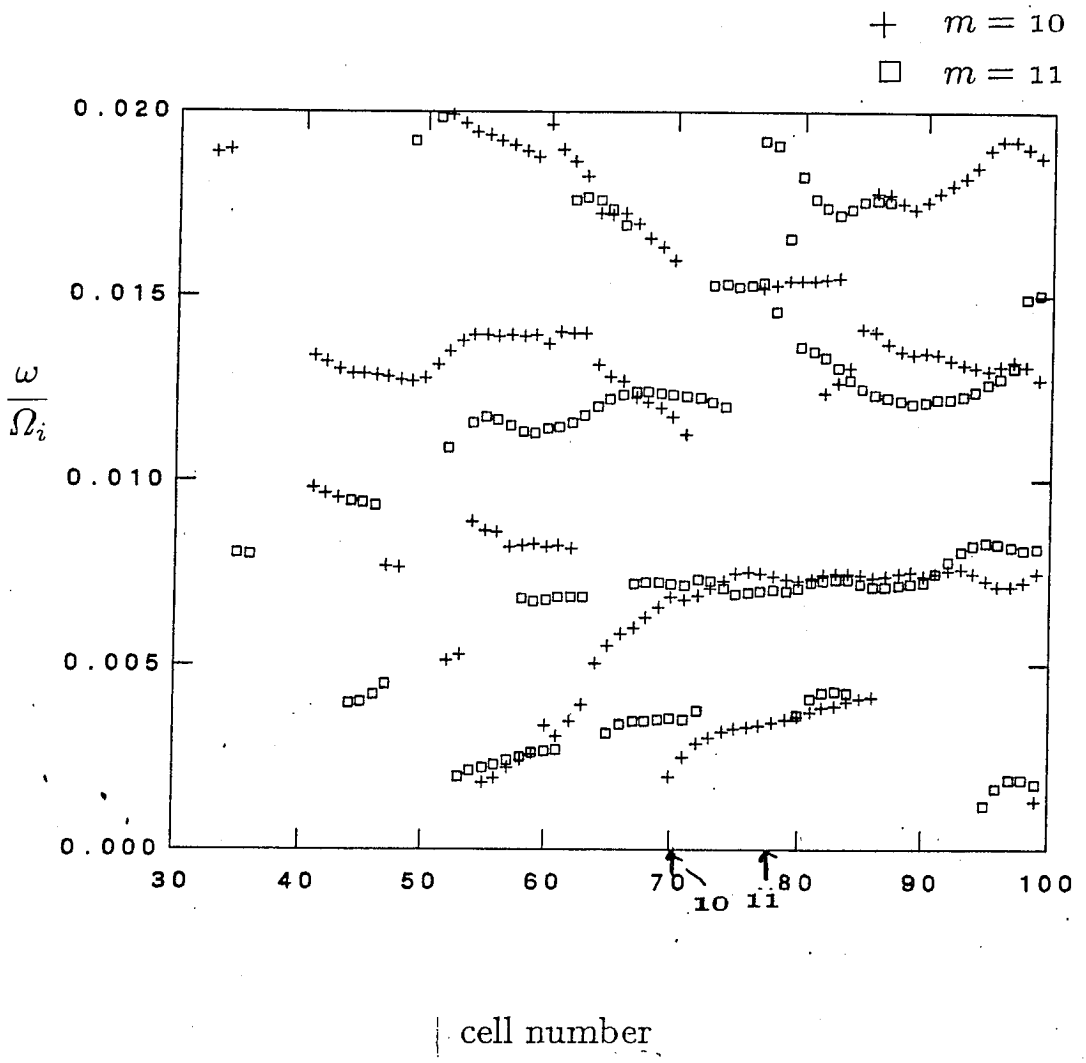

Figure 4.33: Frequency plotted versus radial cell number for the $m = 10$ mode (denoted by a "+") and for the $m = 11$ mode (denoted by a "□") The arrows mark the locations of the mode rational surfaces.

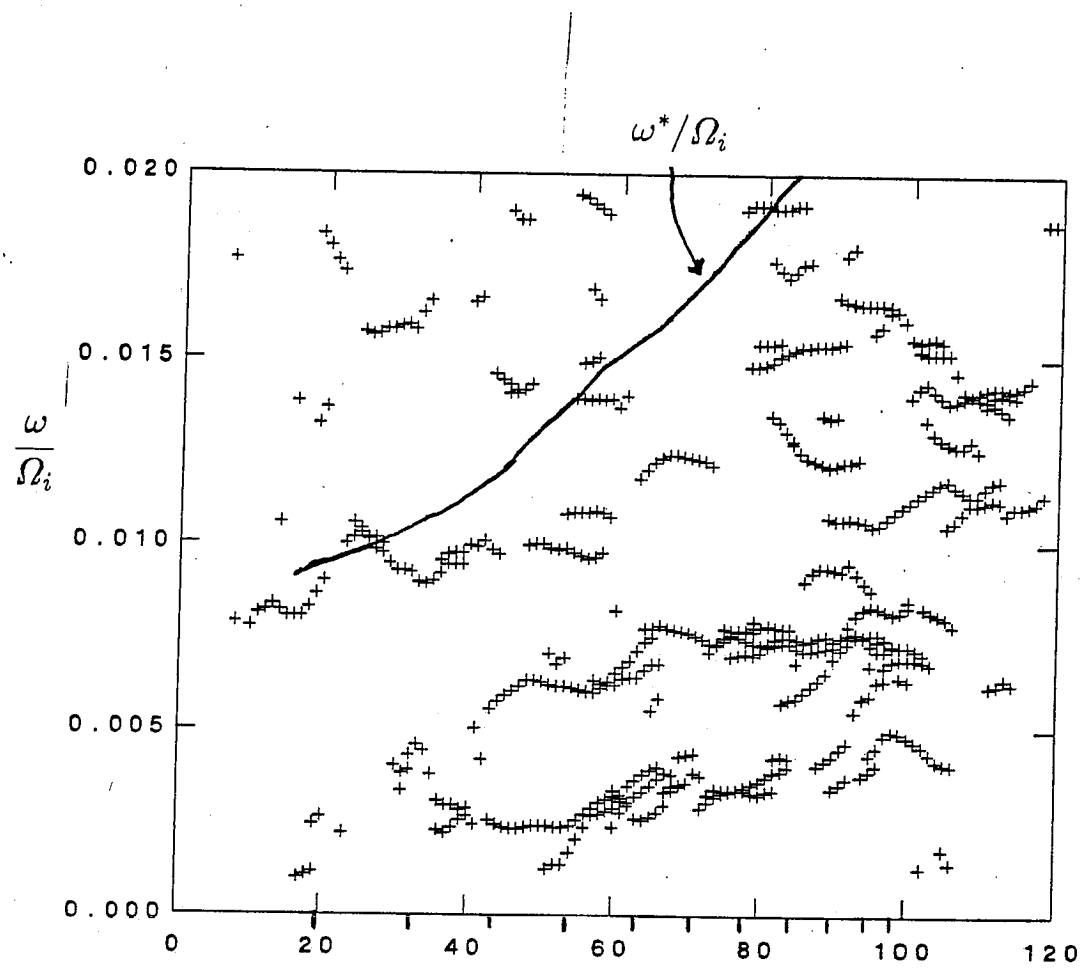

Figure 4.34: Frequency (ω/Ω_i) versus radial cell number for all poloidal mode numbers. The mode rational surfaces are indicated by the marks at bottom, and the solid line gives the variation of the diamagnetic frequency.

estimated at only about ± 0.0005, it is likely that these represent single modes that exist across multiple mode rational surfaces, or toroidicity-induced modes.

The "banded" structure seen in the frequency spectrum is characteristic of the strong poloidal mode coupling introduced through the toroidal geometry effects. These modes are not observed to exist across the entire radial extent of the mode rational surfaces, however, but a significant number of the mode rational surfaces are involved in any one mode. This is consistent with the physics of the parameter regime studied. The variation of the diamagnetic frequency with m will decrease the amount of mode coupling; here ω^* varies by a factor of 3 between the highest and lowest mode numbers. (The strong variation of the shear may decrease mode coupling as well.) This situation may not be completely described by either the strong coupling (ballooning mode) or weak coupling (Fourier mode) behavior, but a mix of aspects of each. Qualitatively, the variation of ω^* with radius will reduce the number of m-modes involved in a single quasimode, and limit the radial extent. The changing ω^* is expected to give a radial variation to the resulting frequency spectrum, although the exact dependence is not known. This behavior is seen in the simulation results via an upward trend in frequency with increasing radial position.

Another diagnostic which confirms the toroidal nature of these modes is an interferogram in the poloidal angle, which returns the mode structure in θ at a given frequency. Theoretically, strongly coupled modes exhibit "ballooning" towards the outside of the torus (see the discussion in the last section). This ballooning behavior is observed in the simulation, for several frequency ranges and at many radial grid points. The interferogram amplitude at two representative radius/frequency choices are displayed in Figure 4.35. In one of these, the maximum amplitude occurs near $\theta = 0$ (center), while in the other,

the maximum occurs off axis. The short wavelength noise is due to the emphasis of the last harmonic harmonic kept in the poloidal mode spectrum (due to the manner of truncation).

Finally, the radial structure has also been investigated via the interferogram diagnostic. Strong peaking of the potential is observed near the mode rational surface for the observed frequencies. The waveforms are typically very oscillatory in r, which is a consequence of the weakly dampled (or unstable), radially extended character of the mode. In addition, the waveforms generally overlap an appreciable number of adjacent mode rational surfaces. This is in contrast to the rapid radial decay expected of the slab-like mode for the current parameters. Radial interferograms for three of the observed frequency bands are given for several mode numbers in Figures 4.36–4.37. The interfered potential is shown at right, with the real part indicated by the solid line and the imaginary part by the dotted line. The amplitude of the mode is shown at left. Although adjacent mode numbers generally show similar mode structures, more widely separated mode numbers may not. It is also seen that the radial width of the waveform tends to increase with increasing mode number. This behavior may be understood as resulting from stronger coupling, due to a smaller fractional change in ω^* between mode rational surfaces ($\sim \Delta m/m$) as the mode number increases. In addition, the waveforms at different frequency often shows significantly different structure.

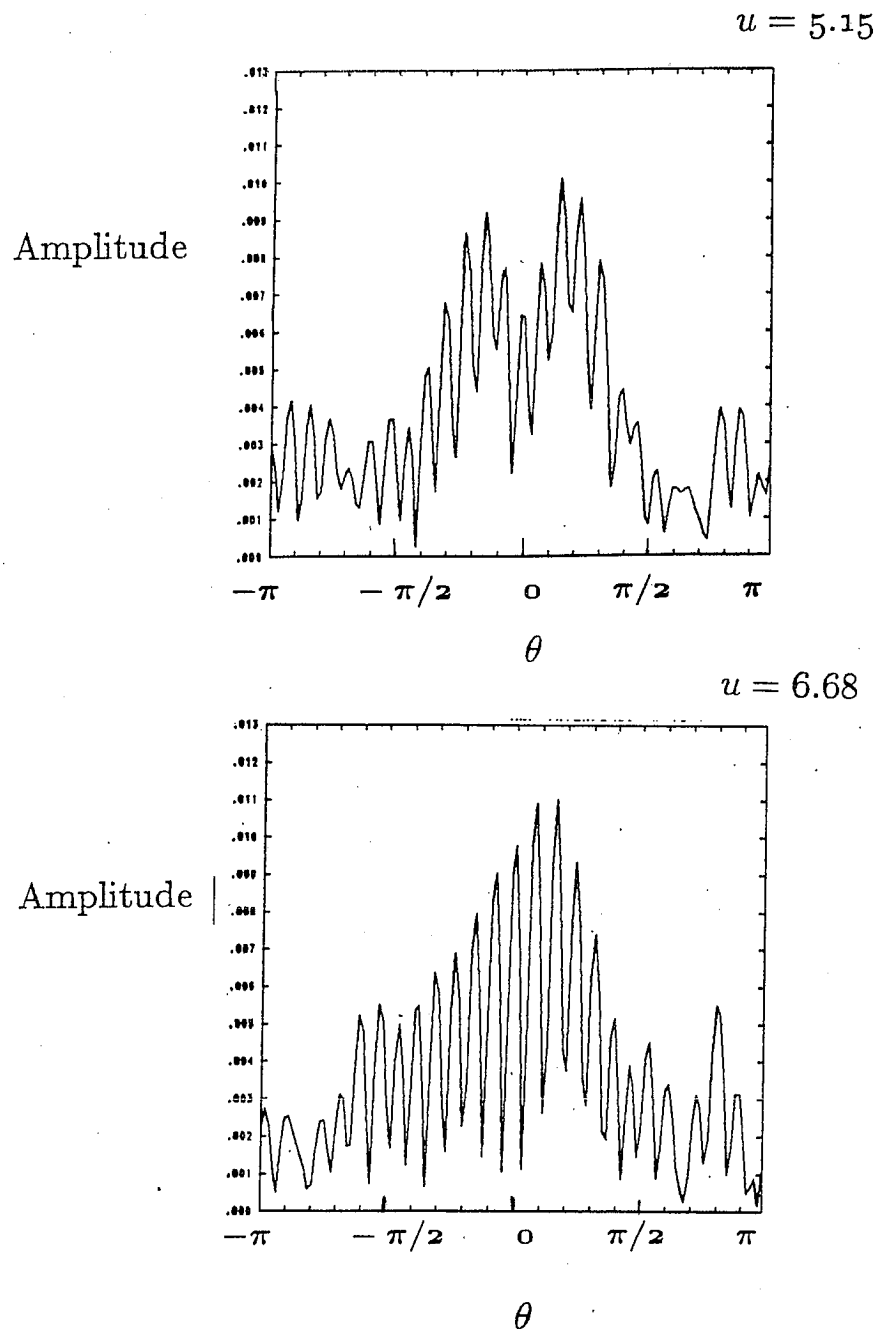

Figure 4.35: Interferogram of the potential versus θ, at two radial positions. A pump frequency of $\omega/\Omega_i \sim 0.007$ was used.

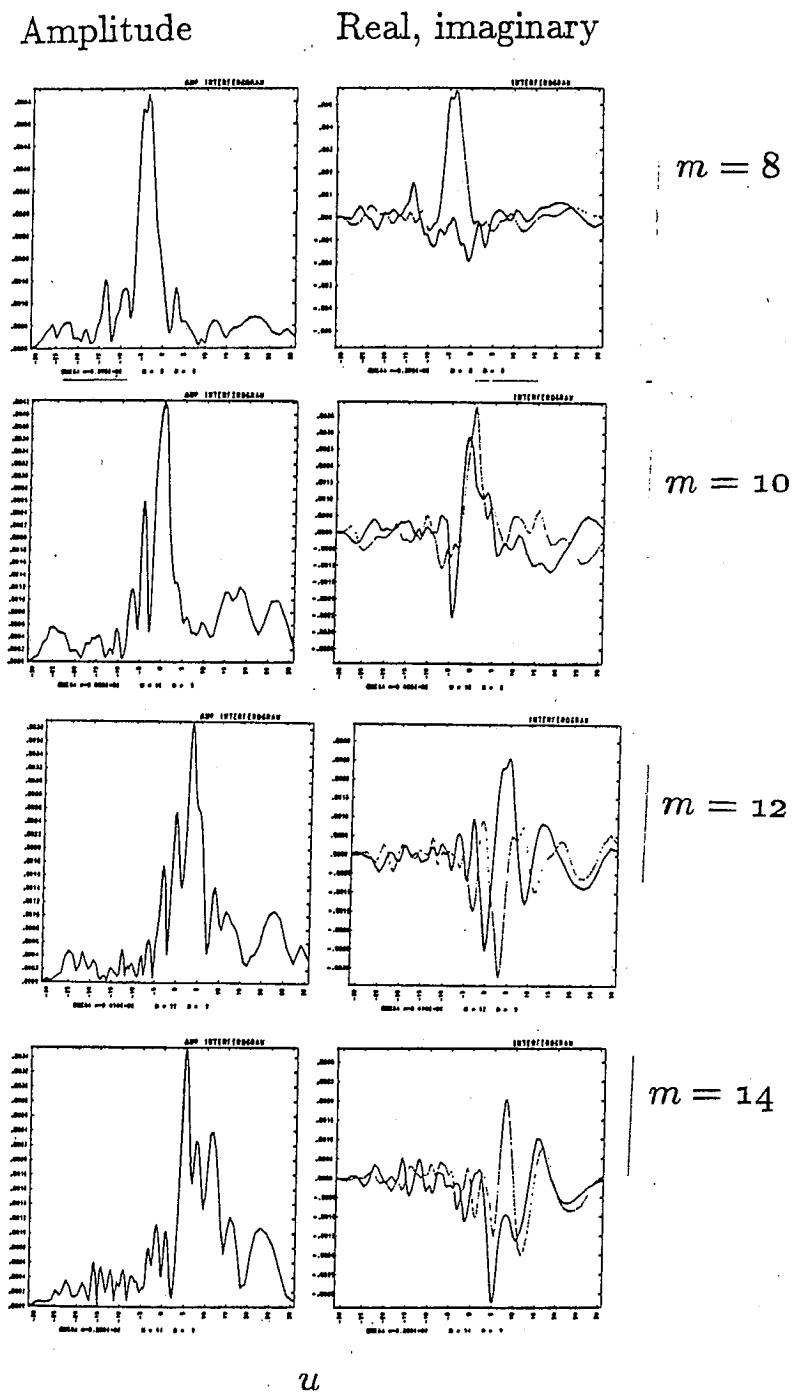

Figure 4.36: Interferogram of the potential versus r, using $\omega/\Omega_i \sim 0.004$ as the pump frequency. Shown are the m = 8, 10, 12, and 14 mode numbers, from top to bottom.

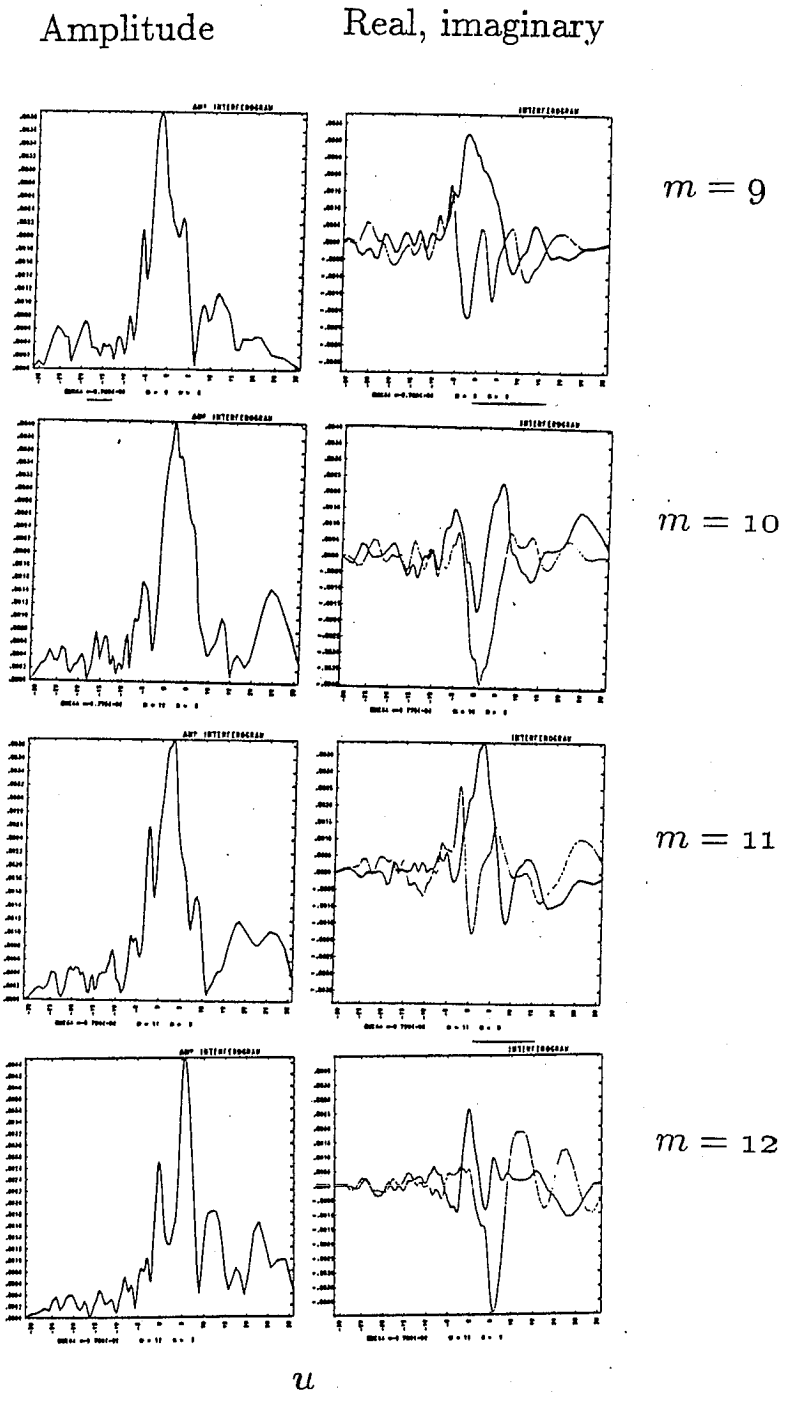

Figure 4.37: Interferogram of the potential versus r, using $\omega/\Omega_i \sim 0.0075$ as the pump frequency. Shown are the m = 9, 10, 11, 12 mode numbers, from top to bottom.

Chapter 5

Summary and Conclusions

A major goal of this research effort involved the extension of particle simulation methods to nearly arbitrary curvilinear coordinates. Kinetic and nonlinear effects play an important role in plasma behavior; thus the capability for modelling realistic geometries via particle simulation is greatly desired. The toroidal coordinate system considered here has many features of more complex metrics, including the vanishing of the transformation Jacobian at $r = 0$ and the nonseparable field equations. The algorithm developed in the course of this research thus is virtually metric-independent, and extensions of this work to other coordinate systems are envisioned.

We have found that few major conceptual changes are required by the introduction of the toroidal metric, though structural changes are significant. The use of a radial nonuniform grid is a natural construct in a cylindrical or toroidal system, giving increased radial resolution while maintaining nearly uniform particle/cell ratios. Implementation of the nonuniform grid is reasonably straightforward, requiring only a finite-difference (real space) handling of the radial coordinate and the adoption of a real-space or digital filter for smoothing of the interpolated quantities. The association of the curvature of space with the grid (instead of with the particles) in the charge density calculation avoids difficulties with the vanishing of the coordinate metric, as well as being conceptually simple. The resulting accumulation/filter/field-solver/filter/interpolation process is shown to be rigorously momentum-conserving, as with the usual slab

methods.

The particle equations of motion in the toroidal metric contain nonlinearities that makes integration considerably more difficult than in slab geometry. Therefore the ions are advanced using a transformation pusher, which models the cyclotron gyration well. (The parallel motion, however, is not as accurately reproduced. An improved model, mentioned in the text, is being considered for future simulations.) The electron dynamics is modeled via a guiding center formulation, which is well-suited to this system. The parallel motion is separated from the perpendicular drift motion in the usual predictor-corrector scheme, employing only two additional particle quantities than the slab model—the magnetic moment (μ) and velocity along the field line ($v_{\|}$). These pushing algorithms have been extensively tested in a variety of configurations, including tokamak magnetic fields; the particle orbits are consistently obtained regardless of the pushing method, with excellent conservation of particle invariants (energy, magnetic moment, and toroidal canonical momentum).

The ability of the simulation code to reproduce collective plasma effects has been demonstrated in the code's slab limit, for the plasma wave and ion Bernstein wave. In each case the simulation results closely followed the theoretical response, with the exception of a small systematic deviation increasing with mode number (this resulted from grid effects, which was not accounted for in the analysis). A good test is possible only when the theory is well understood, so that the source of discrepancies can be identified. Thus, reliance on tests in the slab limit for testing of the code is entirely reasonable. (Note that the accurate reproduction of the theoretical perpendicular plasma wave response in the slab limit required that the $n = 1$ and $n = 2$ ion cyclotron contributions be kept. This is surprising in light of the "usual" approxima-

tions, and points out the importance of verifying the approximations made in the theory when a close comparison is sought.) The correctness of the toroidal field-solver itself has been verified via internal consistency checks and through observation of test particle motion.

An additional question which appears with the simulation model concerns the initialization of stationary particle distributions. This is necessary in a particle simulation so that subtle stability effects can be observed. In the toroidal system, the broken symmetry in the poloidal variable causes large-scale charge separation when the distributions are loaded in the usual way. This problem has been solved through a "phase-mixing" procedure, for which the ion distribution is allowed to evolve to a steady state (without electric fields), prior to starting the simulation. A quiet simulation thereby results with fluctuation levels on the order of thermal equilibrium levels.

The simulation of the slab drift mode was performed in order to gain insight into the nature of the mode and for comparison to the toroidal result. The slab limit of the toroidal particle code was employed, and reasonable comparison to theoretical expectation was seen. The radial mode structure displayed the characteristic localization about the mode rational surface expected for the slab drift mode, becoming increasingly narrow with increasing $k_\perp \rho_i$. The observed frequencies agreed with the theoretical values by a factor of two or less, and the modes exhibited no growth. The difference in frequencies is significantly larger than the accuracy of the spectral estimator, and may result from the neglect of important terms in the theory. Inadequate spatial resolution or fluctuations in the background profile (from a small number of particles per cell) may have also had an effect.

The simulation of the drift wave in toroidal geometry utilized a sin-

gle toroidal harmonic ($n = 9$), with multiple poloidal harmonics ($m = 5$ to $m = 15$). The poloidal inhomogeneity in the magnetic field and the Laplacian operator strongly couples the poloidal mode numbers. The drift wave thus takes on a ballooning structure, and this new branch is known as the toroidicity-induced drift mode. This mode is predicted by theory to be unstable for fairly small perpendicular wavenumbers ($k_\perp \rho_i \sim 0.2$) and values of the shear relevant to tokamaks ($\hat{s} \sim 1$). This instability results from the inhibition of the radial convection of energy by the strongly coupled mode rational surfaces.

The simulation parameters were chosen roughly similar to the parameter regime used in the theoretical study by Schep and Venema [17]. The electric potential was observed to grow exponentially for the $m = 8$ to $m = 10$ modes, and saturation occured at a time $t = 1000\,\Omega_i^{-1}$ at a fluctuation level of $|e\Phi/T| \sim 0.04$. This was accompanied by profile flattening in the vicinity of the $m = 8$ to $m = 9$ mode rational surfaces. After the saturation time was reached, further significant profile modification did not occur. The growth rate was measured at $\gamma/\omega^* \sim 0.075$, or roughly a factor of three greater than the theoretical prediction. The difference between the measured and predicted growth rates may be due to the rough correspondence between parameters used by the simulation and theoretical model. (Specifically, the values of the inverse aspect ratio and mass ratio were greater in the simulation than in Ref. [17], which has a destabilizing effect on the mode.)

The long time-scale response of the simulation exhibited a "banded" frequency structure, not unlike the discrete frequencies seen in a crystal lattice. This structure results from the additional degrees of freedom in the presence of strongly coupled poloidal modes. Although variation of equilibrium quantities

such as the diamagnetic frequency results in decreased mode coupling, certain frequencies are observed to persist across a significant radial extent of the plasma. The observed modes can therefore be identified as the theoretically predicted toroidicity-induced modes. The fundamental harmonic observed in the simulation occured at a frequency of approximately $\omega/\omega^* \sim 0.26$, in reasonable agreement with the theoretically-predicted value of $\omega/\omega^* \sim 0.4$ (considering the differences in parameters).

The toroidal nature of these modes is further supported through examination of the radial and poloidal mode structure. Interferogram analysis of the potential shows a strong peak in amplitude near each mode rational surface, and the radial mode width is much greater than that seen in the slab-like drift mode (as well as being more oscillatory). In addition, interferogram analysis in the poloidal variable shows a localization in theta centered roughly about $\theta = 0$, that is, the mode "balloons" toward the outside of the torus. The theoretical expectation of a marginally damped, radially extended mode (i.e. ballooning mode) is thus confirmed by the simulation results.

The success of the particle simulation model in modeling the toroidal drift wave is highly significant, for this mode appears only when toroidal effects are considered. This research demonstrates that particle simulation in complex geometries can be an important tool in the understanding of the underlying physics. However, despite the difficulty of the associated theory and the complexity of the observed phenomena, this investigation is only the starting point. Many additional effects may be added, such as multiple toroidal modes or temperature gradients, in the electrostatic model alone. The extension to longer time scales via gyrokinetic and/or implicit formulation of the field equations is under consideration, as well as inclusion of self-consistent magnetic field effects.

Finally, the methods developed in the course of this research may be well-suited for the geometries encountered in astrophysical problems as well. This might include simulation of the magnetosphere, or the region near a black hole (for which a Schwartzschild metric would be necessary).

Appendix A

Here we consider further the properties of the charge-conserving filter given in section 2.5 near the point where the Jacobian vanishes, that is, near $r = 0$ in a cylindrical system. We apply the filter to the first grid point, which is a distance of $\Delta/2$ away from the origin for a uniform grid. The charge-conserving filter is given by

$$\mathcal{S} \circ \rho_i = \rho_i + \frac{\Delta^2}{4}\left[\frac{1}{J}\frac{\partial}{\partial\psi}\left(J\frac{\partial\rho}{\partial\psi}\right)\right]_i \tag{A.1}$$

Expanding the derivatives in the above expression in terms of finite-differences, we obtain

$$\rho_i \rightarrow \rho_i + \frac{\Delta^2}{4}\left[\frac{\rho_{i+1} - 2\rho_i + \rho_{i-1}}{\Delta^2} + \frac{1}{r_i}\frac{\rho_{i+1} - \rho_{i-1}}{2\Delta}\right]$$

At the first grid point, the $i - 1$ index refers to a *virtual* grid-point outside the system, and is defined only in terms of the parity at the boundary and the known charge density. Indexing the charge density array by distance (in number of cells from the origin), a single pass of the filter at the first grid-point yields

$$\rho_{1/2} \rightarrow \rho_{1/2} + \frac{\Delta^2}{4}\left[\frac{\rho_{3/2} - 2\rho_{1/2} + \rho_{-1/2}}{\Delta^2} + \frac{1}{\Delta/2}\frac{\rho_{3/2} - \rho_{-1/2}}{2\Delta}\right]$$

which reduces to

$$\rho_{1/2} \rightarrow \frac{1}{2}\left[\rho_{1/2} + \rho_{3/2}\right]$$

The filtered value of ρ at the first grid point is thus completely independent of the boundary condition at the origin, since no boundary conditions were used in deriving the above expression.

The above filter is essentially *one-sided* at the origin—a reasonable result considering the intent on conserving charge. However, this is not the behavior we desire at the origin; the charge should be smoothed *through* the origin, to minimize fluctuations and to more faithfully represent the continuity boundary conditions there. This is especially critical given the small cell size at the origin; the number of particles in these cells will be very small for any reasonable plasma profile, enhancing fluctuation levels there. In addition to the charge density fluctuations, the E_θ field component is a concern due to its $1/r$ dependence. A filter which does not conserve charge will smooth through the origin, thereby helping with this problem (as does stretching the radial grid near $r = 0$, to increase the number of particles in the innermost cells).

BIBLIOGRAPHY

[1] P. C. Liewer, Nucl. Fusion **25**, 543 (1985).

[2] W. M. Tang, Nucl. Fusion **18**, 1089 (1978).

[3] B. B. Kadomtsev and O. P. Pogutse, in *Reviews of Plasma Physics*, edited by M. A. Leontovich, p. 249 (Consultants Bureau, New York, 1970).

[4] A. Y. Aydemir and R. D. Hazeltine, Technical Report 250, Institute for Fusion Studies, University of Texas at Austin (1986).

[5] R. E. Denton, J. F. Drake, R. G. Kleva, and D. A. Boyd, Phys. Rev. Lett. **56**, 2477 (1986).

[6] L. D. Pearlstein and H. L. Berk, Phys. Rev. Lett. **23**, 220 (1969).

[7] D. W. Ross and S. M. Mahajan, Phys. Rev. Lett. **40**, 324 (1978).

[8] K. T. Tsang, P. J. Catto, J. C. Whitson, and J. Smith, Phys. Rev. Lett. **40**, 327 (1978).

[9] S. P. Hirshman and K. Molvig, Phys. Rev. Lett. **42**, 648 (1979).

[10] K. Molvig, J. P. Freidberg, R. Potok, S. P. Hirshman, J. C. Whitson, and T. Tajima, in *Long-Time Prediction in Dynamics*, edited by J. C. W. Horton, L. E. Reichl, and V. G. Szebehely, p. 319 (Wiley, 1983).

[11] R. D. Sydora, J. N. Leboeuf, D. R. Thayer, P. H. Diamond, and T. Tajima, Phys. Rev. Lett. **57**, 3269 (1986).

[12] C. F. Zhang, R. Marchand, and Y. C. Lee, Phys. Fluids **25**, 2264 (1982).

[13] J. B. Taylor, in *Plasma Physics and Controlled Nuclear Fusion Research*, p. 323 (1977).

[14] L. Chen and C. Z. Cheng, Phys. Fluids **23**, 2242 (1980).

[15] C. Z. Cheng and K. T. Tsang, Nucl. Fusion **21**, 643 (1981).

[16] K. W. Hesketh, Nucl. Fusion **21**, 275 (1981).

[17] T. J. Schep and M. Venema, Plasma Physics and Controlled Fusion **27**, 653 (1985).

[18] D. C. Barnes, T. Kamimura, J. Leboeuf, and T. Tajima, J. Comp. Phys. **52**, 480 (1983).

[19] J. L. Geary, T. Tajima, J. Lebocuf, E. G. Zaidman, and J. H. Han, Computer Phys. Comm. **42**, 313 (1986).

[20] C. Z. Cheng and H. Okuda, J. Comp. Phys. **25**, 133 (1977).

[21] C. K. Birdsall and A. B. Langdon, *Plasma Physics via Computer Simulation* (McGraw-Hill, New York, 1985).

[22] H. Naitou, S. Tokuda, and T. Kamimura, J. Comp. Phys. **38**, 265 (1980).

[23] J. M. Dawson, Phys. Fluids **5**, 445 (1962).

[24] S. P. Yu, G. P. Kooyers, and O. Buneman, J. Appl. Phys. **36**, 2550 (1965).

[25] R. W. Hockney, Phys. Fluids **9**, 1826 (1966).

[26] E. Detyna, in *Sparse Matrices and Their Uses*, edited by I. S. Duff, p. 245 (Academic Press, 1981).

[27] J. M. Dawson, Astrophysics and Space Science **13**, 446 (1971).

[28] A. B. Langdon, J. Comp. Phys. **6**, 247 (1970).

[29] H. Okuda, A. T. Lin, C. C. Lin, and J. M. Dawson, Computer Phys. Comm. **17**, 227 (1979).

[30] H. Abe, N. Sakairi, R. Itatani, and H. Okuda, J. Comp. Phys. **63**, 247 (1986).

[31] J. F. Thompson and Z. U. A. Warsi, J. Comp. Phys. **47**, 1 (1982).

[32] S. C. Jardin, J. L. Johnson, J. M. Greene, and R. C. Grimm, J. Comp. Phys. **29**, 101 (1978).

[33] A. B. Cain, J. H. Ferziger, and W. C. Reynolds, J. Comp. Phys. **56**, 272 (1984).

[34] E. K. De Rivas, J. Comp. Phys. **10**, 202 (1972).

[35] F. G. Blottner and P. J. Roache, J. Comp. Phys. **8**, 498 (1971).

[36] J. D. Hoffman, J. Comp. Phys. **46**, 469 (1982).

[37] D. Potter, *Computational Physics* (Wiley, New York, NY, 1973).

[38] R. W. Hockney and J. W. Eastwood, *Computer Simulation Using Particles* (McGraw-Hill, New York, NY, 1981).

[39] F. Marsh and D. E. Potter, Computer Phys. Comm. **24**, 185 (1981).

[40] W. H. Press, B. P. Flannery, S. A. Teukolsky, and W. T. Vetterling, *Numerical Recipes: The Art of Scientific Computing* (Cambridge University Press, Cambridge, 1986).

[41] J. U. Brackbill and H. M. Ruppel, J. Comp. Phys. **65**, 314 (1986).

[42] V. K. Decyk, J. Comp. Phys. **56**, 461 (1984).

[43] H. L. Berk, H. Momota, and T. Tajima, Technical Report 275, Institute for Fusion Studies, University of Texas at Austin (1987).

[44] J. N. Leboeuf, D. R. Thayer, R. D. Sydora, and P. H. Diamond, Phys. Fluids **29**, 4147 (1986).

[45] T. G. Northrop, *The Adiabatic Motion of Charged Particles* (Interscience, New York, 1963).

[46] G. Arfken, *Mathematical Methods for Physicists, second edition* (Academic Press, New York, 1970).

[47] A. Y. Aydemir and D. C. Barnes, J. Comp. Phys. **53**, 100 (1984).

[48] M. B. Priestley, *Spectral Analysis and Time Series* (Academic Press, London, 1981).

[49] T. Kamimura, T. Wagner, and J. M. Dawson, Phys. Fluids **21**, 1151 (1978).

[50] C. Temperton, J. Comp. Phys. **52**, 198 (1983).

[51] N. Rostoker, Nucl. Fusion **1**, 101 (1961).

[52] C. R. Oberman and E. A. Williams, in *Handbook of Plasma Physics: Basic Plasma Physics I*, edited by M. N. Rosenbluth and R. Z. Sagdeev, p. 279 (North-Holland Publishing Company, 1983).

[53] T. J. Ulrych and M. Ooe, in *Topics in Applied Physics: Nonlinear Methods of Spectral Analysis*, edited by S. Haykin, p. 73 (Springer-Verlag, 1979).

[54] S. J. Levinson, *Space-time Statistics of the Turbulence in the PRETEXT and TEXT Tokamak Edge Plasmas*, PhD thesis, University of Texas at Austin, 1986.

[55] R. D. Sydora, *Particle Simulation of Low Frequency Fluctuations in a Sheared Magnetic Field*, PhD thesis, University of Texas at Austin, 1985.

[56] J. M. Dawson, Reviews of Modern Physics **55**, 403 (1983).

[57] J. L. G. Jr., *Computer Simulation of Driven Alfvén Waves*, PhD thesis, University of Texas at Austin, 1986.

[58] S. Ichimaru, *Basic Principles of Plasma Physics* (Benjamin/Cummings, London, 1973).

[59] R. C. Davidson, in *Handbook of Plasma Physics: Basic Plasma Physics I*, edited by M. N. Rosenbluth and R. Z. Sagdeev, p. 519 (North-Holland Publishing Company, 1983).

[60] N. A. Krall and A. W. Trivelpiece, *Principles of Plasma Physics* (McGraw-Hill, New York, 1973).

[61] B. D. Fried and S. D. Conte, *The Plasma Dispersion Function* (Academic Press, New York, 1961).

[62] F. F. Chen, *Introduction to Plasma Physics* (Plenum Press, New York, 1974).

[63] H. Naitou, S. Tokuda, and T. Kamimura, J. Comp. Phys. **33**, 86 (1979).

[64] N. A. Krall and M. N. Rosenbluth, Phys. Fluids **8**, 1488 (1965).

[65] N. T. Gladd and J. Wendell Horton, Phys. Fluids **16**, 879 (1973).

[66] J. Thomas M. Antonsen, Phys. Rev. Lett. **41**, 33 (1978).

[67] W. W. Lee and H. Okuda, Phys. Rev. Lett. **36**, 870 (1976).

[68] W. W. Lee, Y. Y. Kuo, and H. Okuda, Phys. Fluids **21**, 617 (1978).

[69] W. W. Lee, W. M. Nevins, H. Okuda, and R. B. White, Phys. Rev. Lett. **43**, 347 (1979).

[70] R. D. Sydora, J. N. Leboeuf, and T. Tajima, Phys. Fluids **28**, 528 (1985).

[71] D. W. Ross and S. M. Mahajan, Phys. Fluids **22**, 294 (1979).

[72] J. N. Davidson and T. Kammash, Nucl. Fusion **8**, 203 (1968).

[73] W. W. Lee, J. Comp. Phys. **72**, 243 (1987).

[74] W. M. Tang, G. Rewoldt, and E. A. Frieman, Phys. Fluids **23**, 2454 (1980).

[75] R. Linsker, Phys. Fluids **24**, 1485 (1981).

[76] D. W. Ross and W. H. Miner, Phys. Fluids **20**, 1957 (1977).

[77] J. Wendell Horton, R. Estes, H. Kwak, and D. Choi, Phys. Fluids **21**, 1366 (1978).

[78] R. J. Hastie, K. W. Hesketh, and J. B. Taylor, Nucl. Fusion **19**, 1223 (1979).

[79] D. Choi and W. Horton, Phys. Fluids **23**, 356 (1980).

[80] L. Chen, M. S. Chance, and C. Z. Cheng, Nucl. Fusion **20**, 901 (1980).

[81] C. Z. Cheng and L. Chen, Phys. Fluids **23**, 1770 (1980).

VITA

Maurice Joseph LeBrun III was born in Baltimore, Maryland, on July 3, 1958, the son of Maurice Joseph LeBrun Jr and Betty Lou LeBrun. After completing his work at Overlea High School, Baltimore, Maryland, in 1976, he entered the University of Maryland, Baltimore County. In 1977 he transferred to the University of Maryland in College Park, Maryland, where he received the degrees of Bachelor of Science in Mathematics and Bachelor of Science in Physics in May, 1981. On August 16, 1981, he was married to Kathleen Elizabeth Amrhein. In the fall of 1981 he entered the University of Texas at Austin, and was employed as a teaching assistant in physics until January, 1983. He has been employed as a research assistant from January 1983 until the present.

Permanent address: 5504 Fence Row
Austin, Texas 78744

This dissertation was typeset[1] with LaTeX by the author.

[1] LaTeX document preparation system was developed by Leslie Lamport as a special version of Donald Knuth's TeX program for computer typesetting. TeX is a trademark of the American Mathematical Society. The LaTeX macro package for The University of Texas at Austin dissertation format was written by Khe-Sing The.

[82] K. W. Hesketh, Nucl. Fusion **20**, 1013 (1980).

[83] J. W. Connor, R. J. Hastie, and J. B. Taylor, Plasma Phys. **22**, 757 (1980).

[84] T. J. Schep, B. J. Braams, and F. Pegoraro, Phys. Fluids **25**, 1871 (1982).

[85] T. J. Schep and M. Venema, Plasma Physics and Controlled Fusion **27**, 211 (1985).

[86] J. W. Connor and J. B. Taylor, Phys. Fluids **30**, 3180 (1987).

[87] Y. C. Lee and J. W. Van Dam, in *Proceedings of the Finite Beta Theory Workshop*, p. 93 (1979).

[88] J. W. Connor, R. J. Hastie, and J. B. Taylor, Proceedings of the Royal Society of London **365**, 1 (1979).